UNIVERSITY OF SOUTHAMPTON

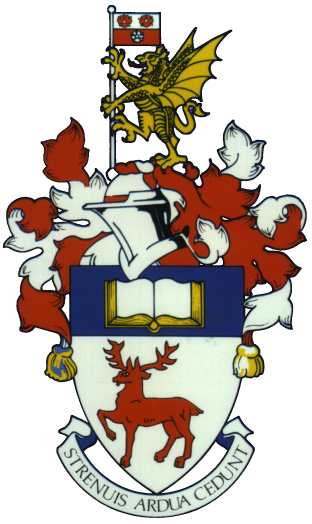

Stability of split structures: degeneracy breaking and the role of coupling

by

Andrii Iakovliev

A thesis submitted for the degree of
Doctor of Philosophy

in the
Faculty of Engineering and Physical Sciences

January 2021

UNIVERSITY OF SOUTHAMPTON
FACULTY OF ENGINEERING AND PHYSICAL SCIENCES

Doctor of Philosophy

STABILITY OF SPLIT STRUCTURES: DEGENERACY BREAKING AND THE ROLE OF COUPLING

by Andrii Iakovliev

ABSTRACT

The present work is inspired by the need to understand the elastic stability of a class of structures that appear in a variety of seemingly unrelated fields. Here we consider several problems involving the stability of two or more slender structures coupled at the ends. In a sequence, we consider a bilayer beam, then a multilayer split beam, chains of elastically coupled rigid rods, a plate with a symmetric cut out, and finally several plate strips elastically coupled. We also study the instability of a biological structure known as the mitotic spindle.

We report cooperative, competitive, and antisymmetric buckling of the bilayer split beam; and their dependence on the geometric parameters. Then we identify the mechanisms of elastic deformation, including additional strain induced by the misfit of two layers tied together at ends, that explains the observed behaviour. This is extended to buckling of a multilayer structure, i.e. a stack of thin elastic layers coupled at the ends. We also report rapid decay of the buckling amplitude of layers along the stacking direction, observed in simple experiments. We theoretically study a chain of elastically coupled rigid rods as the simplest model of this behaviour and report that coupled identical members, in the absence of any disorder, show spatially extended buckling modes, i.e. buckling amplitudes are periodically modulated. Analogies are drawn with a physically unrelated, yet mathematically close problem of wave propagation in periodic media. Introduction of irregularity leads to the spatial exponential decay of the amplitudes, i.e. localisation of buckling modes and thus associated Lyapunov exponents. We show that the strength of buckling localisation depends on the coupling-to-disorder ratio.

Next, we study the instability of rectangular plates with one or more cut outs placed periodically. The first problem reveals two types of buckling modes – in-phase buckling and out-of-phase buckling of the two elastically coupled plate strips. Energy contributions from cylindrical bending and twist of the coupling region drive the structure from degeneracy to where the mode character changes. The second problem of multiple strips elastically connected reveals that the in-phase and out-of-phase modes become periodically modulated and the respective buckling loads appear in clusters. If the structure is perfectly ordered, the entire clusters of buckling loads are inverted in the degeneracy point via N-fold crossing. Infinitesimally small disorder triggers repulsion of eigenvalues and strong localisation occurs. We characterise this effect comprehensively by calculating Lyapunov localisation factors and report regions of structural parameters for which high and moderate sensitivity to disorder is observed.

Finally, mitotic spindles were studied using continuum modelling of the slender bio-structures also accounting for the interaction with the environment of the cell. Interesting buckling modes with spatial features such as coupled bending and torsion of filaments were observed.

Contents

List of Figures

Page

Abbreviations

aMT astral microtubule xv, xvi, 155, 156, 158, 159, 167, 169–173

DSMM Dynamic Stiffness Matrix Method 12

EVP eigenvalue problem 9, 12, 57, 64, 74, 80, 133, 141, 152, 185

FEA finite element analysis x, xi, xiii, 1, 11–13, 15, 38, 41, 42, 45, 46, 51, 52, 57, 59, 65–68, 71, 94, 96, 117, 120, 124, 157, 166, 183

ipMT interpolar microtubule xv, xvi, 155, 158, 159, 162, 164, 165, 169–172, 175

khMT kinetochore microtubule 155

MAC Modal Assurance Criteria 45, 46

MT microtubule 154, 156, 159

SDSBT Shear Deformable Split Bilayer Beam Theory 13

SEM scanning electron microscopy ix, xv, 27, 154, 155

Nomenclature

A cross-section area 56, 62

E elastic modulus of the material 41, 42

EI bending stiffness of a beam 58, 60

EI_c bending stiffness of a protein motor/connector 158

G shear modulus of the material 62

I second moment of cross-section area 42

L beam, rod or plate length in meters ix, 33, 41, 76, 77

L_c length of a protein motor/connector 158

L_m length of the antiparallel overlap between bundles of ipMTs 155

L_p distance between the centrosomes in a bipolar spindle 155, 158

P compressive loading in newtons ix, 31, 33, 38, 41, 58, 77

P_{cr} a critical value of compressive loading at which structural stability is lost due to buckling 31, 33, 41

T absolute temperature in K 156

U elastic strain energy of a structure 41, 58, 59

V potential energy due to external loading 41, 59

$\Delta(x)$ misfit between the upper and the lower half of the split beam 54

Π total potential energy of a structure 41, 59

$\bar{P}$ non-dimensional critical buckling load 42, 44, 108, 109, 118

$\bar{\alpha}$ ratio of cut out width to the overall width of a plate xiii, xiv, 103, 107–112, 115–119, 133, 144, 181

$\bar{h}$ is a beam thickness relative to the beam length x, xi, 35, 38, 41–47, 49, 52, 55, 61, 62, 64–68

$\bar{k}$ unit-cell coupling parameter $\bar{k} = kL$ 77

$\bar{k}_0$ unit-cell parameter for the chain of rigid rods. $\bar{k}_0 = k_t/L + 2kL$ 77

Glossary

Fission Yeast also called *Schizosaccharomyces pombe* is a unicellular eukaryote and a species of yeast used in traditional brewing. They are useful model organisms to study mitosis as they produce daughter cells of equal size. (Definition form Wikipedia) 6

hourglass effect is a numerical effect of FEA due to reduced integration scheme in elements. Reduced integration improves computational efficiency and reduces shear locking but makes elements excessively soft. An insufficient number of integration points may not capture all the deformation energy accumulated in the solid thus allowing for softer non-physical response [Sun, 2006]. 39

reference point is a convenient construct within *ABAQUS* that allows the specification of loads, boundary conditions, contact properties, etc. at a single point which is then linked to the respective nodes in the actual geometry. The full benefit of reference points is realised in scripting for *ABAQUS*, where a single variable can reflect complex loading or boundary conditions thus minimising the amount of code. 40

shear locking is a numerical effect of FEA due to the linear nature of quadrilateral elements which cannot assume a curved shape. Instead, they develop "parasitic" shear deformation which makes structural response stiffer than in reality [Sun, 2006]. 39

Anaphase B is the late stage of Anaphase coming after Metaphase and before Telophase in mitosis. It is characterised by the chromosomes of the parent cell being split and moved towards centrosomes (poles) of the daughter cells [Tolić, 2017]. 6

bundle of microtubules is an organised collection of microtubule filaments stiffly coupled by protein bridges and motors. ix, 28, 29

centrosome is a special region of the cytoplasm from which the microtubules grow towards the cell membrane. xv, 27, 154, 159

connector is short protein links that bind microtubules together in bundles. xv, 154, 159, 165

instability cluster is a subset of the eigenvalue spectrum of the generalised eigenvalue problem of a periodic structure in buckling. All the eigenvectors associated with the eigenvalues in the cluster differ by phase only. This is reflected in a spatial modulation of buckling amplitude of each member of a periodic structure. 88

localisation factor is the factor of Lyapunov exponent that represents strength of localisation 86

microtubule is a hollow protein filament with a cylindrical cross-section. The stiffest member of the cytoskeleton. xv, 27, 29, 154, 173, 179, 182

Mid-zone is a subregion of the interpole region in a spindle where the growing ends of interoplar microtubules are linked with connectors and motors. The main spindle pull is generated here. xv, xvi, 155, 158, 159, 165, 172

mitosis is a cell division mechanism, following which, a cell divides its genetic information between the two daughter cells and ensures that they are genetically identical to the parent cell. 27, 29, 153, 157, 165, 167, 182

mitotic spindle is a complex hierarchical structure composed of microtubules, centrosomes and connectors. Its main function is to preserve the structural shape of the cell and to generate forces needed to split the parent cell into two daughter cells. ix, xv, 6, 27, 29, 154, 156, 164, 166, 167, 172, 177, 179, 182

near-degeneracy is characterised by two or more eigenvalues spaced so close that the inner product of the associated eigenvectors is not zero. x, 47, 48

Near-pole zone is a subregion of the interpole region in a spindle where interoplar microtubules are attached to centrosomes. xvi, 155, 165

phase is a region within a phase diagram that characterises a certain type of behaviour. 45–48

phase boundary is a line on a phase diagram that separates regions with qualitatively different behaviour. 45–48

phase diagram is a type of chart used in physics, material sciences and other branches of science to characterise the variability of the system's behaviour depending on a set of parameters. Phase diagrams can be constructed if one is able to identify intervals of governing parameters characterised by the same type of behaviour. 45, 46, 48, 51

spindle length is a distance between two centrosomes in a bipolar spindle typically labelled as L_p 155

transfer matrix is a matrix that relates the state vector of cell i to the state vector of cell $i+1$ in a periodic structure. 85

unit cell the smallest member of a periodic structure which has the symmetry properties of a whole structure 77

Declaration of Authorship

I, Andrii Iakovliev, declare that this thesis entitled 'Stability of split structures: degeneracy breaking and the role of coupling' and the work presented in the thesis are my own, and have been generated by me as the result of my own original research.

I confirm that:

- This work was done wholly or mainly while in candidature for a research degree at this University;
- Where any part of this thesis has previously been submitted for a degree or any other qualification at this University or any other institution, this has been clearly stated;
- Where I have consulted the published work of others, this is always clearly attributed;
- Where I have quoted from the work of others, the source is always given. With the exception of such quotations, this thesis is entirely my own work;
- I have acknowledged all main sources of help;
- Where the thesis is based on work done by myself jointly with others, I have made clear exactly what was done by others and what I have contributed myself;
- Parts of this work have been published as described further.

Signed:

Date: 5 January 2021

Parts of this work were published in research journals, conference proceedings and presented in conferences.

Journal and conference publications

1. Andrii Iakovliev. Response localization in disordered structures governed by the Sturm-Liouville differential equation. (Review). Journal of Mechanical Engineering NTUU Kyiv Polytechnic Institute, (74):123–132, January 2015. doi:10.20535/2305-9001.2015.74.51048

2. Andrii Iakovliev. Exact Elastic Stability Analysis Based On Dynamic Stiff- ness Method. Journal of Mechanical Engineering NTUU "Kyiv Polytechnic Institute", 2(77):108–118, 2016. ISSN 2409-5966. doi:10.20535/2305- 9001.2016.77.78904

3. Andrii Iakovliev, Srinandan Dasmahapatra, and Atul Bhaskar. Stability of mitotic spindle using computational mechanics. In ACM Conference Proceedings, page 8, Singapore, January 2019. ACM. ISBN 978-1-4503- 6654-0

Conference presentations and posters

1. Andrii Iakovliev. Instability of split elastic structures. Bologna, Italy, July 2018. ESMC 2018

2. Andrii Iakovliev. Structural stability of a Mitotic Spindle: Parametric Finite element approach. Harrogate, UK, September 2018. PhysCell 2018

3. Andrii Iakovliev. Stability of mitotic spindle using computational mechanics. Singapore, January 2019. ICBBB 2019

In preparation

1. Andrii Iakovliev, Srinandan Dasmahapatra, and Atul Bhaskar. Cooperative vs competitive buckling of split structures: Instability behaviour and phase diagrams. Proceedings of the National Academy of Sciences

2. Andrii Iakovliev, Srinandan Dasmahapatra, and Atul Bhaskar. Buckling phase diagram of a plate with a cutout. Tentative

3. Iakovliev, Andrii; Dasmahaptra, Srinandan; Bhaskar, Atul. Inverted modulation of buckling mode amplitudes in a plate with periodic cutouts. Tentative

4. Iakovliev, Andrii; Dasmahaptra, Srinandan; Bhaskar, Atul. Patterns of buckling mode localisation in Anaphase B of mitosis. Tentative

Acknowledgements

This project was supervised by Prof. Atul Bhaskar and Dr. Srinandan Dasmahapatra, whose guidance and support throughout this Ph.D. have been very valuable.

The Ph.D. was funded in part by a grant from Erasmus Mundus ACTIVE programme.

The author acknowledges the use of the IRIDIS High Performance Computing Facility, and associated support services at the University of Southampton, in the completion of this work.

The author also acknowledges Dr. Svitlana Braichenko, Kevin Jose, Dr. Enrique Cuan Urquizo and Hayk Vasilyan for most valuable discussions and support at various stages of this work.

Chapter 1

Introduction

The study of elastic instability is of great importance to a number of practical problems in science and engineering. The phenomenon was first studied for classical engineering structural elements such as beams, plates and shells usually subjected to compression. The problem of the structural stability of tall columns in architecture has interested engineers for a long time in human history. Structures exhibit small elastic deformations but remain stable as the applied loading is gradually increased from zero. However, this externally imposed load may reach a certain critical value at which the structure goes through a transition – from being stable to unstable. Following this, the elastic structure collapses, if the loading is increased further, leading to a catastrophic failure accompanied by large post-buckling deformations. Such a situation is common in many practical engineering sectors – from civil to automotive engineering, mechanical and aeronautical engineering, or bio-mechanics.

Beyond simple structural shapes and boundary conditions, the prediction of forces that destabilise a structure is analytically difficult due to the mathematical complexity associated with the problem. Traditionally, buckling of structures, typically encountered in engineering, have been modelled numerically. A common approach is that of FEA. It converts a continuum problem of elastic instability, which involves differential equations leading to an operator eigenvalue problem, to one with a finite number of degrees of freedom, resulting in an algebraic eigenvalue problem. The compromise inherent to the procedure is that the results are approximate. For most practical situations, this is satisfactory, if the size of the discretised model is large enough. However, such an approach lacks a generic understanding of the phenomenon. In particular, the parametric dependence of the critical force associated with instability (known as buckling force) are not available in a functional form, and only answers to specific structural geometries could be approximately computed.

In the last few decades, structures made of composite materials such as laminates have widely replaced the classical use of metal alloys within many high-performance structures due to light-weight, high strength, impact and fatigue resistance. Nevertheless, the structural performance of laminates is highly affected by the bonding between the layers, and the presence of inter-ply delaminations dramatically weakens the composite. Delaminations critically reduce the structural performance of laminates under compression leading to instability, rapid debonding of entire plies due to propagation of delaminations and abrupt failure of such structures in operation. Furthermore, identification of instability regimes for such structures is more challenging compared to the traditional materials due to layered morphology, inhomogeneity and anisotropy. Physical dimensions of the structures, the number of layers and their stacking orientation, the

type of adhesive materials, the position and orientation of delaminations in multilayered composites affect their instability. Surprisingly, the survey of the literature in the field [Kachanov, 1976, Chai et al., 1981, Cho and Kim, 2001, Liu et al., 2011, Juhász and Szekrényes, 2017] suggests that despite such a number of factors and complexity of interactions between them, most laminated beams and plates assume certain specific types of buckled shapes. While the mentioned factors greatly affect structural capacity and the critical buckling loads of the composites, there seems to be a generic underlying mechanism that is associated with the geometry, and particularly with the layered morphology, that drives delamination buckling to occur in a specific manner. Instability behaviour of plates and beams with holes and cut outs that are widely used in construction also suggest that there may be generic geometric features of these structures that favour specific types of buckling.

The study of elastic instability is also important to several problems outside of the domain of traditional structural mechanics. For example, thin films on compliant substrates are often viewed as bilayer systems [Xu et al., 2015] whose wrinkling (instability phenomenon) is found in printed electronics, microelectronics and flexible semiconductor devices. At a large scale, instability of multilayer structures is found in the folding of geological strata formations [Dodwell and Hunt, 2012], where the folded shape of the strata is affected by instability as well as by lateral compression from the surrounding soil. The morphological similarities between these structures also suggest certain similarity in the shapes that these structures assume when unstable.

Buckling is usually associated with harmful effects, however, in innovative designs, it could be potentially profitably used. For example, the shape change due to large deformations induced by buckling is beneficial for actuation of soft mechanisms [Yang et al., 2015]. Desired shape reconfiguration may be also induced into soft structures via large deformations due to wrinkling and folding [Shim et al., 2012, Yang et al., 2015]. Particularly, auxetic metamaterials contract instead of expanding under compression due to reconfiguration of the cuts [Bertoldi et al., 2010].

The deformed shape assumed by the structures with regularly placed holes and cut outs may be controlled by changing the relative size and orientation of these features [Javid et al., 2016]. Regularly perforated soft structures are also used for tailored wave propagation – phononic crystals. Compression of these structures leads to instability induced shape reconfiguration which alters wave propagation characteristics allowing fine-tuning of these devices [Wang et al., 2013]. A curious device for wave-like translation of a mechanical signal is suggested by Raney et al. [2016] who consider a chain of coupled bistable beams. Snap-through buckling of the first beam triggers buckling of the following ones along the chain leading to the translation of the mechanical signal. Interestingly, due to rapid, switch-like onset, buckling may be used as a control mechanism in nano-scale electromechanical devices as suggested by Weick et al. [2010]. Also, Savel'ev et al. [2006] investigate the possibility of creating qubits operating on buckling of nano-bars in an alternating electric field.

Instability phenomena also widely occur in living organisms. For example, organisms, such as *Vibrio alginolyticus* bacteria, move by exploiting finely tuned buckling of their hook [Son et al., 2013] induced by the alternating hydrodynamic load as they swim. Furthermore, elastic instability, or buckling, was shown to play a crucial role in morphogenesis and the development of living organisms from individual cells [Ward et al., 2014] to tissues and even entire organs [Richman et al., 1975, Budday et al., 2014].

Most of the mentioned problems share certain geometric similarities – either layered morphology with delaminations or of the presence of holes, cut outs and perforations that affect the behaviour. A most important aspect of multi-layer structures is the translational periodicity from one layer to the next. Again resorting to idealisations, here we consider several elastic layers coupled at the ends using other elastic structures. Likewise, the structures with holes and cut outs are periodic due to the regular placement of these features.

We identify interesting analogies between this problem and that of waves in periodic media that have been studied before. The one-dimensional case is mathematically treated by the Floquet-Bloch theory. For media with two or three-dimensional periodicity, the generalisation was provided by Brillouin. In this work, we consider the one-dimensional case only.

Periodicity plays a crucial role in problems of propagation of electromagnetic waves in crystals [Brillouin, 2003, Anderson, 1958], waves in period elastic structures [Phani et al., 2006], a vibration of regularly assembled coupled structures such as multi-span beams and chains of oscillators [Hodges and Woodhouse, 1983, Castanier and Pierre, 1995]. These problems are relatively well understood. It has been demonstrated that the properties of individual members forming periodic assemblies as well as the properties of coupling between them may be viewed as determinants of the behaviour.

Surprisingly, very little fundamental research has been dedicated to buckling of structural assemblies consisting of coupled members. Mostly, this research was carried out along the studies of wave propagation with the notion that buckling problems reveal similar behaviour to vibration problems due to mathematical similarity [Pierre and Plaut, 1989, Xie, 1995, Li et al., 1995]. Also, the analysis of the available literature [Chai et al., 1981, Cho and Kim, 2001, Rodman et al., 2008, Juhász and Szekrényes, 2017] suggests that studies focused on the buckling of layered structures such as laminated composites rarely make connection with the studies of buckling of periodic structures carried out by researchers from the wave propagation field. Furthermore, there is no evidence of any research concerning the transverse localisation of a buckling mode across layers of layered structures except for several studies in the geology of strata [Hunt et al., 2006, Dodwell et al., 2012b, Dodwell and Hunt, 2014].

1.1 Motivation

The motivation of the present work arises from a number of related problems in seemingly unrelated fields. All of these problems have some common features, despite apparent differences in their physical or technological contexts. In particular, structures in aeronautical constructions are frequently composed of laminates that delaminate due to the failure of inter-lamina bonding. It is of interest to assess the structural performance of such delaminated structures and its residual resistance to instability. While real laminates are invariably made of orthotropic plies, here we consider various abstractions leading to a bilayer structure composed of isotropic material. One of the reasons for this simplification is to study a mechanical abstraction that retains just one specific geometric feature of the problem – the split within the structure. Moreover, when laminates split apart, the two sides may be unequal in thickness and their properties may be neither purely orthotropic, nor isotropic, but a stack of orthotropic layers bonded together, whose mechanics is governed by the classical laminate theory. However, in the present work, we

consciously simplify these aspects of realism in order to understand the role of the end structures that join the ends of the split parts together. Further, only symmetric splits are studied here.

Instability of bilayer beams also occurs in a number of cases outside of composite materials. Consider an example of the bilayer beam buckling in a simple practical example – a carrying pouch shown in Fig. 1.1 (a). The scaffold of the pouch is made of two identical metal strips coupled at

FIGURE 1.1: Example of a bilayer beam buckling – compression of the pouch from both ends triggers opening (a) via buckling of the internal metal frame (b).

their ends. Compression typically applied by fingers at both ends, triggers buckling of the strips driving them in the opposite directions thus opening the pouch as shown in Fig. 1.1 (b). This is a simple and obvious manifestation of bilayer beam buckling. There are also many examples where instability of bilayer beam may be of interest outside of the mechanical engineering context, such as in nano-electromechanical devices as previously discussed.

Cold-formed beams and plates with holes, cut outs and perforations also assume specific types of buckling shapes that indicate the particular role of these geometric features and the regularity of their placement on the behaviour. From the geometric point of view, this places them in the same class of structures as the bilayer beam mentioned earlier. Motivated by this, we study a representative problem – a plate with a single symmetric rectangular cut out under compression followed by the same problem with multiple identical orderly placed cut outs.

Finally, the instability behaviour of assemblies of nominally identical structures joined at the ends that appear in living organisms, such as bundles of microtubules [Soheilypour et al., 2015], resembles the buckling modes of the bilayer and multilayer beams. This motivates us to consider the sub-cellular protein filaments and their bundles as from a geometric point of view, they also fall within a class of structures that motivate this study.

1.2 Aims and objectives

The present work aims to understand the instability behaviour of bilayer structures with splits in a comprehensive way, as opposed to previous attempts that are specific to certain geometrical parameters. Another aim is to understand this when the structures are multilayered. Following this, we aim to explore the phenomenon generically in the case of coupled plates. Finally, we aim to study the role of disorder in the instability of coupled periodic elastic structures.

The objectives of the present work are:

- To study the instability behaviour of a bilayer beam with a symmetrically positioned split and to explain the observed behaviour in terms of fundamental geometric features of the problem.
- To explore the case of a multilayer structure by studying a number of identical orderly positioned coupled members.
- To understand the effects of disorder on the otherwise regular assembly of coupled members.
- To study the instability behaviour of a plate with a single symmetrically positioned rectangular cut out as another case of a structure consisting of coupled members.
- To understand the behaviour of a similar plate with multiple cut outs.
- To study how the disorder in the plate with multiple identical cut outs affects the instability behaviour.
- To study a more generic case of buckling of a structural assembly of protein filaments within the sub-cellular structures such as a mitotic spindle during the cell division process.

Note, that we start with one-dimensional structures such as a bilayer beam, and proceed to the two-dimensional problem of coupled plates followed by a three-dimensional spatial assembly of beam-like protein filaments. This allows us to study the instability of the entire class of structures by considering a number of representative problems.

1.3 The scope of the research

Elastic instability phenomena in a number of seemingly unrelated contexts share several common geometric features. The studied structural systems either consist of arrangements of coupled members (such as layered composites, strata, bundles of microtubules) or possess certain geometrical features such as holes, cuts, splits, etc., (such as beams/plates with holes/cuts) that can be considered local relative to the overall size of the structure.

Therefore, we set out to study a minimal case of the instability of a beam having a longitudinal cut out. If the split is long compared to the length of the beam, the model effectively represents a bilayer structure. Both layers are thus coupled at the ends. In the other extreme, the split is short. This reflects the case of a structure having local geometric discontinuity or defect such as a small split, hole or delamination. All cases in between are captured by changing the length of the split in small increments. Assuming the split length and the beam-column thickness as two principal parameters, we describe the instability behaviour comprehensively via a map of buckling states in the parameter space. The phase diagram here resembles those encountered in material science and physics.

We seek to expand the analysis to the case of a multilayer structure. We perform a simple experiment on a stack of cardboard sheets to observe the rapid decay of the buckling amplitude along the stacking direction. We associate the behaviour with the effect of localisation. Then, we study a simple problem to demonstrate how periodic structures buckle. A chain of coupled rods is proposed as an expository device to determine the principal characteristics of such behaviour.

Finally, we study the effect of small random irregularity (disorder) on buckling of the chain of nominally identical rods and report weak and strong localisation of buckling mode (similar to Anderson localisation in waves [Anderson, 1958]).

Then we study a two-dimensional case of a coupled or split structure, i.e., instability of a plate with a single rectangular symmetrically placed cut out. We develop a comprehensive description of the instability behaviour in the form of a phase diagram calculated in the plane of structural parameters. We suggest such a map to be used as a helping tool in selecting the appropriate designs in engineering. This may be particularly useful in the design of fire doors with windows as they often undergo thermal buckling and a precise prediction of the buckling mode is crucial.

The plate problem is then extended to account for a number of regularly placed cuts. We approach this problem making use of geometric periodicity. We adopt the mathematics employed in the analysis of a chain of rigid rods here as well. We also present a phase diagram for this problem and track how the buckling loads change as we move within the phase plane. We observe an inversion of the entire spectrum of the problem upon traversing the phase boundary. As a result, the highest buckling mode of the plate becomes the fundamental one in the adjacent phase. This is accompanied by a dramatic change of buckling character. Finally, we also study the effect of disorder on the localisation of buckling amplitudes of the plate.

Bilayer beam and a plate with cut outs inspired us to look at a more complex case – elastic stability of 3D arrangement of coupled members. Such assemblies are observed within a mitotic spindle and are called bundles of microtubules. Owing to the complexity of the problem, we study the buckling of an entire mitotic spindle of *Fission Yeast* cell in late Anaphase B computationally. The study is performed using a custom-made software called SpindleFEA. We report cases of strong localisation of buckling amplitude in the spindle followed by bending-torsion modes of microtubules under high compression. Resembling behaviour has recently been observed in an experiment by Novak et al. [2018].

1.4 Layout of the thesis

The introduction, motivation and scope of the research is highlighted in the present chapter. Chapter 2 provides a review of the literature specific to the instability behaviour of layered structures and other curious examples of buckling. Chapter 3 is focused on the numerical study of a beam column with a longitudinal cut in compression. The study on the buckling of the same split beam using an assumed modes approximation followed by the application of the principle of minimum total potential energy is covered in Chapter 4. Chapter 5 is focused on the study of buckling of a chain of regularly placed identical coupled rigid rods as an expository problem, which possesses the two essential features – periodicity and coupling specified in the simplest possible form. In Chapter 6 we analyse the instability behaviour of a plate with a rectangular symmetrically placed cut out. Moreover, Chapter 7 extends the previous analysis to the case of a plate with multiple cut outs. The manifestation of buckling in a biological problem is presented in Chapter 8 where we focus on elastic stability of a mitotic spindle of *Fission Yeast* cells in Anaphase B. Finally, conclusions and directions for future research are discussed in Chapter 9.

Chapter 2

Review of relevant literature

Layered structures frequently delaminate because of the failure of adhesive bonding. It is of great interest to assess the residual buckling strength of such structures, as it is expected that this would depend on the size and the geometry of delamination. Other structures found in seemingly unrelated scientific contexts often exhibit instability behaviour that depends on geometric features such as holes, cuts and joints significantly. For example, perforated beams and plates in engineering, nano-electromechanical switches, assemblies of protein filaments in cells often reveal puzzling instability behaviour that is also reviewed in this chapter.

The subject of stability of laminates with existing delamination developed along with the composite materials technology itself and spans over the last forty years. Similarly, the study of structures with holes, splits and cut-outs in beams and plates have a major impact on technologies in civil and mechanical engineering. There is also a body of research focused on functional buckling of structured materials and buckling induced shape transformations as well as instability controlled deformation. The idea of functional buckling is to use instability phenomenon to one's advantage by intentionally encouraging buckling to occur in a pre-designed manner.

Here we review representative papers from all these seemingly unconnected areas of science. We demonstrate how instability induced deformation patterns appear at a range of length scales for different physical problems, thus suggesting common ground in terms of the mechanics and the observed behaviour thus arising. These similarities in the observed behaviour across different fields, as identified in this chapter, serve as motivation for the present study.

2.1 Buckling of delaminated composites

Delamination is the long-known problem in the mechanics of layered composite materials. Multiple internal defects in composite beams, columns and plates often initiate inter-ply delaminations and result in de-bonding of layers. Stress and strain distribution, as well as an inter-ply coupling strength in laminates, alter dramatically as de-bonding occurs and consequentially the strength of the laminates considerably reduces. Therefore, laminates are particularly sensitive to axial compression leading to buckling of delaminated plies which is a major cause of failure of such structures under compression or bending [Lee et al., 1996, Hu et al., 1999, Remmers and de Borst, 2001, Juhász and Szekrényes, 2017]. The optical microscopy image of single-ply delamination shown in Fig. 2.1 (a), taken from Remmers and de Borst [2001], shows local flaking

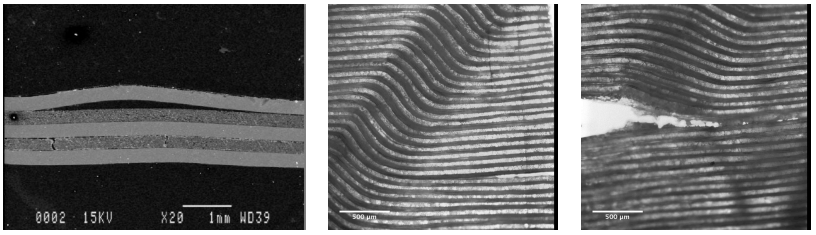

(a) (b) (c)

FIGURE 2.1: Examples of inter-ply delamination in laminated composites under compressive loading. (a) Microscope photography of a layered composite with delaminated top ply obtained by Remmers and de Borst [2001]. This is an example of small-scale delamination. For comparison, a micro-scale view of a laminated composite under compression with well-bonded layers is shown in (b). The photo is adapted from [Peralta, 2013]. Micro-scale view of a laminated composite under compression with splitting symmetric delamination is shown in (c). The photo is adapted from [Peralta, 2013].

of a top layer of a laminate under compression. A structure with well-bonded layers in buckling is shown in Fig. 2.1 (b), while a large centrally splitting delamination is shown in Fig. 2.1 (c). The last two images are reprinted from [Peralta, 2013].

Laminated composites have been studied in the past to assess failure characteristics and to calculate buckling forces when a failure occurs. Many studies are focused on increasing the accuracy of the stress calculation, better resolution of deformation fields, fracture due to delamination, etc., as they aim to develop better calculation procedures for structural engineers. A natural starting point to study the stability of layered structures is to consider a bilayer structure. Following this, the next step would be to consider multilayered structures. The connection between the buckling of layered structures and buckling of periodic structures has not been made in the past. Since we found this connection, here we also present the literature with the concepts of periodicity and coupling in mind to suggest where the gap between the fields of layered structures and periodic structures may be filled with the help of a bilayer beam beam investigated within this thesis.

One of the earliest investigations in the area of the mechanics of layered structures is the study of the splitting strength of layers of mica by Obreimoff [1930]. The author analysed the strength of a thin layer peeling off a sufficiently stiffer sub-layer of mica, as schematically depicted in Fig. 2.2. In the model, the sub-layer was considered rigid. Hence, the total energy of the delaminated

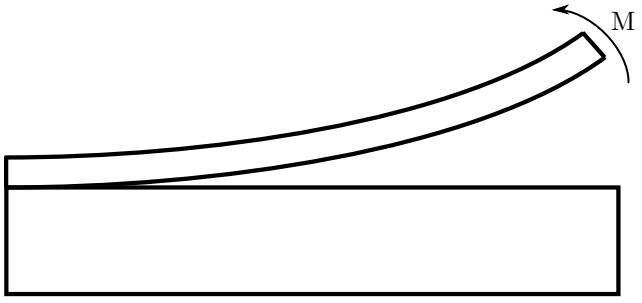

FIGURE 2.2: A schematic representation of a thin layer of mica split from the rigid sub-layer by applying bending moment M. The figure is adapted from Obreimoff [1930].

layer was calculated relatively easily, and the force required to separate the top thin layer was obtained. The study by Obreimoff [1930] is one of the earliest attempts to model each member of the layered structure independently and then consider the interaction or coupling between the

members. The key simplifying assumption of the model is the perfect rigidity of the sub-layer which is a reasonable assumption when the thickness difference between the single layer and the substrate is large. However, despite the similarity in the geometry, the key motivation of the present study is very different, i.e. to study the stability of *an already delaminated structure* under compressive loading, rather than the existing work that is about the separation of the two elastic layers when one is peeled off due to bending moment applied.

Vizzini and Lagace [1987] proposed a simple but comprehensive model of a single lamina assuming the sub-layer to be infinitely rigid, which is also an assumption made by Obreimoff [1930]. The model contains two structural parameters – the length of delamination relative to the length of the lamina and the stiffness of coupling between the lamina and the sub-layer, as schematically shown in Fig. 2.3. The effect of coupling was modelled via a distributed spring, where the

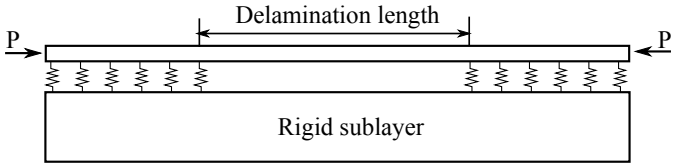

FIGURE 2.3: A schematic representation of the model proposed by Vizzini and Lagace [1987]. A single delaminated lamina is studied to be split from the absolutely rigid sub-layer due to the compressive loading P. Delamination length and the strength of coupling are the two governing parameters.

stiffness of the spring mimics the strength of elastic coupling and the length over which the spring is distributed is the length of the coupling part. The minimum total potential energy principle was applied with the assumed functional form for the deflected shape of the lamina. The strain energy of the lamina was assumed to consist of the bending and coupling energies coming from the distributed spring. The stiffness of the spring was specified in a piecewise manner. The minimisation of the total potential energy leads to the generalised eigenvalue problem (EVP) from which the critical buckling load was computed for various delamination lengths and coupling parameters.

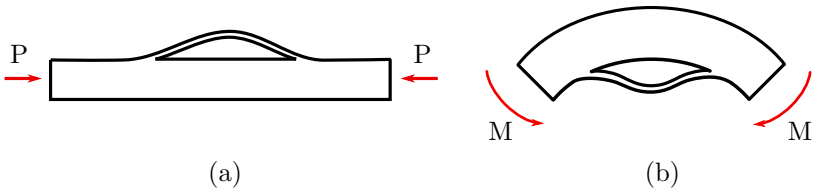

FIGURE 2.4: Schematics of the delamination in a compressed laminate (a) and the laminate in bending (b) studied by Kachanov [1976]. The figures are reproduced from [Kachanov, 1976].

The separation of delaminated layers under compression was studied using the energy principles by Kachanov [1976]. Two types of flaking of the delaminated layer were studied – the compression case (depicted in Fig. 2.4 (a)) and the bending case (depicted in Fig. 2.4 (b)). The author considered the delamination as a loss of equilibrium which occurs when the elastic compression energy U_1 accumulated in a straight structure becomes equal to the sum of the bending energy U_2 and the work of rupture W as $U_1 = U_2 + W$. Using assumed deflected shape of a lamina, the author derives a scaling expression for the bending energy in compression case (a) $U_2 \sim \sigma h^3$ and bending case (b) $U_2 \sim Eh^3$. Here, σ is compressive stress induced by P, E is the elastic modulus of the material and h is the thickness of the delaminated layer. These simple energy

expressions allow the estimation of the critical stress (and load) by minimising the total energy with respect to generalised coordinates.

All the above-mentioned studies share the same principal assumption of a single flexible layer delaminated from a much stiffer substrate. While this supports a relatively simple calculation to be carried out to estimate the buckling stress and the delamination energy, such an assumption becomes invalid when the layers have comparable stiffness. Therefore, the scope of the studies that benefit from a thin strip assumption (for example [Wan-Lee, 1985]), is limited to predicting local buckling of a single layer. These studies do not allow the behaviour of an entire structure to be resolved, not to mention a delaminated structure with multiple layers.

A delaminated structure with layers that possess various ratios of stiffness on the two sides (one side infinitely stiff, one side very thin compared to other side that has finite stiffness, both sides with equal stiffness, or the two sides with unequal but comparable stiffness) was first studied by Chai et al. [1981]. They adopted the previously studied case of a thin delaminated layer from a rigid sub-layer but also introduced the model of a thick but flexible column with delamination, a column with multiple delaminations, a column with symmetrical delamination and a general case of an arbitrary positioned single delamination. The latter is depicted schematically in Fig. 2.5. Although their approach was analytical, their assumption of the buckled mode shape did not enable them to explore the rich mode types that buckling of symmetrically split structures afford. The "thick column" model introduced by the authors is an intermediate step between

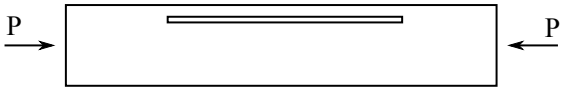

FIGURE 2.5: A schematic representation of a beam with arbitrarily placed delamination studied by Chai et al. [1981]. Depending on the location of the split, the model corresponds to either thin film assumption or to layers with comparable stiffness assumption.

the single-layer models proposed before and a generic case of an arbitrarily placed delamination later introduced by the authors. Here, the delaminated layer is assumed to be flexible and the sub-layer is assumed to have large but finite rigidity. Thus, the sub-layer is allowed to deform although very little compared to the delaminated layer. The next step is a "symmetric" model assuming the split layer and the sub-layer are equally rigid. Finally, in a general case, the authors resolve the behaviour depending on the arbitrary ratio of rigidity between the delaminated layer and the sub-layer. Similarly to the previous studies, the authors made assumptions about the buckling mode shapes and employed the minimisation of the total potential energy to estimate the critical buckling load. In the case of arbitrarily placed delamination, the assumed mode was defined in a piecewise manner. However, this study did not attempt to categorise lowest mode types according to their shapes–something we look at in details in the next chapter. Also, it appears that the assumed mode is committed to just one type, a restriction we remove later in this thesis, which enables us to provide a comprehensive picture for the buckling mode types for the lowest mode, using a so-called *instability phase diagram*.

Having abandoned the assumption of a rigid sub-layer, Chai et al. [1981] studied the interplay between the local buckling mode of each member in a structure and the global buckling mode of the whole structure for the first time. The authors showed that the actual buckling mode consisting of a superposition of local and global modes that are equally important. Larsson [1989] applied this idea to study the buckling and delamination growth in circular plates. They

demonstrated how the interplay of local and global buckling affects the resulting instability mode for the case of axisymmetric circular plates for isotropic and circumferentially orthotropic material.

Lee et al. [1996] studied the buckling of circular plates with a penny-shaped delamination using a finite element procedure. Their analysis is based on the non-linear von Karman plate theory with a criterion that ensures the avoidance of ply overlap. That was the first attempt to impose rules on the interpenetration of structural members. The authors calculated the buckling load for a set of design scenarios characterised by different delamination radius a and plotted the dependence of the buckling load on a. They report the three principal buckling characters exhibited by the structure for different a – a global one-wave mode, a local one-wave mode and a global two-waves mode. The authors explained this behaviour by an interplay of local buckling, in the vicinity of delamination, and global buckling, which is associated with the instability of an entire plate.

Hu et al. [1999] applied FEA using a customised element, based on Mindlin plate theory, to the buckling of laminated plates with multiple embedded delaminations. They also considered the ply overlapping possibility by introducing artificial springs proportional to the fictitious forces in the contact area. The authors reported that the delamination size, shape and placement has a strong effect on the critical buckling load and the lowest buckling mode.

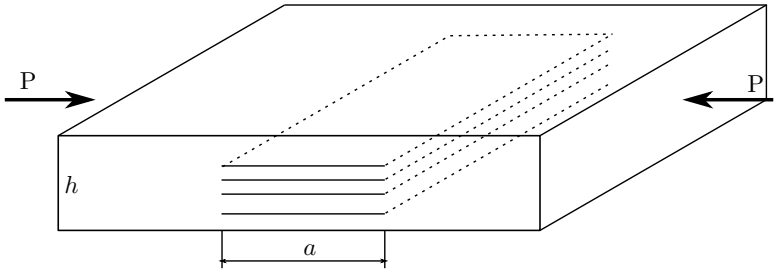

FIGURE 2.6: A schematic diagram of a plate studied by Cho and Kim [2001]. It features multiple delaminations a stacked across the plate thickness h. Adapted from Cho and Kim [2001].

Cho and Kim [2001] implemented a higher-order Zig-Zag theory in their study of a composite plate with multiple delaminations. A schematic rendering of the problem geometry is depicted in Fig. 2.6. The authors performed a more detailed parametric study varying the relative delamination length in small increments and evaluating the critical buckling load and the associated mode at each step. They consider that delaminations are located arbitrarily with respect to thickness h (see Fig. 2.6). They then report several buckling load-delamination length dependencies for various placements of the delaminations with respect to thickness. Based on comparison with the alternative studies, the authors report an excellent accuracy of the customised FEA based results. The authors also report the observation of the three qualitatively distinctive buckling mode types (similar to the ones reported by Lee et al. [1996]). These are also attributed to an interplay between the local and the global buckling.

Timoshenko-Mindlin plate theory along with the other higher-order plate theories (such as Zig-Zag theory) that account for shear distribution along plate thickness are widely used in engineering practice. They tend to predict the experimental observations reasonably well. It should be noted, however, that their strict variational consistence was not proven. For example, Elishakoff et al. [2015] presented a comprehensive discussion of the Timoshenko beam theory

with the recapitulation of the Bresse-Rayleigh's and Timoshenko's equations. Further, the authors proposed an alternative formulation of the governing differential equation by correcting the original Timoshenko's correction. This allowed the authors to come up with a rigorous variational- asymptotic proof of the proposed theory in the case of plane strain. Formal proofs of the high-order shear correction theories for the plates are not yet present.

In contrast to all the previous studies, Damghani et al. [2011] implemented the Dynamic Stiffness Matrix Method (DSMM) to study the buckling of plates with a single split. The geometry of the problem considered by the authors was similar to the schematic diagram shown in Fig. 2.6 but for a single delamination. The authors formulated the transcendental eigenvalue problem based on the dynamic stiffness matrix and solved it using the Wittrick-Williams algorithm for the critical buckling load and the associated mode shapes. Cases of through-the-length and through-the-width delamination and the effect of split placement along the thickness of the plate were studied. The solution was also validated against FEA. The key strength of this study lies in the exactness of the solution as the dynamic stiffness matrix makes use of exact solutions of member stiffness equations, followed by dynamic continuity at the joints. Often, DSMM is computationally efficient compared to FEA as fewer elements are required, but the solution procedure could be rather complicated as one gets a transcendental eigenvalue problem using this method, unlike FEA which leads to algebraic eigenvalue problems. However, the application of this method is limited to structures consisting of a few types of structural members for which exact solutions are known.

Damghani et al. [2011] formulated the eigenvalue problem(EVP) in such a way that parametric dependence on the delamination length a is not retained. Therefore, the solution could only be calculated for each discrete value of a and, thus, the parametric dependence of the buckling load on a was calculated indirectly similar to any FEA method. The authors report three characters of buckling similar to those reported in the previous studies, i.e., single wave global mode, single wave local mode and two waves global mode.

Rodman et al. [2008] propose a different analytical solution to buckling of a laminated beam and plate with an arbitrary number and placement of delaminations while accounting for shear effects. The model is based on nonlinear Reissner beam theory. The structure is divided into several beam elements, each of which are governed by non-linear equations. The continuity conditions are also imposed between the neighbouring elements. The constitutive equations are further linearised by introducing variations about the equilibrium state. The resulting set of linearised equations along with boundary conditions and continuity conditions is then solved analytically. This approach provides an analytical solution, even for non-uniform columns with shear correction. Compared to FEA, the proposed approach requires much fewer equations that can be solved analytically. The authors also applied the methodology developed by them, to delaminated plates with various boundary conditions. The solution was generalised for the number and position of delaminations, also accounting for shear between the layers.

A recent study on the buckling of delaminated plates by Juhász and Szekrényes [2017], contains experimental observations of the three buckling mode characters: single wave global mode, single wave local mode and two waves global mode previously reported in numerous studies. These are depicted in Fig. 2.7. The authors also carry out parametric FEA study varying the delamination length in small increments. For the first time, the authors considered a second buckling load,

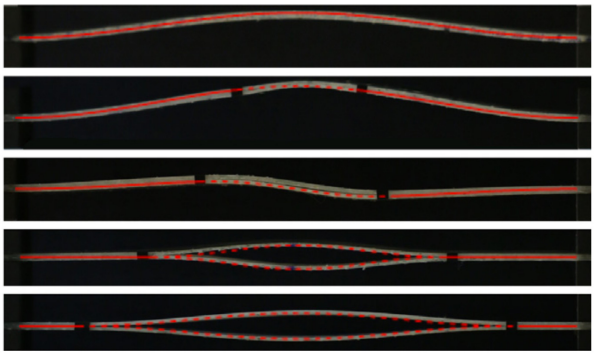

FIGURE 2.7: Experimentally observed buckling modes of a thin laminated composite. (*First from the top*) A classical buckling of a composite plate with well-bonded layers. (*Second*) A single wave global buckling mode of a plate with short delamination. (*Third*) A two waves global buckling mode of a plate with an intermediately long delamination. (*Fourth* and *Fifth*) A single wave local buckling mode of a plate with long delamination. The red lines superimposed on the photographs depict buckling modes computed numerically by the authors. The figure is reprinted from Juhász and Szekrényes [2017].

in addition to the fundamental one, and reported that the numerical trajectories of the two buckling loads (when plotted as functions of the delamination length) cross in the vicinity of a structure changing its principal buckling character.

In parallel to the above mentioned, some researchers [Argyris and Tenek, 1994, Wang and Qiao, 2005, Pizhong Qiao and Fangliang Chen, 2011] argued that the exact resolution of the complex deformation state between the layers when delaminations are present is as important as the understanding of the buckling type. It is especially crucial for the correct estimation of the critical compressive stress. Therefore, Shear Deformable Split Bilayer Beam Theory (SDSBT) is developed and successfully applied to some structures with delaminations [Wang and Qiao, 2005]. This theory is focused on the exact resolution of the deformation field at the split tip. The approach is designed to accurately predict the deformation of the material at the tip of the split. It gives a refined representation of the structure and in many cases surpasses the accuracy of the previous studies performed with FEA. Flexible, semi-rigid and rigid models for the split interface were derived [Pizhong Qiao and Fangliang Chen, 2011]. Wang and Qiao [2005] showed that flexibility of the split interface has an important effect and that it should be taken into account as it results in a lower critical buckling load compared with that obtained assuming clamped boundary conditions or modelling interaction with springs. A comprehensive review of SDSBT can be found in the paper by Qiao and Chen [Pizhong Qiao and Fangliang Chen, 2011].

Accuracy makes SDSBT a particularly useful tool for the design of critical structures. However, the solution of the associated differential equations is often complicated. A separate calculation has to be carried out at each design point. Therefore, the functional dependence of the behaviour on the structural parameters cannot be embedded and has to be obtained indirectly by solving numerous nearly identical problems while changing the parameters. An approximate but simpler model may be useful in identifying the generic trends in behaviour, which is of particular interest within the current study. A review of literature in the area of the stability of structures with repetitive features is performed next. This has relevance to the buckling of multilayer structures.

2.2 Buckling of cold-formed sections, lattices, frameworks and structured materials

The repetitive arrangement of nominally identical structural members elastically coupled to each other through fasteners or welding is a cost-effective design approach for mass-manufacturing large structures such as buildings, vessels, bridges, etc. One reason is the economy in manufacturing which thrives on the production of identical parts. For example, consider a wall framing manufactured by STUDCO Building Systems in Fig. 2.8 (a). Typically, such lattice assemblies consist of beam-columns or plates with holes and perforations which reduces the overall weight without much loss of stiffness as shown in Fig. 2.8 (b). Such cold-formed steel beam-columns and

(a) (b) (c)

FIGURE 2.8: Examples of common engineering structures with holes and perforations. (a) Wall framing manufactured by STUDCO Building Systems [Studco, 2019] consisting of a framework of nominally identical steel bars. (b) A close view of a cold formed steel framework with circular holes. The image is adapted from [Engineering, 2019]. (c) An example of the local buckling in the vicinity of a circular hole in a C beam-column with C-section. The photo is adapted from [Bauer, 2019].

plates are found ubiquitously in construction as well as in many critical parts of vehicles, ships and aircraft and are often subject to compressive loading risking the possibility of buckling. An example of local buckling in the vicinity of a circular hole in a beam with a C-section is shown in Fig. 2.8 (c). In contrast to uniform beams, buckling of which is well understood, failure induced by the local buckling in perforated and holed structures has drawn considerable research interest [Moen and Schafer, 2009a,b, Cheng and Zhao, 2010, Pihler-Puzović et al., 2016]. Here we review the principal body of literature in the field that is focused on the structures with geometries similar to those considered in this research, especially with regards to its spatially repetitive nature.

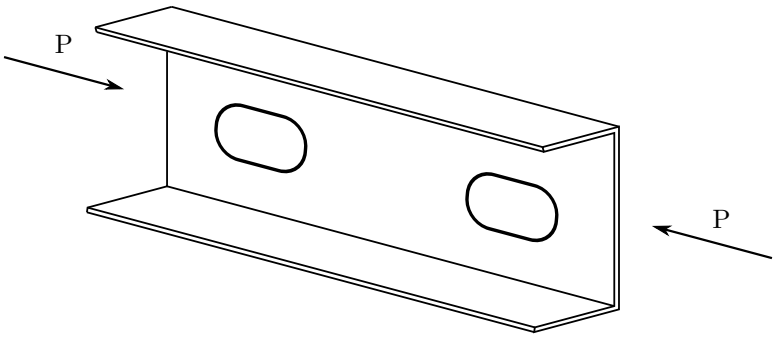

FIGURE 2.9: A schematic diagram of a column with C-section with slotted holes under compression studied by Moen and Schafer [2009a]. Adapted from [Moen and Schafer, 2009a].

Consider the elastic stability of a slender cold-formed steel column with holes shown in Fig. 2.9, which was studied by Moen and Schafer [2009b]. The authors employ the Rayleigh-Ritz based finite strips modelling procedure as well as FEA to study how various structural parameters such as slenderness of the column, shape, size and location of holes affect the fundamental buckling load and the associated buckling mode shape. Similar to the research on delaminated layered composites, the authors associate the variability in the instability behaviour with the interplay between the local (near holes) and the global (at the scale of an entire structure) buckling of the column. Thus, the three mode types are reported, i.e., wavy bulging of the material between the holes (local buckling), distortion of the flanges throughout the column (distortional buckling at a local and global scale) and the global bending and torsion buckling of an entire column.

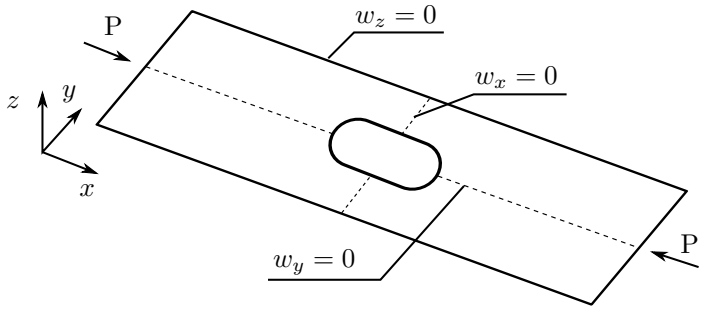

FIGURE 2.10: A schematic diagram of the plate with a hole considered by Moen and Schafer [2009b]. The contour of the plate is simply supported $w_z = 0$ and the additional constraints are indicated with the dashed lines. Adapted from Moen and Schafer [2009b].

A comprehensive study on the effect of holes on buckling of cold-formed steel plates was carried out by Moen and Schafer [2009b]. A diagram showing the geometry of the problem is presented in Fig. 2.10. The authors assumed the plate to be simply supported at all edges. In addition, the central line parallel to the loading is restrained from movement along y-direction and the central line perpendicular to it is restrained in the x-direction (see Fig. 2.10).

In Fig. 2.11 the buckling modes, as computed by Moen and Schafer [2009b] for a case of a uniform plate (*left*) and a plate with a single hole (*right*) are shown. Note a mode resembling a standing wave with the wavelength L_{cr} as opposed to the two bulges at the ends and a flat region around the hole. The authors report that, surprisingly, the presence of a hole of a specific size and shape dampens the buckling mode compared to a uniform plate. They report an increase

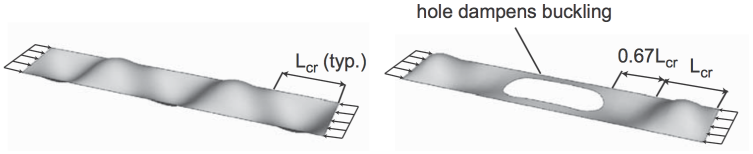

FIGURE 2.11: A comparison between instability modes of a short plate without holes (*left*) and a plate with a large centrally placed hole (*right*). Moen and Schafer [2009b] report that the hole dramatically reduces plate deflection thus dumping buckling mode. Reprinted from Moen and Schafer [2009b].

in the buckling threshold (critical buckling stress) for a wide hole in a short plate by up to 7% compared to that for the uniform one. This can be attributed to the damping effect of the hole. It should be noted that the increase in the buckling stress does not imply the higher strength of the plate with a hole. In fact, as the net cross-section reduces with the size of the hole,

the ultimate strength of the plate will be smaller. On the other hand, thinner holes localise buckling deformation, as seen from Fig. 2.12. Comparing buckling of a long uniform plate (*top*)

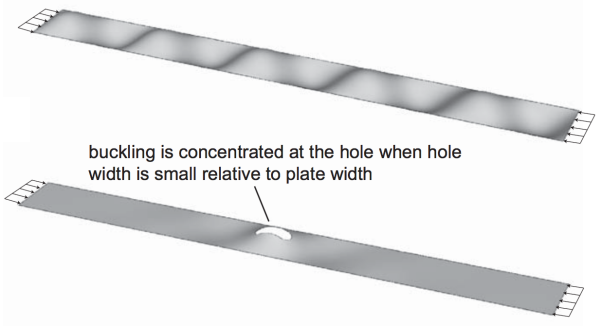

FIGURE 2.12: A comparison between instability behaviour of a long uniform plate (*top*) and a plate with a thin hole (*bottom*). Here, the hole localises buckling mode. Reprinted from Moen and Schafer [2009b].

with buckling of the same plate featuring a thin cut (*bottom*), we see that the former exhibits a standing wave mode which is periodic with the wavelength L_{cr}. A small hole in the latter acts as a perturbation in the otherwise regular deformation field thus triggering localisation. The buckling damping effect in a plate with a large hole can be explained from the same point of view. The fundamental physical mechanism of such a behaviour will be discussed in details in our study of elastic stability of a chain of coupled rods and a plate with multiple cut outs in the further chapters.

As the number of geometric features such as holes, cuts and splits in a column or plate is large but well-controlled, the competition between local and global buckling superimposes with the periodicity related effects and leads to a complex instability behaviour. The prediction of the buckling patterns emerging in such structures is of interest in many engineering applications. Historically, structures with complex shapes such as beam-columns and plates with multiple holes and cut outs were rarely considered for detailed analytical modelling. Most of the practical engineering knowledge of the behaviour of such structures under loading has been determined empirically. These structures often are too complex to be treated analytically. Furthermore, a precise prediction of the buckling thresholds was not crucial since most of the engineering structures were designed to be much stronger than strictly needed for operational loading due to the safety factors routinely applied at the design stage. However, as novel design approaches focus on reducing the cost of manufacturing and operation, a growing need for a more detailed understanding of the structural mechanics of the complex geometries has emerged. Therefore, in the present work, considerable attention is devoted to applying concepts of periodicity to obtain the analytical or semi-analytical models of structures featuring cut outs and holes.

Architectured structures and structured materials are often designed for specific properties such as contraction instead of expansion under compression (auxetic metamaterials) facilitated by buckling induced transformation of the perforation patterns [Bertoldi et al., 2010] and other types of controlled behaviour. In the studies of architectured structures/materials [Pihler-Puzović et al., 2016, Johnson et al., 2017, Javid et al., 2016], dependences of the behaviour on the geometry (void to material ratio, number, shape and orientation of holes and cuts) is crucial. For example, Pihler-Puzović et al. [2016] considered a simple beam-column with regularly placed circular holes and compared its buckling with a uniform beam. The observed modes are superimposed on each

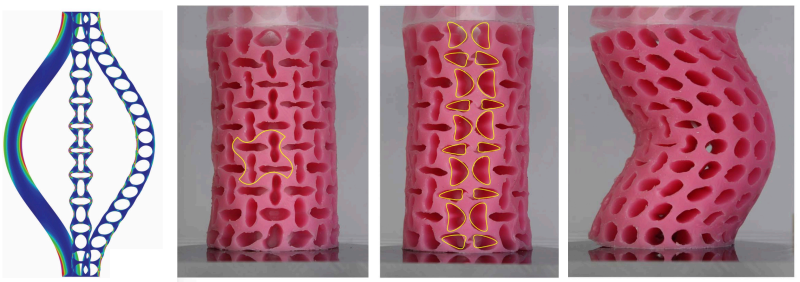

(a) (b) (c) (d)

FIGURE 2.13: (a) A uniform beam buckling superimposed with the localised buckling of a beam with holes and with a global Euler-like buckling of a holed beam with a slightly altered void to material ratio reported by Pihler-Puzović et al. [2016]. (b) and (c) show localised buckling of a holed cylinder induced by hole shape transformation. (d) Euler-like global buckling mode exhibited by the similar cylinder with slightly different geometry and location of holes. The figures are adapted from [Javid et al., 2016].

other in Fig. 2.13 (a). A buckling mode to the left corresponds to buckling of a uniform beam consistent with the Euler buckling theory. The mode in the middle (Fig. 2.13 (c)) shows a dramatically different behaviour as no global arch is seen. Instead, the deformation is highly localised around the holes. But if the parameters of the holes are slightly tuned, one observes a single arch buckling again as shown in the right mode in Fig. 2.13 (d). Javid et al. [2016] show a similar alteration of buckling mode but for a holed cylinder depicted in Fig. 2.13 (b)–(d).

The finding of Pihler-Puzović et al. [2016] were further extended by Johnson et al. [2017]. The authors show that if a line of holes is present in the otherwise homogeneous column, the buckling mode of the structure appears either on the global scale, e.g., Euler type of buckling or on the local scale, e.g., the adjacent holes collapse in the orthogonal directions. Such a dramatic change in the instability character was shown to be governed by the geometry of the problem alone. The behaviour was presented in a generic form using a phase diagram of the buckling modes as shown in Fig. 2.14.

Fig. 2.14 demonstrates that three modes are exhibited by the holey column depending only on the geometry – hole diameter relative to column width D/W and unit cell height relative to column width h/W. Here, a unit cell encompasses a single hole and is translated vertically to form a column with periodically arranged holes. When the holes are small relative to the column width, a Euler-like buckling mode occurs. However, as hole size increases, an alternate buckling mode is observed for a vast region of geometric parameters. Finally, when the size of the holes surpasses certain value, a localised Euler-like mode is exhibited.

Mullin et al. [2007] view the onset of buckling in structured materials as a boundary between the two different deformation patterns. The authors performed numerical and experimental studies of the uniaxial compression of the square plate with periodically placed circular holes. They report that the deformation pattern developed below the buckling limit is mainly characterised by the compression of the material between the holes. However, this pattern is rapidly transformed after the onset of buckling as the circular holes evolve into cylinders whose major axis are alternating by 90°. This pattern is further magnified in the nonlinear post-buckling regime.

Bertoldi et al. [2010] showed that the same holed plate exhibits a negative Poisson ratio effect. The circular holes transform to elliptical holes which are then squashed resulting in the overall

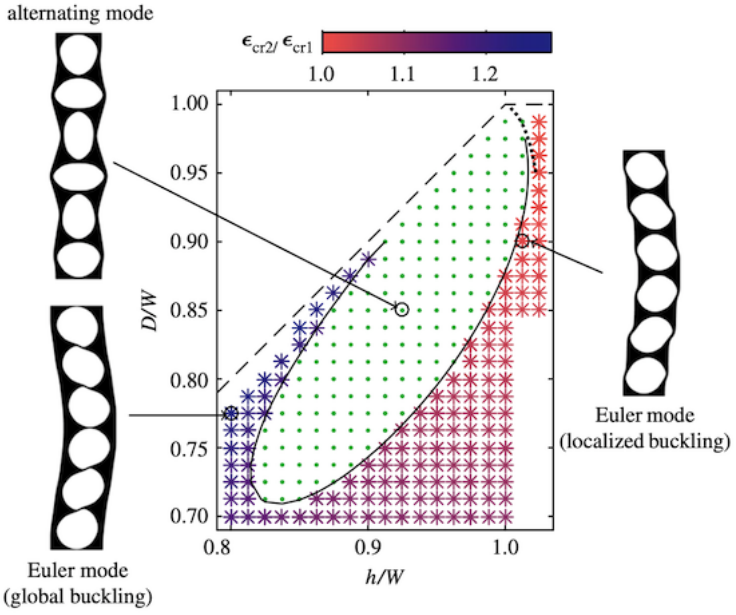

FIGURE 2.14: A phase diagram of the buckling modes exhibited by the holey column depending on the hole diameter relative to column width D/W and unit cell height relative to column width h/W. The green dots correspond to alternating mode, while the start are associated with the Euler-like buckling mode. Localized Euler mode is also observed for large holes. The boundary between the alternating mode and the localised mode is given by the dotted line. The image is reprinted from [Johnson et al., 2017].

shrinkage of the material under large compressive strain (25%). The transformations of the deformation patterns induced by buckling in the linear and non-linear regimes have been shown to alter the characteristics of wave propagation through the holed plate [Wang et al., 2013]. This makes such a structure a highly tenable phononic crystal.

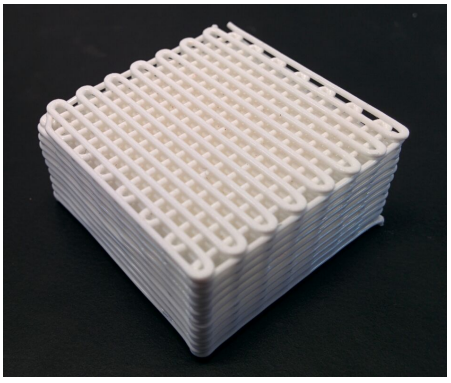

FIGURE 2.15: An example of a 3D printed lattice material consisting of multi-coupled filaments that can be modelled by beam-columns.

Recent advances in additive manufacturing fuelled manufacturing of lattice-like elastic structures. An example of a woodpile lattice manufactured using Fused Deposition Modelling process is shown in Fig. 2.15. Notice, that the lattice consists of regularly spaced nominally identical filaments elastically coupled to each other. At the current stage of 3D printing technology, one can manufacture lattice structures of almost arbitrary shape out of various types of plastic, metal and ceramics enormously expanding the applicability of such structures to biomedical engineering [Kim et al., 2015], prosthetics [He et al., 2015], rapid prototyping and manufacturing

of structures with complex geometries and function [Raviv et al., 2015]. This class of structures when compressed, are likely to suffer local buckling of the filaments. The present study is also motivated by the repetitive nature of such modern materials and their elastic stability under external loading.

With the rapid development of 3D printing and the possibility to cheaply manufacture complex geometries, a thorough understanding of the structural performance of various lattice assemblies is vital. Therefore, numerous studies are devoted to predicting the structural response of additively manufactured lattices. In particular, the structural stability of implants [Kim et al., 2015], complex hierarchical and porous structures [Chen et al., 2018] and metastructures [Coulais et al., 2015] has been studied. An example of a lattice structure performing under compression in the human thoracolumbar spine is shown in Fig. 2.16 (a). Lattice may be constructed of continuous

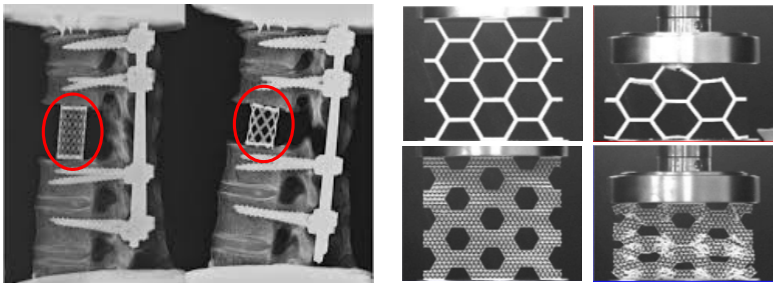

(a) (b)

FIGURE 2.16: (a) A lattice structure studied as possible support for the human spine. The photo is adapted from [Kim et al., 2015]. (b) Buckling of a continuous honeycomb (*top*) versus buckling of a honeycomb made of structured material (*bottom*). The photos are adapted from [Chen et al., 2018].

and uniform filaments or made out of structured material. This could give a performance advantage, as one can control the hierarchical geometry. For example, Chen et al. [2018] report that a honeycomb made out of specifically structured material has a much stiffer response. An example of a compression test performed on a continuous honeycomb is shown in Fig. 2.16 (b) (*top*) and the same test with the structured honeycomb is shown in Fig. 2.16 (b) (*bottom*). Note that a continuous honeycomb exhibits a more brittle deformation while the structured one demonstrates a high degree of local buckling (bright white regions).

In summary, we see that buckling of structures that either contain geometrical features such as holes, splits and cut outs or are made of the structured materials may exhibit dramatically different buckling when even small variations in the geometrical features are introduced. This may increase the complexity of engineering calculations requiring a more sophisticated analysis to be applied to ensure the required structural performance. On the other hand, this also allows structures to be designed that are intended to buckle under loading. In either case, apart from posing an interesting challenge for a researcher, the problem of elastic stability of beam-columns, cylinders, plates, etc. with various types of repetitive geometrical features is extremely important from a practical point of view.

Another class of problems in the field of the stability of layered structures with weak inter-layer bonding arises in geology. This is reviewed next.

2.3 Folding of layered strata

Buckling of structural assemblies with nominally identical coupled members is most commonly encountered in structural engineering. However, similar physical behaviour occurs also in a variety of other situations. For example, consider the layered strata formation of Durdle Door photographed by Embleton [2006] and shown in Fig. 2.17 (a) or a Jurassic coast strata formation shown in Fig. 2.17 (b). The strata are approximately regularly formed alternatively with rock and soft sediments. In general, strata resemble a geological version of a laminate composite.

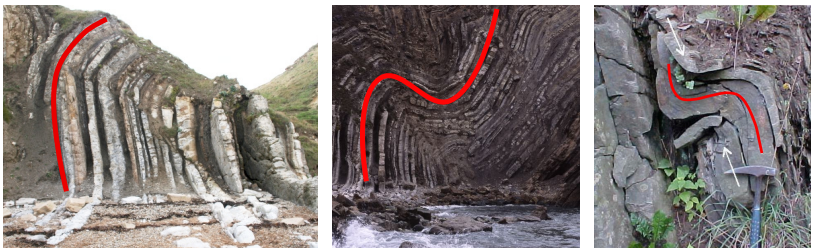

(a) (b) (c)

FIGURE 2.17: (a) Folded layers of solid rock alternated by soft sediments at Durdle Door photographed by Embleton [2006]. The characteristic shape of the fold is indicated with the thick red line. (b) Layered strata at Jurassic Coast exhibiting a double-curvature folding. The image is adapted from [Photos, 2019]. (c) A detailed view of a small-scale section of the larger strata folds at Devonian Brallier Formation photographed by McDowell et al. [2005]. The white arrows indicate the axis of compression and the red line shows a double-curvature folding.

As composites may buckle under compression, strata may fold under their weight and the pressure from the upper layers of soil. However, strata are usually also embedded in surrounding sediments and rock which provides strong lateral support and considerably restrict buckling. An example of a small region of larger strata at Devonian Brallier Formation in Fig. 2.17 (c) indicates how a single layer of rock (highlighted with a red line) is folded in a double-curvature manner under the compression indicated with the white arrows. Notice that the single layer in Fig. 2.17 (c) is enclosed in the sediment soil and the surrounding rock. This creates a physical constraint for the buckling mode. Hence, a double-curvature fold is formed instead of a single arch buckling.

Although strata folding is not an elastic buckling process but a complex nonlinear plastic instability problem, the geometric principles, i.e., the morphology of layers and coupling between them plays an important role here. Inspired by the geological context, Edmunds et al. [2006] conducted experiments compressing the layers of paper gripped between the rubber sheets restrained from lateral movement and reported the formation of parallel folds similarly as observed in strata. Dodwell et al. [2012a] studied the apparent periodicity in the layers of strata and the localisation of folds due to the constraint imposed on the strata by the surrounding rock. Experiments performed on the layers of paper enclosed within the rubber foam with variable stiffness (see Fig. 2.18) demonstrate the short-wavelength folding depending on the stiffness of the embedding. Apparently, the geometric properties of strata affect the resulting fold to a great extent. However, the short-wavelength buckling as the one shown in Fig. 2.18 is triggered by the confinement of the system between the two stiff plates producing a restriction on a single arch buckling which is predicted by Euler theory of buckling.

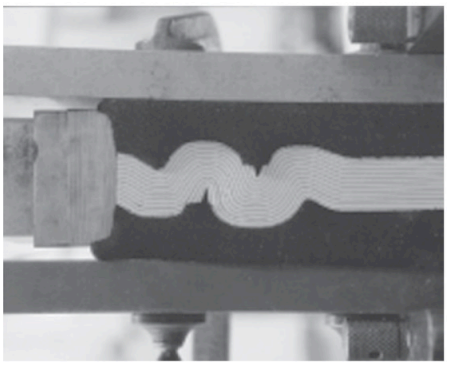

FIGURE 2.18: A compression test of a stack of layers of paper enclosed in a rubber foam performed by Dodwell et al. [2012a]. Two thick parallel plates at both sides restrain the system and are used to mimic the embedding of the strata in the surrounding soil and rock.

The short-wavelength buckling is the most interesting observation for us here. Later, we will see how the similar effect of elastic confinement as well as coupling between slender members leads to some curious effects in contexts outside of geology.

2.4 Buckling of layered nano-structures

We presented several structural systems composed of coupled elastic members in the review earlier. Here we shall discuss the instability behaviour of entirely different structural systems – layers of graphene at a length scale of dozens of nanometers. Yet, as we will see, many of these systems retain a considerable geometric resemblance to much larger structures, and with that comes surprisingly similar instability behaviour.

Consider nano-structure schematically shown in Fig. 2.19 [Cranford, 2013, Atif and Inam, 2016]. The study by Cranford [2013] is focused on the compression of graphene sandwich composites. They consist of one or two layers of graphene sandwiched between the two elastic mono-layers as shown in Fig. 2.19 (a) and Fig. 2.19 (d) that are based on the molecular dynamics simulations performed by the authors. The mono-layer-to-mono-layer interaction provides weak coupling – usually due to Van der Waals interactions. Although coupling has a different underlying physics, it has the same mechanical role, i.e. holding the individual structural members together. In the simulations performed by Cranford [2013], strength of adhesion (coupling) is a parameter that defines the variability of the behaviour.

Cranford [2013] reports that if the adhesion between the layers is weak, buckling drives elastic nano-layers (red lines in Fig. 2.19 (b)) in the opposite direction and the graphene layer (blue line) holds to either of them. This behaviour resembles a classical delamination buckling in composite laminates such as the one in Fig. 2.1 (a),(c). However, as adhesion is increased, the layers remain connected and buckle in the same direction (as shown in Fig. 2.19 (c)) thus resembling a single bulge Euler type buckling mode. This agrees well with buckling of well-bonded laminates as shown in Fig. 2.1 (b).

In the case of a two-layer sandwich, the behaviour is more complex. The layers deform in the opposite directions for weaker adhesion and stick together for stronger adhesion. In contrast, the

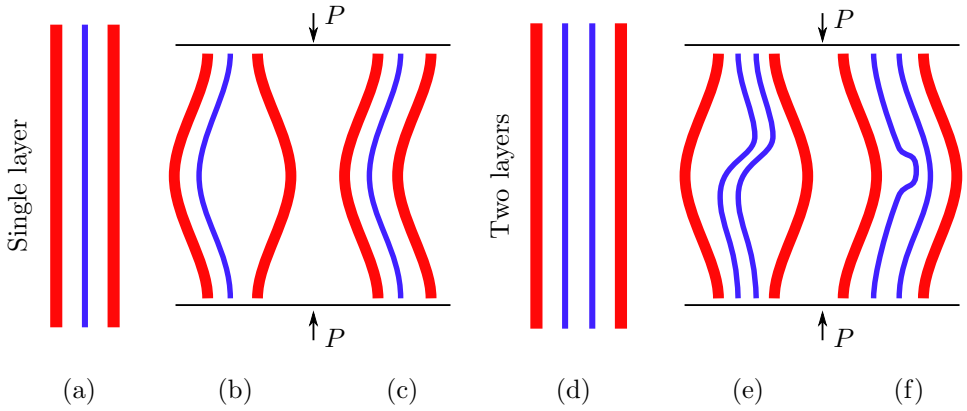

FIGURE 2.19: A cartoon based on the molecular dynamics simulations conducted by [Cranford, 2013]. (a) A single layer graphene nanocomposite free from loading. The red lines represent layers of ideal elastic material, while the blue line is a single layer of graphene. (b) The same composite under compressive loading P exhibits a nontrivial buckling characterised by elastic layers bulging in the opposite directions (delamination) under a weaker coupling. (c) The composite demonstrates an Euler-like buckling for stronger coupling. (d) A two layer graphene nanocomposite free from loading. (e) The elastic layers bulge in the opposite directions while graphene develops an antisymmetric mode for weaker coupling. (f) All layers deflect jointly in the same direction, but graphene layer also exhibits local bulging in the middle for stronger coupling.

graphene layers develop an antisymmetric buckling for weaker coupling as shown in Fig. 2.19 (e). In the case of a stronger coupling, the graphene layers bulge in the same direction as the plates but develop a local high curvature buckling as demonstrated in Fig. 2.19 (f).

The buckling mode at nanometer scales has been shown to also depend on dislocations [Lehtinen et al., 2013]. Judging by their effect on the character of buckling, the dislocation dipoles may be related to the geometrical features like thin splits, cut outs and cracks in ordinary engineering structures at much larger scales. Notice, that this analogy is purely geometrical since the physics of both problems is very different. An experimental and numerical study by Lehtinen et al. [2013] performed on a single layer of graphene with dislocations suggest that such features in an otherwise ideal atomic structure can induce buckling of an entire graphene sheet. The authors considered $\approx 25 \times 25$ nm sheet of graphene with $\approx 24,000$ atoms that contains a dislocation dipole nucleated by the removal of a string of carbon atoms.

Lehtinen et al. [2013] generalise the observed behaviour in a form of a map of buckling modes superimposed onto the simulated energy landscape of the system specified in a plane spanned by the two characteristic parameters of the dislocation dipole – glide distance and the climb distance between the two dislocations as shown in Fig. 2.20 (a). Two types of buckling modes were reported, each of which is associated with the respective phase in Fig. 2.20 (a) – symmetric and antisymmetric modes which are depicted in Fig. 2.20 (b). The qualitative change of buckling character observed from such a phase diagram relates to an important principle that underlies the present study. Further we show that it is the geometry of the structure which is the primary factor that governs the change of the mode character.

In connection with the idea of phase diagrams by Lehtinen et al. [2013], the study of buckling state transitions in the vicinity of the near-degeneracy point proposed by Savel'ev et al. [2006] fostered a different point of view for the classical buckling problems adopted in this research. Consider a compressed nano-bar made of a carbon nanotube shown in Fig. 2.21. It

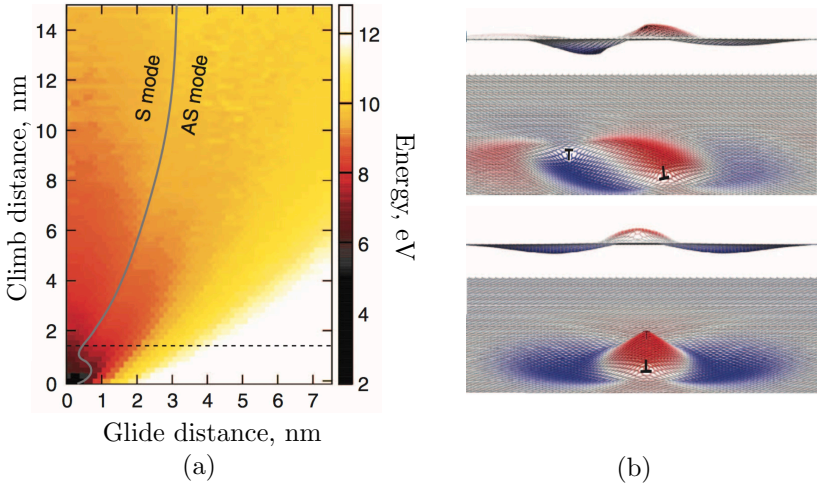

FIGURE 2.20: Dislocation induced buckling of a single layer graphene sheet with $\approx 24,000$ carbon atoms. (a) A map of symmetric and antisymmetric modes (grey curve separating S and AS modes) superimposed on a potential energy landscape (colour) specified in the coordinates of glide and climb distances between the dislocations. The images are adapted from [Lehtinen et al., 2013]. (b) The simulated buckling profile of a layer of graphene. The *top* two plots demonstrate the edge view and the top view of an antisymmetric mode for antisymmetric extension of dislocations. The *bottom* two plots show the edge and the top view of the symmetric mode observed for symmetrically extending dislocations. The red (blue) colour indicates ascend (descend) of carbon atoms. The figures are reprinted from [Lehtinen et al., 2013].

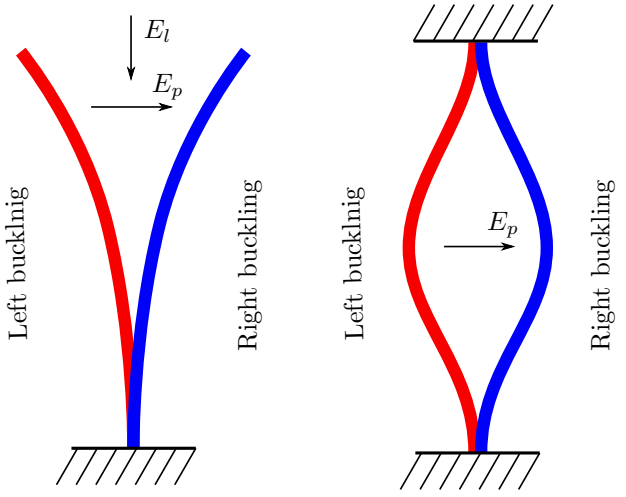

FIGURE 2.21: Two qubit designs suggested by Savel'ev et al. [2006]. Each design consists of a single charged nanorod (carbon nanotube). In the first case (*left*), the beam is buckled under the electric field E_l and the control between the left and right states is realised via changing the perpendicular electric field E_p. In the second case (*right*), the nanorod buckles being compressed between two plates and the left-right states are controlled via the perpendicular field E_p.

may be regarded as a nano-electromechanical system that is small enough to exhibit both mechanical and quantum effects as suggested by Savel'ev et al. [2006]. As the rod is charged, one can induce compression either by applying a longitudinally oriented electric field E_l (as shown in Fig. 2.21 (*left*)) or by pulling the two constraints to which the rod ends are attached closer (as shown in Fig. 2.21 (*right*)). A double-well potential $U = -\alpha y^2 + \beta y^4$ plotted in Fig. 2.22 (a) can be used to describe the energy landscape of the system. The bar thermally fluctuates around

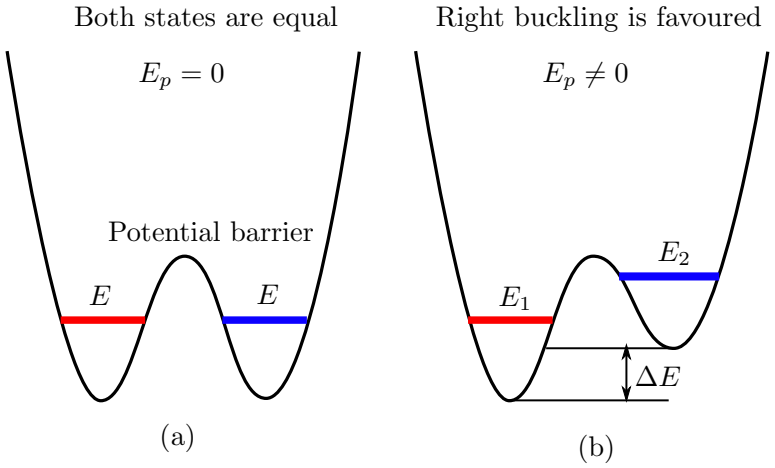

FIGURE 2.22: A double-well potential of a buckled nano-rod. (a) The symmetric potential for the rod compressed to the buckling limit by the longitudinal electric field E_l for perpendicular field $E_p = 0$. Both left (red) and right (blue) states have equal energy E separated by the potential barrier. (b) The symmetric potential is skewed by favouring the right state over the left one via application of the perpendicular electric field E_p which leads to energy splitting ΔE. The schematics is adapted from [Savel'ev et al., 2006].

the equilibrium energy state.

In the absence of external factors, the energy states of the rod are degenerate but separated by a potential barrier which does not allow the system to freely transit between them. This is similar to the potential energy of an ordinary rod. Being compressed to a buckling limit, it exhibits the left or right deflection. One can replicate this behaviour by applying a perpendicular electric field E_p to the charged nano-bar as shown in Fig. 2.21. In such a way, the energy of the left (right) mode is reduced (increased) and an energy splitting occurs $E_1 - E_2 = \Delta E$ as depicted in Fig. 2.22 (b). Savel'ev et al. [2006] suggest hat by changing the strength of E_p, one can tune the system to its degeneracy point characterised by non-uniqueness of states (for example, raising the energy E_2 up to the top of the barrier). The authors argue that the nano-rods shown in Fig. 2.21 are legitimate candidates for mechanical qubits and they may have an advantage compared to conventional designs by having a much higher crossover temperature due to carbon nanotubes being stiff.

The discussed application of the Euler buckling theory to a quantum mechanics problem is a fascinating example of interdisciplinary research. Apart from that, it also inspired us to study the critical buckling load trajectories in the design space similarly to how energy (eigenvalue) trajectories are studied in the parameter space in quantum mechanics [Novotny, 2010, Zener, 1932], wave propagation and dynamics [Pierre, 1988, Bhaskar, 2003] and other contexts. This will be discussed in detail in the further chapters. Also, apart from quantum theory, there is a considerable interest to the application of the classical Euler buckling theory to various small-scale electromechanical systems and switches [Savel'ev and Nori, 2004, Weick et al., 2010, 2011].

This subsection has covered many unusual manifestations of buckling. However, in all the examples discussed, we have seen principal scenarios. The first scenario constitutes buckling of a structure with geometrical features (splitting discontinuities), while the second scenario constitutes buckling of several nominally identical coupled members that exhibit a single arch buckling

mode or a more complex buckling pattern which depends on the coupling and the actual geometric configuration. The research reviewed has also inspired a different view of the classical buckling problem which leads to novel conclusions and understanding of instability behaviour of split and coupled structures as discussed in the further chapters.

2.5 Analogies with multi-component structures with contrast properties

Layered composites, nanoscale size sandwich panels, geological strata, etc., can all be regarded as a subset of the so-called multi-component structures – complex systems consisting of multiple parts. Some of the parts in multi-component structures may have material properties that drastically differ from the others. For example, the multilayer strata formation consists of layers of rock that are orders of magnitude stiffer than the surrounding sedimentary soil. Similarly, photovoltaic panels [Aßmus et al., 2016] are plates consisting of three layers (polymeric layer sandwiched between the two layers of glass), which dramatically differ in stiffness.

It is natural to expect that the contrast in material properties will strongly affect the structural response of such systems. The emphasis on the contrast in material properties in such systems is usually made in a context of vibration and the propagation of waves through such structures [Borcherdt, 2009, Kudaibergenov et al., 2016, Kaplunov et al., 2017, 2019]. Such differentiation from the static problems occurs due to a remarkable alteration of the wave propagation and vibration character in multi-component contrast structures compared with the homogeneous ones. For example, Kaplunov et al. [2017] studied wave propagation in a three-layer strongly inhomogeneous plate. The authors proposed an asymptotic approach for deriving the two-mode polynomial approximations of the dispersion relation for the plate. The necessity to account for the second mode arises because, in contrast to the homogeneous plate, the vibration spectrum of the three-layer plate involves the first harmonic mode in addition to the fundamental bending mode. Kaplunov et al. [2019] focus on studying the low-frequency vibration of a rod that consists of several parts with contrasting material properties. The authors developed an asymptotic procedure allowing the onset of the local and global vibration modes for low frequency vibration to be predicted. While the global vibration is natural for low frequencies, the onset of a short-wave local mode is attributed to the so-called “almost rigid body motion” of the stiff components of the rod. Most interestingly, the authors also discuss the analogy between the vibration of the high contrast structures and the layered media and periodic structures. Indeed, one can consider a multi-component high contrast structure with identical components as one approaching periodicity.

Literature that focuses on the buckling of multi-component systems with contrasting material properties is scarce. However, since buckling shares considerable mathematical similarity with vibration problems, a number of interesting effects associated with strong inhomogeneity are expected to be observed if the multi-component structures are studied under compression. Beams and plates with cut outs that are a focus of the present study may be regarded to have highly contrasting properties if the stiffnesses of the structure material is compared with the zero stiffness of splits and cut outs. Even more interesting behaviour may be observed if the splits and cut outs are considered to be filled with some soft material instead of the voids. Then, such

high contrast multi-component structures may be considered to approach periodicity when the number of identical components becomes sufficiently large.

2.6 Analogies with periodic structures

There is a characteristic common to laminates, cold-formed structures with holes and perforations, nano-composites, etc., which is rarely considered in detail – a geometric periodicity of these structures. It is easier to manufacture nominally identical geometries stacked or positioned regularly in space and such structures often perform under compression, which may lead to buckling. Yet, the buckling of layered and regularly perforated structures is normally not analysed from the perspective of their periodicity. Very few problems were identified where instability of periodic structures was considered. These mainly are multi-span beams [Li et al., 1995, Xie, 1995], beams on an elastic foundation [Xie, 1997, Luongo, 2001], rib-stiffened plates [Xie and Ibrahim, 2000, Li et al., 2005] and, recently, a numerical study of the buckling of laminated plates [Paik et al., 2015].

In the present study, we identify that the considered problems of buckling of multilayer beams and plates with regular cut outs share considerable mathematical similarity with a well-established field of wave propagation in periodic structures, where the connection is primarily made via the geometric periodicity. Periodicity plays a crucial role in crystals [Wang et al., 2013, 2015], the vibration of solids [Hodges and Woodhouse, 1983, Castanier and Pierre, 1995] and other applications. A more detailed review of the field is given in the introduction to Chapter 5, whereas here we outline the key ideas and suggest how they are relevant to this study.

The periodic structures in one dimension are invariant over translation by a period T. If the state of the structure is described by $\psi(x)$, where x is a coordinate, the solutions thus can be found in the form of Bloch's waves (or states) according to Floquet-Bloch theorem [Ziman, 1972]

$$\psi(x) = \mathrm{e}^{ikT} u(x), \tag{2.1}$$

where $i = \sqrt{-1}$, k is the wave number and $u(x+T) = u(x)$ is a periodic function.

Although the concept of Bloch's waves is typically used in connection to dynamics, there is no constraint on the nature of the underlying problem, provided it is periodic. This is directly applicable to our study. If, for example, a multilayer beam is split every regular distance along its thickness, or if a plate has holes in regular intervals, these structures possess translational symmetry with respect to T. Therefore, if the buckling amplitude of a given structural member is $\psi(x)$, then, according to Floquet-Bloch theorem, the modulation of the buckling amplitude under translation to the member k is equivalent to multiplying by e^{ikT} called the phase factor.

Applicability of the Floquet-Bloch theory suggests that instability of periodic structures with complex geometries can be relatively easy modelled making use of periodicity. This also implies that mathematical methods developed in the field of wave propagation in periodic media may be tailored to address static instability problems as well. This brings another motivation to the present study, as moving from a bilayer beam to multilayer structures, to periodic plates and, finally, to assemblies of beam-like protein filaments (microtubules), we incorporate the concepts of periodicity and bridge the gap between a number of specialist fields.

2.7 Buckling of protein filaments in sub-cellular structures

A fascinating example of elastic buckling, particularly of the effect of coupling in ordered assemblies of members, is found in living organisms at a cellular level. A typical cell is a highly complex organism consisting of a nucleus, membrane and numerous organelles. Often cells have to withstand considerable mechanical stress induced by their elastic environment. Hence, they evolved a dense network of interconnected sub-cellular filaments called cytoskeleton, whose primary function is to ensure the mechanical integrity of a cell. The cytoskeleton is typically composed of various protein filaments with significant variation of cross-section diameter, length and stiffness.

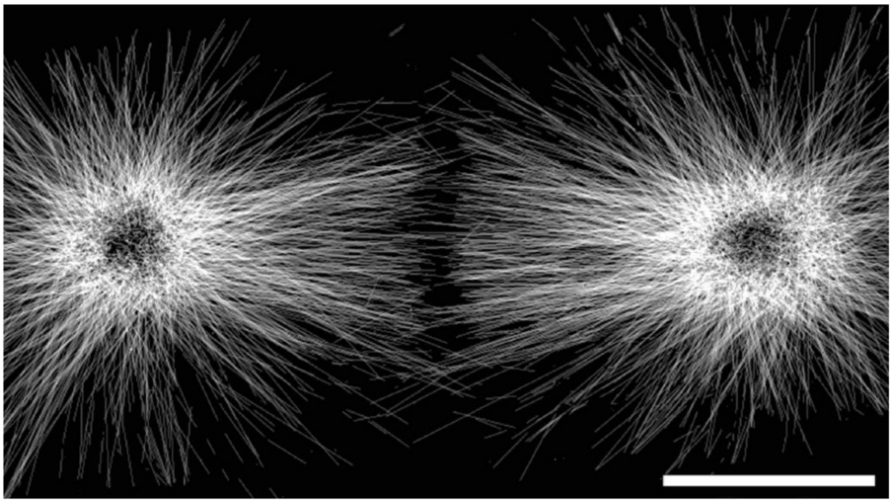

FIGURE 2.23: A SEM image of a mitotic spindle in a living cell reprinted from Müller-Reichert et al. [2018]. The white lines are individual microtubules and the two black circles are the poles of daughter cells. The connectors are not visible in this image due to their size. The length of a scale bar is 5μm.

As cells pass through various phases of their life cycle, they come to an important stage called division, which is realised via mitosis. Mitosis is a highly complex and extremely reliable process of splitting a parent cell into two daughter cells ensuring exact cloning of the parent DNA (chromosomes) between the daughter cells [Bernfield and Slack, 2019]. This process is facilitated by a formation within the cytoskeleton called the mitotic spindle which is responsible for the generation of the force needed to divide the cell and preserve its shape during division [Müller-Reichert et al., 2018]. Mitotic spindles consist of protein filaments, the so-called microtubules – mechanically coupled to each other by protein connectors. A reconstructed scattering electron microscopy image of a typical mitotic spindle is shown in Fig. 2.23. Individual protein filaments (microtubules) appear as white lines. The two dark circles in the middle of a high-density network of microtubules are called centrosomes, or poles of the daughter cells, that are in the process of formation. The individual connectors that couple microtubules to each other are not visible due to their small size. The length of a scale bar in the figure is 5μm.

In order to segregate chromosomes and to split the parent cell, the mitotic spindle exerts a strong push against the cell membrane which leads to compressive loading applied to microtubules (MT). Joglekar et al. [2008] report that microtubules act as compression-supporting struts and can be regarded as beam-columns under axially compressive loading. Therefore, the Euler theory of beam-column buckling may be applicable to study the instability behaviour of microtubules.

An image of experimentally observed buckling of MTs in *Drosophila S2* cell studied by Kulić et al. [2008] is shown in Fig. 2.24 with bundles of microtubules indicated by red lines and individual MTs indicated by white lines. The green dots are peroxisomes that act as anchors for

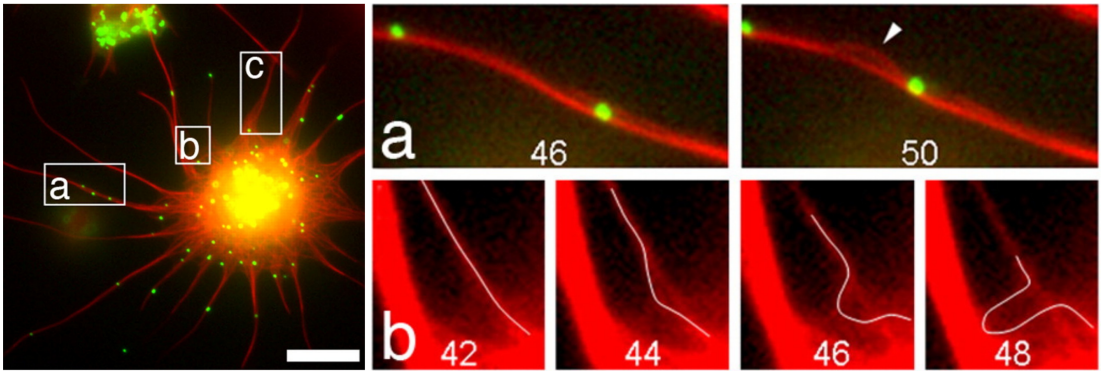

FIGURE 2.24: Two-color fluorescence image of *Drosophila S2* cell with bundles of microtubules shown in red and individual MTs shown in white. The scale bar length is 10 μm. Zoomed images of the rectangles (a) and (b) are shown in the subfigures (a) and (b) for a timeframe in seconds specified on each subfigure. The green dots are peroxisomes that act as anchors for MTs. (a) A micro-tubule is seen buckling out of a bundle. (b) More extreme buckling cases. The images are reprinted from [Kulić et al., 2008].

microtubules restraining them from movement [Kulić et al., 2008]. Note that in Fig. 2.24 (a) the onset of buckling of an individual MT can be seen, whose mode resembles the one of a beam-column with both ends fixed. Further in Fig. 2.24 (b), we see an onset of buckling with further development of the non-linear post-buckling deformation of an individual MT (white line) within the bundle of microtubules. An example of buckling of an entire bundle of MTs is adapted from the numerical study by Soheilypour et al. [2015] and is shown in Fig. 2.25. The bundle has a

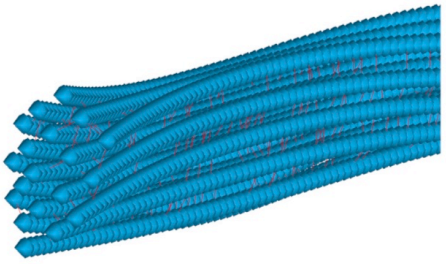

FIGURE 2.25: End view of a bundle of microtubules in buckling as reported by Soheilypour et al. [2015]. The blue thick filaments are individual microtubules coupled by connectors (short thin red lines). Notice the wavy character of the mode along the bundle length as well as the deflection of MT tips within the cross-section. The images is reprinted from [Soheilypour et al., 2015].

global mode which extends along the length and is characterised by the buckling of an entire structure and a local mode occurring within any cross section due to buckling of individual MTs and these two types of behaviour are connected. Consider also that a bundle of microtubules is, effectively, a repetitive assembly of microtubules coupled to each other elastically. Similarly, at a level of organisation of an entire spindle, the bundles of microtubules and individual microtubules form repetitive arrangements of smaller assemblies coupled to each other elastically by a network of proteins called the mesh [Nixon et al., 2015]. Therefore, an entire spindle is a hierarchical arrangement of coupled elastic members with an extremely complex architecture [Petry, 2016].

Buckling of mitotic spindles, i.e. bundles of microtubules and individual microtubules, is of high interest [Novak et al., 2018, Soheilypour et al., 2015, Brangwynne et al., 2006] since it plays a crucial role in cell division. However, the number of approaches of studying buckling of an entire spindle is small [Rubinstein et al., 2009, Ward et al., 2014, Malgaretti and Muhuri, 2016] and a better understanding of the mechanics of spindles for various cell types in various stages of mitosis would provide insight into the biophysics of this problem.

Inspired by the need for a comprehensive framework incorporating spindle mechanics and by the apparent effect that coupling of MTs in bundles and coupling of bundles in a spindle has on the buckling behaviour, in Chapter 8 we also set out to develop a generic mechanical framework of mitotic spindles and apply it to a particular case of *Fission Yeast* mitosis.

2.8 Conclusions

It is apparent from the literature reviewed that elastic instability is an extremely common phenomenon with numerous surprising manifestations in a well-established engineering field. Much of the variability in the behaviour in buckling of delaminated composites and cold-formed structures with perforations, cut outs and holes is characterised solely by the underlying geometric features of the problems. Likewise, similar geometric features drive the variability of instability behaviour in a number of specialist fields from tunable metamaterials to graphene nanocomposites and bundles of sub-cellular protein filaments. The suggestion of the profound geometric connection between wave propagation and vibration in periodic structures and buckling of periodic structures is promising.

In the present study, we are driven by the identified connections between the manifestations of buckling in seemingly unrelated fields characterised by the similarities in the geometry of the problems. Therefore, we dispense with most of the specifics of the mentioned contexts and focus instead on the fundamentals of the behaviour in association with the particulars of the geometries of the considered problems. Hence, we start by studying the instability behaviour of the isotropic bilayer beam later extended to a chain of coupled rods to model the static buckling problem making use of periodicity. Thereafter, we study a plate with a single symmetric cut out as a plane analogy of the bilayer beam problem. Then, we consider the periodic placement of multiple cut outs within the plate to introduce periodicity in a 2D buckling problem. Finally, we focus on modelling the compression of spatial assemblies of sub-cellular protein filaments and buckling of an entire mitotic spindle during the cell division process.

Chapter 3

Buckling of a bilayer beam: instability phase diagram

The extreme sensitivity of buckling behaviour to geometrical features have been reported in a number of applications from mechanics of civil structures to nano-electromechanical devices. Numerous studies focused on the buckling of composites report three distinctive characters of bucking attributed to the interplay between the local and the global buckling in the context of coupled structures.

In this chapter, we consider a rectangular beam-column with a single symmetric longitudinal split under compression. This isotropic bilayer structure serves as an expository problem to study the effect of the geometry on the buckling characteristics. Unlike previous studies, the focus here is to describe the behaviour in terms of several distinct buckling types as will be discussed in detail further.

3.1 Instability of a rod in compression

Buckling was first studied by Euler [Love, 1906] who derived the governing differential equation of an elastica in terms of the local slope of the buckled shape θ as a function of longitudinal coordinate x

$$EI\theta'' + P\sin(\theta) = 0. \tag{3.1}$$

The equation always has a trivial solution $\theta = 0$. But when P reaches its critical value P_{cr}, a supercritical pitchfork bifurcation [Strogatz, 2018] takes place with one unstable trivial solution $\theta = 0$ and two stable solutions $\theta(x)$ and $-\theta(x)$ as the governing equation is invariant under transformation $\theta \to -\theta$. In the vicinity of the bifurcation, a linearised system ($\sin\theta \approx \theta$) is usually solved for the critical buckling loads. It can be expressed as a fourth-order linear ordinary differential equation in lateral displacement w [Timoshenko and Gere, 2012]

$$EIw'''' + Pw'' = 0. \tag{3.2}$$

This represents a differential eigenvalue problem whose solutions have four constants in addition to the eigenvalue P, which is interpreted as the critical buckling load. The solution has the form $w(x) = A\cos\lambda x + B\sin\lambda x + Cx + D$, where $\lambda^2 = P/EI$ and A, B, C and D unknowns. Three of

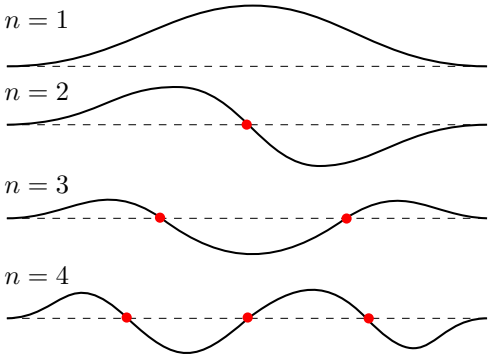

FIGURE 3.1: The sequence of the four lowest buckling modes exhibited by the clamped-clamped beam. The higher modes ($n = 2, 3, 4, \dots$) usually occur only if intermediate supports (nodes) are introduced as indicated with red dots.

the four constants can be determined from the respective boundary conditions, in addition to a family of values of P. This yields a sequence of critical buckling loads (the bifurcation points) and the associated buckling modes which are identified up to an unknown scale factor. The lowest four are shown in Fig. 3.1. While the bifurcation point is not reached, a single stable solution $\theta(x) = 0$ exists. In the bifurcation point, two stable nonlinear branches occur characterised by either left or right buckling deflection. Notice, that the trivial solution is still present but is unstable. The higher bifurcation points are never realised in practice unless additional supports are introduced.

3.2 Instability of a rod with a symmetric split

Recall the compression of a pouch presented in Section 1.1 as shown in Fig. 1.1 as an example of functional buckling, i.e. buckling being used to one's advantage rather than as a problem. Instability ensures a sudden response, unlike, say, some sort of spring that would respond gradually. Here the response is from a fully closed position to a fully open one. A similar idea has also been used in mechanical on-off switches or in other devices such as a pressure release valve. For the pouch structure, the inner frame consists of two flexible elastic strips joined at the ends. Compression beyond a critical value triggers buckling. In general, the two elastic members may deflect together on one side (so that the pouch remains closed) or separate on the two opposite sides (i.e. the pouch opens).

If we model a structure consisting of two flat strips joined by a rotational spring at the two ends, two obvious alternatives: one where both strips buckle on the same side (we will designate this as the cooperative mode) and the other when they open up in the opposite side (we will call this mode a competitive or splitting mode) have a clear ordering. It so turns out that in order to ensure the pouch always opens, an additional curvature was introduced to the beams favouring opposite deflection instead of a cooperative one.

Considering a more general bilayer structure: the two split parts are connected by an elastic structure that not only connects the two sides but also possesses its own flexibility that influences the overall stability in a complex way. The rod has a rectangular cross-section with constant depth throughout. A symmetrically placed cut is parametrised using two geometric

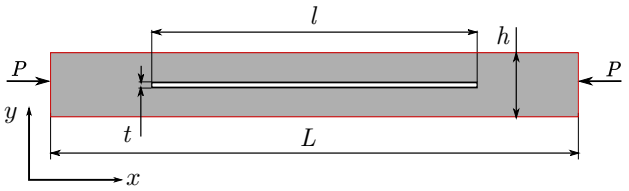

FIGURE 3.2: A schematic diagram of an $h \times L$ beam with a symmetric through-the-width cut represented by an empty rectangle $t \times l$. The structure is axially compressed at both ends by the loading P.

parameters as shown schematically in Fig. 3.2. The beam has a length L, thickness h and width b which is perpendicular to the plane of the paper. The empty rectangle of length l and width t represents a symmetrically positioned through-the-width split. The structure is subjected to axially compressive loading P which may trigger buckling at a force exceeding a critical value of P_{cr}.

When the relative length of the split $\bar{l} = l/L$ is close to one, we have the special case of the double elastic strip connected at the end, as if they were welded together. Further to this, continuous variation of $\bar{l}$ makes the proposed bilayer beam a suitable expository device for a host of other problems mentioned in Chapter 2. Notice that from here onwards, all geometrical and physical parameters with over-bars are dimensionless quantities scaled by the characteristic dimension.

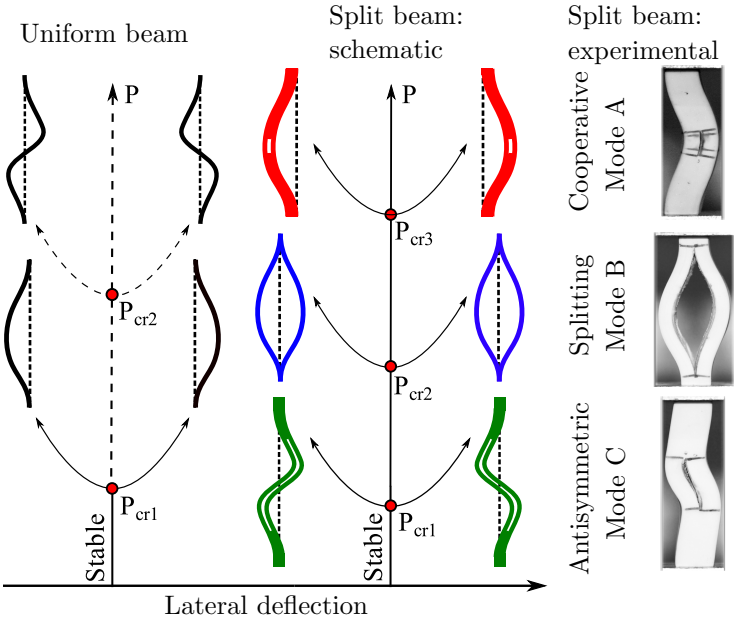

FIGURE 3.3: Conceptual comparison of bifurcation happening in the classical Euler beam-column (*left*) and a split beam-column (*centre*) with the experimentally observed buckling (*right*).

The instability modes of such a bilayer structure afford highly rich behaviour. Unlike the classical Euler beam-column that has well-defined modes that alternate up the modal series, the lowest mode has a node at the end and an anti-node at the centre, each higher mode has one extra node progressively and so on, the buckling behaviour of a split beam is rather complex and such organisation in terms of shapes is not straightforward. The ordering of the modes depends on the geometric parameters, especially the length of the split relative to the overall length. This is schematically shown in Fig. 3.3.

Contrary to an unsplit beam, the buckling behaviour of a bilayer beam-column is unusual. It is shown schematically via the bifurcation diagram Fig. 3.3 (*centre*) which can be compared to the bifurcation diagram of Euler beam-column in Fig. 3.3 (*left*). Depending on the relative length of the split part, the structure has three different buckling modes corresponding to the lowest bifurcation point.

We carried out simple experiments with rubber samples to qualitatively observe different instability types by making longitudinal cuts within original samples of rectangular parallelpiped shape. Images of buckled shapes as observed in these preliminary experiments are shown in Fig. 3.3 (*right*). Each mode is associated with the respective bifurcation point (P_{cr1}, P_{cr2} and P_{cr3}). We observe that as split length changes, the relative position of P_{cr1}, P_{cr2} and P_{cr3} on the P axis alters as well. Therefore, only the lowest bifurcation occurs, but whether it is P_{cr1}, P_{cr2} or P_{cr3} is controlled by the geometry of the structure, which includes, for example, the length of the split part relative to the overall length. Having noticed that the lowest mode could have a very different looking shape that depends on the length of the cut, we set out to explore the dependence of mode shapes of the lowest mode upon structural parameters that describe a bilayer beam.

3.3 Materials and methods

We investigate the behaviour of the bilayer beam by performing a comprehensive experimental study first. Compression testing was carried out on sets of samples made of two polymer materials – Ultra High Molecular Weight Polyethylene (UHMWPE) and Structural Polypropylene Homopolymer (PP PE500) as well as rubber. Notice that the choice of material does not affect the buckling mode type, which is governed by the geometry of the structure. However, it affects the magnitude of the buckling load due to differences in the elastic properties between the materials. Further, we will discuss the experimentation on the polymer samples in detail. The experiment on rubber samples was performed for demonstration purposes and is not discussed in detail.

The choice of material is made based on strength – fracture toughness map of materials [Departement, 2003] under several constraints. Firstly, the sample material should have high fracture toughness to avoid brittle response in buckling. Secondly, it should have low stiffness and hardness to allow cheap tooling, as cutting long thin slots in a bulk of hard material is expensive. Finally, the samples should be softer than the material of the custom-made steel grips for the testing machine. Therefore, we chose relatively soft and crack resistant polymers.

The polymer samples were manufactured using a single sheet of UHMWPE and a single sheet of PP PE500 with CNC high precision machining. Samples of each type are characterised by a combination of values of cut length relative to beam length $\bar{l} = l/L$ and by beam thickness relative to beam length $\bar{h} = h/L$. Also, each sample is specified in terms of overall length L, width b, thickness h and split length l. The width b and thickness h are restricted by the machine grips. Hence, they were kept constant $b = 35\,\text{mm}$ and $h = 24\,\text{mm}$. The overall length L and split length l were varied between sample types to account for different ratios of $\bar{l} = l/L$ and $\bar{h} = h/L$. All the parameters of the UHMWPE samples are assembled in Table 3.1. Five samples of each type were manufactured and tested. These samples were tested to observe the types of

TABLE 3.1: Geometric and material properties of the samples made of UHMWPE

Parameter name	Sample type 1 (mode A)	Sample type 2 (mode C)	Sample type 3 (mode A)	Sample type 4 (mode B)
Length, mm	228 ± 1	228 ± 1	628 ± 1	124 ± 1
Split length, mm	20	68	330	67
Split thickness, mm	3	3	3	3
Number of tests	5	5	5	5
Thickness: 24 mm, width: 35 ± 1 mm				
Material: UHMWPE, Modulus of Elasticity E =400 MPa, Poisson ratio $\nu = 0.31$				

instability behaviour shown in Fig. 3.3 (*right*) such as cooperative buckling (mode $\mathbb{A}$), splitting buckling (mode $\mathbb{B}$) and antisymmetric buckling (mode $\mathbb{C}$) associated with the specific values of geometric ratio $\bar{l}$ and $\bar{h}$.

At the same time, the samples made of PP PE500 were used to probe the behaviour in a small range of $\bar{l}$ and $\bar{h}$. The particular choice of the geometric ratio will be discussed later. In total, 8 different types of these samples were manufactured to probe 8 different geometric ratios. The parameters of PP PE500 samples are assembled in Table 3.2. As before, five samples of each type were manufactured and tested.

TABLE 3.2: Geometric and material properties of the samples made of PP PE500

Sample type	Length, mm	Split length, mm	Split thickness, mm	Number of tests
1	135	39	3	8
2	135	46	3	8
3	108	30	3	8
4	108	36	3	8
5	126	44	3	8
6	126	39	3	8
7	116	37	3	8
8	117	36	3	8
Thickness: 24 mm, width: 35 ± 1 mm				
Material: PP PE500, Modulus of Elasticity E =1300 MPa, Poisson ratio $\nu = 0.31$				

The cut in each sample was made using a CNC milling machine with a Kennedy 3.0 mm 4FL L/SERIES carbide end mill with a shank diameter of 3 mm, overall length 60 mm and flute length 20 mm. Here the diameter of the mill dictated the smallest possible cut thickness being 3 mm. The manufactured samples were gripped by a specifically designed grips that provide extra support for the samples through extended gripping length of 14 mm. This suppressed any rotation of the ends which ensured that clamped boundary conditions were applied. The grips were made of stainless steel with Young's modulus of 2×10^5 MPa which was much higher than the modulus of UHMWPE (400 MPa) or PP PE500 (1300 MPa). Although all reasonable measures were taken to ensure compliance between the samples and the grips, even the smallest irregularities in the experimental setup caused appearance of the mixed buckling modes in the high sensitivity region of geometric parameters as discussed further.

The testing was performed by compressing the samples using the displacement-controlled regime of the *INSTRON* electro-mechanical testing machine with the 2 kN loading cell. The compressive loading and the displacement of the grips were recorded every 0.1 s. The loading speed was kept

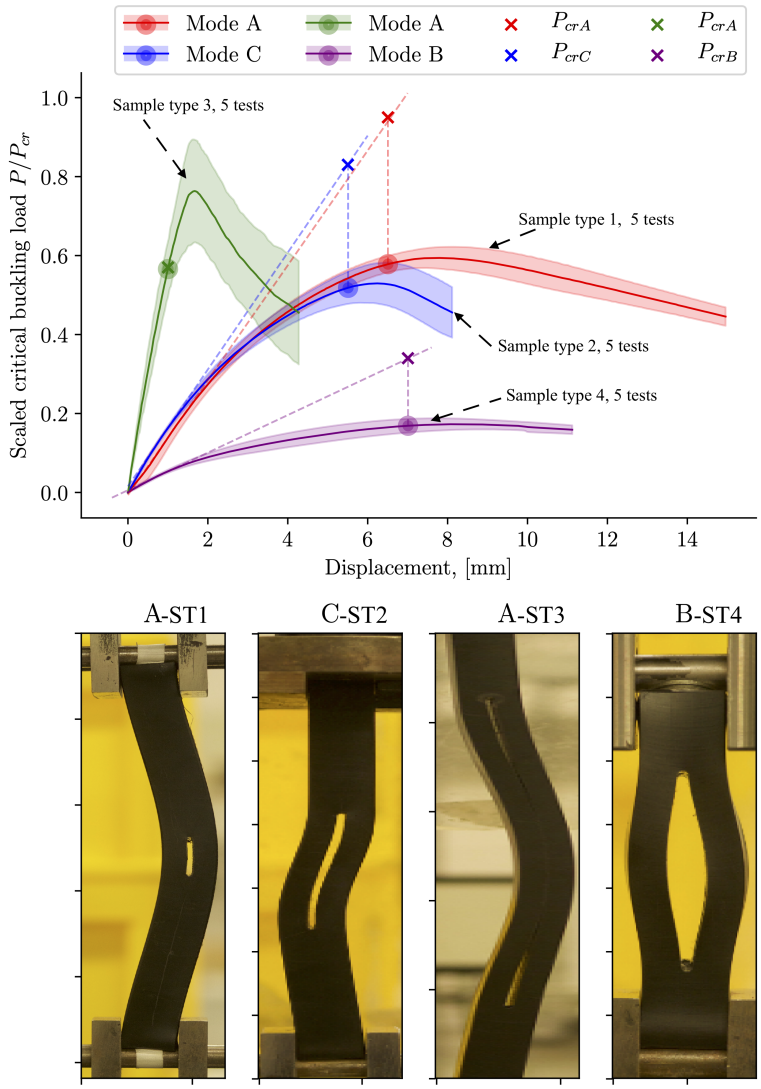

FIGURE 3.4: The experimental load-deflection curves scaled by the Euler critical buckling load for the fixed-fixed beam (solid lines) and the error range (shaded regions around the curves) with the critical buckling loads (solid circles). The dashed lines represent the extended linear parts of the load-deflection curves and the crosses indicate projected critical buckling loads if the material was to follow linear law. The photos below show the observed buckling modes exhibited by the samples. The data is obtained from UHMWPE samples with five samples of each type.

constant at 0.01 mm/s which agrees well with the quasi-static assumption. Photographs of each sample buckled configuration were taken approximately at each mm of displacement. The displacement for which the buckling mode becomes first visible was recorded.

The recorded load-displacement data was post-processed, i.e., the recorded loading was rescaled by the magnitude of the Euler buckling load for the clamped beam (P_{cr}) and the mean and the standard deviation of experimental measurements were calculated along with the identification of the experimental buckling loads. The processed experimental data for the UHMWPE samples is presented in Fig. 3.4 (*top*), the photographs of the four types of UHMWPE samples are labeled A, B, C, and D in Fig. 3.4 (*bottom*). The plots of the mean scaled load versus displacement for each sample type are depicted in solid lines while the shaded areas around them indicate the

standard deviations of the measurements. The mean and the standard deviation were computed for five tests repeated for each sample type. The thick coloured dots represent the points when the buckling load became first visible. Each load-deflection curve is associated with the respective buckling modes, such as cooperative mode $\mathbb{A}$, splitting mode $\mathbb{B}$ and antisymmetric mode $\mathbb{C}$. Notice, that in Fig. 3.4 (*top*) the red curve and the green curve both correspond to mode type $\mathbb{A}$. This reflects that two sample types with very different dimensions, such as shown in the first and the third photographs in Fig. 3.4 (*bottom*) reliably exhibit cooperative buckling of the same character. Thus, the *red curve* corresponds to mode type $\mathbb{A}$ exhibited by sample type 1 and the *green curve* corresponds to sample type 3.

It is apparent from Fig. 3.4 that the measured load-deflection curves have short linear regions that quickly become considerably nonlinear. The quick onset of nonlinear behaviour is major disadvantage of soft polymer samples. Therefore, the critical loads for mode $\mathbb{A}$ (red) mode $\mathbb{B}$ (purple) and mode $\mathbb{C}$ (blue) appear in the nonlinear parts of the respective curves. This means that the material deforms plastically in compression prior to buckling.

Our further numerical and theoretical modelling assumes linearity of the behaviour which is a reasonable assumption for most structural materials at the levels of compression $< 5\%$ which is also the case here. Choice of stiffer materials which have a longer elastic deformation part of the load-deflection curve was not possible due to the restriction on the possible stiffness of the samples. Therefore, to match the experimentally observed loads with the linear prediction, we extended the linear parts of the curves as indicated by the dashed lines in Fig. 3.4 (*top*) as if the materials were to follow the initial linear law. Notice, that by doing so, we retain the initial slope of the load-deflection curve. Then, we draw vertical lines from the buckling points on the original curves until they intersect with the linear predictions. This gives us an approximation of the critical buckling load at which the structures would have buckled in case they remained linearly elastic. The linearised approximation to the buckling load was not chosen for the sample type 1 (green curve in Fig. 3.4 (*top*)) because the load-deflection dependence remains very close to linear for the compressive displacements well beyond the onset of buckling. This is explained by the geometry of this type of samples as they are much more slender compared to other sample types. Thus, the onset of buckling happens before the material exhibits any nonlinearity. Notice, that although the actual buckling loads often differ from linearly predicted ones due to nonlinear effects, this does not affect the buckling mode shapes. Therefore, the performed experiments show true buckling modes.

The photographs of the modes in Fig. 3.4 are shown not to scale. To give a visual representation of the variability of the samples tested, we show a selection of magnified views of the experimentally observed modes in Fig. 3.5 that are brought to the same scale indicated by the scale bar with length 24 mm. The black samples were made of UHMWPE, while the white samples were made of PP PE500. Both materials are polymers with moderate elastic modulus and high fracture resistance. PP PE500 has a higher modulus, higher brittle strength and can be cheaply machined to a higher precision than UHMWPE.

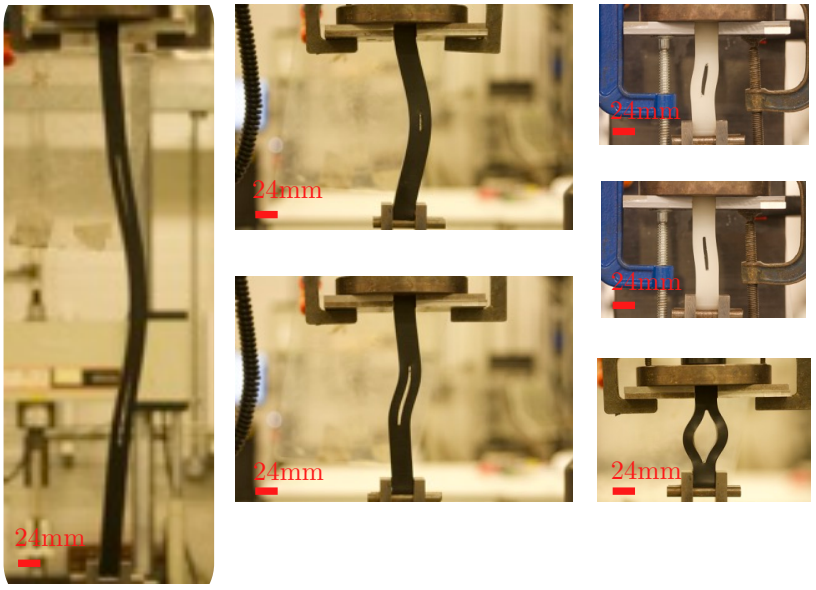

FIGURE 3.5: A collage of images of samples in their true size, as tested in laboratory experiments. The photographs are brought to the same scale indicated by the red bar located in the bottom-left corner of each image. Samples made of UHMWPE are black. The samples made of PP PE500 are white.

3.4 Computational modelling of the split beam

Consider split structure shown in Fig. 3.2. The beam is compressed along the x-axis by the force P and is restrained at both ends from rotation and lateral deflection. The displacement of the right end of the beam along the x-axis is allowed. When the split length is equal to zero ($l = 0$), the structure becomes the same as the classical Euler beam with both ends clamped. The lowest critical buckling load and the corresponding instability mode of such a non-split structure are easily calculated by solving the fourth-order differential equation with four boundary conditions as described in Timoshenko and Gere [2012]. When the cut runs all along, i.e. $l = L$ splitting the beam completely, each half is also a beam-column of thickness $h/2$ with both ends clamped and is solved in the same manner. However, when the split of finite length $l < L$ exists, it creates a discontinuity in the geometry of the beam. Therefore, the solutions can no longer be obtained easily and detailed understanding of the effect of the new structured topology is required. Here we perform a parametric study using FEA by varying $\bar{l}$ and $\bar{h}$ and calculating the buckling load, associated mode shape and the stress, strain and deformation fields for each combination of the parameters.

The Euler buckling problem uses a one-dimensional model of the structure. The bilayer beam, however, requires a more detailed model due to the presence of a cut, which may have localised deformation field, especially at the ends. These two-dimensional effects need to be captured in a simple way. Three-dimensional finite element modelling requires significantly more computational resources due to its complexity but may not give a substantial gain in accuracy compared to the two-dimensional formations. In the case of a split beam, the model is sensitive to split length to beam length ratio $\bar{l}$ in the x-direction and to beam thickness to beam length ratio $\bar{h}$ as well as split thickness to beam length ratio $\bar{t}$ in the y-direction (recall Fig. 3.2). To remove three-dimensional effects, here we consider the split beam that is relatively deep perpendicular

to the plane of the paper. Thus, it is reasonable to assume that all cross-sections along the width are essentially equivalent and b is just a constant scaler of beam stiffness. Therefore, finite element analysis employing the plane strain elements is appropriate.

Following the general guidance from *ABAQUS* user's guide [Dassault Systèmes, 2014], we chose a finite element from the list in *ABAQUS/Standard* solid element library. Firstly, we have to decide which order of an element is required. It is a good practice to use second-order elements if the detailed resolution of the stress/strain/deformation fields around geometric features of the model is important [Dassault Systèmes, 2014]. Furthermore, *ABAQUS* second-order elements are most effective when bending is the main type of behaviour [Dassault Systèmes, 2014]. They generally converge better than the first-order elements thus requiring fewer elements for accurate results. Therefore, we select a second-order plane strain element type.

Next, the choice between full integration and reduced integration techniques has to be made. Typically the elements with reduced integration are more efficient than those with full integration [Dassault Systèmes, 2014], but they may be subject to numerical effects such as shear locking and hourglass effect. In *ABAQUS*, the reduced integration elements have a built-in hourglass control and second-order reduced integration elements are reported to yield more accurate results comparing to the fully integrated ones [Dassault Systèmes, 2014]. The second-order reduced integration elements are recommended in *ABAQUS/Standard* for all problems where a smooth solution is required. The second-order elements with reduced integration are not sensitive to shear locking as the displacements are approximated with quadratic functions within an element making it capable of modelling pure bending without "parasitic" shear.

We expect the mechanics of the split beam buckling to be bending-dominated but with high shear-sensitivity in local areas around the split tip. Therefore, our model should be sensitive to local geometric discontinuities, and be able to accurately represent bending and shear deformation without hourglass effect and shear locking. Taking this into account, we chose eight nodes biquadratic element with reduced integration, CPE8R.

The mesh density needs controlling next. The major requirement that we pose to the mesh is scalability, as it should automatically adapt to the geometrical changes in a parametric study. The mesh size and shape should be adapted in such a way that it captures all the essential mechanics both at small scales near the split tip and at the scale of the whole beam. In such cases, mesh with gradual refinement towards the edges of the split as well as with step-dependent size variation is appropriate.

Standard structured meshes do not satisfy these requirements as they need to be manually adjusted for each case. Therefore, we employ the built-in automatic mesh generator specifying all the mesh parameters at each step of modelling via a dedicated script. Within *ABAQUS*, a mesh based on triangular elements is most suitable for automatic mesh generation [Dassault Systèmes, 2014] as the mesh generation algorithm handles gradual mesh refinement in the vicinity of a geometrical feature without distorting the elements. One disadvantage of the automatically generated triangular mesh compared to the structured mesh is the lack of uniformity which may introduce small deviations from the perfect symmetry about two planes that is inherent to our structure. To make sure that this does not affect our solution, we compared the results using structured and automatic meshes for several selected cases and found that they are in excellent agreement. An example of the automatically generated mesh with the controlled element-size

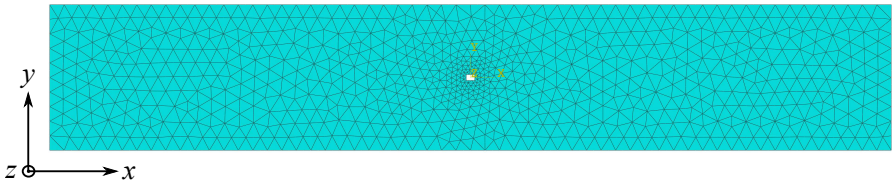

FIGURE 3.6: Example of a finite element mesh consisting of CPE8R elements. The structure is the beam characterised by $\bar{h} = 0.3$ and $\bar{l} = 0.01$.

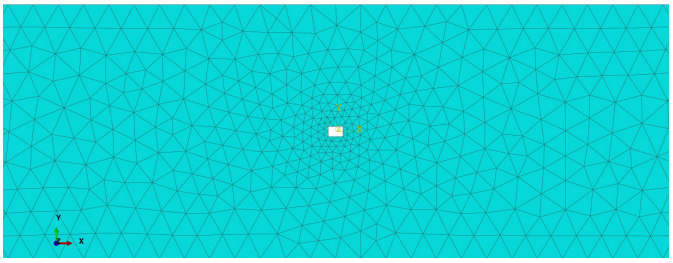

FIGURE 3.7: A detailed view of the mesh with gradual mesh refinement near the edges of the split.

transition at the split tip is shown in Fig. 3.6. A detailed view of the same mesh near the split showing the level of mesh refinement is presented in Fig. 3.7.

The element size transition is kept constant at each step of modelling and is scaled by the average element size. This transition is defined by the difference between the number of elements along the thickness of the beam and along the thickness of the split. We specify that for all cases, the number of elements along beam thickness is 20 and along split thickness is 2. These numbers should give fairly accurate solutions even for extreme cases corresponding to very thin and very thick beams.

Finally, boundary conditions need to be specified. In *ABAQUS*, it is useful to specify the boundary conditions and the loading at abstract points called reference points that are kinematically coupled to the actual nodes of finite elements. The use of such reference points allows a user to implement boundary conditions over the entire surfaces by specifying them at several abstract points which are then translated to each node on the surface.

Consider the schematic diagram of beam in Fig. 3.8. The edges where the boundary conditions

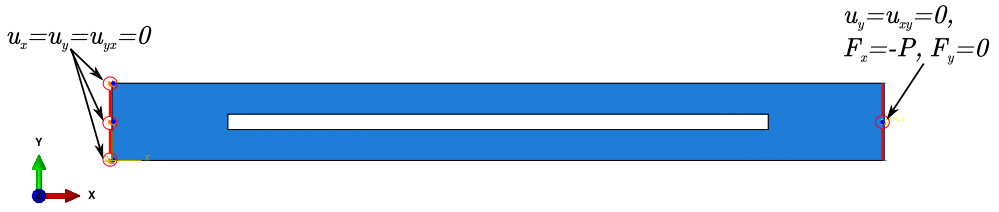

FIGURE 3.8: Schematic diagram of the split beam featuring boundary conditions in the finite element model.

are applied are indicated with the red lines. We impose that the left end of the beam is fixed, thus, the boundary conditions at the left reference point are $u_x = u_y = u_{xy} = 0$, where u_x, u_y are displacements along x and y coordinates and u_{xy} is the rotation in xy plane respectively.

The right end is fixed from all displacements except u_x, thus the boundary conditions read as $u_y = u_{xy} = 0$. Instead, the right end is compressed by the load P which results in $F_x = -P$ and $F_y = 0$. We do not need to specify any conditions in the z-direction as plane strain elements do not have any out-of-plane degrees of freedom.

The structural material of the beam is assumed homogeneous with elastic modulus $E = 2 \times 10^5$ MPa and Poisson's ratio $\nu = 0.3$. The geometrical parameters are considered as non-dimensional ratios of L spanning the following values. The relative split length is $\bar{l} = l/L$ and $0.01 \leq \bar{l} \leq 0.99$, the relative beam thickness is $\bar{h} = h/L$ and $0.01 \leq \bar{h} \leq 0.5$, the relative beam width is $\bar{b} = b/L = 0.1$ and the relative split thickness is $\bar{t} = t/(\bar{h}L) = 0.04$. Note, that the split length and the beam thickness are specified as intervals. These are the two governing parameters, upon which we study how the behaviour changes. For each case specified by a combination of $\bar{l}$ and $\bar{h}$, a full FEA-based stability analysis is performed. The parameters span a grid of 100×100 values, each point corresponding to a combination of $\bar{l}$ and $\bar{h}$ and a particular FEA analysis. Such a number of cases results in a good balance between computation cost and smoothness of the change in behaviour within the parameter space. Thus we have $10,000$ buckling analyses to be carried out.

The linear stability analysis performed for each combination of $\bar{l}$ and $\bar{h}$ is based on the minimum of the total potential energy principle. The total potential energy Π is the sum of the elastic strain energy U and the potential energy of external loading V defined as the negative of work done by external forces and moments. In case of a Bernoulli-Euler beam, $U = \int (EI/2) \left(w''\right)^2 \mathrm{d}x$, and $V = -\int (P/2) \left(w'\right)^2 \mathrm{d}x$, where $w(x)$ is the shape of the buckled profile; a prime denotes a derivative with respect to x. Here V equals to force P times the axial shortening (i.e. work done by external forces), which is proportional to the square of the local slope of the buckled shape. Equilibrium requires that over all the choices for $w(x)$, the actual configuration corresponds to the minimal value of Π. Mathematically, this is expressed as $\delta\Pi = 0$, where δ means "variation of".

In FEA the displacements within each element are approximated using local shape functions – typically polynomials evaluated at nodal points, where each nodal displacement is a generalised coordinate q. Under the small displacement assumptions of the linear elasticity, the integrals take the form $U = (1/2)\, \mathbf{q}^\intercal \mathbf{K} \mathbf{q}$ and $V = (1/2)\, \mathbf{q}^\intercal \mathbf{K}_g \mathbf{q}$ that are both quadratic forms of $\mathbf{q}$, where $\mathbf{q}$ is the vector containing all generalised coordinates. $\mathbf{K}$ and $\mathbf{K}_g$ are assembled stiffness and geometric stiffness matrices. After taking variations of the total potential energy $\delta\Pi$ and equating them to zero (given that the system is in an equilibrium state), one arrives at a generalised eigenvalue problem

$$\mathbf{K}\mathbf{q} = P\mathbf{K}_g\mathbf{q}. \tag{3.3}$$

The eigenvalues of Equation (3.3) are the critical buckling loads P_{cr} whose magnitudes define the position of red points on the P axis in Fig. 3.3. At the same time, the associated eigenvectors $\mathbf{q}$ specify the buckling mode of the structure. The stiffness and geometric stiffness matrices assembled in FEA are usually large and generally sparse. *ABAQUS* provides two built-in algorithms for eigenvalue computation, e.g., Lanczos and subspace iteration algorithm [Dassault Systèmes, 2014]. According to Nour-Omid et al. [1983], the Lanczos method converges faster than the subspace iteration algorithm and requires less computational resources. However, in *ABAQUS*, the subspace iteration algorithm is the default for linear buckling and preferred over Lanczos for large bifurcation problems. Additionally, the Lanczos algorithm cannot be used

TABLE 3.3: A summary of the parameters specified to *ABAQUS* solver.

Parameter	Value	Summary
Number of eigenvalues	8	Number of eigenvalues requested to be calculated at each case.
Subspace iteration vectors	16	Number of assumed vectors per iteration. Parameter of the subspace iteration algorithm.
Number of iterations	300	Maximum number of subspace iterations. Ensures convergence.
Number of elements	≈ 6000	Average number of finite elements per model. Was chosen based on the study of convergence.
Parallelisation	MPI, 1 GB/core, 2 nodes/16 cores	Type of parallelisation, allocated memory and CPU
Number of cases	10,000	Total number of FEA simulations performed.

in bifurcation problems for models containing contact regions, connectors, hybrid elements and coupling constraints [Dassault Systèmes, 2014] which is the case here. Therefore, we chose the subspace iteration algorithm, especially considering that according to Nour-Omid et al. [1983], the performance gain by the Lanczos algorithm is not substantial for the lowest few eigenvalues.

ABAQUS conveniently provides a scripting interface applicable for parametric studies. Therefore the modelling could be automated using a list of the parameters presented in Table 3.3 as the only user input. Thus, by running the computations on IRIDIS high-performance computing facility complemented by the execution of supporting tasks on a workstation, we explored the wide $\bar{l}$–$\bar{h}$ space automatically.

3.5 Results and discussion

After solving Equation (3.3) for each of the 10^4 combinations of $\bar{l}$ and $\bar{h}$, we scale the eigenvalues by the fundamental buckling load for clamped boundary conditions $P_E = 4\pi^2 EI/\left((1-\nu^2)L^2\right)$. Here, E is the elastic modulus, ν is the Poisson ratio and I is the second moment of inertia. The $1-\nu^2$ factor is not present in the buckling load of a beam-column and is introduced here to account for plate effects. The factor arises if one considers buckling load of a thin plate $P_{\text{cr}} = 4\pi^2 Db/L^2$, where $D = Eh^3/[12(1-\nu^2)]$ is the flexural rigidity of a thin plate. For beams, the bending stiffness $EI = bh^3/12$, we can write $P_E = 4\pi^2 EI/((1-\nu^2)L^2)$. Non-dimensionalisation with respect to P_E stated above is a fair scaling factor to use, since plane strain resembles a thin plate in its edge view.

A continuous structure has infinitely many buckling loads, but only the lowest (fundamental) one is of practical interest. Consider the surface shown in Fig. 3.9 (a), which is a plot of the scaled buckling load $\bar{P}_1 = P_1/P_E$ in the parameter space $\bar{l}$–$\bar{h}$ obtained from the finite element analysis. We will designate the lowest surface in the parametric space as the *fundamental instability surface*. To probe the behaviour of the bilayer beam further, we can slice the hyper-surface with planes of constant $\bar{h}$=0.04, $\bar{h}$=0.1 and $\bar{h}$=0.21 and then pick four points on the lines of

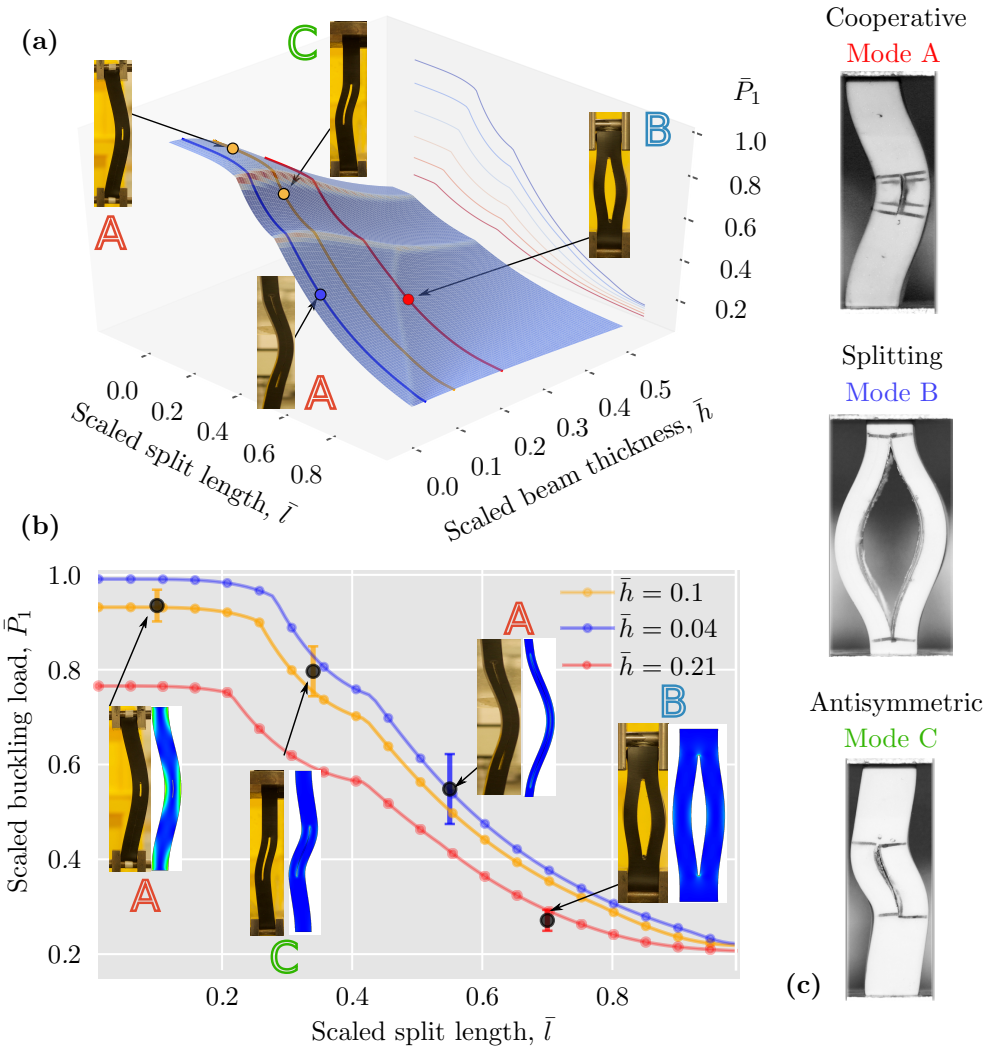

FIGURE 3.9: Characteristics of the instability behaviour of a bilayer beam. (a) A fundamental instability surface – a plot of the lowest buckling load as a function of $\bar{l}$ and $\bar{h}$. The colour of the surface reflects the mean curvature. Selected scenario for experimental testing performed on polyethylene samples are indicated by dots with the associated observed modes. (b) The surface is sliced by planes of constant $\bar{h}$ (colour lines). Experimentally measured buckling force values (solid black dots with error bars) as well modes shapes (sepia) compare well with computational instability modes (blue). (c) The black and white photographs of the three characteristic modes as observed from compression of rubber samples.

intersection as indicated by the colour dots in Fig. 3.9 (a). Then, we manufactured and tested the samples characterised by $\bar{l}$ and $\bar{h}$ of each point and report the observed buckling mode as indicated by the photographs (sepia) in Fig. 3.9 (a). The choice of $\bar{l}$ and $\bar{h}$ for the samples is not arbitrary. Notice a colour map superimposed onto the fundamental instability surface. The colour indicates the mean curvature of the surface. The high curvature ridge-like areas (highlighted in red) separate the vast flat regions (blue). The ridges are relatively small regions over which a rapid change of buckling character is expected. Therefore, we select points to lie further from the ridges and closer to the centres of the flat regions as they are more likely to be characteristic of the behaviour types.

In an experimental study, we report three distinctive buckling types of the bilayer beam, i.e., the cooperative buckling (mode $\mathbb{A}$), splitting buckling (mode $\mathbb{B}$) and the antisymmetric buckling

(mode ℂ). The robustness of the behaviour was verified by repeating experiments for several samples made of the same material and for the samples made of different materials. The three observed modes exhibited by UHMWPE samples are shown in (sepia) in Fig. 3.9 (a). The same mode types observed in a simple experiment on rubber samples are shown in Fig. 3.9 (c).

Three vertical sections characterised by the constant $\bar{h}$=0.04 (blue dotted curve), $\bar{h}$=0.1 (orange dotted curve) and $\bar{h}$=0.21 (red dotted curve) are depicted in Fig. 3.9 (b). Previously selected points for experimentation are labelled on these sections with thick black dots with error bars. The position of each dot on the $\bar{P}_1 - \bar{l}$ plane is dictated by the magnitude of the scaled critical buckling load $\bar{P}$ averaged over five measurements while the error bars reflect the scatter in the experimental data (see Section 3.3 for details). There is an excellent agreement between numerical (blue modes) and experimentally observed modes (sepia) as seen from Fig. 3.9 (b). The ridge-like regions in Fig. 3.9 (a) are marked by the high curvatures of the fundamental

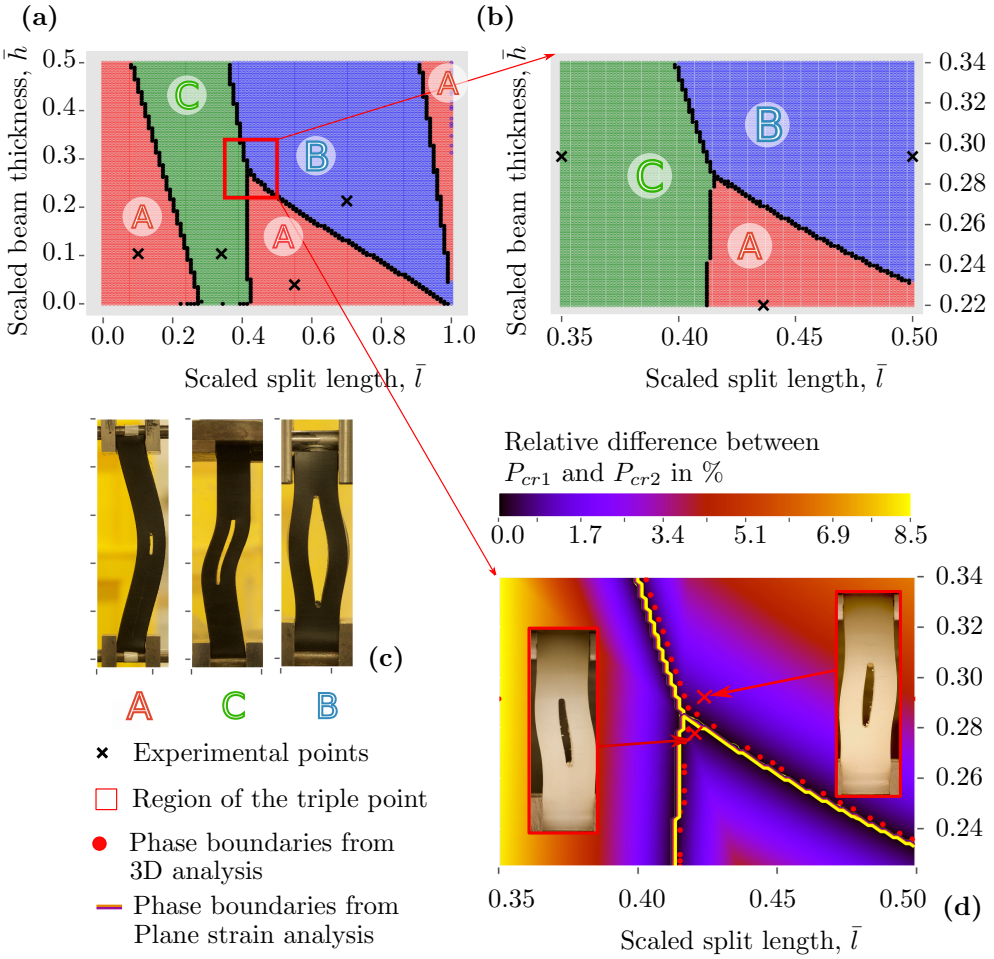

FIGURE 3.10: Phase diagram of buckling states of the bilayer beam computed using MAC classification. (a) Regions on a $\bar{l}$–$\bar{h}$ plane characterised by cooperative buckling (𝔸), splitting buckling (𝔹) and antisymmetric buckling (ℂ). The black crosses indicate $\bar{l}$–$\bar{h}$ used in experiments. (b) A zoomed view near the triple point. (c) Mode shapes observed in experiments for the selected $\bar{l}$–$\bar{h}$ values. (d) Points of near degeneracy of the lowest two buckling loads (red dots) fall on the phase boundaries computed using MAC (yellow line). The experimental modes for the samples indicated by the red crosses exhibit mixed buckling in the vicinity of the triple point.

surface (highlighted in red). From the view of the slices of the surface by the planes of constant

$\bar{h}$ in Fig. 3.9 (b) we see the ridges as highly curved parts of the buckling load trajectories. These extreme zones form boundaries on a map of instability behaviour as shown in Fig. 3.10 (a),(b),(d).

Fig. 3.10 (a) shows a map with five regions in three colours –each colour representing an instability mode labelled $\mathbb{A}$, $\mathbb{B}$ and $\mathbb{C}$. Three different colours are assigned on a 100×100 grid of $\bar{h}$ and $\bar{l}$ combinations, where each point is assigned colour according to one of the three instability modes observed. By analogy to phase diagrams in physics and material science, we call a chart that maps different behaviour to the regions of parameters a phase diagram.

Visual classification of the thousands of data points according to instability modes is not easy, especially for a large number of cases. Here we use an approach based on semi-supervised machine learning for automated classification of the mode types. A standard k-nearest neighbours algorithm with Euclidean metric performs poorly due to high dimensionality and a complex structure of the eigenvectors returned by FEA. Hence, we employ an alternative scalar quantity, commonly used by the structural dynamics community when comparing eigenmodes (usually an experimentally measured one against a theoretically obtained one), the so-called Modal Assurance Criteria (MAC) [Allemang, 2003]. MAC, between two n-dimensional eigenvectors $\mathbf{\Psi}_i$ and $\mathbf{\Psi}_j$, normalised to unit length, is given by

$$\mathrm{MAC} = (\mathbf{\Psi}_i^\intercal \mathbf{\Psi}_j)^2 \tag{3.4}$$

It is a measure of a degree of resemblance between modes, which is relatively forgiving to small irrelevant features and noise in the compared vectors, while it can capture broad features of mode shapes being compared reliably [Pastor et al., 2012]. This has been reported especially for high dimensional vectors. The employed MAC-based classification procedure consists of the following steps. Firstly, the five reference points are selected, each one approximately in the centre of each flat region in Fig. 3.9 (a) to guarantee pureness of the eigenvector Ψ_i associated with each reference point $i \in [1, 5]$. Secondly, MAC value $(\mathbf{\Psi}_i^\intercal \mathbf{\Psi}_j)^2$, $i \neq j$ between each reference eigenvector i and every other eigenvector j on the $\bar{h}$–$\bar{l}$ plane is calculated. If the MAC value between a reference eigenvector and a probed eigenvector is close to one (up to some tolerance value), the respective probed point is assigned the colour of the reference mode and is left blank otherwise. Finally, repeating the classification for each of the five reference eigenvectors, we assign colours to all points on the $\bar{h}$–$\bar{l}$ plane.

Five regions on $\bar{h}$–$\bar{l}$ plane characterised by buckling modes of the same type are plotted in Fig. 3.10. By analogy with thermodynamic phase diagrams, material phase diagrams, and Ashby maps sometimes called deformation mechanism maps [Hutchinson and Wu, 1983], we call each such region of parameters a phase. Therefore, the MAC-based map in Fig. 3.10 is a phase diagram of buckling states. The black dotted lines between the adjacent phases are, thus, called phase boundaries. Each phase boundary is a line when crossed on the phase diagram, is accompanied by a dramatic change in the instability mode type, reminiscent of a phase transformation. Phase boundaries overlap with the red ridges of the fundamental buckling surface in Fig. 3.9 (a). Consider the split beams characterised by the combinations of $\bar{h}$ and $\bar{l}$ which fall exactly on the phase boundary. These structures exhibit two nearly degenerate buckling modes and are extremely sensitive to small perturbations in parameters and boundary conditions so that any physical differences in the nominally identical structures would lead to the realisation of one mode type or another.

The black crosses in Fig. 3.10 (a) denote combinations of $\bar{h}$ and $\bar{l}$ for which the testing on UHMWPE samples was carried out. These points are the same as those in Fig. 3.9 (a). The observed buckling modes are also depicted in Fig. 3.10 (c) for clarity and to demonstrate the behaviour characteristic to each phase of the phase diagram.

A closer look at the phase diagram reveals that while most of the boundaries exist between two adjacent phases, there is a region within the red box in Fig. 3.10 (a) where all three phases come close to each other. A zoomed calculation of this area of the phase diagram is shown in Fig. 3.10 (b). These calculations required finer resolution of the map-making use of reduced steps so that the zoomed window contains instability calculations for 10,000 cases of $\bar{h}$ and $\bar{l}$ combinations. To show that the phase boundaries correspond to the degenerate eigenvalues of Equation (3.3) and to further study the behaviour where three phases meet, we calculate the distance between the fundamental surface of $\bar{P}_1$ and the similar but higher surface of $\bar{P}_2$ (not displayed here). In Fig. 3.10 (d) we plot $\left|\bar{P}_1 - \bar{P}_2\right|$ in percents of $\bar{P}_1$ on the $\bar{h}$–$\bar{l}$ plane (colour code). We also plot the local minima of the separation between the two surfaces (red dots) which fall precisely on the phase boundary (yellow line) computed with MAC as seen in Fig. 3.10 (d). The magnitudes of the minimums of $\left|\bar{P}_1 - \bar{P}_2\right|$ are not exactly zeros but very small numbers. Therefore, we shall further assume that on the phase boundary two different buckling modes have nearly the same critical loads – they are *nearly degenerate*.

In addition to plane strain modelling discussed so far, we have also computed the phase diagrams using full 3D FEA to make sure that the phase boundaries are invariant of the employed simplifications. We report that in all three cases, the phase boundaries nearly coincide, such as the red dots and the yellow lines in Fig. 3.10 (d).

Consider a point shared by the three phases within the zoomed rectangle in Fig. 3.10 (b),(d). This point is reminiscent of the *triple point* (such as those found in water-ice-vapour system) and is associated now with a near-triple-degeneracy of instability modes. Location of this point is confirmed by MAC-based classification of eigenvectors of 3.3 for 2D plane strain (yellow boundary in Fig. 3.10 (d)) and by 3D FEA (red dots in Fig. 3.10 (d)) followed by the calculation of nearness between the eigenvalues of 3.3.

In the vicinity of the triple point, the buckling character of the split beam is extremely sensitive to small perturbations in structural parameters and boundary conditions. In practice, this high sensitivity would push the unstable structure into one of the three possible buckling mode types, depending on slight imperfections that are inevitable. To demonstrate this, we performed experiments on PP PE500 samples (see Section 3.3 for details) close to the triple point and report that opposed to the clearly distinct mode type away from the phase boundaries (Fig. 3.10 (c)), experimentally observed modes near the triple point lack this clarity as seen from Fig. 3.10 (d). In this region, the buckling behaviour is extremely sensitive to the slightest perturbations in the experimental setup as well as to the smallest shifts within the parameter plane. A mixture of the three mode types, e.g. $\mathbb{A}$, $\mathbb{B}$ and $\mathbb{C}$, is observed experimentally (white samples in Fig. 3.10 (d)), which demonstrates the uncertainty in buckling character in the vicinity of the triple point.

Consider the structural behaviour generalised in Fig. 3.10 (a),(b),(d). MAC shows that the character of the instability mode changes abruptly when traversing the phase boundaries. Linking these observations to the discussion of the bifurcation diagram of a bilayer beam (Section 3.2),

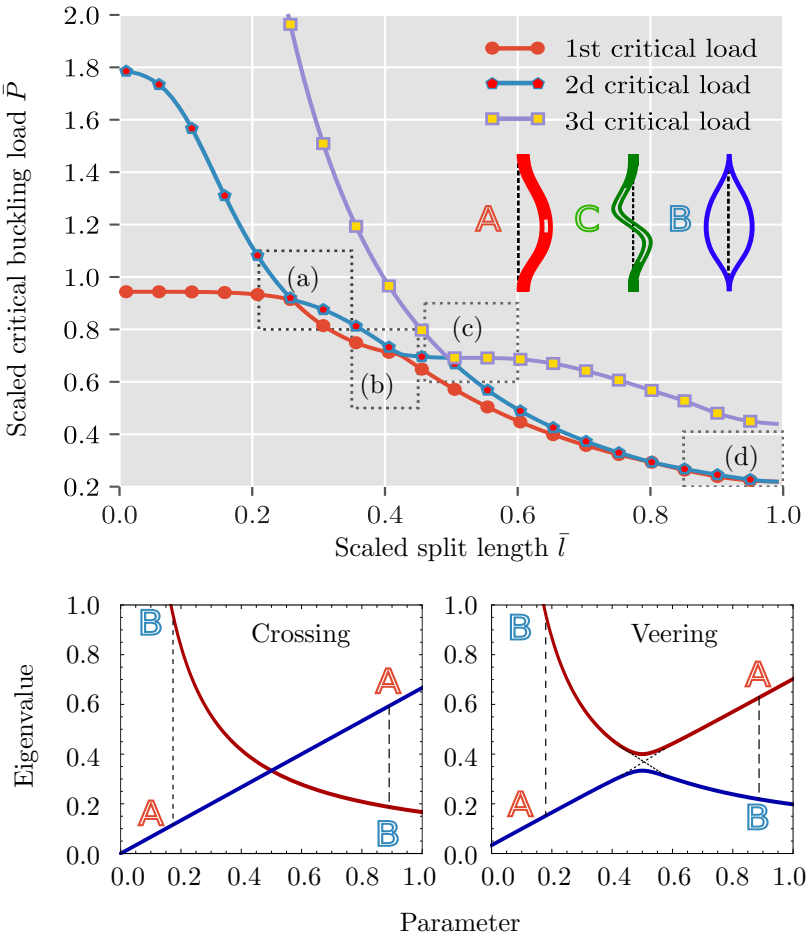

FIGURE 3.11: Three lowest buckling load trajectories plotted as functions of $\bar{l}$ for $\bar{h}$= 0.035 (*top*). Dashed rectangles (a)-(d) contain the zones of near-degeneracy of buckling loads within which qualitative changes to the instability type occur. (*bottom*) A cartoon depicting two possible scenario of near-degeneracy – a crossing of eigenvalue trajectories and the avoided crossing via eigenvalue veering phenomenon. In either case, the relative order of modes changes $(\mathbb{A}, \mathbb{B}) \rightarrow (\mathbb{B}, \mathbb{A})$.

we suggest that the relative order of the three lowest bifurcation points along the P axis (recall Fig. 3.3) alters at a boundary, which is further supported by the near-degeneracy of the buckling loads. To visualise the relative position of the buckling loads on a phase diagram, we slice the three lowest buckling surfaces $\bar{P}_1$, $\bar{P}_2$ and $\bar{P}_3$ with a plane of constant $\bar{h}$=0.035 and study the buckling load trajectories on $\bar{P} - \bar{l}$ plane as shown in Fig. 3.11. The lowest trajectory on $\bar{P} - \bar{l}$ plane closely resembles the trajectories in Fig. 3.9 (b) but for another $\bar{h}$.

The three trajectories appear to intersect at the points of near-degeneracy in Fig. 3.11 (*top*). However, as we zoom in within the dashed rectangles (a)-(d), we cannot locate the exact point of intersection as the trajectories appear to come close to each other but then repulse via a high curvature veering. Although we are unable to exactly resolve the behaviour in the point of near-degeneracy, the fact that the eigenvectors are no longer orthogonal within the rectangles (a)-(d) indicates that a high curvature veering scenario is more likely. In either case, when probed outside of the phase boundaries, the order of the buckling modes when traversing from one phase to another is swapped $(\mathbb{A}, \mathbb{B}) \rightarrow (\mathbb{B}, \mathbb{A})$ – the behaviour is changed. This is best seen from the zoomed view of the rectangles (a)-(d) in Fig. 3.12.

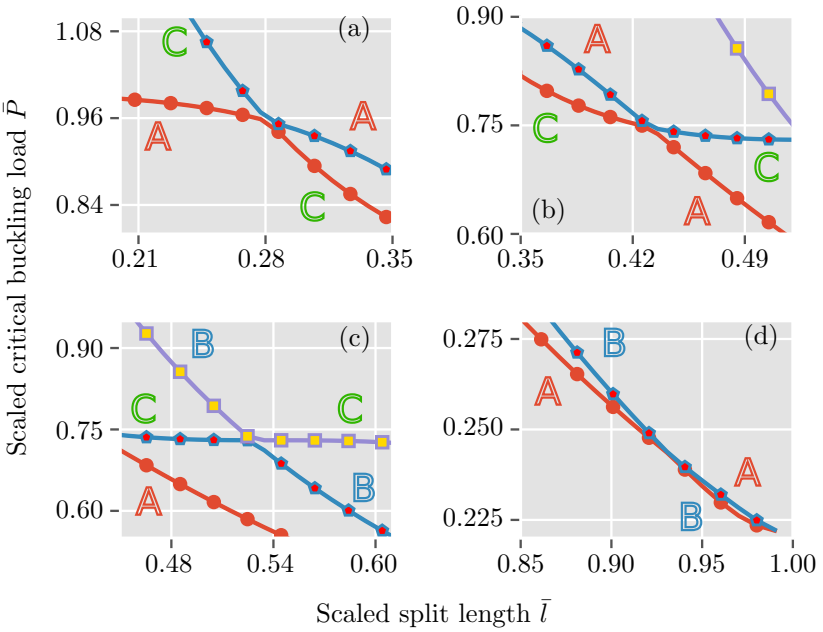

FIGURE 3.12: A magnified view of the near-degenerate regions on the $\bar{P} - \bar{l}$ plane showing transformations of buckling character. (a) Swapping between cooperative and antisymmetric buckling $(\mathbb{A}, \mathbb{C}) \rightarrow (\mathbb{C}, \mathbb{A})$. (b) Reversed swapping between antisymmetric and cooperative buckling $(\mathbb{C}, \mathbb{A}) \rightarrow (\mathbb{A}, \mathbb{C})$. (c) Swapping between antisymmetric and splitting mode $(\mathbb{C}, \mathbb{B}) \rightarrow (\mathbb{B}, \mathbb{C})$. (d) Swapping between cooperative and splitting buckling $(\mathbb{A}, \mathbb{B}) \rightarrow (\mathbb{B}, \mathbb{A})$.

Similar phenomena also occur in a variety of contexts, e.g., in quantum mechanics [Zener, 1932], wave propagation in solids [Pierre, 1988], in dispersion relations [Bhaskar, 2003, 2009, Mace and Manconi, 2012], etc. A comprehensive review of the eigenvalue crossing versus avoided crossing is given by Novotny [2010]. These phenomena are also discussed from a more generic point of view in Appendix 10 of Arnold [1978].

It is apparent from Fig. 3.11 and Fig. 3.12 that the appearance of the various buckling modes associated with the phases of the phase diagram is triggered by a series of transitions through the points of near-degeneracy that a bilayer undergoes as the cut length is changed. And as such transitions involve an exchange of buckling modes between the respective eigenvalues (via crossing or veering of eigenvalues), these phenomena are considered to drive the behaviour on phase boundaries. In particular, the triple point in the phase diagram in Fig. 3.10 (a),(b),(d) is a rather unique example of triple-near-degeneracy of three eigenvalue surfaces with the respective swapping of the three distinct mode types.

3.6 Conclusions

In this chapter, we present a comprehensive picture of the instability behaviour of a bilayer beam. We classify all the instability mode types, observed experimentally and computationally, in a map that presents the behaviour in parameter space. Each region on this phase diagram corresponds to a type of mode shape different from another. Qualitative change of the mode type takes place when traversing the phase boundaries on the diagram. We associate this behaviour with the near degeneracy of the lowest two eigenvalues. We also report the existence of the

triple point on the phase diagram, where three types of buckling coexist. This relates to the near-triple-degeneracy of the respective buckling loads.

We also performed experiments on a number of samples of bilayer beams, by compressing them and observing the buckling modes. We tested the samples described by various $\bar{l}$ and $\bar{h}$ ratio and report that these parameters strongly affect the behaviour. Three types of buckling, i.e., cooperative, splitting and antisymmetric mode were observed experimentally.

Phase diagrams are relatively rare outside the domain of material science, physics and chemistry. However, here we observe that buckling states of a bilayer beam correspond to distinct regions of geometric parameters. The change between the states as the phase boundaries are crossed is sharp. Furthermore, we identified a specific region in the vicinity of the triple point where the buckling character is uncertain. This area, as well as phase boundaries, should be avoided when designing the structures as it is very hard to predict their behaviour. However, in nano-electromechanical devices and other specialist fields, the existence of such regions may be seen to be advantageous as the structure there is in a near-degenerate state which makes transitions between different modes very easy.

Chapter 4

Stability of an elastic bilayer: analysis & kinematic interpretations

---

In this chapter, we present analytical explanations underlying the mode transformation in a bilayer beam. The approach is that of one-dimensional bending theories in conjunction with some adaptations specific to the inherent kinematics of a two-layer structure joined at the ends. We start by studying the deformation fields and strain energy density maps from numerical modelling to understand what types of deformation exist in various mode types. Based on this analysis, we provide analytical explanations while employing the minimum of total potential energy principle that defines the equilibrium. In contrast to all the previous studies, the focus is not on the very accurate prediction of buckling loads, which can indeed be obtained from an FEA analysis with a fine mesh. Instead, here we deliberately compromise on the accuracy in favour of the physical understanding associated with the rich mode types previously observed experimentally and computationally for the lowest mode. Our analysis uses global mode shape approximations of the buckled shapes and returns functional dependencies of the buckling loads and the associated mode types on the parameters, which are crude but provide a novel insight into the mechanics of the behaviour.

4.1 Strain energy distribution in a bilayer beam

We can learn about the deformation mechanisms in each of the three characteristic mode types of the bilayer beam by visually observing the energy density maps extracted from FEA modelling performed in Chapter 3. We choose a single representative point on the phase diagram shown in Fig. 3.10 specified by $\bar{h} = 0.09$ and $\bar{l} = 0.59$ and extract the lowest three modes previously computed by FEA. Then we superimpose the computed contours of strain energy density on top of each deformed configuration and obtain the strain energy density maps of each mode type as shown in Fig. 4.1. As all the mode types are plotted at the same scale in Fig. 4.1, and the magnitudes of the strain energy are scaled by the same peak value of 4.7×10^5 Pa found in the vicinity of the cut tips, the energy maps can be visually compared.

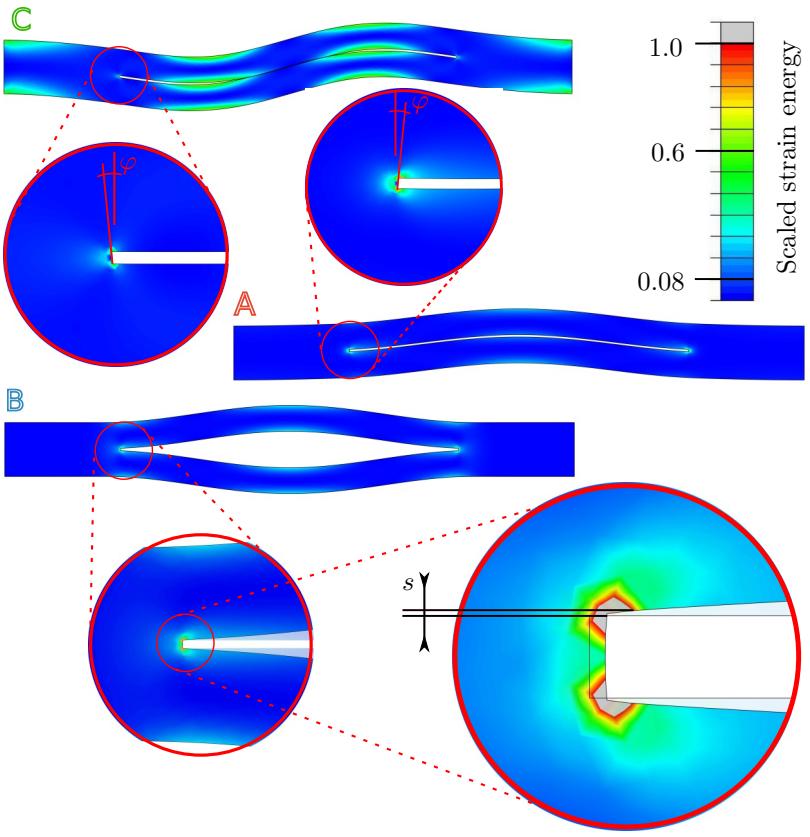

FIGURE 4.1: Strain energy density maps obtained from the FEA computations discussed in Chapter 3. The three computed mode types for $\bar{h}$= 0.035 and $\bar{l}$= 0.59 are considered. The strain energy magnitude is scaled to the peak value of 4.7×10^5 Pa at the cut tip. The zoomed views of the mode 𝔸 and ℂ reveals considerable shear deformation φ in addition to the high strain energy localisation at the cut tip. The zoomed view of the mode 𝔹 reveals a stretch deformation s in the cut tip.

In a uniform rod under compression, bending is the dominant deformation mechanism and the strain energy is proportional to the square of the curvature of the deformed shape. Thus, the highest strain energy density for a buckled shape in the fundamental mode appears at the ends and also in the central part where the curvature is the highest. It is apparent from Fig. 4.1 that the bilayer beam exhibits a fairly different strain energy distribution. High values of strain energy density appear localised around the tips of the cut, as seen from the magnified views of modes 𝔸, 𝔹 and ℂ in Fig. 4.1. A classical solution of plane elasticity problem on the stress distribution near the edge of an elliptic hole [Muskhelishvili, 1977, Timoshenko and Goodier, 1986] indicates that $\sigma \sim 1/\rho$; i.e. stress is inversely proportional to the radius of curvature near the tip. In the case of an elliptic crack, $\rho \to 0$ and the stress is not bounded for a perfectly elastic material. The strain energy density is half of the tensor product of stress and strain tensors at each point. Then, if any stress component is unbound, the strain energy density localises at a small region near the crack tip. The solution for the rectangular cut is more complicated but the dependence of stress field away from the tip largely remains qualitatively similar, which explains the high strain energy density near the tip of a thin cut. Moreover, the cut tip deforms differently leading to different patterns of strain energy localisation as can be seen from the magnified views

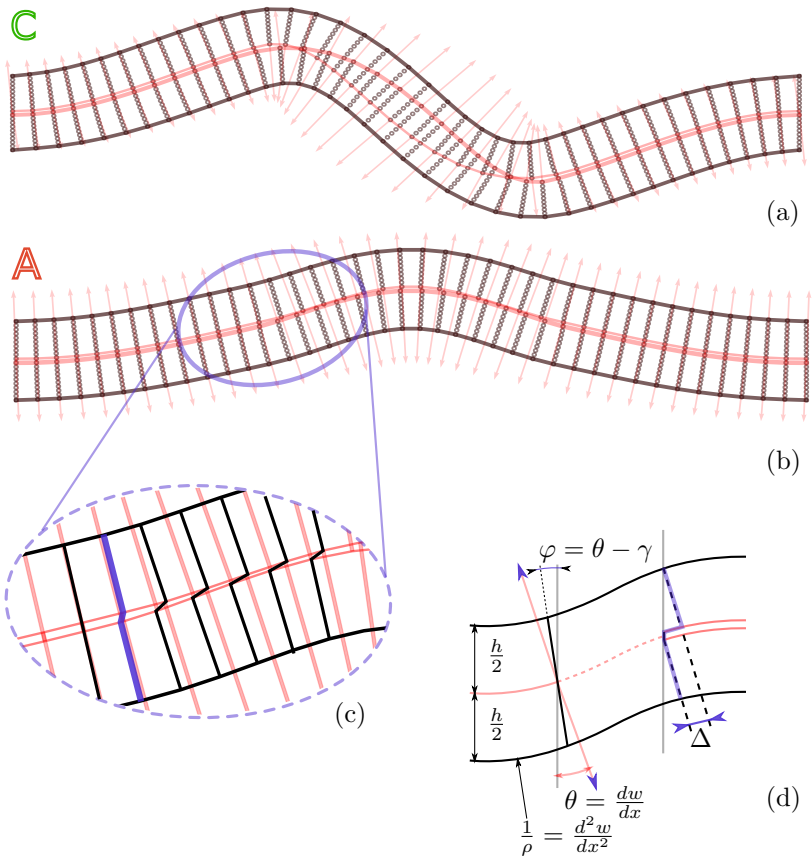

FIGURE 4.2: Mapping of deformations on the computed modes $\mathbb{A}$ and $\mathbb{C}$. (a),(b) Antisymmetric and cooperative modes obtained from computations. The thick red lines are apparent neutral axes of the beam, the red arrows indicate the orientation of cross-sections in pure bending (edge view). The black dotted lines indicate the orientation of the actual cross-sections (edge view). (c) The magnified area in the vicinity of the cut tip. Black lines show the configurations of the cross-sections in edge view. The thick purple line indicates the cross-section at the cut tip. (d) Main deformation types, i.e., bending (characterised by normal orientation α), shear (characterised by shear angle γ) and sliding (due to misfit Δ).

of modes $\mathbb{A}$ and $\mathbb{C}$ as opposed to mode $\mathbb{B}$ in Fig. 4.1. We note a considerable shear deformation reflected within the angle of cross-section orientation φ being tilted by shear angle γ in modes $\mathbb{A}$ and $\mathbb{C}$ as seen from the zoomed view of the respective modes. On the contrary, mode $\mathbb{B}$ does not exhibit much shear deformation but demonstrates some level of stretch s in the cut tip induced by the opposite deflections of the two halves.

The difference in the lowest critical buckling force for the mode types $\mathbb{A}$ and $\mathbb{C}$ can be interpreted in terms of strain energy arising mainly from bending but also shear deformation. For thin structures, the primary contribution comes from flexure or bending, but for thicker sections, shear starts to contribute significantly and needs correcting for. Similarly, the strain energy contribution for mode types $\mathbb{A}$, $\mathbb{C}$ and $\mathbb{B}$ arise from bending, shear and stretch–the last is due to a kinematic misfit which will be discussed later. This is apparent from the diagram showing cross-sectional deformation characteristics, i.e., curvatures and shear angles on the deformed configurations extracted from *ABAQUS* as shown in Fig. 4.2. We identify the neutral axis and its deformed configuration in each mode type as indicated by the two thick red lines in Fig. 4.2. Note, that the single neutral line exists for the unsplit part (the two red lines coincide). However, each half of the split possesses its own neutral line (the two red lines are distinct in the split

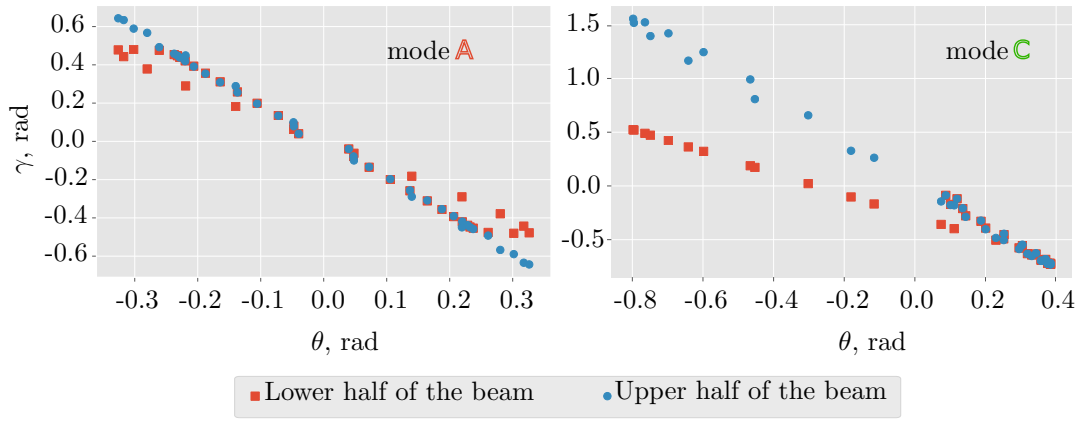

FIGURE 4.3: Graphs of shear angle γ versus tangent slope θ in radians for a cooperative mode $\mathbb{A}$ (*left*) and antisymmetric mode $\mathbb{C}$ (*right*). The red (blue) dots correspond to the lower (upper) half of the split beam.

region). Having identified the neutral line, it is easy to plot the normals (red arrows) that show cross-sections in their edge view, by calculating gradients to the curve at given points. The angle between the vertical axis and the normal vector is the local slope of the deformed shape $\theta = \mathrm{d}w/\mathrm{d}x$ which characterises pure bending deformation in terms of curvature $\theta' = \mathrm{d}^2w/\mathrm{d}x^2$. Comparing θ with the actual slope of the cross-sections φ, we see they are different by an angle γ that reflects shear deformation. Furthermore, we see a sliding deformation in mode $\mathbb{A}$ due to misfit $\Delta(x)$ indicated in Fig. 4.2 (d).

As we move from cross-section to cross-section along the lower and the upper red curves in Fig. 4.2 (a), (b) and record the values of the slope of the buckling mode θ and the shear angle γ, we observe a clear linear dependence between the two as seen in Fig. 4.3 (*left*) for mode $\mathbb{A}$ and Fig. 4.3 (*right*) for mode $\mathbb{C}$. This numerical observation assists us later in choosing simple deflection ansatz, that could accommodate shear correction in our analysis in a simple way. The red (blue) dots represent the $\gamma(\theta)$ dependence for the lower (upper) branch of the bilayer beam. In the case of cooperative buckling, the $\gamma(\theta)$ dependencies for both halves coincide for θ close to zero (corresponds to the unsplit ends and the middle part where red arrows in Fig. 4.2 (a) are vertical). These dependencies are further apart for $-0.1 \leq \theta \leq -0.3$ and $0.1 \leq \theta \leq 0.3$ which corresponds with the cross-sections in the vicinity of the cut tips. In the case of antisymmetric buckling mode $\mathbb{C}$, both $\gamma(\theta)$ dependencies merge near $\theta = 0.4$, which is associated with the unsplit parts of the bilayer beam. The two linear trends for the lower half and the upper half separate at values of θ at the left end of the graph, which is associated with the split part. Note that this figure has the x-axis θ, the local slope at different cross-sections and it does not map with the left-to-right of the split rod.

The difference between the blue dots and the red dots in each subfigure in Fig. 4.3 is a reflection of the relative sliding between the two halves of the bilayer beam. In the case of mode $\mathbb{A}$, the sliding is smaller than in the case of mode $\mathbb{C}$. However, sliding in the cooperative mode leads to the misfit that needs to be taken up by the elastic deformation of the uncut ends of the beam. On the contrary, sliding of the two halves in antisymmetric buckling does not trigger axial deformation since the net length of the two halves remains the same. This is explained by the antisymmetric mode $\mathbb{C}$ having a point of inflexion. Thus, the upper (lower) half stretches (shrinks) along the arch before the inflexion point. This is then mirrored after the inflexion point

and the net sliding appears to be zero. Therefore, axial deformation due to misfit and bending deformation are significant mechanisms in mode $\mathbb{A}$. But axial deformation due to misfit is not present in mode $\mathbb{C}$.

4.2 Simple global assumed modes approximations to estimate critical buckling loads

Bending and shear, axial deformation due to misfit of the material in the cut tips are the key deformation mechanisms that drive the variability in buckling of the bilayer beam depending on the length of the cut $\bar{l}$ and the beam thickness $\bar{h}$. Motivated by the insight obtained from numerical studies, we incorporate the mentioned mechanisms into a number of models based on the appropriate assumed mode shapes which are then used in the total potential energy minimisation procedure to derive functional dependencies of the buckling loads on the geometric parameters.

In contrast to the studies on delaminated composites, here we explicitly specify three assumed modes imposing that each one of them corresponds to one of the three distinct mode types ($\mathbb{A}$, $\mathbb{B}$ and $\mathbb{C}$). Thus, we study the interplay between deformation mechanisms and its effect on the buckling loads associated with the respective buckling states as parameters change.

4.2.1 Kinematics of two split halves joined together at the ends

We extend the model by incorporating the axial deformation due to restricted sliding between the upper and the lower branches of the beam. When the cooperative mode is assumed by the structure, the cross-sections of the upper and the lower branch shift axially with respect to each other by certain amount Δ as seen from Fig. 4.2 (c). This effect can be visually explained

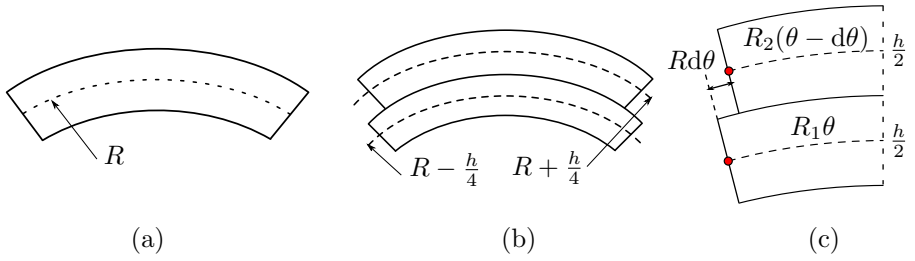

FIGURE 4.4: Bending of uniform beam comparing to bending of two beams stacked on top of each other and allowed to freely slide. (a) Bending of a uniform beam of thickness h following a single arch R. (b) Bending of two beams of thickness $h/2$ stacked on top of each other. (c) Characterisation of the misfit between the two beams.

by comparing the bending of the uniform beam of thickness h depicted in Fig. 4.4 (a) with bending of two branches $h/2$ stacked on top of each other and allowed to slide freely as depicted in Fig. 4.4 (b). The neutral axis of the uniform beam assumes an arch of radius R after the deformation. Naturally, the material above (below) the neutral axis extends (compresses) to take up the difference in arch length between $R-h/2$ and $R+h/2$. In contrast to this, the misfit between the two branches remains as shown in Fig. 4.4 (b). Bending stiffness of the uniform

beam is EI while bending stiffness of the beam composed of the two freely sliding branches is $EI/8$. Thus, a partially split beam should be softer than the uniform one but stiffer than the two freely sliding brunches. The two halves, in this case, are restrained from sliding by the coupling material at two ends.

Consider two branches of differential length $\mathrm{d}x$ stacked on top of each other as depicted in Fig. 4.4 (c). The lengths of the neutral line of the lower and the upper branch are $R_1\theta$ and $R_2\left(\theta - \mathrm{d}\theta\right)$ respectively, where $R_{1,2} = R \mp h/4$. Then, the misfit along the central arch of radius R is $\Delta = R\mathrm{d}\theta$. But, since the branches are of the same length $\mathrm{d}x$, we can write

$$\left(R - \frac{h}{4}\right)\theta = \left(R + \frac{h}{4}\right)\left(\theta - \mathrm{d}\theta\right), \tag{4.1}$$

which simplifies to

$$R\mathrm{d}\theta = \frac{h}{2}\theta - \frac{h}{4}\mathrm{d}\theta, \tag{4.2}$$

where the left side is misfit Δ and the right side simplifies to $\approx h\theta/2$ since $\mathrm{d}\theta \ll \theta$. Accounting for the arch length $\mathrm{d}x$, we can write $\theta = \mathrm{d}x/R = w''\mathrm{d}x$ and the misfit per unit length is

$$\Delta = \frac{h}{2}w''dx. \tag{4.3}$$

The strain energy due to the axial deformation to take up the misfit of the two branches is

$$U_{\text{misfit}} = 2\left(\frac{1}{2}EA\varepsilon^2\right), \tag{4.4}$$

where A is the cross-section area of each branch and ε is the axial strain due to misfit

$$\varepsilon = \frac{2\Delta}{l} = \frac{1}{2\bar{l}}\int_{1-\bar{l}}^{1} hw''\mathrm{d}\xi. \tag{4.5}$$

Substituting ε into Equation (4.4), we derive the expression of the strain energy due to the misfit of two branches in bending

$$U_{\text{misfit}} = \frac{EA}{4\bar{l}^2}\left(\int_{1-\bar{l}}^{1} hw''\mathrm{d}\xi\right)^2. \tag{4.6}$$

This energy appears as a quadratic form of generalised coordinate q and will be used in conjunction with the standard strain energy due to bending when modelling the cooperative mode.

4.2.2 One degree of freedom model using assumed global mode shapes

Solving a 2D elasticity problem of the split beam buckling analytically is challenging. Instead, in our analysis, we incorporate the insights from the 2D numerical modelling into a reduced 1D Bernoulli-Euler beam model. The schematic diagrams of the three characteristic mode types in the one-dimensional model are depicted in Fig. 4.5 (*left*). Noticing the symmetry/antisymmetry of the mode shapes, we reduce the modelling domain to a half-length of the beam $L/2$ as depicted in Fig. 4.5 (*centre*). A closer look at the mode shapes indicates that they may be represented using cubic Hermite polynomials which are plotted in Fig. 4.5 (*right*). These polynomials readily satisfy the kinematic boundary conditions of a beam-column and are easy to integrate, which makes them a good ansatz for the problem. The functional forms of the four Hermite cubics in

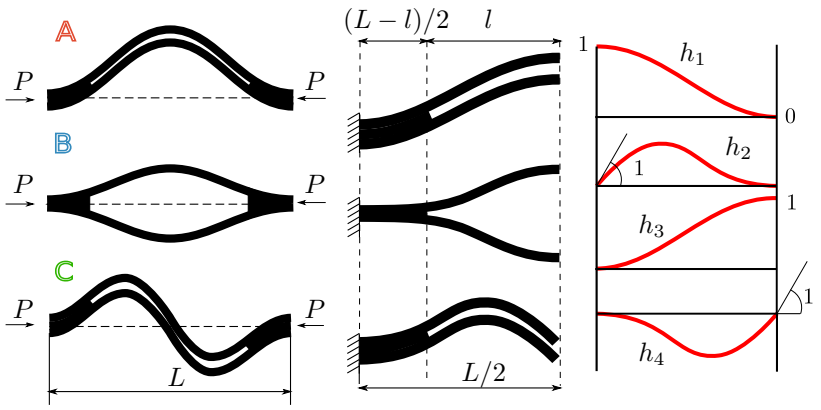

FIGURE 4.5: Schematic diagrams of the cooperative (𝔸), splitting (𝔹) and antisymmetric (ℂ) modes (*left*). Only halves of the modes are to be modelled due to symmetry/antisymmetry (*centre*). Cubic Hermit splines used as assumed buckling shapes (*right*).

terms of the non-dimensional axial coordinate $\xi = 2x/L$ read

$$h_1(\xi) = 2\xi^3 - 3\xi^2 + 1, \tag{4.7}$$
$$h_2(\xi) = \xi^3 - 2\xi^2 + \xi, \tag{4.8}$$
$$h_3(\xi) = 3\xi^2 - 2\xi^3, \tag{4.9}$$
$$h_4(\xi) = \xi^3 - \xi^2. \tag{4.10}$$

Notice, that Hermite cubics are often used in FEA as local basis functions of each finite element. The total potential energy is a function of a vector $\mathbf{q}$ comprised of the general coordinates coming from each element. Minimisation of the total potential energy leads to a generalised EVP (in buckling and vibration) $\mathbf{Kq} = P\mathbf{K}_g\mathbf{q}$, which is solved for P and $\mathbf{q}$. Then, each identified value of q_i characterises the displacements of each element. Together, they specify the buckled shape of the structure. In contrast to this, here we use Hermite cubics as global functions specifying the entire shape. This allows. This allows the size of the problem to be limited to one or two generalised coordinates and to handle all the functional dependencies analytically as opposed to numerically in FEA. Therefore, we retain the physics of the problem.

The assumed modes should satisfy the kinematic boundary conditions which are apparent from Fig. 4.5 (*centre*).

- Mode type 𝔸:

$$w(0) = w'(0) = w'(1) = 0, \tag{4.11}$$

- Mode type 𝔹:

  1. For the unsplit part $0 \leq x \leq (L-l)/2$:

$$w = 0, \tag{4.12}$$

2. The split part $(L-l)/2 \leq x \leq L/2$, $\zeta = 2x/l$ has two branches $w_1(\zeta)$ and $w_2(\zeta)$:

$$w_1(0) = w_1'(0) = w_1'(1) = 0, \tag{4.13}$$
$$w_2(0) = w_2'(0) = w_2'(1) = 0, \tag{4.14}$$

- Mode type $\mathbb{C}$:

$$w(0) = w'(0) = w(1) = 0, \tag{4.15}$$

where w as a function of ξ is the lateral deflection of the beam (modes $\mathbb{A}$ and $\mathbb{C}$). In case of mode $\mathbb{B}$, the two branches are characterised by w_1 and w_2 which are functions of $\zeta = 2x/l$ as only the split part deforms laterally.

The Hermite cubics resemble the shapes of the modes very well (compare Fig. 4.5 (*centre*) and Fig. 4.5 (*right*)) and natively satisfy kinematic boundary conditions, hence the assumed mode shapes for each type of buckling are written in terms of h_3 and h_4 and read

- Mode type $\mathbb{A}$:

$$w_{\mathrm{A}} = q\left(3\xi^2 - 2\xi^3\right), \tag{4.16}$$

- Mode type $\mathbb{B}$:

$$w_{\mathrm{B1}} = q\left(3\zeta^2 - 2\zeta^3\right), \tag{4.17}$$
$$w_{\mathrm{B2}} = -q\left(3\zeta^2 - 2\zeta^3\right), \tag{4.18}$$

- Mode type $\mathbb{C}$:

$$w_{\mathrm{C}} = q\left(\xi^3 - \xi^2\right), \tag{4.19}$$

where q is the generalised coordinate of each mode shape reflecting buckling amplitude.

We use the ansatz given by Equations (4.16)–(4.19) to calculate the elastic strain energy U of the bilayer beam for each mode type. It is the sum of the strain energy of the unsplit part and the strain energy of two brunches corresponding to the split part

$$U = \frac{1}{2}EI\int_0^{1-\bar{l}}(w'')^2\mathrm{d}\xi + \frac{1}{8}EI\int_{1-\bar{l}}^{1}(w'')^2\mathrm{d}\xi. \tag{4.20}$$

Here, EI is the beam bending stiffness. Notice that the stiffness of the unsplit part ($0 \leq \xi \leq 1-\bar{l}$) is $EI = Ebh^3/12$, where b is the beam width and h is the thickness of the unsplit part. The split part ($1-\bar{l} \leq \xi \leq 1$) consists of two branches, each of which has thickness $h/2$ since the cut is assumed infinitesimally thin. Therefore, $Eb(h/2)^3/12 = EI/8$, and since we have two branches, the factors in front of the second integral cancel out leaving $EI/8$ only.

Then, we also substitute Equations (4.16)–(4.19) into an expression of the negative of the work done by the external force

$$V = -\frac{1}{2}P\int_0^1 (w')^2\mathrm{d}\xi, \tag{4.21}$$

where P is the compressive loading as shown in Fig. 4.5 (*left*).

The critical buckling load is such a value of P for which the instability occurs, an energy criterion for which is

$$\delta\Pi = \delta\left(U + V\right) = 0, \tag{4.22}$$

where Π is the total potential energy and U and V are the strain energy and the potential energy of external loading given by Equation (4.20) and Equation (4.21). At this point, we assume only bending strain energy and neglect any other deformation mechanisms to see how the Bernoulli-Euler beam model compares with the full 2D elasticity problem solution obtained with FEA. Taking variation $\delta\Pi$ with respect to the generalised coordinate q results in

$$\frac{\partial\Pi}{\partial q} = 0, \tag{4.23}$$

which yields a linear equation in q for mode types $\mathbb{A}$ and $\mathbb{C}$, easily solvable for P taking q to be an arbitrary non-zero constant.

- Mode type $\mathbb{A}$:

$$qEI\left(4 - 9\bar{l} + 18\bar{l}^2 - 12\bar{l}^3\right) - \frac{2}{5}Pq = 0, \tag{4.24}$$

  which leads to

$$\bar{P}_{\mathrm{A}} = \frac{P}{P_{cr}} = \frac{10}{\pi^2} - \frac{15\bar{l}}{2\pi^2}\left(4\bar{l}^2 - 6\bar{l} + 3\right), \tag{4.25}$$

  or

$$\bar{P}_{\mathrm{A}} \approx 1 - 3\bar{l}\left(\bar{l}^2 - \frac{3}{2}\bar{l} + \frac{3}{4}\right). \tag{4.26}$$

- Mode type $\mathbb{C}$:

$$qEI\left(4 - 12\bar{l} + 18\bar{l}^2 - 9\bar{l}^3\right) - \frac{2}{15}Pq = 0, \tag{4.27}$$

  which leads to

$$\bar{P}_{\mathrm{C}} = \frac{P}{P_{cr}} = \frac{30}{\pi^2} - \frac{15}{2\pi^2}\left(9\bar{l}^3 - 18\bar{l}^2 + 12\bar{l}\right), \tag{4.28}$$

  or

$$\bar{P}_{\mathrm{C}} \approx 3 - 9\bar{l}\left(\frac{3}{4}\bar{l}^2 - \frac{3}{2}\bar{l} + 1\right). \tag{4.29}$$

Here, $\bar{P}_{\mathrm{A}}$ and $\bar{P}_{\mathrm{C}}$ denote critical buckling loads scaled by the buckling load of the clamped uniform beam $P_{cr} = 4\pi^2 EI/L^2$, where for dimensionless length, $P_{cr} = \pi^2 EI$.

The critical load of the splitting mode $\mathbb{B}$ can be obtained simply from the Euler buckling formula noticing that each half of the split beam deforms as a clamped-clamped beam of length $l = \bar{l}L$. Hence,

$$P_{\mathrm{B}} = 2\frac{4\pi^2(EI/8)}{\left(\bar{l}L\right)^2} = \frac{\pi^2 EI}{\left(\bar{l}L\right)^2}, \tag{4.30}$$

or in dimensionless form

$$\bar{P}_{\mathrm{B}} = \frac{\pi^2 EI}{\left(\bar{l}L\right)^2} \Big/ \frac{4\pi^2 EI}{L^2} = \frac{1}{4\bar{l}^2}. \tag{4.31}$$

The plots of $\bar{P}_{\mathrm{A}}$, $\bar{P}_{\mathrm{B}}$ and $\bar{P}_{\mathrm{C}}$ as functions of $\bar{l}$ are depicted as solid lines in Fig. 4.6. The analytical curves are also being compared with the numerical trajectories obtained from FEA and plotted with dots on the same graph. Even the crude cubic polynomial approximation of the mode shapes already reflects some qualitative features of the numerical trajectories, despite that only

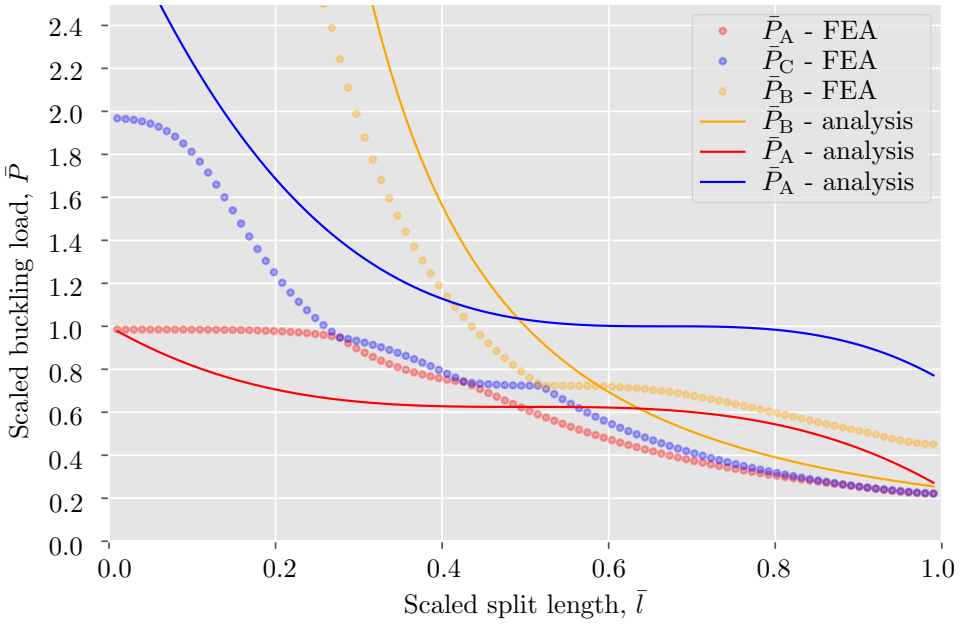

FIGURE 4.6: Analytically derived trajectories of the lowest three buckling loads as functions of the scaled split length $\bar{l}$ (*solid lines*). The numerically computed trajectories (*dotted lines*) are presented for comparison.

the pure bending deformation is accounted for. From the plot, we observe that $\bar{P}_B = 1/(4\bar{l}^2)$ captures the trend of splitting buckling load surprisingly well (compare orange solid line with the orange dotted line). On the other hand, the trajectory corresponding to the antisymmetric buckling appears much stiffer than the numeric one (blue solid line is above the blue dotted line). However, the qualitative trend is roughly similar for the moderate split but deviates far for small split lengths. Particularly, for $\bar{l} = 0$, analytical prediction $\bar{P}_C \approx 3$ compared to the numerical value ≈ 2. The trajectory of the buckling load for cooperative buckling has been captured poorly (compare red solid line with the red dotted line). The prediction is much softer for short splits and much stiffer for long ones. However, at the limit cases of $\bar{l} = 0$ and $\bar{l} = 1$, the prediction precisely matches the numerics as $\bar{P}_A(0) \approx 1$ and $\bar{P}_A(1) \approx 1/4$ respectively. Notice also, that at $\bar{l} = 1$, $\bar{P}_A \approx \bar{P}_B$ which is the same as obtained numerically. The differences between the predicted and the computed trajectories within the range of $\bar{l}$ are likely due to lack of flexibility in the assumed modes, i.e., additional degrees of freedom should be introduced. It is also clear that other deformation mechanisms have to be considered in addition to pure bending to adequately model the behaviour for a wide range of split lengths.

The strain energy of mode $\mathbb{A}$ is thus composed of the bending energies of the unsplit and split parts and half the energy due to misfit (only half of the beam is considered)

$$U_A = \frac{1}{2}EI\int_0^{1-\bar{l}}(w'')^2\mathrm{d}\xi + \frac{1}{8}EI\int_{1-\bar{l}}^{1}(w'')^2\mathrm{d}\xi + \frac{EA}{8\bar{l}^2}\left(\int_{1-\bar{l}}^{1} hw''\mathrm{d}\xi\right)^2, \tag{4.32}$$

and the potential energy of external loading remains the same. Here we also employ the relation $EA = 6EI/h^2$ and the terms EA and h^2 in the last integral are written in terms of EI. Minimising the total potential energy Π, we derive the scaled critical buckling load $\bar{P}_A$ as a function

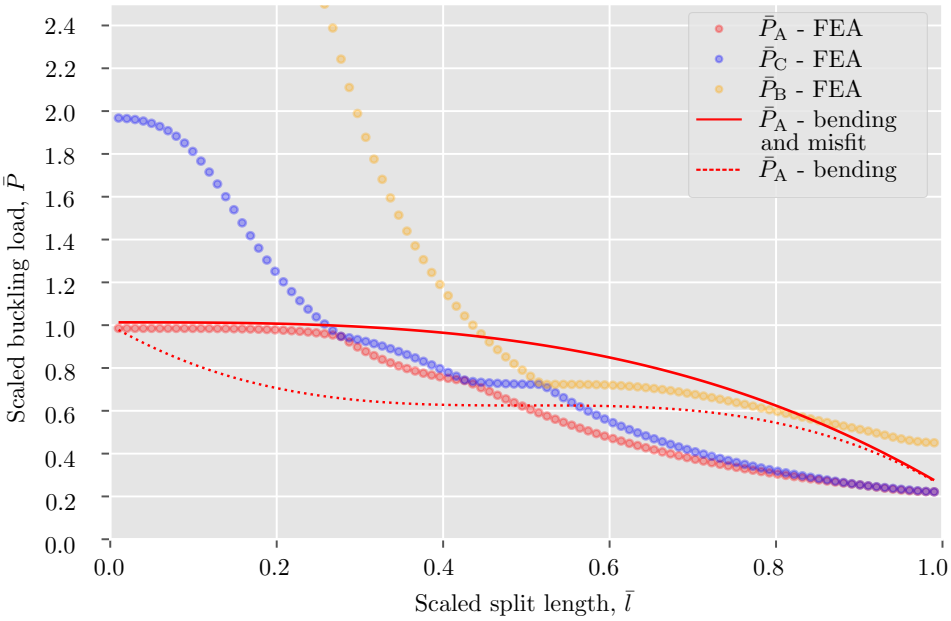

FIGURE 4.7: Analytically derived trajectory of $\bar{P}_A$ accounting for the axial deformation due to misfit (*red solid line*) compared with $\bar{P}_A$ accounting only for bending (*red dashed line*). The two analytical curves are superimposed on the numerically computed trajectories (*dotted lines*).

of $\bar{l}$

$$\bar{P}_A = \frac{20}{2\pi^2} - \frac{15\bar{l}^3}{2\pi^2}, \tag{4.33}$$

or

$$\bar{P}_A \approx 1 - \frac{3}{4}\bar{l}^3. \tag{4.34}$$

Here we compare the critical buckling load trajectories as functions of $\bar{l}$ for the mode $\mathbb{A}$ using the pure bending assumption (red dotted line in Fig. 4.7) with the one for bending and axial deformation due to misfit (red solid line in Fig. 4.7). We superimpose the two curves on the plot of the numerical buckling load trajectories. Visual comparison of the trajectories shows a dramatic improvement of the analytical prediction for $\bar{l} < 0.3$, where the analytical and the numerical curves practically coincide suggesting that bending and axial deformation due to misfit are indeed the main mechanisms governing the cooperative behaviour in this region. However, the extended model gives a rather conservative prediction for the rest of the parameter range. This is likely attributed to an insufficient number of the degrees of freedom in the assumed polynomial shape as the method converges from above. Therefore, next, we will derive the analytical model using polynomials with two degrees of freedom per mode and incorporating shear effects which are expected to play an increasing role as the split beam thickness $\bar{h}$ increases.

4.2.3 Higher order model with corrections due to misfit and shear

The previous ansatz is extended here by considering higher-order polynomials with two generalised coordinates (two degrees of freedom) each. This allows the mode shapes to be adapted for the local effects arising as $\bar{l}$ changes. In addition, we will also account for the beam thickness

related effects by complementing the strain energy expressions with the shear terms according to Timoshenko theory [Timoshenko and Gere, 2012].

It is apparent that shear manifests differently in different mode types. The splitting mode is least affected by it and the analytical prediction for the critical buckling load, in this case, is already satisfactory (recall Fig. 4.6). We will now discuss how shear affects the cooperative and antisymmetric modes.

Buckling load of a beam-column with shear correction is [Timoshenko and Gere, 2012]

$$P_{cr} = \frac{P_{\mathrm{BE}}}{1 + \kappa P_{\mathrm{BE}}/AG}, \tag{4.35}$$

where the buckling load of a Bernoulli-Euler beam-column is P_{BE}, κ= 1.2 is the dimensionless coefficient of beam cross-section, A is the cross-section area and G is the shear modulus of the material. Thus, the Bernoulli-Euler buckling load P_{BE} is reduced due to shear by a factor of $1 + \kappa P_E/AG$. Considering the expression for P_{BE} in terms of buckling mode wavelength λ as $P_{\mathrm{BE}} = \lambda^2 EI/L^2$, we rewrite the shear correction factor

$$1 + \kappa \frac{P_{\mathrm{BE}}}{AG} = 1 + \kappa \lambda^2 \frac{EI}{L^2 GA}. \tag{4.36}$$

Substituting the expressions for EI and GA, we obtain an expression for shear correction

$$Q = 1 + \kappa \frac{\lambda^2}{12} \frac{E}{G} \left(\frac{h}{L}\right)^2, \tag{4.37}$$

which depends on the wavelength λ and the fundamental material ratio E/G and beam ratio h/L. Isotropic materials are usually characterised by $E/G \approx 2$, while the thin beam assumption holds for thickness to length ratio up to $h/L = 0.1$. The wavelength factors for cooperative mode and antisymmetric mode are $\lambda_1^2/12 \approx 3.3$ and $\lambda_2^2/12 \approx 7.5$ respectively [Timoshenko and Gere, 2012]. Hence, in case of uniform beams, the shear corrections for the two modes for $0.01 \leq h/L \leq 0.5$ (the range considered in the phase diagram in Fig. 3.10) are $1.008 \leq Q_{\mathrm{A}} \leq 1.2$ and $1.018 \leq Q_{\mathrm{C}} \leq 1.45$. Therefore, we conclude that shear correction has a much more dramatic effect on the antisymmetric mode due to a shorter wavelength. Thus, we will ignore the shear contribution to the cooperative mode of the bilayer beam for most of this study, except for the very thick beams. In contrast, the shear effect will be modelled in the antisymmetric mode of the bilayer beam for the entire $\bar{h}$–$\bar{l}$ space.

Also, consider that the shear effect should diminish with the split length $\bar{l}$ in the split beam. It should reach its minimum for $\bar{l} = 1$ as each branch takes half of the original beam thickness and $(h/L)^2$ ratio becomes $1/4\,(h/L)^2$ for the fully split beam. Thus, the second component in Equation (4.37) will be a quarter of the one for the uniform beam. Hence, the calculated bounds for the shear effect in the uniform beam are the largest. Also, we expect the shear correction to not change the solution qualitatively but to simply reduce the magnitude of buckling loads proportionally. A comparison between the buckling load trajectories calculated with and without shear correction for the case of the thin beam will be presented later in this subsection.

Now we proceed to constructing the assumed mode shapes with two generalised coordinates to allow for better tuning of the shape as parameters change. Same as before, we seek a polynomial

that satisfies the kinematic boundary conditions of the bilayer beam listed in Equation (4.11) for the cooperative mode and Equation (4.15) for the antisymmetric mode. Recall that we are not extending the ansatz for the splitting mode as it already performs reasonably well.

The new shape function for mode $\mathbb{A}$ should have an original part given by Hermite cubic h_3 (as seen from Fig. 4.5) and an extra term that introduces the second degree of freedom. We start with a generic form of the fourth-order polynomial

$$w(t) = a_0 + a_1\xi + a_2\xi^2 + a_3\xi^3 + a_4\xi^4, \tag{4.38}$$

where $\xi = 2x/L$. We require satisfaction of the kinematic boundary conditions

$$w(0) = 0 \quad \Rightarrow \quad a_0 = 0 \tag{4.39}$$

$$w'(0) = 0 \quad \Rightarrow \quad a_1 = 0 \tag{4.40}$$

$$w'(1) = 0 \quad \Rightarrow \quad 2a_2\xi + 3a_3\xi^2 + 4a_4\xi^3 = 0. \tag{4.41}$$

Equation (4.41) holds for arbitrary ξ if

$$2a_2 + 3a_3 + 4a_4 = 0 \Rightarrow a_4 = -\frac{1}{2}a_2 - \frac{3}{4}a_3. \tag{4.42}$$

Plugging a_0, a_1 and a_4 into Equation (4.38) and renaming constants, we derive the fourth-order polynomial for the cooperative mode

$$w_{\mathrm{A}} = q_1\left(\xi^2 - \frac{1}{2}\xi^4\right) + q_2\left(\xi^3 - \frac{3}{4}\xi^4\right). \tag{4.43}$$

We use a shortcut for mode type $\mathbb{C}$. We construct the new polynomial as h_4 given by Equation (4.10) plus one extra degree of freedom multiplied by ξ

$$w_{\mathrm{C}} = \xi^2(\xi - 1)(q_1 + q_2\xi), \tag{4.44}$$

or

$$w_{\mathrm{C}} = q_1\left(\xi^3 - \xi^2\right) + q_2\left(\xi^4 - \xi^3\right), \tag{4.45}$$

which readily satisfies geometric boundary conditions

$$w(0) = w'(0) = w(1) = 0. \tag{4.46}$$

We can visually compare the mode shapes of type $\mathbb{A}$ and $\mathbb{C}$ reflected by the Hermite cubics (orange lines) and by the derived 4^{th} order polynomials (blue lines) as shown in Fig. 4.8. Notice, that while the higher-order shape functions have shapes similar to cubics, they allow for better tuning of the mode to high curvatures that appear locally.

Having derived new shape functions, we should substitute them into energy expressions for both cooperative and antisymmetric mode. The strain energy for the cooperative mode remains unchanged and is a sum of bending energy of the unsplit part, bending energy of the split part and strain energy due to misfit given by Equation (4.32). The strain energy for the antisymmetric

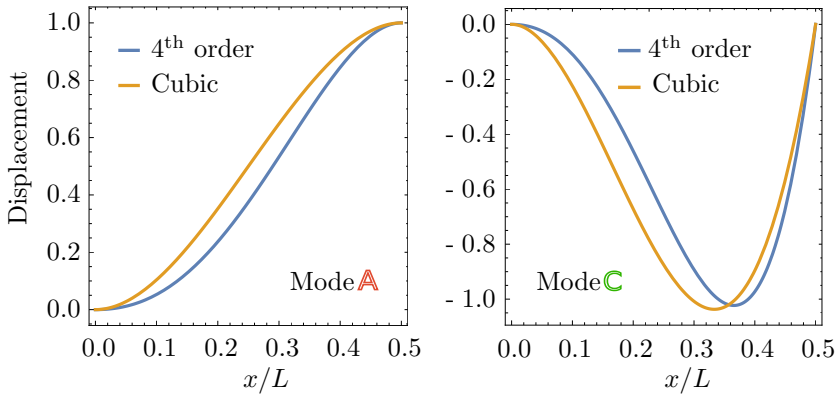

FIGURE 4.8: Comparison of the shape functions for the mode type 𝔸 and ℂ. The orange line corresponds to Hermite cubics and the blue line corresponds to the 4^{th} order polynomials.

mode is different due to the shear effect [Ang and Wang, 1990] and reads

$$U = \frac{1}{2}EI \int_0^{1-\bar{l}} \left[(w'' - \gamma')^2 + \frac{1}{2}\kappa GA\gamma^2 \right] \mathrm{d}\xi + \frac{1}{8}EI \int_{1-\bar{l}}^{1} \left[(w'' - \gamma')^2 + \kappa GA\gamma^2 \right] \mathrm{d}\xi. \tag{4.47}$$

Here the first term is the bending and shear strain energy of unsplit part, the second term is the strain energy due to bending and shear of a single branch times two, γ is the shear strain. Timoshenko beam theory has two independent field variables w and γ. Therefore, to use Equation (4.47), we need to assume the shear strain. From the analysis of the deformation mechanisms and, particularly, from the plot of the numerically obtained dependence between θ and γ for a moderately thick bilayer beam (recall Fig. 4.3), we assume linear dependance $\gamma = qw'$ and write an assumed function for shear deformation

$$\gamma_{\mathrm{C}} = q_3(3\xi^2 - 2\xi) + q_4(4\xi^2 - 3\xi), \tag{4.48}$$

where q_3 and q_4 are two additional generalised coordinates.

Therefore, the strain energy of mode 𝔸 is the quadratic form in q_1 and q_2 derived from Equation (4.32) by substituting w_{A} given by Equation (4.43). The strain energy of mode ℂ is the quadratic form in $q_1, \ldots, q_4$ derived from Equation (4.47) by substituting w_{C} given by Equation (4.45) and γ_{C} given by Equation (4.48). Similarly, we substitute the assumed mode shapes w_{A} and w_{C} into the expression for the potential energy of external loading which remains unchanged and is given by Equation (4.21). Thus, the total potential energy of the mode 𝔸 is the quadratic form in q_1, q_2. However, the total potential energy of the mode ℂ is the quadratic form in $q_1, \ldots, q_4$. To calculate the buckling loads $\bar{P}_{\mathrm{A}}$ and $\bar{P}_{\mathrm{C}}$, we solve the 2×2 and 4×4 eigenvalue problems $\mathbf{Kq} = P\mathbf{K}_g\mathbf{q}$ respectively. The expressions for the strain energies, potentials of external loading and the respective matrices $\mathbf{K}$ and $\mathbf{K}_g$ are given in Appendix A. Notice that, we retain only the lowest eigenvalue of each EVP since it is the best approximation of the actual solution. The calculated expressions for $\bar{P}_{\mathrm{A}}$ and $\bar{P}_{\mathrm{C}}$ are high order polynomials in $\bar{l}$. The expression for $\bar{P}_{\mathrm{A}}$ is 5^{th} order polynomial in $\bar{l}$ and $\bar{P}_{\mathrm{C}}$ is a ratio of 17^{th} order and 12^{th} polynomials in $\bar{l}$ and 4^{th} order polynomial in $\bar{h}$. The expressions of the buckling loads are also presented in Appendix A.

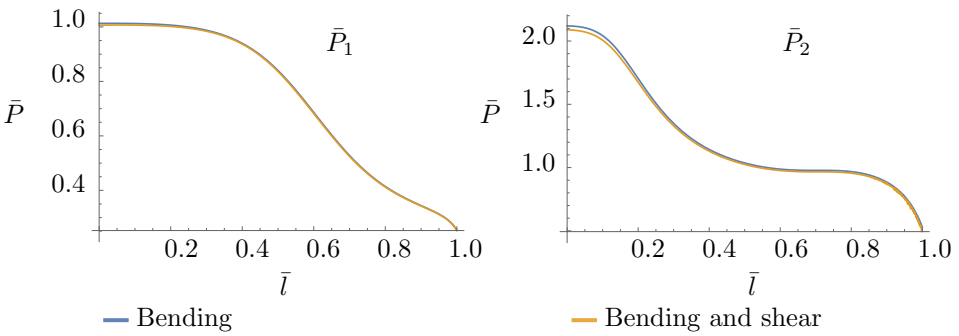

FIGURE 4.9: Comparison between the predicted buckling load trajectories with and without shear correction. The first buckling load trajectories ($\bar{P}_1$) are compared in *left* subfigure while the second buckling load trajectories ($\bar{P}_2$) are compared in *right* subfigure.

Firstly, we study the effect of shear correction given by Equation (4.37) in the case of a thin beam $h/L \ll 1$ to further illustrate the previous discussion. We use the 4^{th} order polynomial shape functions when calculating the strain energy of the beam without shear correction (as given by Equation (4.20) and Equation (4.32)) as well as of the beam with shear correction (as given by Equation (4.47)). The computed scaled critical buckling loads for cooperative and antisymmetric modes with and without shear correction are plotted versus the $\bar{l}$ parameter in Fig. 4.9. Comparing the trajectories, we can see that they indeed differ very little for thin beams. However, it is seen from Fig. 4.9(*right*) that the shear effect is larger for the antisymmetric mode. Also, notice, that the strength of the shear effect will also scale with thickness. Thus, shear correction in the antisymmetric mode is justified.

Compare the buckling load trajectories calculated with the cubic model and with the model based on 4^{th} order polynomials by studying the graph Fig. 4.10. The buckling load trajectory for a splitting mode (*orange solid line*) is unchanged and plotted here for reference, hence we will not discuss it in detail. Firstly, compare the buckling load trajectories for the cooperative mode (*red lines*). We have observed before that the trajectory calculated using the cubic-based model assuming bending and axial deformation due to misfit yields stiffer response for long splits. We report a dramatic improvement in prediction by the extended model (compare *red solid line* with *red dashed line*) in this region. Since the assumed mode has an extra degree of freedom, its shape alters with $\bar{l}$. This leads to a softer response. In the case of the antisymmetric mode, we see a dramatic improvement at the two extremes $\bar{l} \to 0$ and $\bar{l} \to 1$ (*blue solid line* as compared to *blue dashed line*). However, the response does not change for the moderate values of $\bar{l}$. Also, as the trajectories are plotted for a thin beam $h/L = 0.1$, the softening due to shear correction is not considerable, especially for larger $\bar{l}$.

So far we have ignored $\bar{h}$ dependence and studied the bilayer beam under a thin beam approximation. Although we introduced Timoshenko shear correction in the antisymmetric mode, we still considered small h/L ratio. Now we further extend the model, by accounting for shear correction in both cooperative and antisymmetric modes and calculating the dependencies of the buckling modes on both $\bar{l}$ and $\bar{h}$ parameters. Thus, we are able to produce analytical surfaces of critical buckling modes to be compared with FEA. We use the new ansatz given by Equation (4.43) and Equation (4.45) for modes $\mathbb{A}$ and $\mathbb{C}$. We further assume Equation (4.16) to represent the shape of each branch of the splitting mode replacing $\xi = 2x/L$ with $\zeta = 2x/l$. Then, we assume shear deformation to be distributed according to Equation (4.48) in mode $\mathbb{C}$ and according to

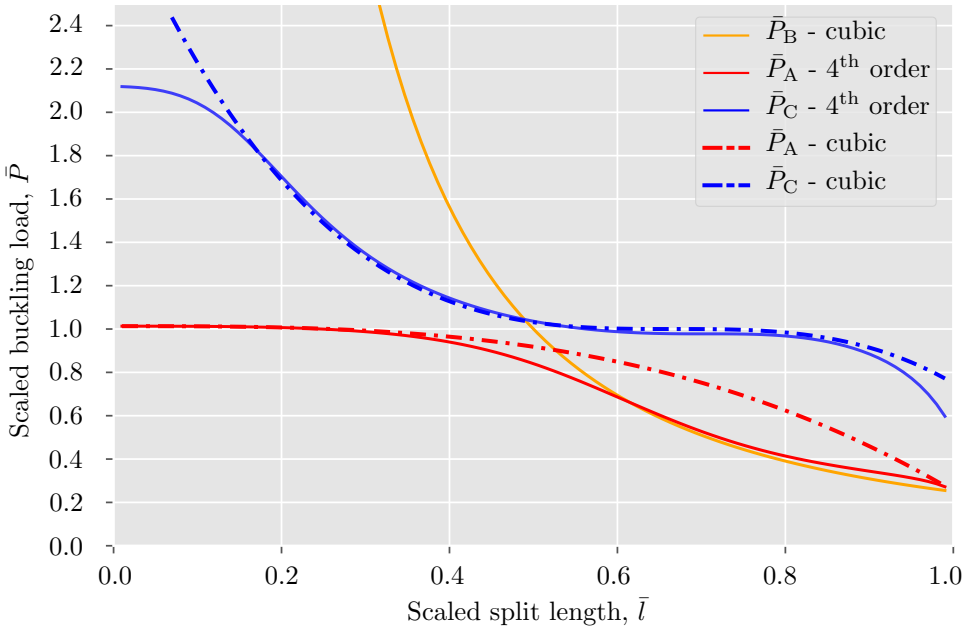

FIGURE 4.10: Comparison of the buckling load trajectories calculated with cubic-based model and with a model based on 4^{th} order polynomials with shear correction for a thin beam ($h/L = 0.1$). (*red dashed line*) The trajectory of $\bar{P}_{\text{A}}$ predicted by a cubic-based model assuming bending and misfit. (*blue dashed line*) The trajectory of $\bar{P}_{\text{C}}$ predicted by a cubic-based model based on pure bending assumption. (*orange solid line*) The trajectory of $\bar{P}_{\text{B}}$ based on pure bending assumption. (*red solid line*) The trajectory of $\bar{P}_{\text{A}}$ derived using 4^{th} order polynomials assuming bending and misfit. (*blue solid line*) The trajectory of $\bar{P}_{\text{C}}$ calculated using 4^{th} order polynomials assuming bending and shear deformation.

$\gamma_{\text{A}} = 2q_3\xi\,(1-\xi)^2 + 3q_4\xi^2\,(1-\xi)$ in modes $\mathbb{A}$ and $\mathbb{B}$. We substitute the expressions for the assumed modes and assumed shear deformation into the strain energy expressions that account for bending and shear as given in Equation (4.47). These are identical for modes $\mathbb{A}$ and $\mathbb{C}$. Mode $\mathbb{B}$ is described only by the second component in Equation (4.47). In addition to that, the strain energy of the cooperative mode also contains a component reflecting energy of the axial deformation due to misfit as given by Equation (4.6).

In Fig. 4.11 we show a detailed comparison between the buckling loads predicted analytically and calculated with FEA. Consider Fig. 4.11 (a) which shows the trajectories of the buckling loads $\bar{P}_{\text{A}}$, $\bar{P}_{\text{B}}$ and $\bar{P}_{\text{C}}$ as functions of $\bar{l}$ calculated analytically under a thin beam assumption $\bar{h}$= 0.1 (*solid lines*). Comparing them with the same trajectories calculated with FEA, we report good qualitative prediction of the analytical model throughout the parameter range. Quantitatively, the analytical prediction is the best at the two extremes ($\bar{l} \to 0$ and $\bar{l} \to 1$) and renders buckling load trajectories above the computed ones for most of $\bar{l}$ values. Particularly, the buckling load of mode $\mathbb{A}$ (*red solid line*) is calculated accurately for $\bar{l} < 0.3$ suggesting that only pure bending and axial deformation due to misfit govern the behaviour for the shorter splits. As we move further along the red trajectory, it deviates slightly from the one computed by FEA (*red dotted line*) indicating a stiffer behaviour in the analytical model. The trajectory for $\bar{P}_{\text{C}}$ (*blue solid line*) also qualitatively compares well with FEA (compare with *blue dotted line* for $\bar{l} < 0.6$ and with *orange dotted line* for $\bar{l} > 0.6$). Quantitatively, the predicted buckling load is higher than the computed one for all $\bar{l}$. An assumed mode with more degrees of freedom is required to converge to the trajectory from FEA in this case. Finally, the predicted trajectory for $\bar{P}_{\text{B}}$ (*orange solid*

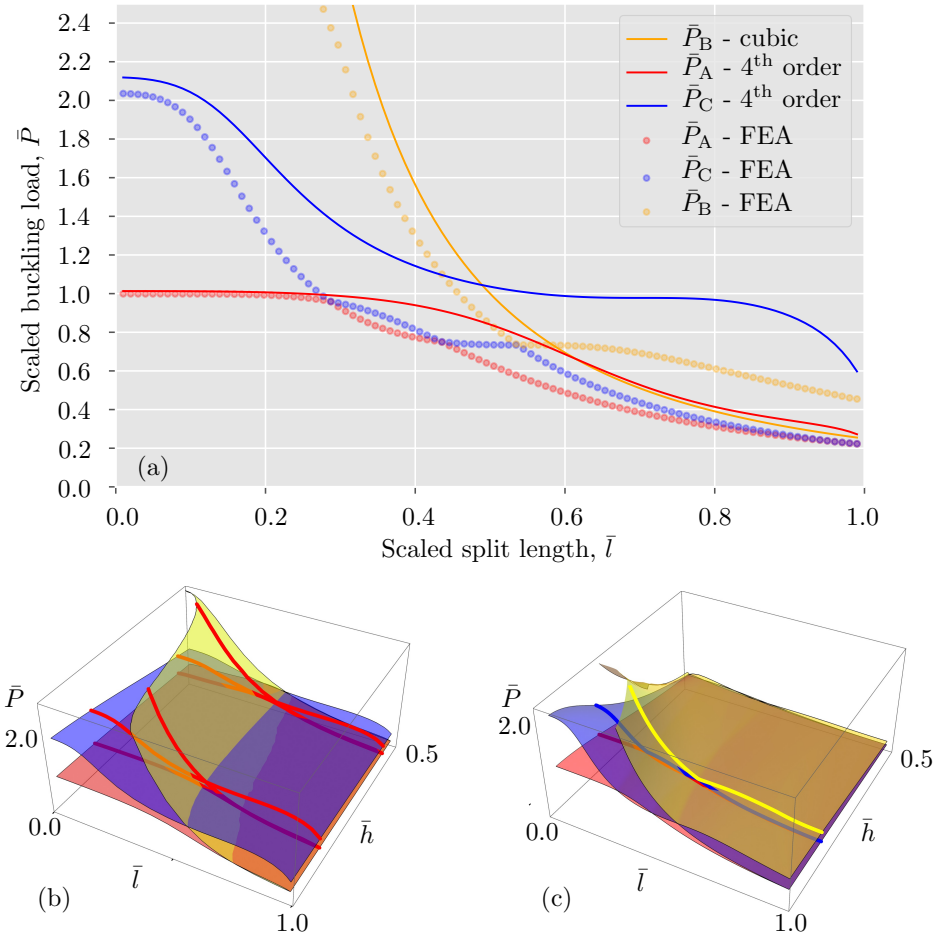

FIGURE 4.11: Comparison between the three buckling loads predicted analytically and computed with FEA. (a) The plot of analytical and computed trajectories of buckling loads as functions of $\bar{l}$ for a thin beam case $\bar{h}$= 0.1. Solid lines are predictions by the model based on 4^{th} order polynomials and the dotted lines are obtained from FEA. (b) Surfaces of the three lowest buckling loads as functions of $\bar{h}$ and $\bar{l}$ calculated analytically using the extended model based on 4^{th} order polynomials with corrections for shear in all mode types. Red, blue and yellow surfaces correspond to $\bar{P}_A$, $\bar{P}_C$ and $\bar{P}_B$ respectively. (c) Surfaces of the three lowest buckling loads, as computed with FEA, plotted versus $\bar{h}$ and $\bar{l}$.

line) is very close to the computations (*orange dotted line*) which suggests that the mechanics of this mode is captured correctly. Notice that we also captured two crossing points between $\bar{P}_A$ and $\bar{P}_B$ and between $\bar{P}_C$ and $\bar{P}_B$. This further gives evidence of how the interplay between different deformation mechanisms in the three modes for various cut lengths leads to the crossing of buckling load trajectories with swapping of the associated mode order.

Our analysis converges from above, which means that if more degrees of freedom (generalised coordinates) are introduced in the global assumed mode, the prediction becomes more accurate. In the limit case of a large number of degrees of freedom, this method should come very close to FEA (neglecting the 2D elasticity effects which even a fine beam model cannot capture). We do not study the assumed modes with more degrees of freedom as the qualitative behaviour is already captured satisfactory and matching the analytical solutions with FEA is beyond our scope. Instead, we discuss the behaviour in general by comparing the surfaces of the three buckling loads as functions of $\bar{l}$ and $\bar{h}$ from our analysis (Fig. 4.11 (b)) and FEA (Fig. 4.11 (c)). Let us compare the two plots visually. The computed surfaces in Fig. 4.11 (c) have more folds

as FEA captures all the small details of the critical buckling load dependencies on parameters. The analytical surfaces are slightly higher and less reflective of the details of the interactions between the buckling states. Also, the computed surfaces rapidly decrease with $\bar{h}$ suggesting some higher-order non-linear shear effects taking place in thick beams which Timoshenko theory does not capture. Apart from this, we report that qualitatively the behaviour is well reflected by the analytical surfaces. The overall shapes of the surfaces in both graphs are very similar.

4.3 Conclusions

In this chapter, we performed a detailed analysis of the deformation mechanisms in bilayer beam. We started with the mapping of the types of deformation and the associated strain energy density within each of the three mode types obtained from FEA. This allowed us to conclude that axial sliding between the two branches of the split beam as well as shear deformation have a considerable effect on the behaviour. Then we analysed the details of how the deformation mechanisms manifest themselves in each of the mode types and how it affects the associated buckling loads and leads to the practical realisation of the cooperative, splitting and antisymmetric buckling depending on the split length and beam thickness. We built several analytical models incorporating assumptions about bending, axial and shear deformation. In contrast to the previous studies, we used all the three mode types to formulate the suitable ansatz to calculate and minimise the total potential energy and thus were able to analytically calculate the buckling load trajectories for each of the mode types and observe how they interact in the parameter space. Therefore, the model allows the effect of different types of deformation within the modes to be studied. The model also allows the location of the respective buckling load trajectories to be mapped.

The performed analysis leads to the following conclusions. The cooperative buckling is mainly governed by bending of the two branches of the bilayer beam, which are stiffened by the uncut parts whose axial deformation due to misfit between the branches considerably contributes to the strain energy. Shear plays a minor role in cooperative buckling and should be taken into account for very thick beams only. Also, the effect of shear reduces with cut length. The splitting mode is mainly governed by pure bending of each branch. Shear and stretch in the cut interface play a minor role. However, they generally need to be considered for $\bar{l} > 0.6$ as the actual intersection of the respective buckling load trajectory with the one for cooperative buckling depends on them. Finally, the antisymmetric mode is strongly affected by shear for most of $\bar{h}$. The axial deformation, in this case, does not play a significant role. The mode order swapping between the cooperative and the splitting mode is due to an interplay between bending and axial deformation in cooperative buckling versus bending and shear deformation in the antisymmetric buckling. This brings the buckling load of the antisymmetric mode below the buckling mode of the cooperative mode for a range of $\bar{l}$ and $\bar{h}$ values.

Chapter 5

Elastic stability of a chain of coupled rigid rods

In Chapter 3 and Chapter 4, we studied the stability of a bilayer elastic structure experimentally, computationally and analytically. The next question of importance is the behaviour of coupled elastic structures composed of multiple layers that are nominally identical. A good starting point is to consider elastically coupled rigid rods, as they possess the important features of the problem in possibly the simplest way. Periodicity of coupled identical structures is the key aspect of this problem.

It so turns out that there are close mathematical and physical analogies between the instability problem of coupled nominally identical structures and the propagation of waves in periodic media. Indeed, wave propagation in periodic media has been a subject of study in contexts that are non-mechanical, for example in optics, electromagnetism, and conductance of waves in a crystalline material. Waves in repetitive elastic structures have also been studied for some time now. One of the motivations of this is to understand the dynamics of structures that naturally possess periodicity, e.g. stiffened plates [Li et al., 2005, Yu et al., 2010] or shells [Lee and Kim, 2002]. Such periodicity is along the direction of propagation of waves. As opposed to this, periodicity could also be cyclic, such as that found in a host of industrial bladed discs such as gas turbines [Bah et al., 2003]. Structural dynamics of such periodic elastic structures possesses close resemblance with the behaviour of wave propagation in other types of media, mentioned earlier. Although wave propagation is not a motivation of the present work, the close analogy identified by us between the problem of buckling of coupled periodic elastic structures and waves in periodic structures prompts us to review previous work in the field of structural dynamics of repetitive structures. In the case of cyclically periodic structures, an appropriate perspective is that of vibrational modes, rather than propagating waves. On the other hand, wave propagation language is appropriate when this is a well-identified propagation direction. Here, we are mainly concerned with cyclic periodicity, but also consider a case of a long nearly periodic chain. Note that translational periodicity strictly requires infinite length in the propagation direction, however, all systems, mechanical or not, have finite extent: hence it is an accepted approximation, even for finite length periodic structures, such as long chains.

We review the literature on wave propagation in periodic media first, followed by vibration of periodic structures and buckling of periodic multi-span beams. Subsequently, we identify that

very little attention has been placed to the understanding of instability of coupled periodic structures generally. Then, we design and conduct a simple experiment to observe how a multilayer structure–layers weakly coupled at the ends–behaves in buckling. To understand the general features of instability behaviour in coupled periodic structures, here we consider a simple chain of elastically coupled rigid rods. Then, we study the effect of disorder on a two coupled rods problem as well as when a random irregularity is introduced in a cyclic and infinite chain of coupled rods. We report the phenomena of weak and strong localisation of buckling amplitude based on the coupling to disorder ratio, which we identify as analogous to the well-known phenomenon of Anderson localisation in solid-state physics.

5.1 Review of literature on waves in periodic structures

Periodic structures are commonly found in a number of contexts in nature and engineering. Regular lattices in crystalline materials, periodic structural assemblies and lattice metamaterials thrive from repetitiveness in their geometry. This is of great importance to a wide range of problems in photonics [Joannopoulos, 2008], acoustics [Gorishnyy et al., 2005], and mechanics [Phani et al., 2006].

The principal description of wave propagation through a periodic lattice is reflected in the Floquet-Bloch theory [Ziman, 1972, Kittel, 2005]. It allows a wave in a crystal to be expressed as a plane wave modulated by a periodic function that characterises the periodic property of the medium [Joannopoulos, 2008]. Suppose the medium in which waves propagate or vibration occurs is one dimensional with periodicity T, such that if we move from a location x to a new location $x + nT$ where $n \in \mathcal{I}$, the environment is translated into itself (does not change). This usually occurs in three dimensions when electron wave propagates through a crystal lattice of atoms. The Bloch waves in a 1-D medium are perhaps simplest to understand. Consider a periodic function $f(x) = f(x + T)$ and take a Fourier transform of it

$$\int \tilde{f}(n)\mathrm{e}^{2\pi inx}\mathrm{d}n = \int \tilde{f}(n)\mathrm{e}^{2\pi inx}\mathrm{e}^{2\pi inT}\mathrm{d}n, \tag{5.1}$$

or in a compact notation

$$\int \tilde{f}(n)\mathrm{e}^{igx}\mathrm{d}n = \int \tilde{f}(n)\mathrm{e}^{igx}\mathrm{e}^{igT}\mathrm{d}n, \tag{5.2}$$

where $i = \sqrt{-1}$. The equality holds when $\mathrm{e}^{igT} = 1$, or $g = 2\pi n/T$ belongs to a set of reciprocal lattice lengths in one dimension. Then, according to Bloch theorem, a wave in a periodic lattice is a plane wave e^{igT} modulated by the periodic function of the lattice $u(x)$ or

$$\psi(x) = \mathrm{e}^{igT}u(x). \tag{5.3}$$

Notice that a travelling wave has a temporal part given by $\mathrm{e}^{-i\omega t}$, which is omitted for compactness of notation.

The wave propagation characteristics need to be considered only for a set of wavenumbers within $-\pi/T$ and π/T since a wave with a wavenumber $2\pi n/T + k$ corresponds to the same wave with wavenumber k. The $2\pi n/T$ or region between $-\pi/T$ and π/T is called the first Brillouin zone in the 1-D lattice and contains all the unique wavenumbers [Brillouin, 2003]. Derivation of

Brillouin zones for 2 and 3-D lattices is a standard exercise in solid-state physics [Ziman, 1972, Joannopoulos, 2008].

Floquet (as in Floquet-Bloch theorem) formulated the analogous concepts for periodic linear differential equations in his original paper [Floquet, 1883] some 46 years before Bloch [Bloch, 1929]. The Floquet-Bloch theory may be regarded as a major breakthrough in the understanding of waves in periodic crystals.

In mechanics, wave propagation in various lattices composed of beam elements was studied by Phani et al. [2006]. The authors considered hexagonal honeycomb topology, Kagome lattice, triangular honeycomb and square honeycomb topologies. The solutions of the wave states in the unit cell were obtained using FEA while the propagating states were obtained from the unit cell solutions using Bloch wave principles. They identified the so-called band structure of each type of lattice by studying the dispersion curves. An extensive review on the studies of vibration and wave propagation in long multi-span beams and periodically stiffened plates is presented by Mead [1996].

Movchan et al. [2007] applied the Floquet-Bloch theory to study wave propagation in infinite perforated thin plates. The authors investigate the vibration of the plate with regularly placed circular holes as a two-dimensional periodic structure. The application of the Floquet-Bloch theory allowed the authors to solve the vibration problem at a unit cell containing a single hole analytically and then obtain the dispersion diagrams for the whole structure. The dispersion diagram for the case of the plate with holes that are fixed at the edges shows a band gap – a frequency range at which waves do not propagate through the plate. At the same time, if the holes are free, they do not alter the character of wave propagation much when compared with the uniform plate.

Movchan et al. [2006] studied two-dimensional periodic structures with high-contrast material properties, defects, and the inclusion of various materials. The wave propagation through perfectly periodic structures occurs according to passbands in the frequency spectrum. However, in the presence of irregularities such as inclusions, contrasting materials, etc., the waves that correspond to passbands may localise in a sub-domain of the structure. The authors employ the Floquet-Bloch theory, define a two-dimensional Brillouin zone for the structure and report the existence of stop bands (or band gaps) in a composite with coated inclusions and also discuss the localisation of waves in these inclusions. Furthermore, the authors proposed to study the vibration of a two-dimensional inhomogeneous lattice composed of point masses coupled with the springs. Two types of point masses were introduced and some of the springs were considered broken to introduce the inhomogeneity in the lattice. Such a model was then used to predict the localisation of the vibratory motion for high frequencies. A more detailed review of the phenomena of localisation is presented.

The works by the above-mentioned authors made a connection between the theory of periodicity in solid-state physics and the vibration of engineering structures. The application of the Floquet-Bloch theory in mechanics allowed the problems of vibration and wave propagation in complex multi-component structures to be solved for the first time.

5.2 Review of literature on disordered periodic structures

Most real-life structures possess defects such as dislocations in crystals, irregularities in structures due to manufacturing defects, deformations in operation, etc. Anderson in his famous paper on the absence of diffusion in random lattices [Anderson, 1958] demonstrated that if a certain irregularity is introduced in a lattice, the Bloch wave solution decays exponentially in a disordered periodic medium. In the case of electron waves, it leads to a conducting material becoming an insulator as the electrons get localised and fluctuate in the lattice points and do not propagate as waves.

In general, localisation is observed in waves of all types that propagate through the disordered media. Similar behaviour is also observed in the vibration of disordered linear chains as was shown by Rosenstock and McGill [1962] and Rosenstock and Richard [1968]. In structural vibration, this effect was demonstrated experimentally by Hodges and Woodhouse [1983]. A light string with point masses positioned every regular interval was excited and the standard normal modes reported. However, if the masses were slightly misplaced, the mode shapes of the string became localised within certain bays between the masses. This experiment showed the effect of localisation in standing wave modes of a vibrating structure. Hodges and Woodhouse [1983] also proposed a simple model based on coupled pendula to explain the observed localisation behaviour.

Later, Castanier and Pierre [1995] used a transfer matrix method to study localisation in a vibrating multi-span beam and quantify the effect via Lyapunov exponents. The method relies on writing the state vector $\mathbf{s}_i$ of the $i-$th bay of a periodic structure in terms of a Transfer matrix $\mathbf{T}$ times the state vector of the previous bay $\mathbf{s}_{i-1}$ of a chain

$$\mathbf{s}_i = \mathbf{T}_i \mathbf{s}_{i-1}. \tag{5.4}$$

Here, matrix $\mathbf{T}_i$ depends on the frequency of motion. Castanier and Pierre [1995] considered that if the state vector of the first bay is $\mathbf{s}_1$, the state of the $n-$th bay $\mathbf{s}_n$ can be defined in terms of the product of n transfer matrices $\mathbf{W} = \mathbf{T}_1 \mathbf{T}_2 \cdots \mathbf{T}_n$. Then, one can relate the singular values σ_i of $\mathbf{W}$ to the rate of change of the state vector with the number of bays n. In the limit of an infinite chain

$$\lambda_i = \lim_{N \to \infty} \frac{1}{N} \ln |\sigma_i| \tag{5.5}$$

are Lyapunov exponents that characterise the strength of localisation of the vibratory motion.

The ergodic multiplicative theorem of Oseledets [1968] relates asymptotic behaviour of products of random matrices to Lyapunov exponents in a formal way. A similar theorem on noncommuting random products has been proven by Furstenberg [1963] a few years earlier and bears his name. Furstenberg's theorem states that given $\mathbf{T}_m, \quad m = 1, \ldots, N$ non-singular, independent, identically distributed matrices, where $\mathbf{T}_m = \mathbf{T}_m(\boldsymbol{\epsilon})$ is a function of a random vector $\boldsymbol{\epsilon}$ with probability density $p(\boldsymbol{\epsilon})$, if at least two of these matrices do not have common eigenvectors, and if

$$\lim_{N \to \infty} \frac{1}{N} \ln \left(\prod_{m=1}^{N} |\det \mathbf{T}_m| \right) = 0, \tag{5.6}$$

then for any state vector $\boldsymbol{s}_1 \neq 0$ a constant λ exists such that

$$\lim_{N\to\infty} \frac{1}{N} \ln \|\boldsymbol{T}_{N-1}\boldsymbol{T}_{N-2}\cdots\boldsymbol{T}_m\cdots\boldsymbol{T}_2\boldsymbol{s}_1\| = \lambda \tag{5.7}$$

with probability 1. Where $\|\cdot\|$ is a suitable norm. Also, the norm of the product of transfer matrices has a similar asymptotic property, given by

$$\lim_{N\to\infty} \frac{1}{N} \ln \|\boldsymbol{T}_{N-1}\boldsymbol{T}_{N-2}\cdots\boldsymbol{T}_m\cdots\boldsymbol{T}_2\| = \lambda \tag{5.8}$$

with probability 1.

Ariaratnam and Xie [1995] applied Furstenberg's theorem to study wave localisation in randomly disordered long periodic continuous beams. Later, Xie and Wang [1997a] applied a method of regular perturbation of linear eigenvalue problems to study mode localisation in disordered chains, while Xie and Wang [1997b] applied the same method to 2-D assemblies of coupled cantilever beams.

Castanier and Pierre [1997] applied the numerical algorithm by Wolf et al. [1985] for the approximate calculation of Lyapunov localisation factors

$$\lambda_1 \approx \frac{1}{N}\sum_{i=1}^{N} \ln \|\mathbf{T}_i \frac{\mathbf{s}_{i-1}}{\|\mathbf{s}_{i-1}\|}\|, \tag{5.9}$$

where $\mathbf{T}_i$ is the transfer matrix of $i-$th bay, $\mathbf{s}_{i-1}$ is the state vector of bay $i-1$, N is the number of bays, and $\|\cdot\|$ is the Euclidean norm. This equation converges to the exact Lyapunov exponent for large N [Wolf et al., 1985]. The authors focused on the identification of the frequency regions for which the amplitude decay happens purely due to spatial localisation and not because of other factors such as damping. The authors studied the statistical properties of Lyapunov exponents by executing Wolf's algorithm multiple times and suggested that the covariance between the localisation factors for subsequent studies may indicate the conversion of waves in certain ranges of frequencies.

The field of wave propagation in periodic media is well-established. However, we have identified only a few studies of the instability behaviour of periodic structures. Pierre and Plaut [1989] studied the buckling of a two-span beam compressed along the beam axis by loading P. The spans were considered to be connected by a torsional spring k. A length imperfection Δl was introduced in the structure. The characteristic equation for the buckling load was solved numerically and the lowest two loads λ_1 and λ_2 plotted as functions of the disorder Δl. The authors showed that for strong coupling, the two buckling load trajectories are well separated and changing the disorder does not affect the behaviour. However, as the coupling becomes small, the two trajectories approach and veer from each other as the disorder is changed. The associated modes experience apparent localisation.

Xie [1995] studied the localisation of a buckling mode in multi-span disordered continuous beams using Lyapunov exponents as a measure of confinement of buckling amplitude. A numerical procedure similar to Wolf's algorithm was used to calculate localisation factors of beams with hundreds of spans numerically.

Similarly, Li et al. [1995] studied the buckling of multi-span beams with the disorder in a single span. They approached the problem by writing a differential equation for i-th span in a general form. Then, the solution of an entire structure was written using transcendental equations in terms of buckling load. These equations were assembled in an eigenvalue problem which was numerically solved for the buckling loads. The employed approach is similar to a Dynamic stiffness method, which implies the assembly of the exact member stiffness equations in a special kind of stiffness matrix called the Dynamic stiffness matrix [Banerjee, 1997]. Such an eigenvalue problem can be solved accurately using Wittrick-Williams algorithm [Williams and Wittrick, 1970]. The algorithm ensures that all eigenvalues of the transcendental EVP are computed with arbitrary precision in a given interval. The assembly of the Dynamic stiffness matrix and calculations of its eigenvalues for beams in buckling is automatised [Iakovliev, 2016]. Li et al. [1995] report that based on the strength of coupling between the spans, magnitude of disorder and the location of the disordered span, weak and strong localisation of the buckling amplitude near the disordered segment may be obtained.

Except for multi-span beams, studies on the buckling of periodic elastic structures are few and far between. The study of bilayer beam buckling suggests interesting instability behaviour may be also observed in a compressed multilayer structure composed of identical weakly coupled layers.

5.3 Compression of stacked cardboard paper sheets suggests localisation of buckling amplitudes

Inspired by the layered structures in composites, strata and other contexts, we study the instability of a structure that consists of multiple identical layers coupled at the ends. A schematic diagram is shown in Fig. 5.1. The richness of instability behaviour of the bilayer beam suggests

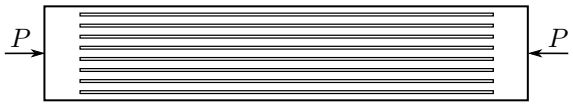

FIGURE 5.1: A schematic diagram of a structure consisting of identical layers stacked on top of each other and coupled at the ends. If the number of layers is large, the structure may be considered to approach periodicity in the stacking direction which is perpendicular to the axis of loading.

complex elastic deformation of the coupling material between the layers. It is reasonable to expect a similar level of complexity of buckling behaviour in the case of a multilayer structure such as the one shown in Fig. 5.1.

Simple experiments to qualitatively understand the buckling behaviour were carried out next. Milling numerous splits in a beam is expensive and is impractical. Instead, we made samples using cardboard sheets. Cardboard is much stiffer compared to paper, and even a single layer does not bend under its own weight. It is also much easier to cut to the desired shape and requires only several newtons of loading to trigger buckling. Therefore, complex procedures of milling and then testing using custom-made grips on bulky experimental equipment designed for testing of large and stiff samples are not needed. Finally, the coupling between the sheets can

be achieved by simply glueing their ends to each other. Note that a sophisticated experimental characterisation of such structures is beyond the scope of this study. The main purpose of this experiment is to gain qualitative insight.

The tested samples consist of a number of cardboard sheets stacked on top of each other and glued at the ends. This structure closely resembles the layered geometry in Fig. 5.1. The remaining parts of the sheets were uncoupled and allowed to deform freely. These samples practically do not have gaps between the layers thickness-wise. Thus, the layers are unable to deflect towards each other, only repulse. This limitation will be resolved in future studies. The gaps between the layers will be introduced by inserting short strips of cardboard between the layers in the glueing zone. The schematic view of a single layer in the stack with indicated gripping, gluing and glue-free areas is shown in Figure 5.3. The details of the sample geometry and properties are given in Table 5.1.

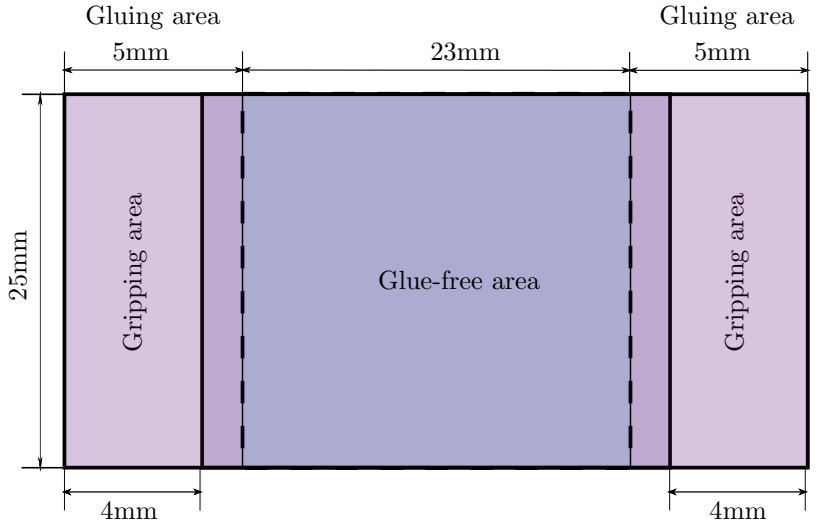

FIGURE 5.2: The schematic view of the sample showing gripping area (purple), gluing area (dark purple) and glue-free are (blue).

TABLE 5.1: Geometric and material properties of the cardboard samples

Structure	Each layer between grips	Modulus of Elasticity, E	Poisson ratio	Grips
8 sheets glued at the ends	25×25 mm	2×10^7 MPa [Ayrilmis et al., 2008]	0.3	25×4 mm

The compression testing was performed using *DEBEN MICROTEST* tensile testing machine. The benefit of this type of machine its extremely sensitive loading cell which allows testing materials with small stiffness. The maximum distance between the grips of the machine is 25 mm. The loading cell permits small load resolution of 0.01 N. The samples consisted of eight 25×23 mm layers of cardboard paper $\approx$1 mm thick glued along the strips $\approx$1 mm wide. The ends were tightly gripped by the two grips of the machine and compressed at a rate 0.1mm/min which agrees with the quasistatic assumption. The compression testing was controlled by displacement and the load-deflection curves were recorded. A more detailed description of the testing machine and the experimental setup used in further experiments are given in Chapter 6.

The photographs of the mode shapes observed in the experiment are shown in Fig. 5.3 (a) and Fig. 5.3 (b). Various modes were observed in the experiment as the structure turned out

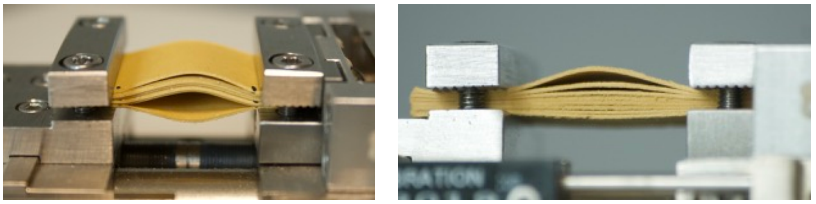

(a) (b)

FIGURE 5.3: The photographs of the experimentally observed modes. (a) The top and the bottom layers exhibit two opposite deflections, while the middle layers buckle cooperatively in one direction. (b) Rapid decay of the buckling amplitude is observed along the stacking direction.

to be very sensitive to any small irregularities in the layers and the coupling between them. However, a generic trend is observed in most of the test cases. Either the top or the bottom layer exhibits a relatively large buckling amplitude which then reduces quickly along the stacking direction. Often, the layers in the middle would not exhibit any noticeable deformation while the layers at the boundaries appear in the post-buckling regime. Even far in the post-buckling regime (as shown in Fig. 5.3 (a)), the layers in the middle part exhibit relatively small amplitude compared to the boundaries.

Although other effects may affect the behaviour and thorough further experimentation and modelling is planned in the future to make conclusions with certainty, we report that the observed behaviour strongly resembles the localisation of waves in the periodic media with disorder first reported by Anderson [1958] for electromagnetic waves in crystals and later observed in vibration of mechanical structures with disorder [Hodges and Woodhouse, 1983, Xie and Wang, 1997a].

Next, we present and discuss a simple model consisting of a chain of identical rigid rods coupled by a light spring. Although it does not capture the complex elasticity of the layered structure, it allows the analytical investigation of the effect of a regular placement of nominally identical members on the character of buckling. Then we introduce small disorder into the chain and observe the exponential decay of buckling mode from one rod to another. This suggests a mechanism of localisation of buckling amplitude similar to the one observed in the experiment with stacked sheets.

5.4 Elastic stability of a cyclic chain of elastically coupled rigid rods

A chain of masses coupled with springs and coupled pendula have been traditionally used as simple models to study *wave propagation* [Brillouin, 2003] and *vibration of periodic structures* in one dimension [Rosenstock and Richard, 1968, Hodges and Woodhouse, 1983, Castanier and Pierre, 1995]. A buckling analogy of such chains would be a chain of one degree of freedom rigid rods coupled by springs, as schematically shown in Fig. 5.4. The chain consists of rigid rods of length L supported by a hinge with torsional spring k_t. Each rod is subject to a compressive

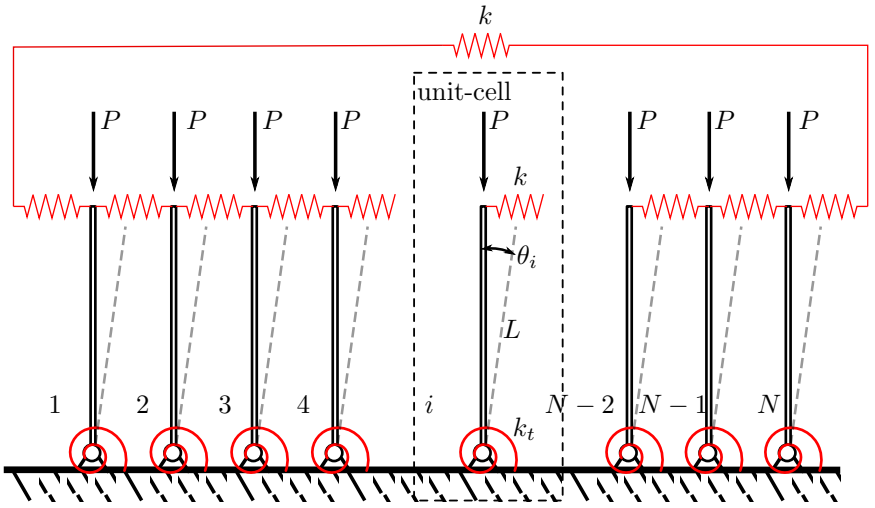

FIGURE 5.4: A chain of N identical rigid rods. Each rod has length L and is attached to a hinge bearing and a torsional spring k_t. Rods are coupled with light springs k and each is loaded with a force P. The deflected shape of each rod when buckled is indicated with dashed grey lines and the angle of deflection is labelled by θ.

force P at the top. Rods are coupled by light springs k and the deflection of each rod from the initial position is defined by angle θ.

Consider the stability of a single isolated rod on a bearing support. The hinge allows free rotation which is, however, restricted by the torsional spring. As the compressive loading increases from zero, the rod remains stable while the moments about the hinge support are in equilibrium $PL\sin\theta_i = k_t\theta_i$. For small angle approximation $PL\theta_i = k_t\theta_i$. The structure is in stable equilibrium for $P < k_t/L$ and destabilises when P reaches its critical value $P_{\text{cr}} = k_t/L$. Here, a bifurcation occurs leading to a left or a right buckling mode characterised by the deflection angle θ_b. The behaviour is schematically represented on a bifurcation diagram in Fig. 5.5. Note the difference between the bifurcation diagram for the rigid rod and a continuous beam-column (recall Fig. 3.3 (*left*)). The rigid rod is a one degree of freedom idealisation. When the bifurcation point is reached, it does not have a nonlinear post-buckling regime as beam-columns, which stabilises real buckled structures. Instead, the structure in Fig. 5.5 fails at the onset of buckling.

Now consider a rigid rod coupled by light spring k to its neighbours in a cyclic chain. We select $i-$th rod in the chain as shown within the dashed rectangle in Fig. 5.4 and consider it a unit cell of the chain. Applying the moment equilibrium condition for a unit cell leads to a recursive relation between the defections of the neighbouring rods

$$-kL^2\theta_{m-1} + (k_t + 2kL^2 - PL)\theta_m - kL^2\theta_{m+1} = 0. \tag{5.10}$$

We divide both sides of Equation (5.10) by L and introduce stiffness parameter $\bar{k}_0 = k_t/L + 2kL$ and coupling parameter $\bar{k} = kL$. Then, rearranging terms, we write

$$-\bar{k}\theta_{m-1} + \bar{k}_0\theta_m - \bar{k}\theta_{m+1} = P\theta_m, \tag{5.11}$$

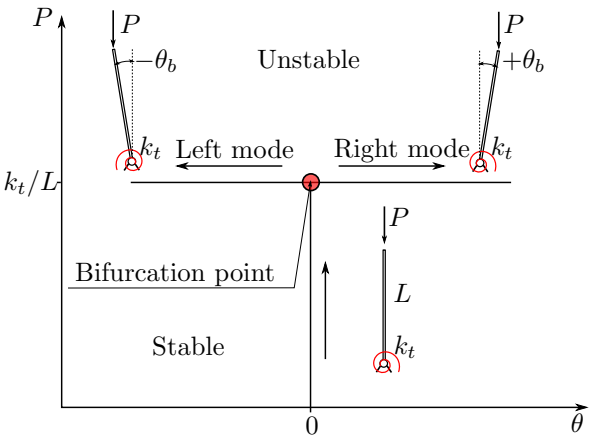

FIGURE 5.5: Schematic diagram in the coordinates of compressing load P and deflection angle θ for a rigid rod subject to compression P. The rod is stable for $P < k_t/L$. The bifurcation occurs in the bifurcation point (red circle) $P_{\text{cr}} = k_t/L$ where the structure becomes unstable.

We consider a chain of N rods forming a closed loop. This implies that the deflection of the first rod is equal to the deflection of the last $\theta_1 = \theta_{N+1}$. Equation (5.11) along with the cyclic boundary conditions can be written in the form of an eigenvalue problem in terms of a circulant matrix

$$\begin{bmatrix} \bar{k}_0 & -\bar{k} & \cdots & -\bar{k} \\ -\bar{k} & \bar{k}_0 & \ddots & \vdots \\ \vdots & \ddots & \ddots & \vdots \\ -\bar{k} & \cdots & -\bar{k} & \bar{k}_0 \end{bmatrix} \begin{Bmatrix} \theta_1 \\ \theta_2 \\ \vdots \\ \theta_N \end{Bmatrix} = P \begin{Bmatrix} \theta_1 \\ \theta_2 \\ \vdots \\ \theta_N \end{Bmatrix}. \tag{5.12}$$

In a compact form, this is expressed as $\mathbf{C}\boldsymbol{s} = P\boldsymbol{s}$, where $\mathbf{C}$ is the circulant matrix of the chain, the θ_m components form a vector of generalised coordinates $\boldsymbol{s}$, and P is the critical buckling load of the chain. The eigensolution of Equation (5.12) can be calculated *analytically* for any size of the chain N [Gray, 2005, Olson et al., 2014].

Note, that Equation (5.11) or its matrix form – Equation (5.12) is a set of linear difference equations that can be viewed as a discrete form of a second-order differential equation for which the solution is typically assumed in the form e^{kx}. Matrix $\boldsymbol{C}$ has eigenvectors $\mathbf{s}_n$, where $n = 1, \ldots, N$, and N is the size of the matrix. And each eigenvector $\mathbf{s}_n$ has m components, $m = 1, \ldots, N$, where $s_{n,m} = \theta_m$ – the angle of rotation of the m-th rod in a chain. Therefore, we can assume

$$s_{n,m} = z^{(n-1)(m-1)}, \quad n = 1, \ldots, N; \quad m = 1, \ldots, N. \tag{5.13}$$

Substituting $s_{n,m}$ into the cyclic boundary conditions $s_{n,1} = s_{n,N+1}$ we get

$$z^{(n-1)0} = z^{(n-1)N}, \tag{5.14}$$

and in the form of complex exponents $z^{(n-1)0} = r_0 \mathrm{e}^{i\varphi_0}$, where $\varphi_0 = 0$, and $z^{(n-1)} = r\mathrm{e}^{i\varphi}$

$$r_0 \mathrm{e}^{i0} = r^N \mathrm{e}^{iN\varphi}. \tag{5.15}$$

Equation (5.15) holds only if $r_0 = r^N = 1$ and $N\varphi = 2\pi l$, where l is an integer. Only N such integers correspond to unique solutions, thus, we consider $l = n-1$, where $m = 1, \cdots, N$. Thus, we define a family of *N Roots of Unity* along the unit-radius circle in the complex plane, where *n-th Root of Unity* is

$$z_N^n = \mathrm{e}^{\frac{2\pi i(n-1)}{N}}. \tag{5.16}$$

Here the subscript N indicates how many roots there is (size of the matrix $\mathbf{C}$) and the superscript n tells the number of the root.

Then, the m-th component of the n-th eigenvector of matrix $\mathbf{C}$ is

$$s_{n,m} = z^{(n-1)(m-1)} = \mathrm{e}^{\frac{2\pi i(n-1)(m-1)}{N}}. \tag{5.17}$$

We substitute Equation (5.17) back in Equation (5.11) and obtain

$$-\bar{k} z_N^{n(m-1)} + \bar{k}_0 z_N^{nm} - \bar{k} z_N^{n(m+1)} = P_n z_N^{nm}.$$

Dividing both sides of the above equation by z_N^{nm} yields

$$-\bar{k} z_N^{-n} + \bar{k}_0 - \bar{k} z_N^{n} = P_n.$$

Further, we scale the critical load P_n by the critical load of a single rod $P_{\mathrm{cr}} = k_t/L$. Since $\mathrm{e}^{-i\varphi} + \mathrm{e}^{i\varphi} = 2\cos\varphi$ and $1 - \cos\varphi = 2(\sin\varphi/2)^2$, we write the $n-$th scaled critical buckling load of the chain

$$\widetilde{P}_n = 1 + 4\widetilde{k}\left(\sin\frac{\pi(n-1)}{N}\right)^2 = 1 + 4\widetilde{k}\left(\sin\varphi_n\right)^2, \tag{5.18}$$

where $\widetilde{k} = kL^2/k_t$ is the ratio of coupling strength to rod stiffness, N is the number of the rigid rods, n is the sequential number of the critical load.

It is convenient to define $\varphi_n = \pi(n-1)/N$, or $\varphi_n/\pi = (n-1)/N$ which we call a *general mode number*. It closely resembles $g = \frac{2\pi n}{T}$ – a set of reciprocal numbers used in wave propagation literature [Ziman, 1972], which was discussed in Section 5.1. Here, $\widetilde{P}_n$ has a period of $\pi/\varphi_n = N/(n-1)$ which reflects the periodicity of roots of unity on a complex circle and is analogous to the first Brillouin zone. A mode corresponding to the buckling load $\widetilde{P}_l = 1 + 4\widetilde{k}\left(\sin\varphi_n + \varphi_l\right)^2$ is the same as the one corresponding to $\widetilde{P}_l = 1 + 4\widetilde{k}\left(\sin\varphi_l\right)^2$, since φ_n spans an entire circle.

In Fig. 5.6 we plot the values of the n-th buckling load of the chain $\widetilde{P}_n$ versus the general mode number $(n-1)/N$ using Equation (5.18) for $n = 1, \ldots, N$. The discrete points form a continuous blue line in Fig. 5.6 if the matrix size $N \to \infty$ (infinite chain). Indeed, in the limit of an infinite chain, the discrete variable $(n-1)/N$ becomes a continuous one, which is reflected by a continuous blue curve in Fig. 5.6. The red dots on the blue curve, however, correspond to buckling loads of a chain with $N = 10$ rods considered as a simple example. The mode shapes of a chain with $N = 10$ rods are plotted on the same figure for four selected general mode numbers to demonstrate the character of the behaviour. All the buckling loads that correspond to the first Brillouin zone appear within a single group with the magnitudes ranging between $\widetilde{P} = 1$ and $\widetilde{P} = 1 + 4\widetilde{k}$ (in Fig. 5.6 $\widetilde{k} = 0.1$). Further, we will refer to such a packed group of buckling loads as an *Instability cluster*. In the case of one degree of freedom structure, the first instability cluster plotted in Fig. 5.6 is the entire spectrum of the eigenvalue problem. The

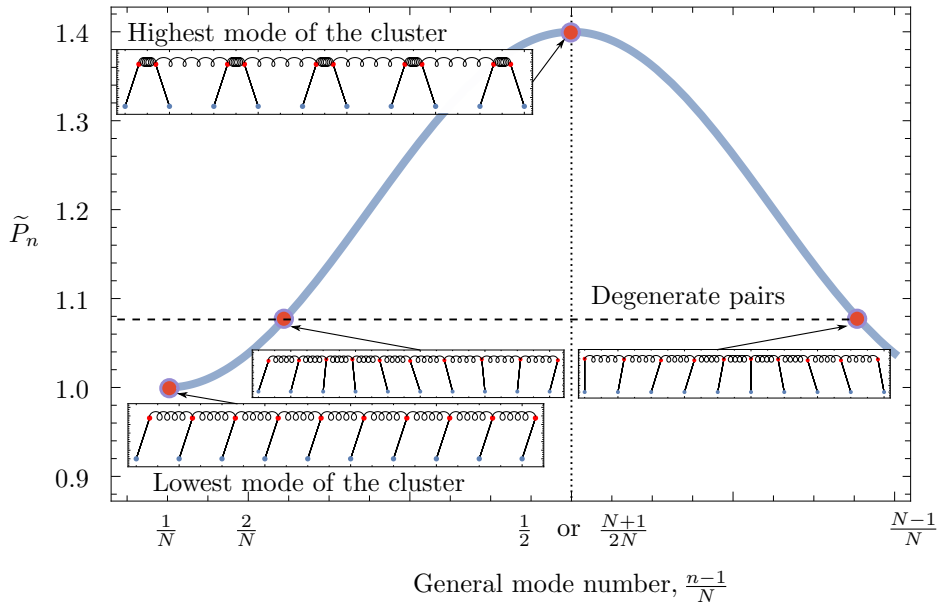

FIGURE 5.6: The plot of $\widetilde{P}_{cr}$ versus general mode number $(n-1)/N$ (blue line) for an infinite chain $N \to \infty$. It contains the instability cluster of the arbitrarily long chain. The mode types associated with the chosen general mode numbers are shown with the subplots.

cluster is symmetric with respect to $n = N/2$ for N being even and $n = (N+1)/2$ for odd N. The exceptions to this rule are the lowest $(n = 1)$ and the highest $(n = N/2$ or $n = (N+1)/2)$ buckling loads. This implies the cluster contains pairs of degenerate buckling loads.

Consider the selected mode shapes plotted in Fig. 5.6. The smallest buckling load corresponds to the mode with the least energy – all rods deflect in the same direction and coupling springs do not contribute to the energy. This is the buckling mode practically observable in the chain. The highest buckling load of the cluster is associated with the mode in which all the coupling springs contribute equal amounts to the energy. Any modes associated with the degenerate pairs are mere left-right reflection since the chain is invariant under $\theta \to -\theta$ transformation. The modes suggest that the deflection of m-th rod in the chain is spatially modulated due to the shape of the n-th eigenvector of matrix $\boldsymbol{C}$.

The n-th eigenvector of Equation (5.12) is written using roots of unity as

$$\boldsymbol{s}_n = \frac{1}{\sqrt{N}} \left(1, z_N^{(n-1)}, z_N^{2(n-1)}, \ldots, z_N^{(N-1)(n-1)}\right)^{\mathsf{T}}. \tag{5.19}$$

And all the eigenvectors of the circulant EVP can be assembled in a Fourier matrix [Olson et al., 2014]

$$\mathbf{F} = \frac{1}{\sqrt{N}} \begin{bmatrix} 1 & 1 & 1 & \cdots & 1 \\ 1 & z_N^1 & z_N^2 & \cdots & z_N^{N-1} \\ 1 & z_N^2 & z_N^4 & \cdots & z_N^{2(N-1)} \\ \vdots & \vdots & \vdots & \ddots & \vdots \\ 1 & z_N^{N-1} & z_N^{2(N-1)} & \cdots & z_N^{(N-1)(N-1)} \end{bmatrix}. \tag{5.20}$$

Each entry of the Fourier matrix is the buckling amplitude $s_{n,m} = \theta_m$, where m denotes rod number and n is the mode number. In practice, each column of the Fourier matrix contains the buckling amplitude of each rod modulated by some spatial periodic function with $n-$th shape.

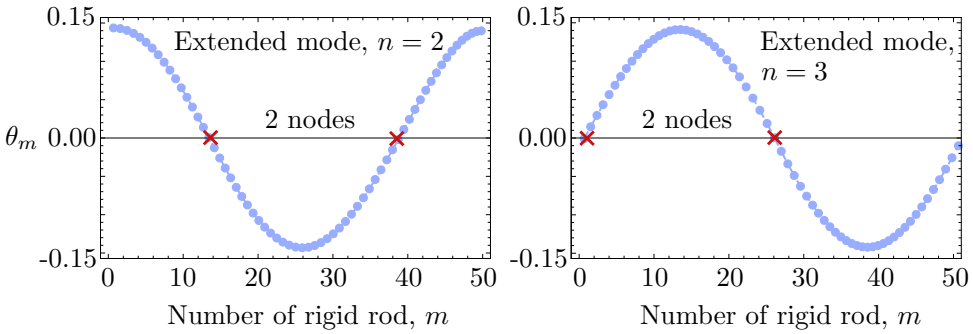

FIGURE 5.7: The angular displacement θ_m of m-th rod plotted versus its number m. Extended buckling mode 2 (*left*) and extend buckling mode 3 (*right*) appear as spatially modulated values of θ_m. The spatial coordinate is discrete and corresponds to rod numbers m.

Fig. 5.7 gives a visual representation of such behaviour. For example, spatial modes 2 and 3 are plotted. Each blue circle is a buckling angle of $m-$th rod in the chain θ_m plotted versus its position m. Since the chain is discrete, number m is, essentially, a discrete representation of the continuous spatial variable x along the chain. We see from the figure that the amplitude of rod is modulated by a periodic function.

Thus here, we observe a buckling counterpart of Bloch waves in the one-dimensional periodic chain. Note the key aspects of the behaviour specific to this problem. In contrast to wave propagation and vibration, here we are studying a static problem. Hence, the chain assumes a static configuration such that buckling amplitudes of the rods modulated in space due to the periodicity of the structure. Here and later we call such spatial modulation of buckling amplitudes of discrete members an *Extended buckling mode*. This name is chosen by analogy with the wave propagation literature where an extended mode is spatially spread and is associated with the conductivity of matter [Ziman, 1972].

Note that only the lowest mode of the chain of rigid rods is achievable in practice, as the chain fails above the lowest buckling load. To observe the second mode, one needs to fix a single rod on the chain to provide an artificial node to the extended buckling mode. Similarly, higher modes are achieved by providing more nodes.

Next, we study the behaviour of the two elastically coupled rigid rods with length imperfection. We aim to understand how the irregularity in the problem affects buckling behaviour. Then, we will extend this example to an entire disordered chain.

5.5 Elastic stability of two coupled rods with disorder

So far we have studied a case of perfect periodicity – a cyclic chain of identical rigid rods. As any real structure would inevitably possess some degree of irregularity, we need to account for it in our modelling. We start here by considering two rigid rods coupled by a spring and assume that they possess a small irregularity. For example, let their lengths be slightly different. This is shown in the schematic diagram in Fig. 5.8.

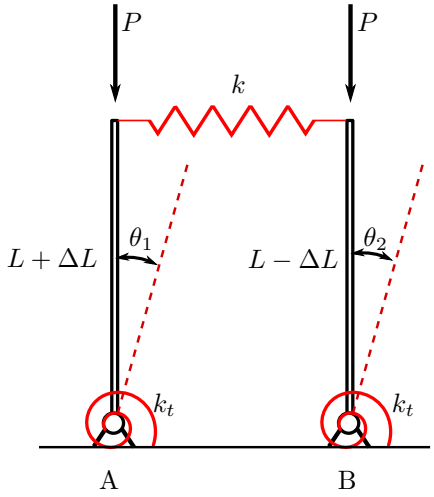

FIGURE 5.8: A model of two rigid rods on hinge supports with torsional springs k_t coupled by a weak spring k and loaded with a compressive loading P. The rods have a length imperfection of $\pm\Delta L$.

A moment equilibrium about points A and B under the small angle approximation results in a system of two linear equations

$$\begin{cases} k_t\theta_1 - P(L+\Delta L)\theta_1 + k\left[(L+\Delta L)\theta_1 - (L-\Delta L)\theta_2\right](L+\Delta L) = 0, \\ k_t\theta_2 - P(L-\Delta L)\theta_2 + k\left[(L-\Delta L)\theta_2 - (L+\Delta L)\theta_1\right](L-\Delta L) = 0. \end{cases} \tag{5.21}$$

We divide the first equation by $L+\Delta L$ and the second equation by $L-\Delta L$ and write

$$\begin{cases} -P\theta_1 + \frac{k_t}{L+\Delta L}\theta_1 + k\left[(L+\Delta L)\theta_1 - (L-\Delta L)\theta_2\right] = 0, \\ -P\theta_2 + \frac{k_t}{L-\Delta L}\theta_2 + k\left[(L-\Delta L)\theta_2 - (L+\Delta L)\theta_1\right] = 0, \end{cases} \tag{5.22}$$

which is equivalent to the generalised eigenvalue problem

$$\mathbf{K}\boldsymbol{s} = P\mathbf{K}_g\boldsymbol{s}, \tag{5.23}$$

where $\mathbf{K}$ is the stiffness matrix, $\mathbf{K}_g$ is the geometric stiffness matrix, $\boldsymbol{s} = [\theta_1, \theta_2]$ contains the buckling angle amplitudes of each rod. Note that due to normalisation by $L-\Delta L$ and $L+\Delta L$, the geometric stiffness matrix is the identity matrix.

The expressions for the two eigenvalues $P_{1,2}$ are analytically calculated

$$P_{1,2} = \frac{k_tL^2 + kL^2(L^2-\Delta L^2) \mp L\sqrt{k_t^2\Delta L^2 + k(L^2-\Delta L^2)\left(kL^4 - \Delta L^2\left(kL^2+2k_t\right)\right)}}{k_t(L^2-\Delta L^2)}. \tag{5.24}$$

We introduce a non-dimensional measure of irregularity $\varepsilon = \Delta L/L$ and the scaled coupling $\widetilde{k} = \bar{k}L/k_t = kL^2/k_t$ as a ratio of the coupling stiffness k and the torsional stiffness of each rod k_t. Then, we define a scaled buckling load as $\widetilde{P} = P/P_{cr}$, where $P_{cr} = k_t/L$ is the buckling load of an individual rod. Therefore, we can write the non-dimensional form

$$\widetilde{P}_{1,2} = \widetilde{k} + \frac{1}{1-\varepsilon^2} \mp \sqrt{\widetilde{k}^2 + \frac{\varepsilon^2\left(1-2\widetilde{k}(1-\varepsilon^2)\right)}{(1-\varepsilon^2)^2}}. \tag{5.25}$$

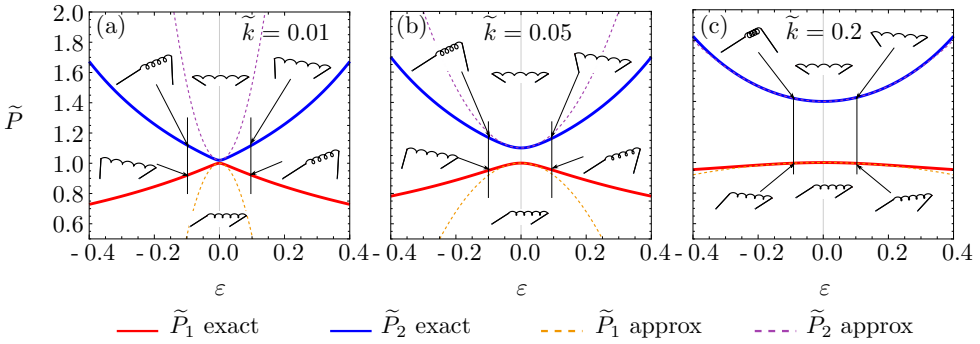

FIGURE 5.9: Plots of the first and the second critical buckling loads of two coupled rods as functions of disorder ε for non-dimensional coupling $\widetilde{k} = 0.01$ (a), $\widetilde{k} = 0.05$ (b) and $\widetilde{k} = 0.2$ (c). The solid lines represent the exact solution from Equation (5.25) while the dashed lines correspond to the second order series expansion from Equation (5.26).

Note, that $\widetilde{P}_{1,2}$ depend only on coupling $\widetilde{k}$ and disorder ε. We assume disorder to be small, i.e., $\varepsilon \to 0$ and use a power series expansion of $\widetilde{P}_{1,2}$ around ε

$$\begin{cases} \widetilde{P}_1 = 1 + \left(2 - \frac{1}{2\widetilde{k}}\right)\varepsilon^2 + O\left(\varepsilon^3\right), \\ \widetilde{P}_2 = (1 + 2\widetilde{k}) + \frac{1}{2\widetilde{k}}\varepsilon^2 + O\left(\varepsilon^3\right). \end{cases} \tag{5.26}$$

Equation (5.26) is a second-order approximation of the exact functional forms in Equation (5.25) for small disorder.

It is apparent that when $\varepsilon = 0$, we have a perfectly ordered structure with critical loads being $\widetilde{P}_1 = 1$ and $\widetilde{P}_2 = 1 + 2\widetilde{k}$. These are the same as the lowest and the highest buckling loads of an ordered chain given by Equation (5.18). This is in a good agreement with the Floquet-Bloch theorem as the solutions of the unit cell should specify the fundamental states which are then extended periodically for an entire medium.

When ε is close to zero, the critical buckling loads have a functional dependence on disorder given by Equation (5.26). As the disorder increases further, the approximate solution is expected to diverge from the exact solution in Fig. 5.25. This is demonstrated in Fig. 5.9 (a) for $\widetilde{k} = 0.01$, Fig. 5.9 (b) for $\widetilde{k} = 0.05$ and Fig. 5.9 (c) for $\widetilde{k} = 0.2$. The buckling load trajectories depend on the disorder. However, this dependence is either magnified by small coupling or reduced by a strong coupling. Therefore, it is apparent that the response should be studied with respect to a ratio of coupling to disorder.

The model of the two coupled rods with the disorder is particularly useful to demonstrate how buckling of a structure made of identical members is affected by coupling and by the disorder. Further explanation will be very useful in discussing the results of the future chapters. The system matrix $\mathbf{A} = \mathbf{K}_g^{-1}\mathbf{K}$ of the two identical uncoupled structural members is

$$\mathbf{A} = \begin{bmatrix} K & 0 \\ 0 & K \end{bmatrix}, \tag{5.27}$$

where K is some stiffness function of structural parameters. The eigenvalues of this matrix are identical for all values of structural parameters and constitute the buckling loads of uncoupled

members. However, consider coupling to be imposed between the members via a coupling matrix

$$\mathbf{A} = \begin{bmatrix} K & 0 \\ 0 & K \end{bmatrix} + \begin{bmatrix} k & -k \\ -k & k \end{bmatrix}. \tag{5.28}$$

Here, k is the coupling coefficient that also may depend on a number of structural parameters. Then, the eigenvalues of the system matrix are $\lambda_1 = K$, $\lambda_2 = K + 2k$. When plotted as functions of one or two parameters of interest, the eigenvalues appear as trajectories or surfaces. In the absence of coupling the trajectories (surfaces) coincide. Then, the introduction of coupling essentially breaks the degeneracy and the trajectories (surfaces) become separated. However, if $k = 0$ in a point (line) in parameter plane (space), this drives crossing the trajectories (surfaces) over that point (line).

Finally, if we introduce a small disorder via a disorder matrix, the last matrix in the following sum

$$\mathbf{A} = \begin{bmatrix} K & 0 \\ 0 & K \end{bmatrix} + \begin{bmatrix} k & -k \\ -k & k \end{bmatrix} + \begin{bmatrix} \epsilon_1 & 0 \\ 0 & \epsilon_2 \end{bmatrix}, \tag{5.29}$$

the crossing in the crossing point (crossing line) is removed and replaced by the repulsion of the respective trajectories (surfaces) as can be seen from Fig. 5.9. Notice, that in the current case, the trajectories as functions of the disorder are studied. However, later we will demonstrate the avoided crossing of trajectories (surfaces) as functions of structural parameters.

By writing a generic parameter-dependent system matrix as a sum of member stiffnesses, coupling and disorder, we present a comprehensive matrix description of all structures considered in the present study. All specific problems are partial examples of this representation. Matrix $\mathbf{A}$ can be large, can have circulant or tridiagonal structure. The present discussion will still be valid.

5.6 Localisation of buckling amplitude in a periodic chain of rods with disorder

Now we extend the analysis to a long chain of coupled rods, instead of just two in the previous section. Here, each rod is randomly disordered. We also abandon cyclic periodicity $\theta_1 \neq \theta_{N+1}$. Therefore, the system matrix $\mathbf{C}$ in Equation (5.30) is tridiagonal

$$\boldsymbol{C} = \begin{bmatrix} \bar{k}_0 & -\bar{k} & \cdots & 0 \\ -\bar{k} & \bar{k}_0 & \ddots & \vdots \\ \vdots & \ddots & \ddots & \vdots \\ 0 & \cdots & -\bar{k} & \bar{k}_0 \end{bmatrix}. \tag{5.30}$$

Note that $C_{1,N} = C_{N,1} = 0$, unlike that in Equation (5.12). Here as before, $\bar{k} = kL$ and $\bar{k}_0 = k_t/L + 2kL$, where k is the strength of the coupling spring and k_t is the strength of the torsional spring in each rod. The spectrum of the tridiagonal matrix that describes A_l, $(l \geq 2)$ Coxeter graph is known exactly [Goodman et al., 2012]. We show that the matrix $\mathbf{C}$ can be

transformed into a similar form. Labelling $\beta = \bar{k}_0/\bar{k}$, we can rewrite the matrix as

$$\mathbf{C} = \beta\mathbf{I} - \bar{k}\mathbf{A}_l, \tag{5.31}$$

where $\mathbf{I}$ is the identity matrix and $\mathbf{A}_l$ is the adjacency matrix of the Coxeter graph. The eigenvalues of $\mathbf{C}$ are then β plus the eigenvalues of $\mathbf{A}_l$ times $\bar{k}$. Hence, after rescaling the eigenvalues P by the critical load of a single rod $P/P_{cr} = k_t/L$ and considering that $\widetilde{k} = \bar{k}L/k_t = kL^2/k_t$ we can write

$$\widetilde{P}_n = 1 + 2\widetilde{k} - 2\widetilde{k}\cos\varphi_n, \tag{5.32}$$

where $\widetilde{P} = P/P_{cr} = PL/k_t$, $\bar{k}_0/k_t = 1 + 2\widetilde{k}$, and φ_n is the general mode number same as before. Equation (5.32) gives the instability cluster of the infinite chain of coupled rods. The extended modes of the chain can be obtained from the eigenvectors of $\mathbf{A}_l$ also derived in Goodman et al. [2012]. Note that the analytical solutions presented in Goodman et al. [2012] are given in the context of graph theory, which is different from ours. Further, we will use the transfer matrix approach instead.

The Transfer matrix method is extensively used in the literature on waves in periodic media and has long become a standard tool [Benaroya, 1997]. It is particularly efficient when a perfectly periodic structure is randomly disordered [Xie and Wang, 1997b,a]. We use Equation (5.11) to formulate a transfer matrix which specifies how buckling amplitude alters from one rod (unit cell) to the next. Mathematically, the state vector of $m-$th unit cell $\mathbf{s}_m$ is related to the state vector of the $m+1$ unit cell $\mathbf{s}_{m+1}$ via $\mathbf{T}_m$ matrix. In our case, $\boldsymbol{s}_{m+1} = [\theta_{m+1}, \theta_m]$, $\boldsymbol{s}_m = [\theta_m, \theta_{m-1}]$ and Equation (5.11) may be written as

$$\begin{Bmatrix} \theta_{m+1} \\ \theta_m \end{Bmatrix} = \begin{bmatrix} 2 + \frac{1}{\widetilde{k}} - \frac{\widetilde{P}}{\widetilde{k}} & -1 \\ 1 & 0 \end{bmatrix} \begin{Bmatrix} \theta_m \\ \theta_{m-1} \end{Bmatrix}, \tag{5.33}$$

where $\widetilde{k} = k\frac{L^2}{k_t}$ and $\widetilde{P} = P\frac{L}{k_t}$. In vector-matrix notation

$$\boldsymbol{s}_{m+1} = \boldsymbol{T}_m\boldsymbol{s}_m, \quad m = 1, \ldots, N, \tag{5.34}$$

where $\boldsymbol{T}_m$ is the transfer matrix between unit cell $m+1$ and unit cell m in a chain with N unit cells (rods). The whole chain or rigid rods may thus be described by a cumulative product of transfer matrices

$$\boldsymbol{s}_N = \boldsymbol{T}_{N-1}\boldsymbol{T}_{N-2}\cdots\boldsymbol{T}_m\cdots\boldsymbol{T}_1\boldsymbol{s}_1. \tag{5.35}$$

If we consider a small random disorder introduced in each rod, the transfer matrices $\boldsymbol{T}_m$ become random. Products like those given by Equation (5.35) appear in many contexts associated with waves in periodic media. Anderson [1958] studied the asymptotic behaviour of state vectors in the disordered lattices and showed that exponential decay of wave-function amplitude due to disorder leads to the development of an insulating property of a conductor as all electrons appear in highly localised states. Later, ergodic multiplicative theorem by Oseledets [1968] and Furstenberg's theorem on noncommuting random products [Furstenberg, 1963] were developed to relate the asymptotic behaviour of products of random matrices to Lyapunov exponents. The first adaptations of these two theorems to the cases of vibration of multi-span beams were made by Castanier and Pierre [1995] and by Ariaratnam and Xie [1995]. At the same time, Xie [1995]

adapted the idea of products of random matrices to studying multi-span beams in buckling. Here, we apply the analysis framework proposed by [Xie, 1995] to a different buckling problem. Note that in the present study the axis of periodicity is perpendicular to the axis of loading in contrast to the previous studies.

Furstenberg's theorem (stated in full in Section 5.2) allows the asymptotic of the products of the transfer matrices to be calculated. If $\boldsymbol{T}_m$, $m = 1, \ldots, N$ non-singular, independent, identically distributed 2×2 matrices, then

$$\lim_{N\to\infty} \frac{1}{N} \ln \|\boldsymbol{T}_{N-1}\boldsymbol{T}_{N-2} \cdots \boldsymbol{T}_m \cdots \boldsymbol{T}_2 \boldsymbol{s}_1\| = \lambda \tag{5.36}$$

and

$$\lim_{N\to\infty} \frac{1}{N} \ln \|\boldsymbol{T}_{N-1}\boldsymbol{T}_{N-2} \cdots \boldsymbol{T}_m \cdots \boldsymbol{T}_2\| = \lambda. \tag{5.37}$$

These two statements hold if

$$\lim_{N\to\infty} \frac{1}{N} \ln \left(\prod_{m=1}^{N} |\det \mathbf{T}_m| \right) = 0, \tag{5.38}$$

where $|\cdot|$ is an absolute value.

In the discussed chain of elastically coupled rigid rods $|\det \boldsymbol{T}_m| = 1$ as can be seen from Equation (5.34) and the limit of $1/N \prod_{m=1}^{N} 1 = 1/N$, where Π represents the product of terms. It approaches zero as $N \to \infty$. The application of the Furstenberg's theorem to Equation (5.35) leads to

$$\lim_{N\to\infty} \frac{1}{N-1} \ln \|\boldsymbol{s}_m\| = \lim_{N\to\infty} \frac{1}{N-1} \ln \|\boldsymbol{T}_{N-1}\boldsymbol{T}_{N-2} \cdots \boldsymbol{T}_m \cdots \boldsymbol{T}_2 \boldsymbol{s}_1\| = \lambda > 0. \tag{5.39}$$

For large N, i.e., a long chain, the following asymptotic relationship can be written

$$\|\boldsymbol{s}_N\| = \mathrm{e}^{(N-1)\lambda} \|\boldsymbol{s}_1\|. \tag{5.40}$$

It shows that changes in the norm of the state vector from unit-cell to unit-cell are governed by an exponential law, where $e^{\lambda N}$ is the Lyapunov exponent, and λ is the localisation factor.

Since the state vector $\boldsymbol{s}_m = [\theta_{m+1}, \theta_m]$ and the state vector $\boldsymbol{s}_1 = [\theta_2, \theta_1]$, the angle of rotation of the $N-$th rod (last) can be expressed in terms of the angle of rotation of the first rod for large N as

$$|\theta_{N+1}| = \mathrm{e}^{\lambda N} |\theta_1| \tag{5.41}$$

which defines how buckling angle changes from rod to rod and characterises the localisation of the angles of rotation. If $\lambda > 0$, the angles of rotation will grow exponentially along the chain. According to Xie [1995], the localisation exponents can be calculated from either end of the beam and have to intersect at a certain point. Then, λ factors will indicate how quickly the buckling amplitudes of rods will decay from that point. At the same time, the extended modes of a periodic chain are characterised by the Fourier matrix or complex exponents. If real Lyapunov exponents are non zero, they govern how quickly buckling amplitudes of each rod deviate from the extended modes. This will be further demonstrated. The λ factors are called *localisation factors* and are generic descriptors of the behaviour in case of disorder.

We start by calculating Lyapunov exponents for a trivial case of all rods being identical. Xie [1995] relates the eigenvalues $e_1 = e_{max}$ and $e_2 = e_{min}$ of the matrix $\mathbf{B}^\top\mathbf{B}$, where matrix $\mathbf{B}$ is defined as $\boldsymbol{B} = \boldsymbol{T}_{N-1}\boldsymbol{T}_{N-2}\cdots\boldsymbol{T}_m\cdots\boldsymbol{T}_2$, to Lyapunov exponents λ_1 and λ_2 using Rayleigh's quotient and the theorem of Oseledets [Oseledets, 1968] as

$$\lambda_1 = \lambda_{max} = \lim_{N\to\infty}\frac{1}{N-1}\ln e_{max}, \tag{5.42}$$

$$\lambda_2 = \lambda_{min} = \lim_{N\to\infty}\frac{1}{N-1}\ln e_{min}. \tag{5.43}$$

We use Equation (5.42) and Equation (5.43) to calculate Lyapunov exponents for the perfectly periodic case when no localisation is expected. This corresponds to all rods being the same and $\mathbf{T}_N = \mathbf{T}_{N-1} = ...\mathbf{T}_m = ... = \mathbf{T}_2 = \mathbf{T}$, so that

$$\begin{Bmatrix}\theta_{N+1}\\ \theta_N\end{Bmatrix} = \begin{bmatrix}\left(2+\frac{1}{\widetilde{k}}-\frac{\widetilde{P}}{\widetilde{k}}\right) & -1\\ 1 & 0\end{bmatrix}^{N-1}\begin{Bmatrix}\theta_1\\ \theta_2\end{Bmatrix}. \tag{5.44}$$

Eigenvalues of $\mathbf{B}^\top\mathbf{B}$ are easy to calculate noticing that $\mathbf{T}^{N-1} = \mathbf{V}^{-1}\mathbf{\Lambda}\mathbf{V}\mathbf{V}^{-1}\mathbf{\Lambda}\mathbf{V}\cdots\mathbf{V}^{-1}\mathbf{\Lambda}\mathbf{V} = \mathbf{V}^{-1}\mathbf{\Lambda}^{N-1}\mathbf{V}$, where $\mathbf{V}$ and $\mathbf{\Lambda}$ are matrices of eigenvectors and eigenvalues of $\mathbf{T}$ respectively. As $\mathbf{\Lambda}$ is the diagonal matrix of eigenvalues of $\mathbf{T}$, the eigenvalues of $\mathbf{B}^\top\mathbf{B}$ are $e_1^2 = |\Lambda_{1,1}|^{2N-2}$ and $e_2^2 = |\Lambda_{2,2}|^{2N-2}$ or $e_1 = |\Lambda_{1,1}|^{N-1}$, $e_2 = |\Lambda_{2,2}|^{N-1}$. Eigenvalues of $\mathbf{T}$ are

$$\Lambda_{1,2} = \frac{1+2\widetilde{k}-\widetilde{P}\pm\sqrt{(1-\widetilde{P})(4\widetilde{k}-\widetilde{P}+1)}}{2\widetilde{k}}, \tag{5.45}$$

then the Lyapunov exponents from Equation (5.42) and Equation (5.43) read

$$\lambda_{1,2} = \operatorname{sgn}(\Lambda_{1,2})\ln|\Lambda_{1,2}|. \tag{5.46}$$

The functional dependencies of $\lambda_{1,2}$ on compressive loading $\widetilde{P} = P/P_{cr} = PL/k_t$ for various values of coupling $\widetilde{k} = kL^2/k_t$ are plotted in Fig. 5.10. Recall that we are studying a perfectly periodic structure now with no disorder. To understand the plot, consider that a transfer matrix in Equation (5.44) is a function of the loading parameter $\widetilde{P}$. If the loading is continuously increased from zero, the chain of rigid rods is stable until the first buckling load of the cluster is reached. In this region, λ_1 and λ_2 are of no interest to us as they do not govern the buckling behaviour. Whereas, within the instability cluster, $\lambda_{1,2}$ reflect localisation. Finally, for the loads beyond the instability cluster, localisation is of no interest since the structure has already failed.

The *top* plot in Fig. 5.10 shows the largest localisation factor λ_1, while the *lower* plot in Fig. 5.10 shows the smallest localisation factor λ_2 as functions of $\widetilde{P}$. Let us study this plot in relation to the properties of the transfer matrix $\boldsymbol{T}$ from Equation (5.44). The eigenvalues of $\boldsymbol{T}$ can be real or complex depending on the value of $\widetilde{P}$. Consider the expression under the radical in Equation (5.45) and recall that $\widetilde{P}$ is the loading factor that increases from zero.

While $\widetilde{P} < 1$:

$$(1-\widetilde{P})(4\widetilde{k}-\widetilde{P}+1) > 0 \tag{5.47}$$

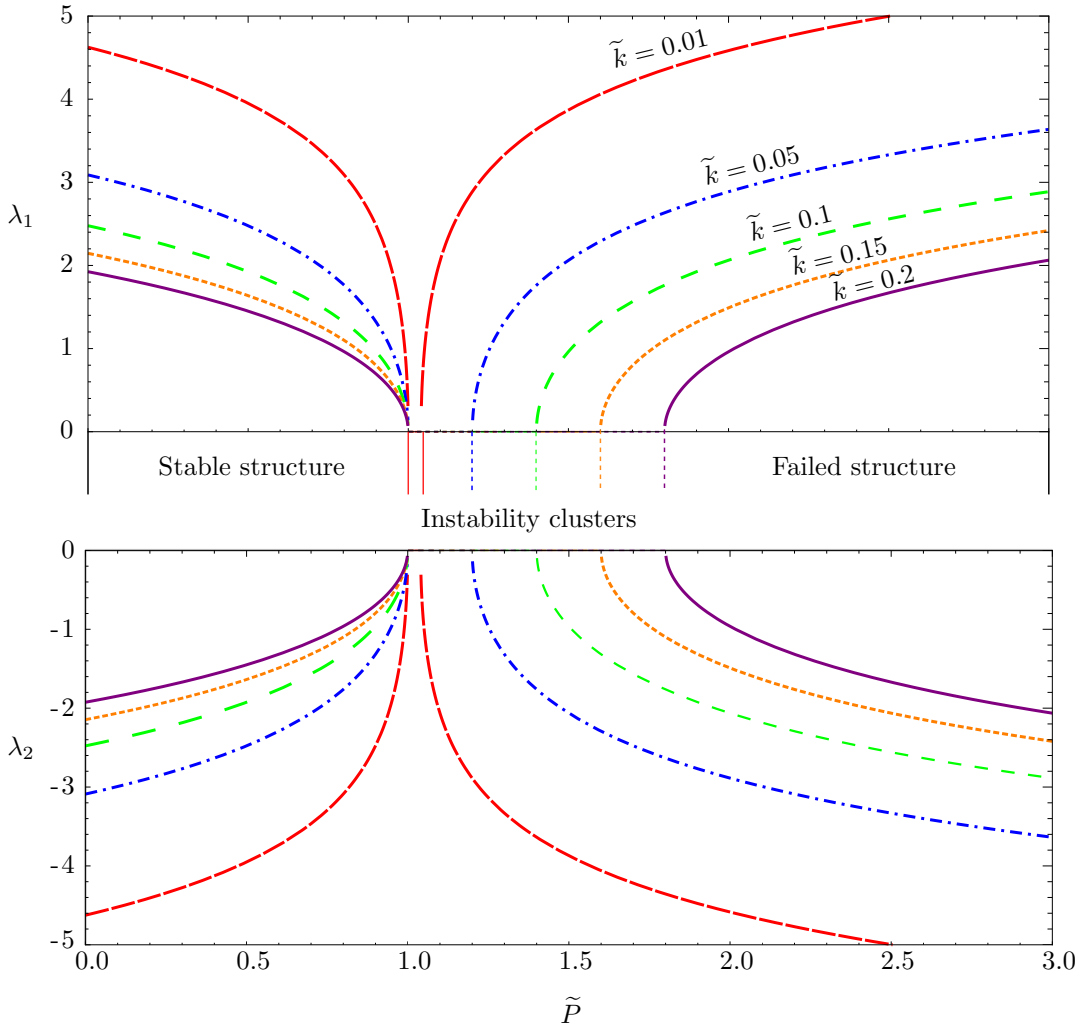

FIGURE 5.10: Plots of λ_1 and λ_2 factors as functions of loading parameter $\widetilde{P} = P/P_{cr}$ for various coupling strengths $\widetilde{k}$.

the Lyapunov exponents $\lambda_{1,2}$ from Equation (5.46) are all real. However, they do not affect the behaviour as the compressive loading is smaller than the critical buckling load and the structure is stable.

The lowest buckling load is $\widetilde{P} = 1$, while the highest buckling load of the chain is $\widetilde{P} = 1 + 4\widetilde{k}$. For both of them

$$(1 - \widetilde{P})(4\widetilde{k} - \widetilde{P} + 1) = 0. \tag{5.48}$$

Here $\Lambda_{1,2} = 1$ from Equation (5.45) and $\lambda_{1,2} = 0$. Thus, the Lyapunov exponents $e^{\lambda_{1,2}} = 1$ – the behaviour of the chain is governed by the Fourier matrix. This corresponds to the boundaries on the instability cluster in Fig. 5.10.

When the expression under the radical in Equation (5.45) is negative, i.e.,

$$(1 - \widetilde{P})(4\widetilde{k} - \widetilde{P} + 1) < 0, \quad \text{for} \quad 1 < \widetilde{P} < 1 + 4\widetilde{k}, \tag{5.49}$$

eigenvalues $\Lambda_{1,2}$ are complex, and the $\lambda_{1,2} = 0$ [Xie, 1995]. This range of $\widetilde{P}$ corresponds to the instability cluster in Fig. 5.10 which corresponds to Equation (5.32). Values of $\widetilde{P}$ in this band

correspond to the critical buckling loads of a periodic structure, buckling occurs and localisation is absent, as expected from a perfectly periodic structure. When $\widetilde{P} > 1 + 4\widetilde{k}$, the Lyapunov exponents are real. However, these loads are not physically achievable as the structure has already failed at critical loads lower than this.

We introduce disorder into each rigid rod now. Furstenberg's theorem only tells us that such an asymptotic value λ exists to which the product of random matrices should converge. It does not specify how to calculate it. And the previously used Equation (5.45) and Equation (5.46) are not applicable here since Equation (5.44) does not hold as all the transfer matrices are different now. Therefore, one has to use numerical algorithms to calculate localisation factors. One such algorithm was employed by [Xie, 1995]. We will make use of this algorithm as well.

Consider the disorder to be introduced into each rigid rod by changing its restoring torsional spring stiffness k_t. The new torsional spring of each disordered rod has a stiffness $k_t = \bar{k}_t + \varepsilon$, where $\bar{k}_t$ is some mean value of torsional spring stiffness and ε is a small parameter, which is a measure of disorder. Values of ε are taken from a uniform distribution. Therefore, using the previously defined scaling $P = \widetilde{P}P_0$ and $k = \widetilde{k}k_0$, we can rewrite the first entry of the transfer matrix in Equation (5.44) accounting for the disorder as

$$2 + \frac{\bar{k}_t + \varepsilon}{kL^2} - \frac{P}{kL} = 2 + \frac{1+\varepsilon}{\widetilde{k}} - \frac{\widetilde{P}}{\widetilde{k}}, \tag{5.50}$$

The $m-$th random transfer matrix is obtained from Equation (5.44) becomes

$$\boldsymbol{T} = \begin{bmatrix} \left(2 + \frac{1+\varepsilon}{\widetilde{k}} - \frac{\widetilde{P}}{\widetilde{k}}\right) & -1 \\ 1 & 0 \end{bmatrix}. \tag{5.51}$$

Now we calculate the norm of the product of transfer matrices by the initial state vector $\|\boldsymbol{T}_{N-1}\boldsymbol{T}_{N-2}\cdots\boldsymbol{T}_m\cdots\boldsymbol{T}_2\boldsymbol{s}_1\|$ numerically and then calculate the logarithm and take the limit. We perform such calculations for $N = 10$, $N = 20$, $N = 50$, $N = 100$ and $N = 1000$ rods as we want to replace theoretical limit of $N \to \infty$ by a large enough number and be sure that the numerical calculation has converged. Practically, it turned out that the values of localisation factors do not change by more than $10\% - 15\%$ but we plot them as functions of $\widetilde{P}$ for $N = 1000$ to have smooth curves that are shown in Fig. 5.11. The functions of localisation factors are plotted for the same disorder magnitude $\varepsilon = 0.1$ but for various coupling. In this case, we calculate positive localisation factor using forward product of matrices $\|\boldsymbol{T}_{N-1}\boldsymbol{T}_{N-2}\cdots\boldsymbol{T}_m\cdots\boldsymbol{T}_2\boldsymbol{s}_1\|$ and the negative localisation factor using backward product $\|\boldsymbol{T}_1\boldsymbol{T}_2\cdots\boldsymbol{T}_m\cdots\boldsymbol{T}_{N-1}\boldsymbol{s}_N\|$. In such a way, if $\lambda_{1,2}$ are mirrors of each other, as in this case, the localisation is symmetric. This means that the decay of the buckling amplitude from the rod with the maximum displacement is symmetric in both directions.

The plot of localisation factors λ_1 and λ_2 in Fig. 5.11 gives valuable insight into the physics of localisation. We observe that the strength of localisation increases as coupling to disorder ratio $\widetilde{k}/\varepsilon \to 1$. If the coupling to disorder ratio $\widetilde{k}/\varepsilon \gg 1$, the chain exhibits weak localisation and the respective λ curves approach those from the perfectly periodic case as in Fig. 5.10. The values of $\lambda_{1,2}$ are no longer zero in the instability cluster. Instead, they also depend on $\widetilde{k}/\varepsilon$. In such a way, we observe that disorder affects the width of the instability cluster and the ordering of the buckling loads in it.

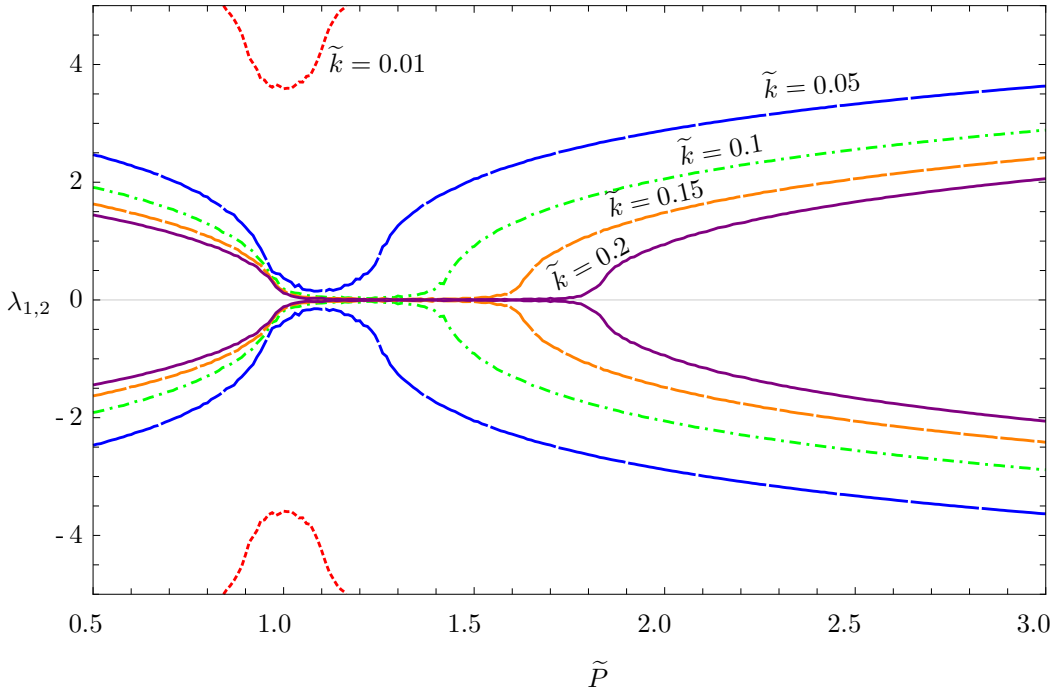

FIGURE 5.11: Positive localisation factor λ_1 and negative localisation factor λ_2 plotted as functions of $\widetilde{P}$ for disorder magnitude $\varepsilon = 0.1$ and for various values of coupling $\widetilde{k}$.

This can be visually observed in Fig. 5.11 which contains the plots of instability clusters for a fixed value of coupling strength $\widetilde{k}$ and various disorder magnitudes. The clusters were calculated numerically for a chain with $N = 100$ rigid rods with $\bar{k}_0 = \widetilde{k}_t + 2kL^2$ and $\widetilde{k}_t$ being a normally distributed variable with mean k_t and standard deviation ε – a measure of disorder.

The red dots in Fig. 5.12 represent values of the buckling load $\widetilde{P}$ plotted versus general mode number. Fig. 5.12 (*top*) displays an instability cluster in a perfectly ordered case $\varepsilon = 0$. Note that this is a discrete representation of Equation (5.32). Then, Fig. 5.12 (*centre*) contains the same cluster for the small but non-zero disorder. We observe that small disorder does not have much effect. Finally, Fig. 5.12 (*bottom*) contains an instability cluster for the case of a moderate disorder. Here, we observe that the overall shape of the cluster is distorted and individual buckling loads have randomly changed magnitudes. This case corresponds to the localisation of the respective modes.

In Fig. 5.13 we plot the extended mode shapes of the chain with $N = 100$ rigid rods associated with the four lowest buckling loads $\widetilde{P}$ in the instability clusters in Fig. 5.12. In the case of no disorder ($\varepsilon = 0$), we observe periodic extended modes as expected from a perfectly ordered structure in Fig. 5.13 (*left column*). However, even for a small disorder, the extended modes start deviating from the periodic solution as seen in Fig. 5.13 (*centre column*). This case corresponds to weak localisation which happens for large coupling to disorder ratio. However, as we increase the disorder until the coupling to disorder ratio approaches one, we observe a strong or Anderson type localisation of the modes as shown in Fig. 5.13 (*right column*). Notice that the location of the rod with maximum localised amplitude is random, but the exponential decay of the amplitude from this rod is symmetric as indicated by both localisation factors in Fig. 5.11.

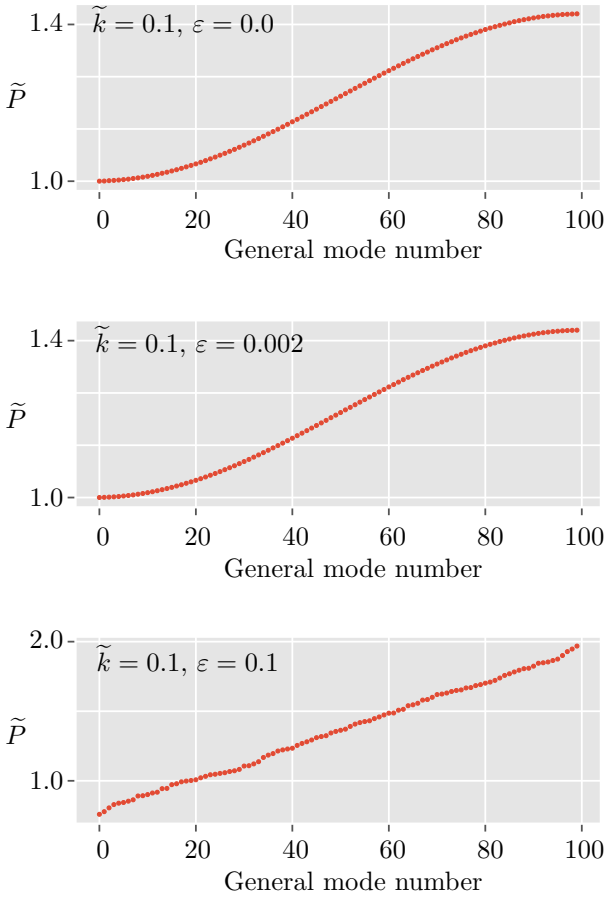

FIGURE 5.12: Instability clusters plotted for various magnitudes of disordered. (*top*) Instability cluster for a perfectly ordered chain. (*centre*) Instability cluster for the small disorder. (*bottom*) Instability cluster for the moderate disorder.

5.7 Conclusions

In this chapter, we extended the discussion on bilayer beam buckling to the problem of elastic stability of a multilayer structure. Having noticed that the geometry of such a structure is periodic, we reviewed the literature in the area of wave propagation in periodic media and vibration of periodic structures, since this is the closest field that has been studied extensively, whereas literature on the buckling of periodic media is very sparse. We also reviewed the literature on the localisation of waves and vibration modes as well as buckling modes in periodic structures with the disorder. We concluded that relatively little attention was devoted to the buckling of periodic structures. Then, we designed and carried out a demonstrative experiment. Having compressed a stack of sheets glued at the ends, we observed exponential decay of the buckling amplitude of each sheet along the stacking direction. This behaviour suggests localisation of the instability modes of the multilayer structure. To study the behaviour mathematically, we proposed a minimalistic model – a chain of elastically coupled rigid rods and modelled its behaviour in buckling. The magnitudes of the buckling loads of each rod are densely packed within a range that we termed an *instability cluster*. The mode numbers associated with the buckling loads within the instability cluster appear inside the buckling analogy of the first Brillouin zone. The buckling amplitudes of each rod are spatially modulated by the periodic functions along

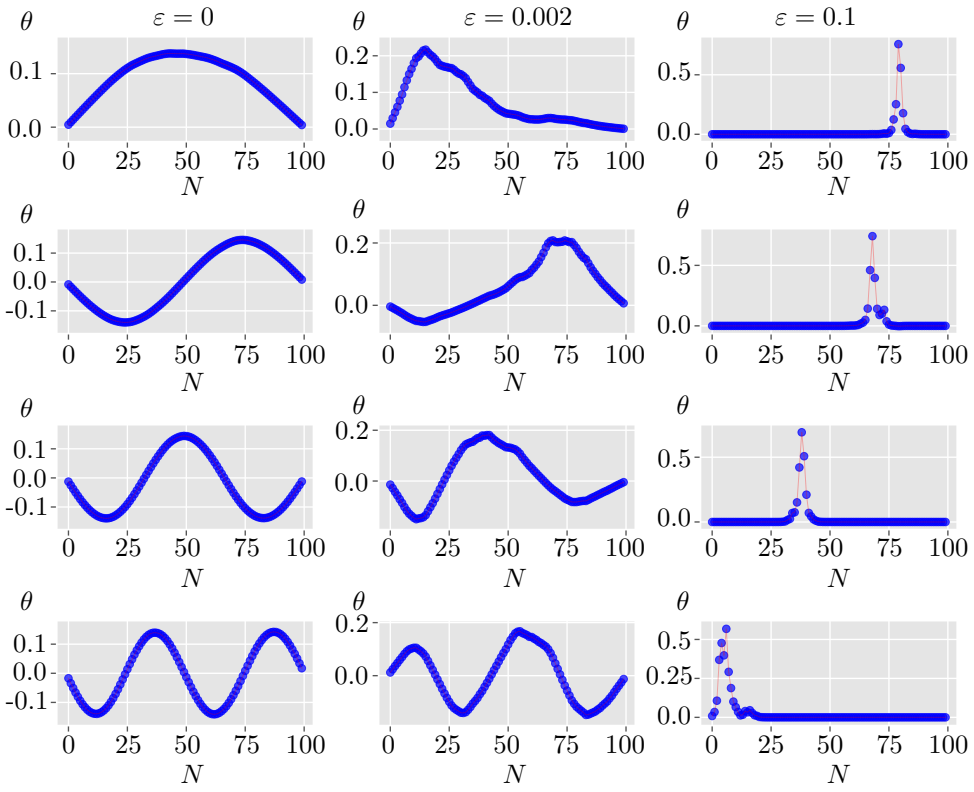

FIGURE 5.13: Four lowest extended buckling modes of a chain with $N = 100$ rigid rods for various magnitudes of disorder. *(left column)* Four extended modes of the chain with no disorder. *(centre column)* Four extended modes of the chain with small disorder. *(right column)* Four extended modes of the chain with moderate disorder.

the chain and form so-called extended buckling modes. This behaviour is characterised by the eigenvectors of the eigenvalue problem of the chain, which are columns of the Fourier matrix.

We studied the effect of the disorder on buckling of two elastically coupled rigid rods next. We reported that the buckling mode of the structure is highly sensitive to the disorder for small coupling and relatively insensitive to disorder in the case of strong coupling. Therefore, coupling to disorder ratio is the parameter that drives the sensitivity to the irregularities.

We then extended this study to the case of a long chain of elastically coupled rigid rods with random disorder introduced in each rod. We reported that in contrast to the extended modes of the ordered chain, defined by the Fourier matrix, the extended modes of the disordered chain exhibit localisation. Amplitude modulation for localised modes is determined by the Lyapunov exponent which drives exponential decay of the amplitude along the chain. The factor of the exponent is known as localisation factor. We used Furstenberg's theorem and numerical methods to calculate the localisation factors for the chain and reported their values for large numbers of rods. Similar to the case of two coupled rods, the chain exhibits stronger localisation as coupling to disorder ratio reduces. For the coupling to disorder ratio close to one, we observe a strong or Anderson localisation of buckling amplitudes along the chain. In this case, only a few neighbouring rods exhibit large buckling amplitudes which exponentially decay and the rest of the chain exhibits very little buckling. The rods at which the extended buckling mode localises in the chain are random.

Chapter 6

Buckling of a plate with a single cut out

In this chapter, we study buckling of a plate with a single symmetrically placed rectangular cut out. This is a typical problem in structural engineering. However, we are looking at it armed with the physical intuition acquired from the study of the bilayer beam. Therefore, we set out to explore the behaviour of this structure by studying how the variation of the size of the cut out affects the mode shapes of the plate. It so turns out that this structure exhibits two distinctive types of buckling modes which resemble the cooperative and the splitting buckling of a bilayer beam. Thus, this structure may be viewed as a plane counterpart of the bilayer beam problem.

The plate with a cut out is of both academic and practical interest. Structural engineers find numerous applications for plates with various geometric features such as holes, splits and cut outs. In many cases, such structures are subject to compressive or thermal loading, which may trigger the thermal buckling of parts with constrained edges. Thus, the prediction of the buckling behaviour of such structures is of high practical importance. Yet, as will be discussed in the literature review below, a comprehensive study of the instability behaviour of a plate with a rectangular cut out reveals novel behaviour.

6.1 Review of literature on buckling of planar bodies with cut outs

Thin steel plates featuring one or multiple holes, cuts and perforations of various shapes and sizes are commonly used in the construction of cars, aircraft and other structures. Frequently, cut outs are deliberately introduced in webs within I-section and C-section beams for weight reduction, as was discussed in Section 2.2).

Plates with perforations and cut outs are commonly used in cooling equipment. For example, an exhaust recovery system, such as the one shown in Fig. 6.1 (a) contains a number of identical plates stacked closed to each other which are coupled at the ends to allow efficient heat exchange. Also, heat exchangers and compressor coolers such as the one in Fig. 6.1 (b) typically have perforated plates to allow efficient cooling. The heat exchanging and cooling equipment operates under increased temperatures. Overheating may trigger considerable thermal expansion of jammed parts, which in turn, may cause thermal buckling. The mentioned structures

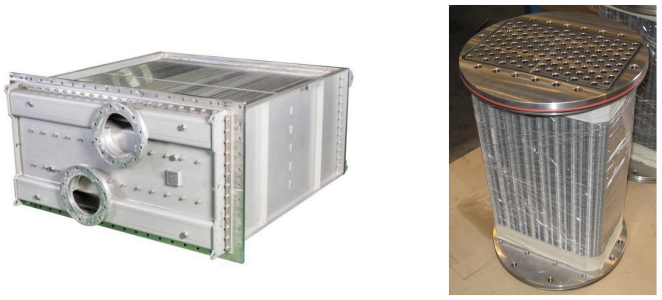

(a) (b)

FIGURE 6.1: Examples of exhaust gas recovery system (a), and compressor cooling system (b) [Ves, 2017]. Both structures contain plates with geometric features such as cut outs and holes. Fins in the top view of the figure on left show a repetitive pattern, typically tens to hundreds of such fins are coupled together by tubes.

often exhibit unusual thermal buckling which needs to be accounted for in design for operation in critical regimes. Here we review several selected research papers on the buckling of perforated and cut plates that are of relevance to the present research.

El-Sawy and Nazmy [2001] applied Finite Element Analysis (FEA) to study the buckling of uniaxially loaded rectangular plates with a single and multiple perforations, and showed that the critical buckling load depends not only on the size, shape and number of perforations but also on their position within the plate and the aspect ratio of the plate. The authors studied plates with all edges simply-supported, with the uniaxial in-plane compressive loading applied at the two opposite edges. Both rectangular and circular cut outs or perforations were considered by the authors. The perforation size and location were changed systematically in a parametric model, which allowed the authors to identify the areas of optimal position of perforations in order to maximise its buckling resistance. This research clearly underlines the importance of parametric modelling of plates with perforations, as the critical buckling load depends considerably on structural parameters.

Moen and Schafer [2009b] studied the bending and buckling of simply supported plates. They derived closed-form expressions to assess the effect of a single or multiple holes on the critical buckling stress of a plate with 3 and 4 edges simply supported. Analytical expressions were validated against a parametric FEA and may serve as an alternative to FEA or as a benchmark for accuracy and convergence of numerical modelling. Especially interesting is their observation that depending on hole size, shape and position, the plate may exhibit some non-classical buckling modes due to local effects near the hole edges. Furthermore, they show that holes of specific configuration may actually damp the development of a buckling mode and even increase the buckling stress compared to a uniform plate. This is a counterintuitive observation since it is typically expected that because holes reduce the amount of material, they should inevitably weaken the structure.

Cheng and Zhao [2010] were driven by the practical need to understand buckling of perforated plates with slotted holes that are used in bridge pylons. They considered a section of the pylon wall between stiffeners which contains a slotted hole and modelled it as a rectangular simply supported plate with a hole compressed by in-plane loading. The authors applied FEA to compute

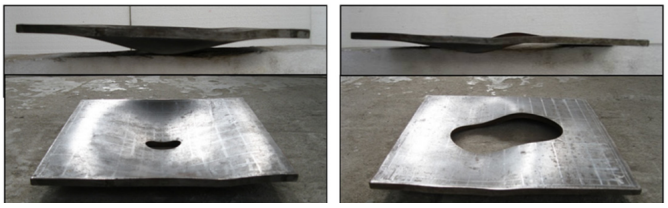

FIGURE 6.2: Classical lowest buckling mode of a simply supported plate with a relatively small hole (left) and the "s"-like buckling mode with a line of inflexion for a plate with a relatively large hole (right). The photos are adapted from [Cheng and Zhao, 2010].

the buckling stress and the buckling modes of perforated plates with, and without, stiffeners in the elastoplastic regime. They also performed real-life experiments on such structures. Cheng and Zhao [2010] reported that depending on the plate aspect ratio and the size of the hole, the plate exhibits several scenarios of dramatically different buckling behaviour. Some of the reported buckling modes are shown in Fig. 6.2. The authors attribute such behaviour to an interplay between the global buckling that unfolds following classical sinusoidal solution for a plate and a local buckling near the hole edges. The local buckling was attributed to the effect of stress concentration at the corners and edges of the hole.

Particularly interesting is the case of a plate featuring multiple periodically arranged circular holes such as the one studied by Scheperboer et al. [2016]. The hole arrangements studied by the authors are shown in Fig. 6.3.

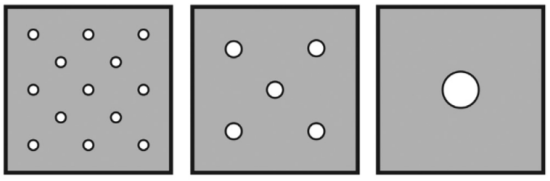

FIGURE 6.3: Three different perforation patterns studied by Scheperboer et al. [2016].

Scheperboer et al. [2016] performed a parametric study by varying the number and the size of the holes as well as plate slenderness. The analysis revealed that a plate with multiple holes generally has smaller resistance than the plate with a single hole. Furthermore, the increase in the number of holes beyond 5 does not affect the plate resistance much. Plates with a single hole were found to be not sensitive to hole size in the range between 10% and 30%.

Another practical context for buckling of plates with geometrical features, similar to those considered here, is the thermal stability of fire doors. Fire doors act as a barrier that prevents a fire from spreading by limiting oxygen influx from outside as well as being a non-flammable barrier. This poses requirements on the design such as critical temperature endurance, critical buckling temperature, structural capacity, etc. Buckling is induced because of expansion within constrained frames. Each new design of a fire door has to undergo stages of modelling and rigorous testing under operational conditions according to industry standards. In the UK, two standards are referred by most of the research focused on fire doors design, modelling and testing. The older standard which is still sometimes used for research purposes is BS EN 1363-1. The newer standard that currently regulates the testing of fire doors is [BS1, 2014]. Among other guidelines these standards provide time-temperature fire curves which are used to define how the doors are

FIGURE 6.4: A photograph of thermal buckling of two-side fire doors at a post-critical temperature observed in a full-scale experiment according to BS EN 1363-1 standard. The photograph is adapted from [Tabaddor et al., 2009].

thermally loaded with time. These curves are also used by researchers in the modelling of new fire door designs before they get tested.

Since the testing of fire doors is a complex and expensive process, taking significant time and resources, computational modelling of new fire door designs is essential to narrow down the scope of the experiments and come up with the optimal structural parameters of the doors before actual testing takes place. Therefore, considerable research is dedicated to establishing the most reliable modelling techniques.

Tabaddor et al. [2009] applied FEA to study the thermal and mechanical response of typical two-sided steel fire doors subjected to a standard fire test. They report that a transient thermal analysis is needed to accurately model heat conditions of the fire doors while non-linear steady-state structural analysis had to be performed to account for the structural response of the fire doors during the test including thermal buckling. The authors also performed physical testing of fire doors and report good agreement between modelling and testing results. In their experiment, the door started bulging towards the fire within the first few minutes of the test and exhibited a visually observed buckling mode after around 1 hour of testing. A photograph of the buckled shape of the fire door after 1 hour of testing when the external temperature reached above 800°C is adapted from Tabaddor et al. [2009] and is shown in Fig. 6.4.

Lai and Lin [2017] studied the fire-resistance of elevator landing doors by performing direct fire tests as well as numerical simulation. The main design difference between the standard fire doors and elevator fire doors is that in the latter the two halves are not coupled in the middle and open by sliding sideways. Therefore, the fire doors of an elevator may be regarded as two independent plates. The left plate is fixed at three edges and free at the right edge while the right plate is fixed at three edges and free at the left edge. The authors identified the optimal thickness of the door, number and shapes of reinforcements to overcome thermal buckling. Interestingly, the results of their simulations suggest that depending on the shape of reinforcements, elevator doors may experience different buckling modes. The two halves either bulge together in a cooperative manner or in the opposite directions, which looks like a competitive (splitting) mode. The two modes are displayed in Fig. 6.5(b). The authors have not studied this behaviour in detail as it was out of the scope of their research, but, seeing the possibility of cooperative versus

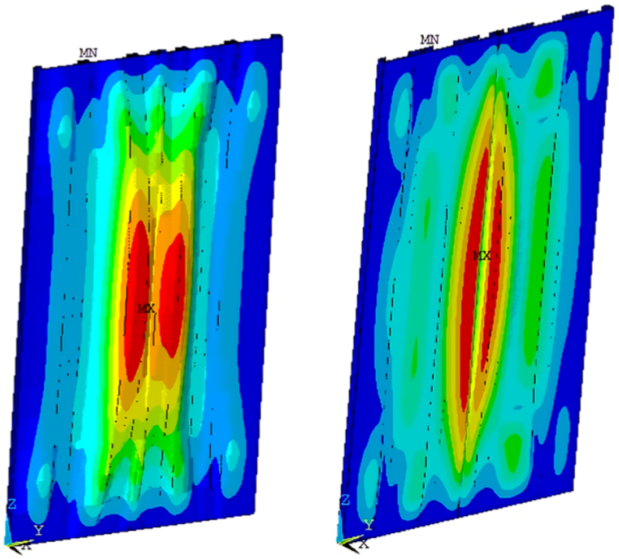

(a) (b)

FIGURE 6.5: Thermal buckling mode of elevator fire doors. (a) Cooperative buckling of the doors with "II"-shaped reinforcement. (b) Competitive (splitting) buckling of elevator fire doors with "I"-shaped reinforcement. The images are from [Lai and Lin, 2017].

splitting buckling of fire doors even from numerical modelling may suggest an interesting physical mechanism at play here.

Bozzolo et al. [2015] studied long sections of sliding fire doors featuring regularly placed flat panels and stiffeners. Such long doors cannot be tested in a laboratory due to their size. Hence, the authors performed computational modelling of the structure. The Von Mises stress distribution computed for such a door is shown in Fig. 6.6. We note in the figure that such a nearly periodic structure may buckle in a manner that resembles those reported in Chapter 5.

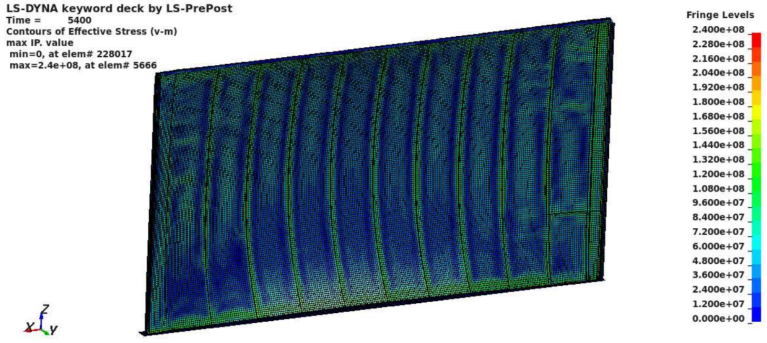

FIGURE 6.6: FEA analysis of thermal buckling of a long section of fire doors with regularly placed stiffeners. The image is adapted from [Bozzolo et al., 2015].

Consider another example of fire doors shown in Fig. 6.7(a) and Fig. 6.7(b). These doors have windows of rectangular shape. The door in Fig. 6.7(a) is a typical household fire door with a window filled with glass. The door in Fig. 6.7(b) is two-sided and has relatively wide cut outs on each side.

We suppose that the buckling mode exhibited by these two doors in the case of thermal loading may have a qualitatively different character purely due to geometrical features such as the size

(a) (b)

FIGURE 6.7: Examples of household fire doors with rectangular windows. (a) A fire door with a single asymmetrically placed window. (b) An example of two-side fire doors with large symmetrically placed windows.

and placement of the cut outs. We have observed in the literature, that typical fire doors with two sides locked to each other buckle in a cooperative (in-phase) manner towards the fire [Tabaddor et al., 2009]. We have also seen an indication that in some cases a two-side elevator sliding door may buckle in a splitting manner with two halves bulging in the opposite directions (out-of-phase) [Lai and Lin, 2017]. We believe that the type of the buckling response of the fire doors as well as of plates with holes and perforations is governed mostly by the geometry of the problem. Hence, in this chapter, we focus on studying elastic stability of a plate with a single rectangular cut out depending on cut out size and plate aspect ratio and on understanding how the geometry of cut plate affects the character of buckling behaviour. While the problem is now two-dimensional, there are similarities with the one-dimensional problem considered in Chapter 3 and Chapter 4.

6.2 Qualitative experimental characterisation of buckling of plates with cut outs

In Chapter 3 and Chapter 4, we reported cooperative, splitting and antisymmetric buckling of a bilayer beam. Consider a plate now with a symmetrically placed rectangular cut, as shown in Fig. 6.8. If the cut out is long and thin, the plate is split by it into two strips, that are coupled at the ends. This resembles a bilayer beam but is rather a 2-D analogy of it. The rich body of literature reviewed in Section 6.1 and the study of the bilayer beam indicates that an interesting buckling behaviour may be expected when such a plate buckles.

We qualitatively characterise the instability behaviour of such a plate experimentally. A schematic diagram of the sample and the boundary condition, as well as loading, are shown in Fig. 6.8. The plate length and width are denoted by L and b respectively, and the plate thickness $\approx$1 mm

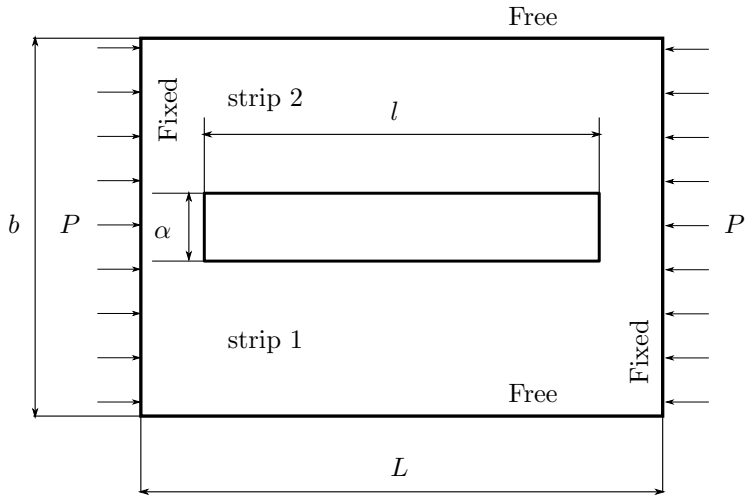

FIGURE 6.8: A view from above of a rectangular plate with a rectangular cut out having two opposite edges fixed from out-of-plane deflection and rotation and the other two edges free. The distributed compressive loading is applied to the fixed edges.

is kept constant for all tests. The cut out has a rectangular shape and is always symmetrically placed within the plate. The cut out width and length are denoted with α and l respectively. The boundary conditions are labelled on the schematic diagram and indicate that two opposite edges of the plate are restrained from out-of-plane displacement and rotation. Their in-plane movement of the right edge is allowed along the direction of the force. The other two edges were kept free. Compressive loading P is applied as indicated by the arrows.

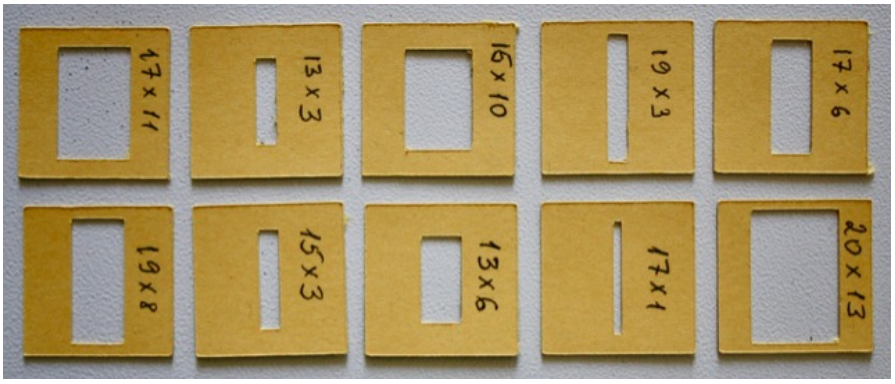

FIGURE 6.9: A photograph of the sample types used in the experiments. The dimensions of the cut outs are shown in mm.

We manufactured a number of samples with cut outs of various sizes. These are shown in Fig. 6.9 and the geometric and material properties are given in Table 6.1. The material was chosen to be a thick cardboard paper. Such a choice was made for several reasons. Firstly, the manufacturing process involved in sample preparation as a result is simple and precise. A thin sheet such as stationery cardboard is also industrially manufactured with excellent tolerance on thickness control. The polymer samples used in testing in Section 3.3 were much cheaper compared to steel, but cutting precise slots in them was still a long and expensive process (it took approximately 4 months to produce all the samples). Here we selected a very soft material. Thus, expensive CNC milling and then testing on the INSTRON machine was not required. Instead, the cardboard samples were cut precisely using a desktop-size card cutter called *Silhouette® Portrait*. The tool

TABLE 6.1: Geometric and material properties of the cardboard samples

Sample type	Cut out size $l \times \alpha$	Plate size $L \times b \times t$	Number of tests
1	17×11 mm	$23 \times 23 \times 1$ mm	5
2	13×3 mm	$23 \times 23 \times 1$ mm	5
3	16×10 mm	$23 \times 23 \times 1$ mm	5
4	19×3 mm	$23 \times 23 \times 1$ mm	5
5	17×6 mm	$23 \times 23 \times 1$ mm	5
6	19×8 mm	$23 \times 23 \times 1$ mm	5
7	15×3 mm	$23 \times 23 \times 1$ mm	5
8	13×6 mm	$23 \times 23 \times 1$ mm	5
9	17×1 mm	$23 \times 23 \times 1$ mm	5
10	20×13 mm	$23 \times 23 \times 1$ mm	5
Modulus of Elasticity $E = 2 \times 10^7$ MPa. Poisson ratio $\nu = 0.3$			

is operated by CAD software and the cutting precision is up to 0.1 mm which is even better than some CNC milling. Using such a cutter, we produced several dozens of precisely cut cardboard samples in a few days.

We used a DEBEN MICROTEST tensile testing machine with the maximum loading capacity of 200 N. The whole test set-up with the cutter, the testing machine as well as a PC occupied a small table and was very convenient to work with, in contrast to INSTRON machine. The sample material cost, manufacturing cost and testing cost as well as time were kept to a minimum this way. The experimental set-up consisting of a *Silhouette® Portrait* cutter, a DEBEN MICROTEST tensile testing machine and a PC is displayed in the photograph in Fig. 6.10 (a). A zoomed view of a tensile testing machine with a measurement processing unit in the background is shown in Fig. 6.10 (b).

(a) (b)

FIGURE 6.10: An experimental setup for testing a plate with a single cut out. (a) *Silhouette® Portrait* electronic cutting tool, DEBEN MICROTEST testing machine and a personal computer. (b) The view of the DEBEN MICROTEST machine.

The experimental study presented here consists of the following steps.

1. A CAD drawing was made for each sample.

2. The *Silhouette® Portrait* electronic cutting tool was used to cut a plate out of a single sheet of cardboard paper. Then, a rectangular cut out of prescribed width and length was made in each sample.

3. The sample was positioned and fixed between the grips of the testing machine and compressed.

4. The compression was controlled by displacement and the loading speed of test was initiated with the magnitude of 1 mm/min. The maximum compressive displacement was set to 5 mm. The visually observable mode appeared within the first 1 mm to 2 mm.

5. During the test, load-displacement values were automatically recorded for every 0.01 mm of displacement.

6. Several photographs of each observed mode were taken.

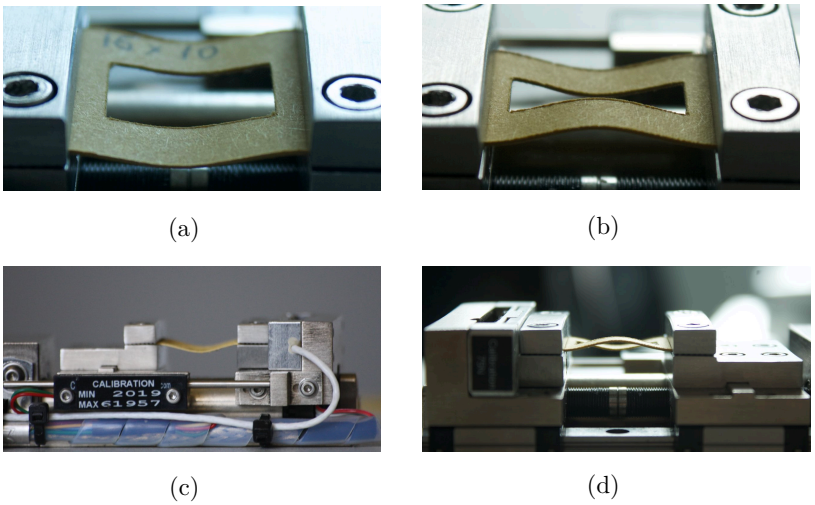

FIGURE 6.11: Experimentally observed buckling of a plate with cut out. (a) Plan view of the in-phase buckling mode. (b) Plan view of the out-of-phase buckling mode. (c) Edge view of the in-phase buckling mode. (d) Edge view of the out-of-phase buckling mode.

The compression tests show that plates with the same dimensions buckle differently depending on the size of the cut out. We observed two buckling types in this experiment. An in-phase also designated as cooperative buckling and an out-of-phase, previously called the splitting buckling mode as shown in Fig. 6.11 are exhibited by the structure.

Further, we call the two parts of the plate on both sides of the cut out left strip or Strip 1 and right strip or Strip 2. These are shown in Fig. 6.8. The region of the plate between the strips is called the *Web region*, or just *Web*. Thus, experimentally observed in-phase buckling mode is characterised by both strips exhibiting out-of-plane displacement in the same direction i.e. cooperatively. In contrast, the out-of-phase buckling is characterised by the opposite sign out-of-plane displacement of the strips. The Web material simply bends in in-phase buckling and exhibits a more complex shape in the out-of-phase buckling as will be discussed further.

6.3 Analytically obtained stability maps

Consider a schematic diagram of the in-phase buckling mode exhibited by the plate in the experiment as shown in Fig. 6.12 as well as a schematic diagram of the out-of-phase buckling mode displayed in Fig. 6.13.

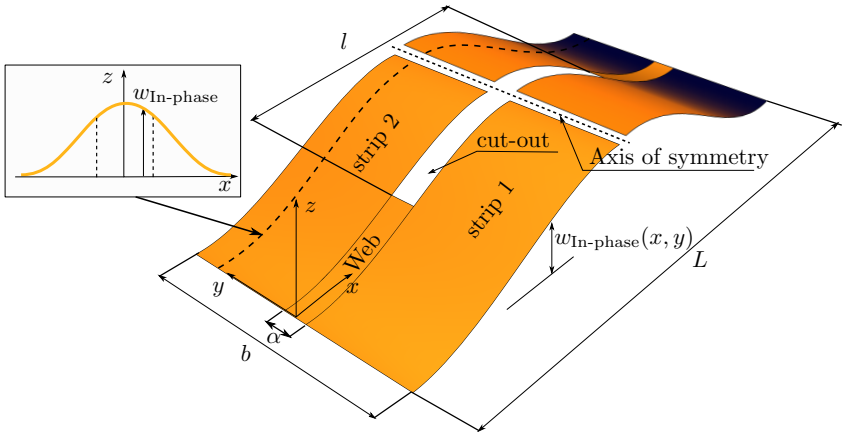

FIGURE 6.12: A schematic representation of the cooperative buckling mode exhibited by a plate with a rectangular cut out

We introduce a reference coordinate system with the $x-$axis parallel to the plate length, $y-$axis parallel to the plate width and the $z-$axis perpendicular to the plate. We also separate the plate into three rectangular regions. e.g., Strip 1, Strip 2 and a Web region for the ease of analysis. We simplify our analysis further by considering only half of the plate length-wise due to the symmetry indicated in Fig. 6.12 and Fig. 6.13.

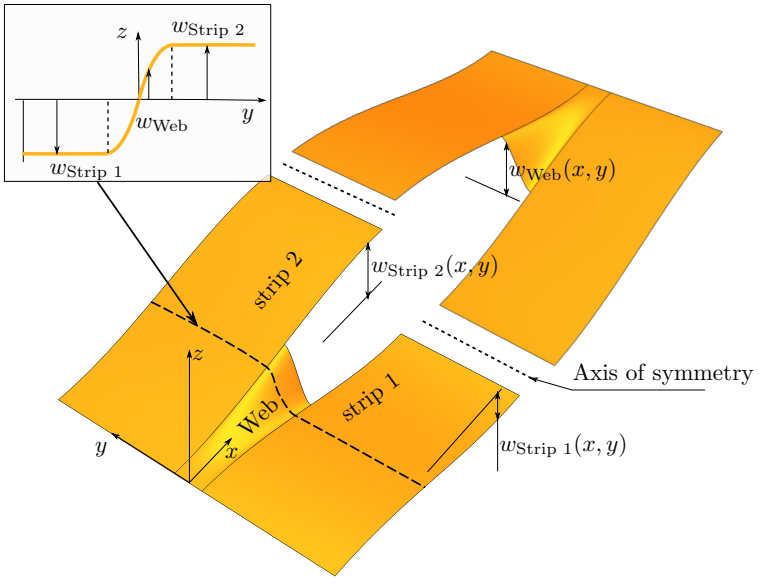

FIGURE 6.13: A schematic representation of the splitting buckling mode exhibited by a plate with a rectangular cut out

Let us have a closer look at both modes in Fig. 6.12 and Fig. 6.13. We can write the displacement field of the plate as a function $w(x, y)$, where x-direction is length-wise and y-direction is width-wise. In the in-phase mode (see Fig. 6.12), the y-component of displacement is constant due to cylindrical bending. This is also supported experimentally as seen in Fig. 6.11 (a),(c). If we

denote the in-phase buckling displacement perpendicular to the plane of the plate as $w_{\text{In-phase}}$, we can write the displacement function as $w_{\text{In-phase}}(x, y) = q_{\text{In-phase}}F(x)$, where $q_{\text{In-phase}}$ is the displacement amplitude, which can be treated as a generalised coordinate, and $F(x)$ is a shape function that depends on x and constant in y. Here, we assumed that the shape function is valid for the entire plate for the case of the in-phase buckling.

In the case of out-of-phase buckling, the mode shape should be a function of x and y (see Fig. 6.13). Strip 1 and Strip 2 have displacements of opposite signs and the Web has a displacement that continuously varies along the y-axis. Note, that this is also supported by experimental observations as shown in Fig. 6.11 (b),(d). We can write the global displacement function for the entire plate or to define it in a piecewise manner, each piece is described by a different function. Note, that we can represent the continuous displacement field in a piecewise manner as long as displacement and rotation between the pieces is matched. This also allows us to integrate pieces separately when calculating the total potential energy of the plate.

The variation of the displacement in the y direction within the strips is small for out-of-phase buckling. To visualise this, we plotted the displacement of the plate along an arbitrary through-the-width slice as indicated with the dashed line in the schematic diagram in Fig. 6.13 (see subplot). We observe that the displacement function along the y-axis has three regions of distinctive character. These are shown within the subplot in Fig. 6.13. The first region, indicated by $w_{\text{Strip 1}}$, corresponds to Strip 1. The displacement here is assumed to be constant in y. The second region, indicated with w_{Web}, corresponds to the Web. Here, displacement varies with y in "s" like manner. Finally, the third region, indicated by $w_{\text{Strip 2}}$, corresponds to Strip 2. Here, displacement has almost no variation with y. Thus, we consider Strip 1, Web and Strip 2 independently and describe them with the appropriate assumed mode functions, that are matched at the boundaries.

We introduce the following non-dimensional quantities. Plate aspect ratio is $A = b/L$, the normalised cut length is $\bar{l}= l/L$ and the normalised cut width is $\bar{\alpha}= \alpha/b$. The non-dimensional coordinate along the x-axis is $\xi = 2x/L$, $0 \leq \xi \leq 1$ for $0 \leq x \leq L/2$. The non-dimensional coordinate along the y-axis for the Web region is $\zeta = (y + \alpha/2)/\alpha$. Thus, $0 \leq \zeta \leq 1$ for $-\alpha/2 \leq y \leq \alpha/2$.

For in-phase buckling, the shape function for the entire plate is specified in terms of Hermite cubic polynomial along the x-direction and a constant along the y-direction. In the non-dimensional coordinates $w_1(x, y) \rightarrow w_1(\xi, \zeta)$, so that

$$w_{\text{In-phase}}(\xi, \zeta) = q\left(-2\xi^3 + 3\xi^2\right), \tag{6.1}$$

where ζ is a constant here.

Here q is the generalised coordinate of an entire plate. Note, that the shape function satisfies kinematic boundary conditions for the whole plate since $w_{\text{In-phase}}(0, \zeta) = w'_{\text{In-phase}}(0, \zeta) = 0$ and $w'_{\text{In-phase}}(1, \zeta) = 0$.

In the case of out-of-phase buckling, the three regions are considered, i.e., Strip 1, Strip 2 and Web region. Strips 1 and 2 exhibit almost no variation of buckling mode along the y-axis.

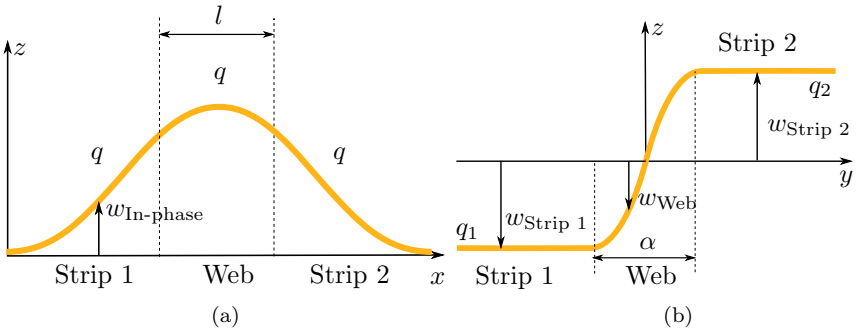

FIGURE 6.14: Buckling shapes of the plate along x and y-axis. (a) The shape of both modes of the plate along the x-axis for Strip 1 and 2. (b) The shape of the out-of-phase buckling of the plate along the y-axis. The non-dimensional coordinates ξ, ζ are replaced with x and y here.

Therefore, we assume the mode shape of each strip to be only ξ dependent

$$w_{\text{Strip i}}(\xi, \zeta) = q_i \left(-2\xi^3 + 3\xi^2\right), \tag{6.2}$$

where $i = 1$ for Strip 1 and $i = 2$ for Strip 2.

It is apparent from Fig. 6.13 and the through-the-width slice in Fig. 6.14(b) that the shape function describing the deformed profile of the "Web" part depends on both x and y coordinates in the out-of-phase buckling. Furthermore, the assumed shape must satisfy the boundary conditions of the plate and the continuity conditions between the Web and each strip. At the same time, it would be ideal to have as few as possible generalised coordinates in the assumed shape function. Therefore, we seek the shape function in the form of a product of a previously defined Hermite cubic along x, and a function along the y-axis, allowing for the rapid transition from q_1 – buckling amplitude of Strip 1 to q_2 – buckling amplitude of Strip 2 as shown in Fig. 6.14(b). The Hermite cubic in x readily satisfies the boundary conditions for the Web part – zero displacement and rotation at $x = 0$ or $\xi = 0$ as can be seen from Equation (6.2). The shape function of the Web must also satisfy the continuity conditions – the displacement and rotation between the Web and the strips must match at $y = \pm\alpha/2$ or $\zeta = 0$ and $\zeta = 1$.

Perhaps the most common function that shows a rapid transition between two levels is the Heaviside step function. However, it is discontinuous, and it does not account for the finite but high local curvatures between Web region and strips as shown in Fig. 6.14(b). Therefore, we construct a continuous counterpart of the Heaviside step function. There exists a class of "S" shape functions such as the logistic function, the sigmoid function, the hyperbolic tangent, etc., that may satisfy our needs. In Fig. 6.15 we provide the plots of the several common "S-shaped" curves for comparison.

The logistic function is given by the expression $A/\left[1 + \exp\left(-k(x - x_0)\right)\right]$, where A specifies the maximum value of the curve, k defines steepness and x_0 defines the centre point. In Fig. 6.15 the logistic function is shifted vertically by -0.5 to account for negative amplitudes to the left and positive amplitudes to the right with $L = 1$, $k = 4$ and $x_0 = 0$. The shifted and scaled version of the logistic function may be represented by the hyperbolic tangent such as $f(x) = \tanh(4x)$ as shown in Fig. 6.15. Here factor 4 is used to artificially increase the steepness of the tangent

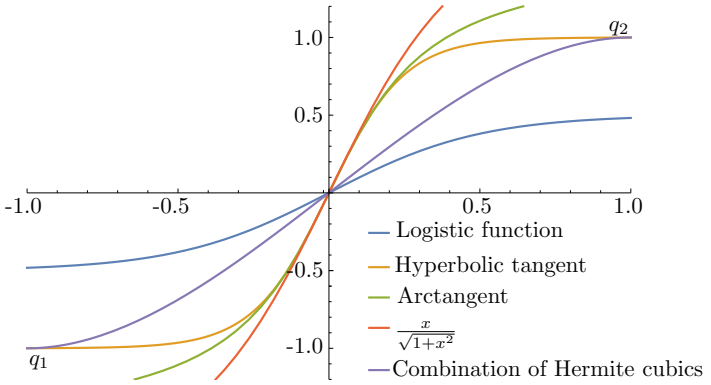

FIGURE 6.15: Plots of several continuous "S" like functions in the range of argument between -1 and 1 given here for comparison.

curve and to better account for local curvatures in the buckling mode. Similarly, we may use $\arctan(4x)$ to get an "S" like curve similar to the logistic function and hyperbolic tangent.

These functions are good candidates for the shape function along the $y-$axis. By introducing a single generalised coordinate which defines the amplitude and by keeping the steepness of the curve as a parameter to tweak, we can write a relatively accurate expression for the buckled shape. However, when the shape function (written as a product of $w_{\text{In-phase}}$ in x and $q\tanh(y/\alpha)$ in y) was used to try to evaluate an integral for the strain energy of the Web (presented further) it resulted in a complex expression. Substituting the shape function as a logistic function or as arctangent did not result in the simpler integration either.

A simpler solution may be given by using polynomial as the assumed shape function in the y-direction. As cubic polynomials are much easier to integrate analytically, we decided to compromise on the steepness variable in favour of simplicity. Therefore, we define the functional form of the Web displacement as a product of $w_{\text{In-phase}}$ in x and a combination of the two Hermite cubics in y. Such a Hermite cubic is plotted in Fig. 6.15 for comparison. In the non-dimensional coordinates ξ and ζ such a shape function reads

$$w_{\text{Web}} = \left[q_1\left(2\zeta^3 - 3\zeta^2 + 1\right) + q_2\left(-2\zeta^3 + 3\zeta^2\right)\right]\left(-2\xi^3 + 3\xi^2\right), \tag{6.3}$$

where w_{Web} is shown in Fig. 6.13 as the "Web" part in the dimensional $x-y$ coordinates, noting that $\xi = 2x/L$ and $\zeta = (y+\alpha/2)/\alpha$. The factor in square brackets represents the "S" shape in the y direction and the factor in round brackets represents the shape in the x direction. Note, that the Web part does not have its own generalised coordinate. Instead, it simply interpolates between the two strips which greatly simplifies further derivations. Also, the use of such functional form readily satisfies the continuity conditions between the Web and the strips. When $y = -\alpha/2$, Equation (6.3) matches with the displacement of the Strip 1, as $w_{\text{Web}} = q_1\left(-2\xi^3 + 3\xi^2\right)$. At the same time, when $y = \alpha/2$, Equation (6.3) matches with the displacement of the Strip 2, as $w_{\text{Web}} = q_2\left(-2\xi^3 + 3\xi^2\right)$. The slopes of w_{Web} are also zero at the boundaries of the Web region ($\zeta = 0$ and $\zeta = 1$).

A detailed diagram of the left half of the plate ($0 \leq x \leq L/2$) is schematically drawn in Fig. 6.16. We assume that due to the presence of the cut out, the effect of the compressive loading P on the Web region (grey rectangle) is negligibly small. A compressive loading per unit length

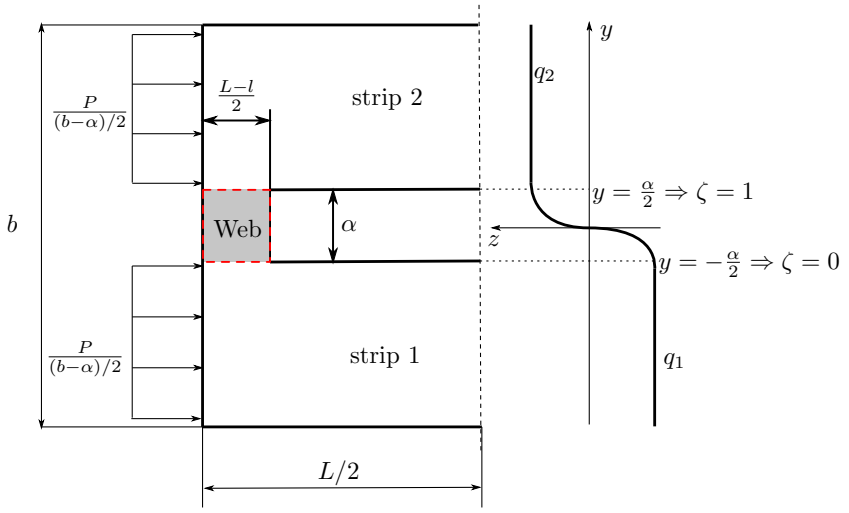

FIGURE 6.16: A schematic representation of the left half of the plate. The Web part is indicated with a grey rectangle. The mode shape of the plate along y-direction in the case of out-of-phase buckling is depicted in $y - z$ coordinates.

$N_x = P/((b-\alpha)/2)$ is applied to each of the strips. This assumption is adopted based on the other studies of plates with rectangular cut outs such as Moen and Schafer [2009b].

The condition for equilibrium is given by the principle of minimum total potential energy. We minimise the total potential energy so that $\delta\Pi = 0$, where $\Pi = U + V$ is the sum of the strain energy U and the potential energy of external loading V. For a plate

$$U = \frac{D}{2} \iint_{\Omega} \left[(w_{,xx} + w_{,yy})^2 - 2(1-\nu) \left(w_{,xx} w_{,yy} - (w_{,xy})^2 \right) \right] dy\, dx, \tag{6.4}$$

and

$$V = -\frac{P}{2} \iint_{\Omega} (w_{,x})^2 \, dy\, dx, \tag{6.5}$$

if uniaxial compression along the x-axis is considered. The factor D in Equation (6.4) is the flexural rigidity of the plate, $D = Eh^3/12(1-\nu^2)$, where ν is Poisson ratio and h is thickness. The rectangular domain Ω is specified within the plate.

The total potential energy in buckling is a quadratic form in generalised coordinates. Therefore, taking the variation of the quantity with respect to the generalised coordinates q_i results in a system of linear equations $\partial\Pi/\partial q_i = 0$. The detailed derivations of the expressions for U and V for in-phase and out-of-phase buckling of the plate with a cut out are given in Appendix B.

The energies U and V of the plate with a cut out can be calculated relative to the strain energy and the work potential of a uniform plate in cylindrical bending. The energies for a single strip are

$$U_{\text{Strip}} = \frac{96AD}{L^2} \left(\frac{1}{2} (1 - \bar{\alpha})\, q_i^2 \right), \tag{6.6}$$

$$V_{\text{Strip}} = \frac{12}{5L} \left(\frac{1}{2} q_i^2 \right), \tag{6.7}$$

where q_i is the generalised coordinate and $i = 1, 2$ corresponds to Strip 1 and Strip 2 respectively. Note that a one-mode approximation inherent in Equation (6.2) leads to a simple expression for each strip above. The strain energy of the Web part is

$$U_{\text{Web}} = \frac{96AD}{L^2}\Bigg(\frac{\bar{\alpha}(-4\bar{l}^3 + 6\bar{l}^2 - 3\bar{l} + 1)}{35}\left[13q_1^2 + 9q_1q_2 + 13q_2^2\right] + \\ \frac{(\bar{l}-1)^3}{2800A^4\bar{\alpha}^3}\Big(168A^2\bar{\alpha}^2\left((2\bar{l}^2 + \bar{l})(5\nu - 3) - 1\right) - 5(\bar{l}-1)^2(20\bar{l}^2 + 30\bar{l} + 13)\Big)\left[q_1 - q_2\right]^2\Bigg), \quad (6.8)$$

which is also a quadratic form in q_1 and q_2 and depends on both governing parameters $\bar{l}$ and $\bar{\alpha}$ and the plate aspect ratio $A = b/L$. The coupling between the generalised coordinates q_1 and q_2 is manifested here by the non-zero q_1q_2 term.

The strain energy of the plate is the sum of the strain energies of two strips and the strain energy of the Web

$$U = 2U_{\text{Strip}} + U_{\text{Web}}. \quad (6.9)$$

The work potential of the plate structure with a cut out is the sum of the work potentials of each strip, given by

$$V = 2V_{\text{Strip}}. \quad (6.10)$$

Taking derivatives of $U + V$ with respect to q_1 and q_2 in turn, and equating them to zero, we obtain a set of homogeneous linear algebraic equations in terms of the generalised coordinates q_1 and q_2. They can be organised in the form of a generalised eigenvalue problem as

$$\mathbf{Kq} = P\mathbf{K}_g\mathbf{q}, \quad (6.11)$$

where $\mathbf{K}$ is the symmetric positive-definite parameter-dependent 2×2 stiffness matrix. The geometric stiffness matrix $\mathbf{K}_g$ is diagonal because of Equation (6.7). Here P is the dimensional buckling load which is then scaled by $P_{cr} = 4\pi^2Db/L^2$ or $P_{cr} \approx 40AD/L$ to define a critical buckling load relative to the buckling load of a uniform plate in buckling assuming cylindrical bending $\bar{P} = P/P_{cr}$.

The eigenvalue problem takes the form

$$\left(\begin{bmatrix} K_{11} & K_{12} \\ K_{21} & K_{22} \end{bmatrix} + \begin{bmatrix} k & -k \\ -k & k \end{bmatrix}\right)\begin{Bmatrix} q_1 \\ q_2 \end{Bmatrix} = P\begin{Bmatrix} q_1 \\ q_2 \end{Bmatrix}. \quad (6.12)$$

Here K_{11} and K_{22} arise from the q_1^2 and q_2^2 terms within U_{Strip}, V_{Strip} and U_{Web}. The off-diagoinal term K_{12} arises from the first term in U_{Web} that containts q_1q_2 product. The second matrix above arises from the term $(q_1 - q_2)^2$ within U_{Web}. All the terms K_{11}, K_{12} and K_{22} and k depend on the structural parameters $\bar{l}$, $\bar{\alpha}$, A. The matrices $\boldsymbol{K}$ and $\boldsymbol{K}_g$ from Equation (6.11) are shown in details in Appendix B.

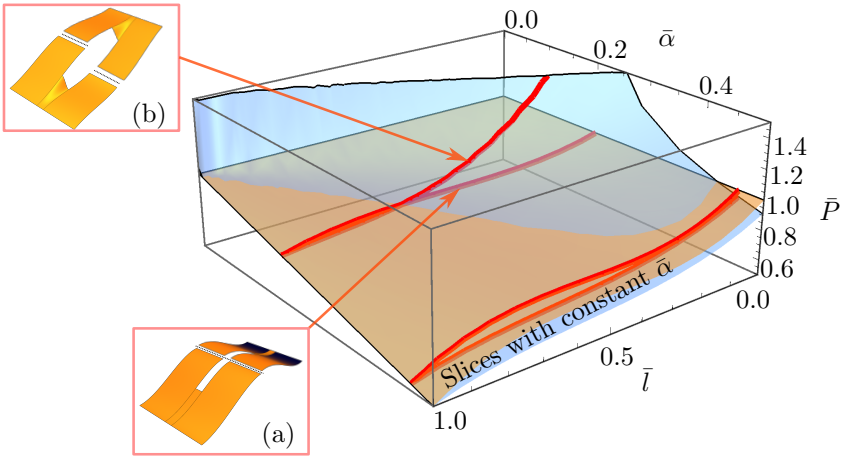

FIGURE 6.17: A plot of $\bar{P}_1$ (orange surface) and $\bar{P}_2$ (blue surface) as functions of $\bar{l}$ and $\bar{\alpha}$ for a fixed Poisson ratio $\nu = 0.3$. The red curves show the slices of the surfaces by planes of constant $\bar{\alpha}$. The schematic representation of the in-phase mode is shown in (a) and the schematic representation of the out-of-phase mode is shown in (b).

We calculate the eigenvalues of Equation (6.11) and scale them by P_{cr} and write the non-dimensional forms for the critical buckling loads

$$\bar{P}_1 = 1 - \bar{\alpha}\left(3\bar{l} - 6\bar{l}^2 + 4\bar{l}^3\right), \tag{6.13}$$

$$\bar{P}_2 = 1 - \frac{\bar{\alpha}\left(18 + 51\bar{l} - 102\bar{l}^2 + 68\bar{l}^3\right)}{35} + \frac{6\left(1-\bar{l}\right)^3\left(2\bar{l}^2(5\nu-3) + \bar{l}(5\nu-3) - 1\right)}{25A^2\bar{\alpha}} + \frac{\left(1-\bar{l}\right)^5\left(13 + 30\bar{l} + 20\bar{l}^2\right)}{140A^4\bar{\alpha}^3}, \tag{6.14}$$

which are functions of the relative cut out length $\bar{l}$, relative cut out width $\bar{\alpha}$, plate aspect ratio $A = b/L$ and Poisson ratio ν. These expressions are plotted as functions of $\bar{l}$ and $\bar{\alpha}$ for a fixed Poisson ratio $\nu = 0.3$ and a fixed plate aspect ratio $A = b/L = 2$ in Fig. 6.17. The relative position of the surfaces of $\bar{P}_1$ and $\bar{P}_2$ generally depends on the Poisson ratio of the material. For now, we assume $\nu = 0.3$ and discuss the effect of Poisson ratio on the critical buckling loads further on in this chapter. The specific choice of the aspect ratio is dictated by the constraints on the samples that were tested in the experiment to validate the behaviour as discussed further. The $\bar{l}$–$\bar{\alpha}$ plane in the figure spans values of $0 \leq \bar{l} \leq 1$ and $0 \leq \bar{\alpha} \leq 0.5$. Here, $\bar{l}$= 0 means the cut is vanishingly short and $\bar{l}$= 1 means the cut splits the plate into two halves. At the same time, $\bar{\alpha}$= 0 means the cut is vanishingly thin and $\bar{\alpha}$= 0.5 means the cut accounts for the half of the plate width. At the same time, each combination of the values of $\bar{l}$ and $\bar{\alpha}$ is substituted into Equation (6.13) and Equation (6.14) to obtain values of $\bar{P}_1$ and $\bar{P}_2$ for each configuration of the plate. These values are plotted along the vertical axis $\bar{P}$ and correspond to the non-dimensional lowest two critical buckling loads. The orange surface in Fig. 6.17 corresponds to $\bar{P}_1$ associated with $\mathbf{q}_1$ (in-phase mode) and the blue surface corresponds to $\bar{P}_2$ associated with $\mathbf{q}_2$ (out-of-phase mode).

Consider the surfaces in Fig. 6.17 in detail. The limiting cases $(\bar{l}, \bar{\alpha}) = (\bar{l}, 0)$ and $(\bar{l}, \bar{\alpha}) = (0, \bar{\alpha})$ correspond to a plate with an infinitesimally small cut out, for which the cooperative buckling is the fundamental (experimentally observable) mode and the buckling load is the same as for the uniform plate $\bar{P}_1 = 1$ (orange surface). However, as we move along the trajectory on the

orange surface specified by $(\bar{l}, \bar{\alpha}) = (0, \bar{\alpha})$, we see that such $\bar{\alpha}$ exists for which the trajectory of $\bar{P}_2$ intersects the one for $\bar{P}_1$ and out-of-phase buckling becomes a fundamental response. Looking at the entire range of parameters, we observe that the orange surface linearly descends with $\bar{\alpha}$ starting from $\bar{P}$= 1 for $(\bar{l}, \bar{\alpha}) = (\bar{l}, 0)$. This indicates that the cooperative buckling linearly "softens" with the cut out width. The slice of the orange surface by the planes of constant $\bar{\alpha}$ shown with the red curves in Fig. 6.17 also reveals softening of the cooperative buckling response with $\bar{l}$ but in a non-linear "wavy" manner which is characterised by the cubic polynomial in $\bar{l}$ in Equation (6.13).

However, we observe that $\bar{P}_2$ (blue surface) rapidly descends with $\bar{l}$ and $\bar{\alpha}$ indicating that the out-of-phase buckling softens dramatically and, eventually, becomes the fundamental response as the buckling load surfaces cross over some spatial curve. Note that U_{Strip} in Equation (6.6) incorporates the strain energy due to the cylindrical bending only. At the same time, U_{Web} in Equation (6.8) contains both the energy due to cylindrical bending and the energy due to twist. The first dominates when $q_1 = q_2$ as happens in in-phase buckling, the letter dominates when $q_1 \neq q_2$ as in out-of-phase buckling. Also note that the work potentials are the same for in-phase and out-of-phase buckling. Taking this into account, we come to the conclusion that the difference between bending and twist characterises the difference between the in-phase and the out-of-phase buckling of the plate. For small cut outs pure bending is much softer than twist in-phase buckling takes place. In contrast, when the twist becomes softer than pure bending, the out-of-phase buckling occurs. Finally, in the case when the twist and the pure bending are equal, the buckling loads become equal defining the position of the phase boundary.

The position of the phase boundary can be calculated by solving the equation $\bar{P}_1 = \bar{P}_2$. Close examination of the expressions of $\bar{P}_1$ and $\bar{P}_2$ given by Equation (6.13) and by Equation (6.14) reveals that $\bar{P}_1 - \bar{P}_2 = 0$ is quadratic in $\bar{\alpha}^2$ and 5-th power in $\bar{l}$. Hence, we seek the solution in the form $\bar{\alpha}^2 = \pm f(\bar{l}, \nu, A)$, where f is some function of the structural parameters. Thus, we have one negative branch leading to complex values of $\bar{\alpha}$ and one positive branch which results in the expression

$$\bar{l} - 1 = 0 \implies \bar{l} = 1, \tag{6.15}$$

which is true for all α, and in the second expression

$$A\bar{\alpha}\sqrt{G(\bar{l}, \nu)} - \frac{1}{2\sqrt{15}} = 0, \tag{6.16}$$

which is true for real values of $\bar{\alpha}$ and $\bar{l}$ as the expression $G(\bar{l}, \nu)$ under the radical is positive. The functional form of $G(\bar{l}, \nu)$ is

$$G(\bar{l}, \nu) = \frac{1 - 2\bar{l} + 4\bar{l}^2}{14 + \bar{l}Q_0 + 28\bar{l}^2 Q_1 + \sqrt{2}\sqrt{8(\bar{l}^4 + \bar{l}^3)Q_2 + \bar{l}^2 Q_3 + \bar{l}Q_4 + 423}}, \tag{6.17}$$

where factors Q_0-Q_4 depend on the Poisson ratio only and read as follows

$$\begin{aligned} &Q_0 = 43 - 70\nu, Q_1 = 3 - 5\nu, Q_2 = 1225\nu^2 - 1470\nu + 691, \\ &Q_3 = 2450\nu^2 - 4900\nu + 2358, Q_4 = 688 - 980\nu. \end{aligned} \tag{6.18}$$

The first solution, which is given by Equation (6.15)), corresponds to the degeneracy of the two buckling loads when the cut length is the same as the plate length. Thus, the cut out separates

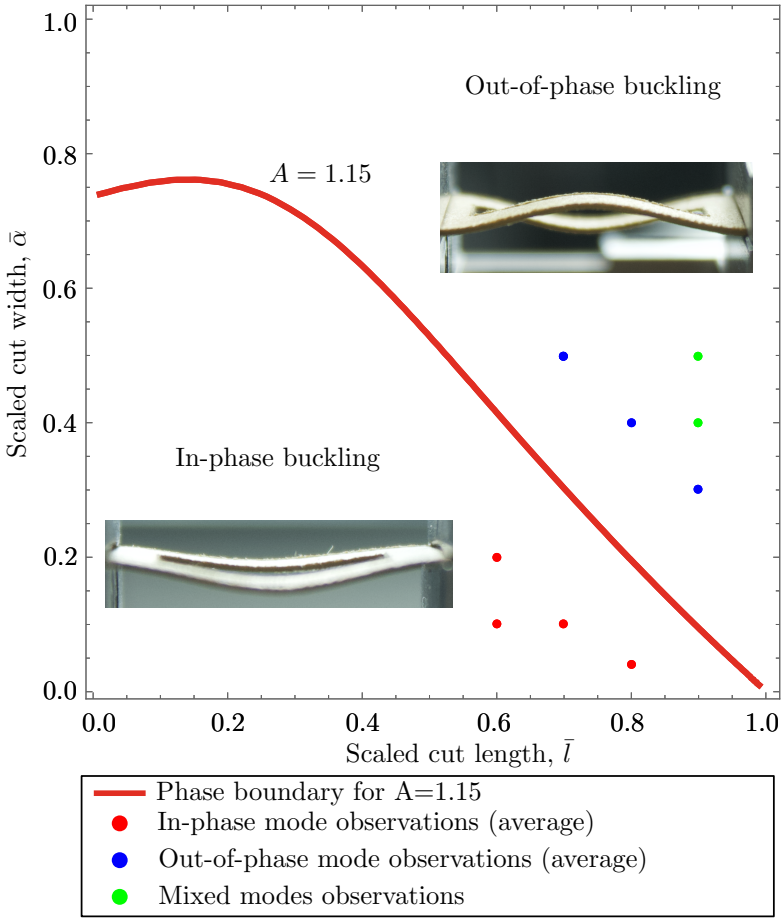

FIGURE 6.18: Phase boundary between the in-phase and the out-of-phase buckling for the aspect ratio $A = 1.15$ and $\nu = 0.3$ plotted in $\bar{l}$–$\bar{\alpha}$ plane. The red dots indicate in-phase buckling observed experimentally. The blue dots indicate out-of-phase buckling observed experimentally. The green dots indicate mixed modes observed experimentally.

the plate in two strips which are decoupled. This corresponds to the merging of the two surfaces in Fig. 6.17 along a line $\bar{l} = 1$ for all $\bar{\alpha}$. The second solution, which is given by Equation (6.16) corresponds to the spatial curve of the intersection of the two surfaces in Fig. 6.17

$$\bar{\alpha} = \frac{1 - \bar{l}}{2\sqrt{15}A\sqrt{G(\bar{l}, \nu)}}, \tag{6.19}$$

where $A = b/L$ is the aspect ratio of the plate and $G(\bar{l}, \nu)$ is positive.

In Fig. 6.18 we present the plots of the solutions derived on the $\bar{l}$–$\bar{\alpha}$ plane for the plate aspect ratio $A = 1.15$ and a fixed Poisson ratio $\nu = 0.3$. The photographs in Fig. 6.18 are characteristic of the in-phase buckling region and the out-of-phase buckling region. The plot portrays a phase diagram characterising buckling of a plate with a single rectangular cut out. The red solid curve is the phase boundary between the in-phase and the out-of-phase buckling for the aspect ratio $A = 1.15$ and is a projection of the spatial curve of the intersection of the two surfaces in Fig. 6.17 onto the $\bar{l}$–$\bar{\alpha}$ plane. The dots on the diagram refer to the experimental points. The testing was performed on the samples cut out of a single sheet of cardboard as discussed in Section 6.2. The sample dimensions were selected to comply with the aspect ratios of the plate $A = 1.15$ for which the phase diagram was obtained. The dimensions were also restricted by the maximal distance

between the grips of *MICROTEST* machine. The geometric ratio of the samples correspond to the dots in Fig. 6.18. The parameters of the samples are assembled in Table 6.1. Each sample type was tested five times and the colour of the dots was assigned based on the mode type observed on average. The red dots correspond to the in-phase buckling as shown by the photograph of a respective mode experimentally observed. The blue dots correspond to the out-of-phase mode as reflected by the respective photograph. The green colour dots correspond to samples exhibiting mixed modes. The mixed modes indicate that when multiple tests were carried out on the samples with the same dimensions, some tests showed in-phase buckling while the others showed out-of-phase buckling. This indicates that for these combinations of parameters the behaviour becomes sensitive even to small irregularities in the experimental setup.

Our model yields a sharp phase boundary produced by the crossing of the respective eigenvalue surfaces. This is possible because we assumed the in-phase and the out-of-phase buckling modes independently and evaluate the respective buckling loads independently thus eliminating coupling between the states. Also, the structure was assumed perfectly symmetric. However, if any disorder is introduced, we expect that the buckling loads will not cross over on the phase boundary but experience an avoided crossing behaviour with the respective modes becoming linear combinations of each other similarly as seen in the case of two coupled rigid rods in Section 5.5.

In practice, due to inevitable imperfections and irregularities in structures, the phase boundary is not sharp – a mixture of in-phase and out-of-phase buckling prevailing in the immediate vicinity of the theoretical phase boundary due to the avoided crossing effect. In fact, all the regions of the phase diagram in Fig. 6.18 for which the distance between the eigenvalue surfaces in Fig. 6.17 is of the same order as or smaller than the magnitude of the disorder will likely exhibit mixed buckling scenario. This is evident from the experiments as the green dots in Fig. 6.18 represent structures with mixed buckling. Therefore, when designing plates with cut outs, one should consider which phase in Fig. 6.18 characterises buckling of a structure with the given $\bar{l}$ and $\bar{\alpha}$. However, in addition to that, one should estimate the magnitude of irregularity or disorder and compare it with the separation between the eigenvalue surfaces in a given point of the phase diagram. Surfaces given in Fig. 6.17 may be used to make an informed prediction of the fundamental buckling mode type in addition to the phase diagram. More importantly one should realise that these would be doublets of buckling modes for a two-strip structure. In the future chapters we observe clusters of instability modes for this class of problems. Here this generic information is useful to a practising designer.

In Fig. 6.19 we plot the phase boundaries of the plate with a single cut out calculated using Equation (6.19) for various values of plate aspect ratio A and for the fixed Poisson ratio $\nu = 0.3$. We see that all the phase boundaries have similar shapes. Changing the aspect ratio affects the slope of the curve in $\bar{l}$-$\bar{\alpha}$ coordinates.

We study the boundary on the phase diagram in Fig. 6.18 and in Fig. 6.19 in detail now. It is apparent that the phase boundaries are the straight lines in $\bar{l}$–$\bar{\alpha}$ coordinates for large values of $\bar{l}$ in the parameter plane, except the region of $\bar{l}< 0.2$ for which it becomes non-linear. We can use this observation to come up with an approximate expression for the boundary.

We expand Equation (6.19) in Taylor series around $\bar{l}= 1$ retaining only linear terms

$$\bar{\alpha} = \frac{\sqrt{28 - 42\nu + \sqrt{14}\sqrt{83 - 168\nu + 126\nu^2}}}{6A} \left(1 - \bar{l}\right) + \mathcal{O}\left((\bar{l} - 1)^2\right). \tag{6.20}$$

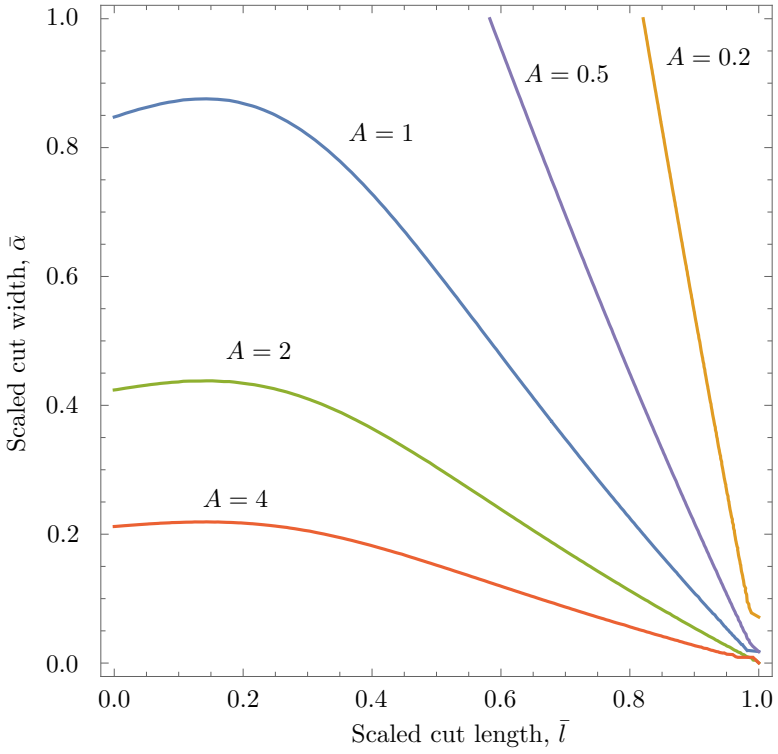

FIGURE 6.19: Phase boundaries in $\bar{l}$-$\bar{\alpha}$ coordinates for various values of plate aspect ratio A and for the fixed value of Poisson ratio $\nu = 0.3$.

Then, the slope of the linearised phase boundary is given by

$$\frac{\sqrt{28 - 42\nu + \sqrt{14}\sqrt{83 - 168\nu + 126\nu^2}}}{6A}, \tag{6.21}$$

which depends on the Poisson ratio of the material ν and the aspect ratio of the plate A. For example,

$$\text{for} \quad \nu = 0.5, \quad \bar{\alpha} \approx \frac{0.88}{A}(1 - \bar{l}), \tag{6.22}$$

$$\text{for} \quad \nu = 0, \quad \bar{\alpha} \approx \frac{1.3}{A}(1 - \bar{l}). \tag{6.23}$$

Thus, the slope of the phase boundary changes between $-0.88/A$ and $-1.3/A$ for Poisson ratio between $\nu = 0$ and $\nu = 0.5$. For the case of standard steel ($\nu = 0.3$), the relation between $\bar{\alpha}$ and $\bar{l}$ has a slope $\approx -1/A$.

$$\bar{\alpha} \approx \frac{1 - \bar{l}}{A}. \tag{6.24}$$

The accuracy of the linear fit can be observed in Fig. 6.20 which shows a comparison between the exact phase boundaries given by Equation (6.19) and the linear approximations are given by Equation (6.24) for $A = 0.5$ (blue solid and dashed lines), $A = 1$ (red solid and dashed lines) and $A = 4$ (green solid and dashed lines). Therefore, Equation (6.19) should be used for a detailed calculation of the phase boundary while the linear function given in Equation (6.24) is good for crude estimation of the location of the phase boundary. Both equations show that one over the aspect ratio of the steel plate is the principal factor which characterises the in-phase and out-of-phase buckling of the plate.

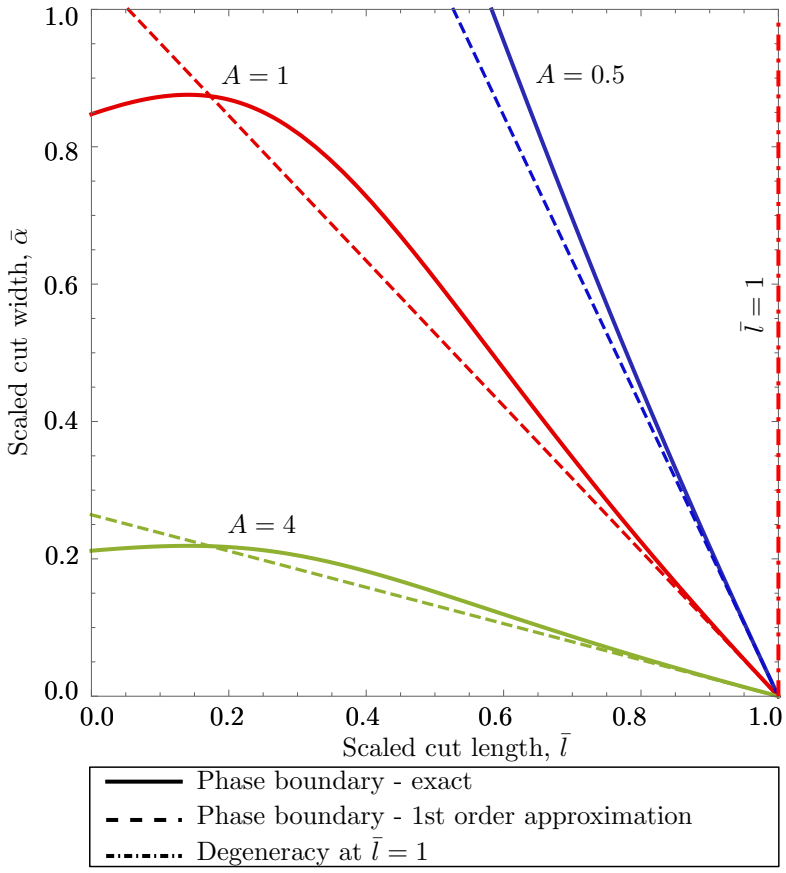

FIGURE 6.20: Comparison between exact phase boundaries (solid lines) and first-order approximation (dashed lines) for several values of plate aspect ratio A. The dashed-dotted line shows the case of critical buckling load degeneracy for $\bar{l}$= 1.

6.4 Classification of computed buckling modes

The experimental investigation of parametric problems is usually limited to a relatively small number of tests performed on samples manufactured for a few fixed combinations of parameter values. In the case of buckling of a plate with a cut out, we have made assumptions about the mode shapes of the plate as well as about the absence of interaction between the modes. While those assumptions were based on experimental observations, they can be further tested against the mode shapes obtained from the finite element analysis (FEA). In our case, FEA proves to be particularly useful as it acts as a virtual lab in which we can run a large number of numerical experiments spanning the vast parameter space within a reasonable time. It is also much easier to mathematically characterise the numerical mode shapes to compare them with the assumed ones than to characterise experimental modes. Therefore, we created a parametric finite element model for the rectangular plate with a cutout (shown in Fig. 6.8) using ABAQUS finite element software package.

6.4.1 Geometry of the model

In computations, we consider the entire domain of the plate in contrast to the left half studied analytically. For all the cases, plate length L is considered fixed as well as plate thickness h,

modulus of elasticity E and Poisson's ratio ν. At the same time, we vary plate width b, cut length l and cut width α for each case. In such a way, each case is uniquely characterised by the two non-dimensional ratios $\bar{l}= l/L$ and $\bar{\alpha} = \alpha/b$, which is similar to the analytical modelling.

In reality, all structures are three-dimensional deformable bodies. However, during modelling, the dimensionality is often reduced by applying assumptions such as plane strain, plane stress, shell, beam, based on mechanics underlying a geometry. In our case, the length and width of the plate are typically much larger (over 10 times) than thickness. This allows us to simplify the three-dimensional equations of elasticity by applying kinematic assumptions inherent in plate theory. The thickness to length ratio $h/L = 0.01$ was kept constant for all cases. Therefore, the buckling behaviour does not qualitatively depend on the plate thickness as it enters the equations as a free multiplier in flexural rigidity $D = Eh^3/12(1-\nu^2)$. In *ABAQUS* such assumption is applied by specifying the plate geometry and using the appropriate finite elements.

6.4.2 Physical properties and boundary conditions

The plate is modelled as a homogeneous shell with a uniform thickness made of linear elastic material with E =2×10^5 MPa and Poisson ratio $\nu = 0.3$. The boundary conditions and loading specification are as shown in Fig. 6.21. The left edge of the plate is clamped implying all in-plane

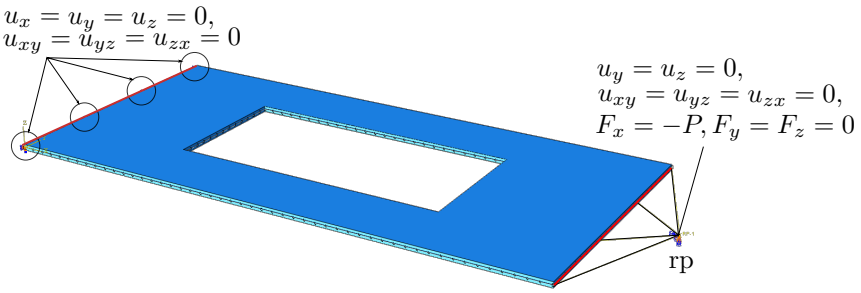

FIGURE 6.21: A schematic representation of the plate geometry used in *ABAQUS*. The left and the right edges (red lines) were assigned boundary conditions - fully fixed left edge and fixed right edge with the allowed displacement along the x-axis. The compressive loading acts along the x-axis and is applied to the reference point labelled "rp".

displacements are zero $u_x = u_y = u_z = 0$. And so are the rotations $u_{xy} = u_{yz} = u_{zx} = 0$. These components are expressed so per *ABAQUS* nomenclature. This incorporates the clamping of the left edge of the plate by the grips in the experiment as shown in Fig. 6.11. The right edge is fixed for all displacements and rotations $u_y = u_z = u_{xy} = u_{yz} = u_{zx} = 0$, except the in-plane displacement along the x-axis $u_x \neq 0$. Similar to the split beam analysis in Chapter 3, the boundary conditions are applied to the abstract entity (a plate edge or a reference point) and then translated to the actual nodes in *ABAQUS*. A unit loading $F_x = -P$ is applied along the x-axis in order to apply compression. Note, that the boundary conditions are applied to the geometrical entities – the right and the left edges. But, similar to Chapter 3, the loading is applied to the reference point labelled "rp" as shown in Fig. 6.21. The reference point is kinematically coupled to the nodes of the plate. In such a way, we avoid the complications of assigning boundary conditions and loading to each individual node on the edge. Such a way of applying the load and the boundary conditions is particularly useful for the parametric study where node IDs change as the mesh is automatically generated from predefined mesh seeds.

6.4.3 Finite element mesh

Buckling of plates typically implies out-of-plane bending. In FEA bending of plates is associated with two main considerations when it comes to selecting an appropriate element. These are computational cost and the necessity to account for the high-order effects such as in-plane strains and shear. Since we consider a linear buckling near the bifurcation point, the out-of-plane deflection of the plate may be considered small compared to plate thickness. As a result the assumption of small deformations is made. Also, the plate is considered thin. Hence, shear deformation within the plate thickness is neglected. These assumptions agree with the Kirchhoff-Love plate theory [Timoshenko and Gere, 2012]. The kinematic assumptions of this theory are as follows.

- Normals to the mid-surface remain normal after the deformation.
- There is no stain in the mid-surface of the plate
- The strains in the thickness direction are zero

Such assumptions are well handled by the general-purpose shell elements in *ABAQUS*. These elements are used to model thin shells and plates under small deformations [Dassault Systèmes, 2014].

There are two commonly used thin shell elements which are, i.e., 6-node elements and 8-node elements. In general, the second-order 8-node elements converge faster than the first-order ones and do not develop "shear-locking" compared to 6-node shell elements. Although we do not expect shear to affect the solution, we still chose the 8-node second-order shell elements to guarantee good accuracy of the computations. We also specify each element to have 6 degrees of freedom per node to allow all types of deformation to be captured. Thus, we select an 8-node doubly curved shell element with reduced integration S8R.

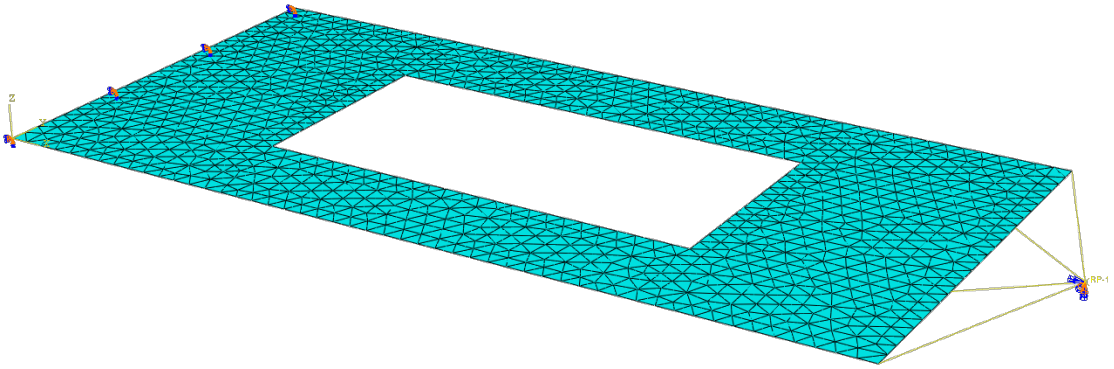

FIGURE 6.22: Example of a finite element mesh consisting of S8R triangular elements. In this example, the cut out has dimensions $\bar{l}$= 0.5 and $\bar{\alpha}$= 0.25.

Often, mesh control poses one of the biggest challenges for the parametric FEA as the mesh has to be adapted at each case of the analysis. Here, the plate problem in simpler than the bilayer beam problem, since it does not require high thickness-wise accuracy of the solution. Therefore, in this case, we allow the automatic mesh generator in *ABAQUS* handle the mesh generation for each analysis case taking only the mesh seeds as an input. We do not specify any iterative

refining of the mesh. Several runs showed that it does not improve the accuracy of the solution. An example of the automatically generated mesh for the present problem is shown in Fig. 6.22.

6.4.4 Parametric linear buckling analysis

We set up a parametric analysis varying cut length and cut width in small steps. The cut length parameter varies in the interval $0.01 \leq \bar{l} \leq 0.99$ with 100 increments. The cut width parameter varies in the interval $0.01 \leq \bar{a} \leq 0.5$ with 100 increments as well. In such a way, we have *ten thousands combinations* of $\bar{l}$ and $\bar{\alpha}$ for each of which a full finite element analysis was carried out.

We are interested in the critical buckling loads and the associated mode shapes for each combination of $\bar{l}$–$\bar{\alpha}$. Hence, we run a linear or eigenvalue buckling analysis using a standard *ABAQUS* solver which builds a sparse generalised eigenvalue problem and solves it for the eigenvalues and the corresponding eigenvectors. The former defines the critical buckling loads, while the latter specifies the associated mode shapes. Based on the reasoning similar to that in Chapter 3, we use the Subspace iteration algorithm to calculate the eigensolution.

This problem is computationally simpler than the one for the bilayer beam. Therefore, we use a standard desktop with the default parallelisation (MPI) for 2 CPUs with the 16 Gb of RAM. The memory threshold was set to 90%. We computed the 8 lowest eigenvalues with 16 guessed vectors supplied for each iteration of the Subspace iteration algorithm. Two guess vectors at least two times larger than the number of requested eigenvalues are advised to be used [Dassault Systèmes, 2014]. The maximal number of iterations was set to 300. Such a configuration, allowed us to perform all ten thousand buckling analysis within a few days of computation.

6.4.5 Classification of computed buckling modes

We computed the eigensolutions for the ten thousands cases for each of the three plate aspect ratio $A = 0.5$, $A = 0.9$ and $A = 1.4$. To further support the choice of the assumed mode shapes for the in-phase and the out-of-phase buckling used in the analytical modelling, we compare those mode shapes with the numerically computed ones for the same geometric parameters.

To perform the comparison between the computed and assumed modes, we use a reliable measure of similarity between shapes. Modal Assurance Criterion (MAC), a measure frequently used in experimental structural dynamics, gives a reliable estimation of how consistent the two given eigenvectors are [Allemang, 2003]. MAC is the scalar quantity that defines closeness between two vectors normalised by their length in the n-dimensional space as given by equation Equation (3.4) which we reproduce here for simplicity

$$\text{MAC} = (\boldsymbol{\Psi}_i^{\intercal} \boldsymbol{\Psi}_j)^2 \tag{6.25}$$

where $\boldsymbol{\Psi}_i$ is the n-dimensional eigenvector to be compared with $\boldsymbol{\Psi}_j$, which is an n-dimensional reference eigenvector. In our case, $\boldsymbol{\Psi}_i$ is the assumed in-phase mode for $i = 1$ and the assumed out-of-phase mode for $i = 2$. At the same time, $\boldsymbol{\Psi}_j$ is the reference in-phase mode extracted from *ABAQUS* for $j = 1$ and a reference out-of-phase mode extracted from *ABAQUS* for $j = 2$.

MAC can take values between 0 and 1. Here, 0 means that the eigenvectors are unrelated and do not correspond. The modes are not consistently corresponding to each other. MAC value of 1 implies that the eigenvectors are identical and the corresponding modes are identical as well. The high values of MAC (between 0.9 and 1) indicate good similarity between the modes. The values lower than 0.9 typically indicate that while the modes may still appear similar, they may not correspond to each other. A comprehensive discussion on how values of MAC identify the similarity between modes is presented by Pastor et al. [2012].

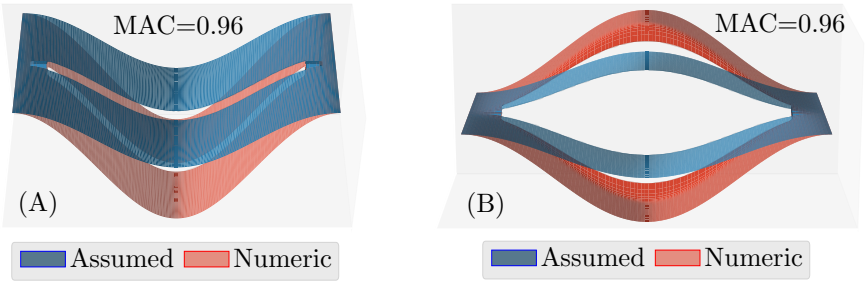

FIGURE 6.23: Visual comparison of in-phase and out-of-phase buckling modes used in analytical modelling and computed by FEA. (A) Comparison of the two in-phase modes. (B) Comparison of the two out-of-phase modes. The blue mode shapes are the assumed ones, while the red mode shapes were calculated using FEA.

The assumed mode shapes $\mathbf{\Psi}_i$ are functions of x and y coordinates. The in-phase buckling mode is given by $w_{\text{In-phase}}$ in Equation (6.1). The assumed mode shape for the out-of-phase buckling is given by a piecewise function. It is $w_{\text{In-phase}}$ for strips and w_{Web} given by Equation (6.3) for web part. FEA returns mode shapes as eigenvectors with the dimensionality of the eigenvalue problem. This means that the eigenvectors contain redundant information, such as rotation at the nodes that are not required for mode classification. We are primarily concerned with the degrees of freedom that constitute out-of-plane displacement. Since the mesh nodes change location between different cases of analysis, we retain the displacement values from a collection of preset points evenly spaced throughout the plate. For this purpose, we use a fixed grid of 100×100 points. Hence, we extract the out-of-plane displacements of the points on the grid from each eigenvector and write them into separate arrays. Then, we numerically evaluate the functional forms w_1 and w_{Web} over the same grid and store this information in other arrays. Therefore, we obtained two sets of numerical arrays of the same shape. The first shape contains the discrete representations of the computed modes while the second array contains the discrete representations of the analytical modes. The part of the eigenvectors extracted in this way now allow MAC classification in a straightforward manner.

The selected in-phase modes and out-of-phase modes are visually compared in Fig. 6.23. The resemblance between the analytical and the computed modes is apparent. The calculated MAC between the respective modes is 0.96 which quantifies the consistency between the modes. This analysis has shown that the assumed modes are very close to the computed ones. For clarity, the ansatz and the FE calculated modes have been plotted with different scaling factors.

The two lowest eigenvalues were calculated for each combination of $\bar{l}$ and $\bar{\alpha}$ parameters for one of the three plate aspect ratio A. When scaled by the critical buckling load for a uniform plate $P_{cr} = 4\pi^2 Ebh^3/12(1-\nu^2)L^2$, the extracted eigenvalues were plotted in Fig. 6.24 as functions of $\bar{l}$ and $\bar{\alpha}$. Notice that the graph is rotated compared to the previous ones (e.g., that in Fig. 6.17)

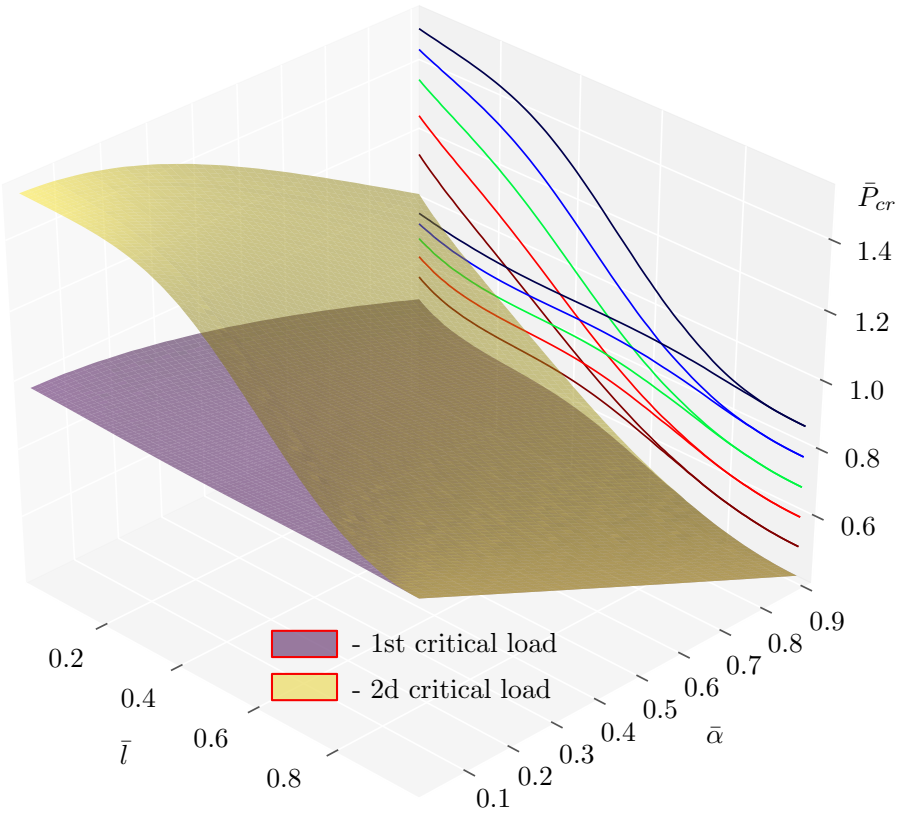

FIGURE 6.24: Surfaces of the first and the second scaled critical buckling load computed in *ABAQUS* and plotted in $\bar{l}$–$\bar{\alpha}$ coordinates.

to make a better visual judgement of the scaled buckling load surfaces. The surfaces in Fig. 6.24 correspond to the plate with the aspect ratio $A = 0.9$. The generic trend in the lowest two critical buckling load surfaces resembles the one from analytical modelling (compare Fig. 6.24 with Fig. 6.17). The lowest two surfaces are far apart from each other for small cut outs (small values of $\bar{l}$ and $\bar{\alpha}$) and get closer to each other as both $\bar{l}$ and $\bar{\alpha}$ increase. Therefore, similarly to the analytical modelling, we can say that an increase in the overall cutout area reduces the difference between the magnitudes of critical buckling loads.

While the general shapes of the buckling load surfaces are similar between computations and analysis, the computed surfaces have one major difference. They do not cross. The reason may be that the small numerical disorder due to mesh irregularity leads to the avoided crossing scenario even when the coupling is zero, which is at the phase boundary. The two computed surfaces approach indistinguishably close to each other in the range of $\bar{l} > 0.8$. They are weakly repulsed then and remain nearly degenerate (separation is of the order of numerical error) for the rest of the parameter plane. This is apparent from the projections of the two buckling loads on the $\bar{P}$–$\bar{l}$ plane in Fig. 6.24 (colour lines).

We apply the Modal Assurance Criterion to classify the lowest buckling modes computed numerically changing $\bar{l}$ and $\bar{\alpha}$. The workflow for MAC-based classification is exactly the same as discussed in Section 3.5. We chose a reference eigenvector for $\bar{l} = 0.01$ and $\bar{\alpha} = 0.01$ (in-phase buckling). Then, we calculate MAC values between the lowest eigenvector for each combination of $\bar{l}$ and $\bar{\alpha}$ and the reference one. If MAC value is > 0.9, the buckling follows in-phase type. If the MAC value is < 0.2, the buckling follows the out-of-phase type. If the MAC value is

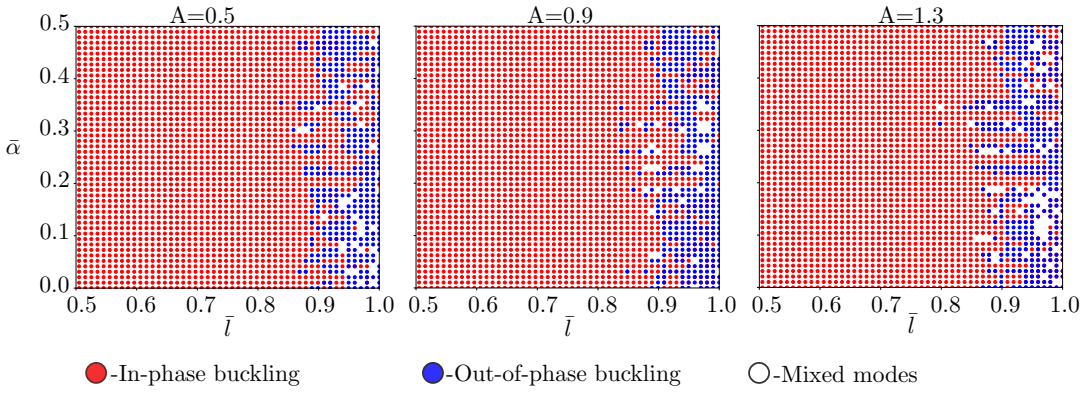

FIGURE 6.25: The mode classification diagrams plotted in $\bar{l}$–$\bar{\alpha}$ coordinates for the plate aspect ratio $A = 0.5$ (*left*), $A = 0.9$ (*centre*) and $A = 1.3$ (*right*). The red dots label in-phase buckling, blue dots label out-of-phase buckling and white dots label linearly dependent modes (uncertainty).

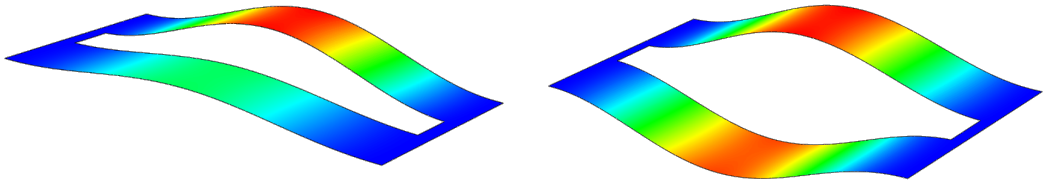

FIGURE 6.26: Two linearly dependent modes computed by *ABAQUS*. Colour labels the absolute magnitude of the out-of-plane displacement.

between 0.2 and 0.9, the modes are linear combination. We also performed a similar MAC-based classification using in-phase mode as a reference one. These steps were repeated for the three values of the plate aspect ratio $A = 0.5$, $A = 0.9$ and $A = 1.3$.

The classification diagrams are shown in Fig. 6.25. The diagram on the left was produced for the plate aspect ratio $A = 0.5$, the diagram in the centre corresponds to $A = 0.9$ and the one to the right corresponds to $A = 1.3$. Each dot on the diagrams represents a specific mode type: red colour is for in-phase buckling, blue is for out-of-phase buckling and white is for linearly combined modes, whose mode type is uncertain. It is apparent from the classification that the numerical modelling did not return a clear boundary between the regions on $\bar{l}$–$\bar{\alpha}$ plane associated with the two-mode types. We see that the out-of-phase mode prevails on average for $\bar{l}> 0.8$ for all values of $\bar{\alpha}$. However, the classification results contain considerable noise (MAC values fluctuate between 0.1 and 0.9) and many points were classified as uncertain mode type. Visual investigation of several randomly picked points indicates that in the regions where the two surfaces come close but do not cross, the eigenvalues are near-degenerate, while the associated modes are not orthogonal. In this case, the numerical investigation of the behaviour becomes very difficult. As the eigenvectors are not unique both in-phase buckling, out-of-phase buckling and their linear combinations can be returned by *ABAQUS*. As an example, consider several mode shapes computed by *ABAQUS* in Fig. 6.26. These modes represent neither a pure in-phase nor pure out-of-phase buckling but are linear combinations of both. This highlights a practical aspect of associated with this class of structural stability problems – while the prediction of critical buckling modes is fairly robust, degeneracy implies inherent difficulty with regards to the prediction of closely appearing modes.

This problem shows strong sensitivity of the behaviour to small perturbation and disorder, which is unlike a bilayer beam, that shows robust mode types in all cases except for direct vicinity to the triple point and the phase boundaries. Here, the two modes are so close that inevitable swapping between nearly degenerate pairs is favoured by the disorder, even due to numerical noise. Practically, we see doublet of modes, even though theoretically there should be two close but distinct modes due to elastic coupling.

6.5 Conclusions

In this chapter, we studied a plane counterpart of the bilayer beam, which is a plate with a rectangular cut out. We carried out compression testing of the plate samples and observed in-phase and out of phase buckling modes depending on cut out length and width. The first type is characterised by the joined deflection of the two halves in the same direction. This is analogous to cooperative buckling of a bilayer beam. The second type is characterised by the opposite deflection of the two halves, e.g., one half deflects upwards while the other deflects downwards. This is analogous to competitive or splitting buckling of a bilayer beam.

To comprehensively characterise the behaviour, we developed an analytical model of the plate and used it to identify the boundary on the cut length – cut width parameter plane that separates in-phase from out-of-phase buckling response. A linear approximation of such a phase boundary in the parameters plane revealed that the aspect ratio of the plate is the principal parameter that characterises which type of buckling will be realised. The phase boundary was possible to obtain thanks to the simple ansatz for in-phase and out-of-phase buckling modes. In contrast, the FEA analysis often returned doublet of modes that are so close that inevitable swapping between nearly degenerate pairs is favoured by the disorder. Such linear combinations of in-phase and out-of-phase buckling are difficult to classify. This highlights the high sensitivity of the mode shapes for this class of problems. The sensitivity to disorder is such that even a numerical disorder in FE modelling can produce linear combinations of modes, even when theoretically they are supposed to be two close, yet distinct modes. In reality, mixed modes may happen due to unavoidable irregularities in the structures as indicated by the experiment. In this case, the phase diagram suggests parameters for which the plate is highly sensitive to defects (region of out-of-phase buckling) and parameters, for which it is relatively forgiving to irregularities (region of in-phase buckling). The modes resembling out-of-phase buckling still occur in the out-of-phase buckling region as evident from the experiments and computations.

Chapter 7

Buckling of a plate with periodic cut outs

We investigated the buckling of a rectangular plate with a symmetrically placed rectangular cut out in the previous chapter. We observed that cylindrical bending of the two strips around the cut out and twist of the web are the dominant mechanisms of plate deformation. These primary modes of deformation, as identified, enable us to successfully predict the in-phase and the out-of-phase buckling of the strips on either side of the cut out. Frequently structures with periodic strips that are elastically linked by similar plate structures are encountered in practical engineering situations. Therefore, the next natural next step is to consider the problem of a plate with multiple rectangular cut outs regularly placed along its width. We consider the parts of the plate on either side of each cut out to be identical strips while the web between these "plate fingers" provides coupling between them. In the following, we investigate the elastic stability of a structure consisting of a long chain of identical elastic members coupled by webs.

Examples of plates with regular cut outs are common in the engineering of the cooling equipment and may also be used in long multi-section industrial fire doors and other structures. For instance, long arrays of thin fins coupled by tubes in heat exchangers, and exhaust gas recovery systems as the one shown in Fig. 6.1 are common. Thus, the instability of these structures is also of practical importance.

7.1 Review of the elastic stability of plates with periodic features

Periodic plates have been studied in relation to their stability when they are long, with perforations and regularly placed holes, as discussed in Chapter 2 and in Section 6.1. Another practical example of the plates with periodic features is plate-like sections that feature regularly placed stiffeners. These structures can be modelled as nearly infinite periodic plates in compression.

In the 1990s and early 2000s the problem of stability of periodic plates drew some attention from researchers who introduced many concepts related to vibration localisation in mechanics. However, the fact that there are strong generic physical and mathematical analogies between the wave propagation in periodic media and the stability of period structures, seems to be not

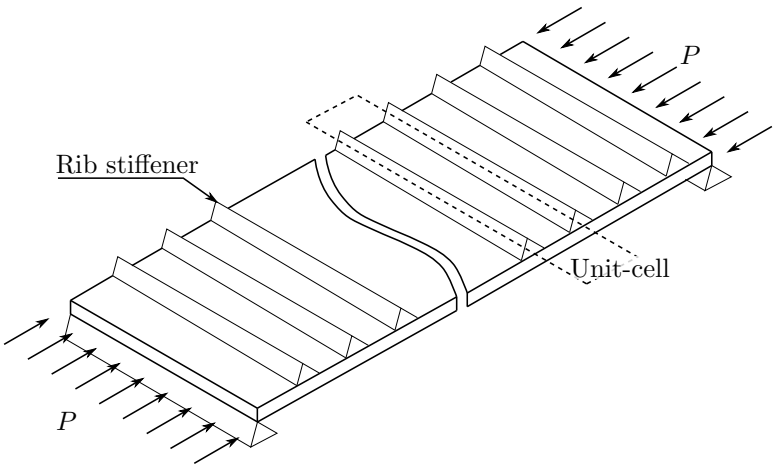

FIGURE 7.1: A schematic representation of a long rectangular plate with two opposite edges simply supported and a number of regularly placed stiffeners compressed by loading P. Based on models by Xie [1997] and [Elishakoff et al., 1995].

that well recognised. Accordingly, the literature on the stability of periodic structures is sparse, despite the ubiquitous presence of such features in structural engineering. Xie [1997], Elishakoff et al. [1995], Li et al. [2005] and others studied the instability behaviour of nominally periodic plates with the disorder. The principal problem considered by them is a long plate with the regularly positioned stiffeners *along its length*, as shown in Fig. 7.1. The plate is typically compressed by loading P distributed along the shorter edges that are also simply supported while the long edges were considered free as shown in Fig. 7.1.

Such a problem was first studied by Elishakoff et al. [1995]. The authors considered the plate simply supported along all edges and subject to uni-axial compression P. They used a series solution of the governing differential equation to write the deflected shape of the plate. The presence of stiffeners was introduced in the continuity conditions between spans. These can be defined in two ways. In the first case, it was assumed that each rib acts as a simple support for the plate, while in the second case, each rib was assumed to have no support. In both cases, an N-span plate problem is formed of 4 boundary conditions and $4 \times (N-1)$ continuity conditions which make $4 \times N$ conditions for the shape function of the plate containing $4 \times N$ unknowns. In matrix notation, such problem yields a transcendental eigenvalue problem

$$\mathbf{K}(\lambda)\mathbf{x} = \mathbf{0}, \tag{7.1}$$

where $\mathbf{K}(\lambda)$ is a symmetric Dynamic stiffness matrix whose entries are transcendental functions of critical buckling load parameter λ, $\mathbf{x}$ is a vector of unknown constants arising after the substitution of the series solution into boundary conditions and continuity conditions and carry instability mode information. The above eigenvalue problem has an infinite number of solutions λ. The smallest of these constitutes the lowest critical buckling load of the plate. At the same time, the associated eigenvector $\mathbf{x}$ defines the lowest buckling shape of the stiffened plate.

Elishakoff et al. [1995] considered only 1, 2 and 3 stiffeners to understand the effect of their misplacement on critical buckling load and the associated buckling mode shape of the structure. Essentially, the sensitivity of the plate buckling behaviour to disorder was studied by them and they reported that as the number of stiffeners increases, i.e. as the plate approaches perfect

periodicity, it becomes more sensitive to disorder. Furthermore, as stiffeners naturally provide coupling between the neighbouring spans of the plate, the sensitivity of the critical buckling load and the buckling mode shape was reported to depend on a single universal factor, e.g., coupling to disorder ratio. These results are in good agreement with those for periodic beams with the disorder and with our own analysis of the chain of rigid rods discussed in Chapter 5.

The Dynamic stiffness matrix is based on exact solutions of the member differential equations. However, it is challenging to solve the transcendental eigenvalue problem thus arising for a sufficiently large number of spans in the stiffened plate. Therefore, Xie [1998] employed the transfer matrix method to study a similar plate but with many stiffeners. The author specified the displacement of each span of the plate in terms of the transfer matrix $\mathbf{T}$ for this span times the displacement of the previous span. The benefit of this approach is that transfer matrices simplify calculations for a large number of periodic structural arrays, and when used in conjunction with approximations within a bay to reduce the number of degrees-of-freedom per bay may lead to really small transfer matrices, even 2×2 matrices whose product can be easily calculated, if the matrices are identical. Such a product is harder to calculate if the structure is disordered and the transfer matrices vary. Nevertheless, if the structure is randomly disordered and contains large enough number of spans and the disorder follows a known distribution, Furstenberg's theorem [Furstenberg, 1963] can be used, which states that the product of such random transfer matrices approaches the asymptotic value λ also called localisation factor. Xie [1998] used the numerical approach to calculate the localisation factors for the long but finite plate with $N = 5 \times 10^5$ stiffeners. Then, he studied the strength of buckling mode localisation depending on the coupling to disorder ratio in the plate.

Xie and Ibrahim [2000] also employ the transfer matrix method to rib-stiffened plates. However, they formulate the transfer matrices using a finite strip method. The idea of the finite strip method is that a continuous span of the plate between the neighbouring stiffeners is split into a number of finite strips for each of which a non-dimensional strip stiffness matrix and a non-dimensional strip geometric stiffness matrix are written. These matrices can then be assembled for the whole span. For each span, the degrees of freedom in these matrices are separated into those that are on the boundary (associated with the stiffeners) and those within the span. Then, the interior degrees of freedom are expressed in terms of the boundary degrees of freedom. Thanks to this, one derives a matrix that relates the degrees of freedom on neighbouring stiffeners which has a dimension of 4×4. When such matrices are assembled for the entire plate, one obtains equations of equilibrium for the plate which have a form of a chain of matrix equations

$$\mathbf{B}_{n-1}\mathbf{x}_{n-1} + \mathbf{A}_n\mathbf{x}_n + \mathbf{B}_{n+1}\mathbf{x}_{n+1} = \mathbf{0} \tag{7.2}$$

where $\mathbf{B}_{n-1}$ contains assembled stiffness and geometric stiffness matrix of the previous span, $\mathbf{A}_n$ contains the stiffness and geometric stiffness matrices of the current span and $\mathbf{B}_{n+1}$ contains assembled stiffness and geometric stiffness matrices for the next span. Recall, that this matrix chain equation closely resembles the transfer relation derived for a chain of rigid rods in Chapter 5. One can also transform it into the transfer matrix relation $\mathbf{x}_{n+1} = \mathbf{T}_n\mathbf{x}_n$, where $\mathbf{T}_n$ is the transfer matrix of the n-th span. Then the localisation factors are calculated for a given coupling to disorder ratio numerically.

[Xie and Elishakoff, 2000] also studied a similar problem of the stiffened plate using Kantarovich approach. This method allows the partial differential equation of the plate to be reduced to an ordinary differential equation. The minimisation of the double integral $\iint_\Omega L(w)\mathrm{d}x\mathrm{d}y$ by considering the separation of variables

$$w(x, y) = f(x)g(y), \tag{7.3}$$

is then carried out, where one of the functions has to be chosen a priori and has to satisfy the boundary conditions. Then, the problem reduces to that of the minimisation of a single integral which is handled by taking the first variation of the integral to zero. An extensive review on the Rayleigh-Ritz, Galerkin, Kantarovich and other methods in mechanics is presented by Singhatanadgid and Singhanart [2019].

[Xie and Elishakoff, 2000] employed Kantarovich method by expressing the plate displacement w as a product of a function in x and another function in y. Then, the integration of the differential equation of the plate was carried out with respect to y coordinated along the plate thickness accounting for simply supported and fixed boundary conditions. This leads to an ordinary differential equation in x (coordinate perpendicular to the stiffeners), which was solved for each span between the stiffeners. The solutions were expressed in terms of four unknown coefficients. Assembling the solutions in a matrix form resulted in a Dynamic stiffness matrix. It was then solved numerically for various boundary conditions. The disorder was introduced by misplacing the stiffeners and the localisation factors were numerically computed. According to the authors, the main benefit of Kantarovich approach over finite strips method and FEA is that this method can produce analytical results when the edges normal to the stiffeners are simply supported.

Effects associated with the localisation of buckling mode in plates with the disorder were also studied by Paik et al. [2015]. They use Mindlin theory and finite element analysis to study buckling mode localisation in fixed rectangular plates made of composite material. They studied cases of axial loading along one direction, axial loading along the other direction, axial loading along both directions and shear loading. The authors also studied how the localisation factor changes if a fixed interior point is introduced to the plate compared to the plate without such point. Their main discovery is that if even a single fixed point is introduced, the plate exhibits a pattern of strong localisation, i.e., the entire domain is separated into two parts, one of which exhibits strong buckling mode, while the other has almost no deformation present. The authors also suggest that their discovery may be used to tailor the response of the plate by controlling the location of the fixed point within the plate.

Here we want to make a distinction with respect to previous studies, even though sparse and limited to about ten papers, as opposed to waves in periodic elastic media where the literature is extensive and easily exceeds several hundreds of pieces of work, if not thousands. Of the few works on the buckling of periodic structures in the spirit of periodic structures theory, nearly all of them are restricted to periodicity *along the direction of compression*. As opposed to this, here we identify another interesting class of problems that presents itself amenable to the periodic structures approach. This class consists of the problems where periodicity is *across the direction of loading*. While the industrial relevance of the buckling of period structures is huge, e.g. that driven by the need to analyse and design structures with stiffener, ribs and spars,

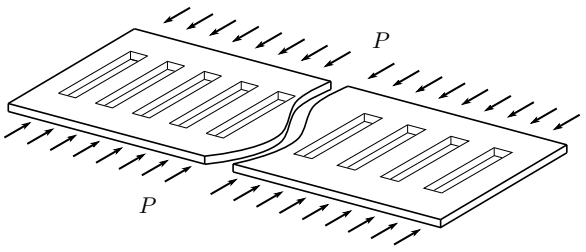

FIGURE 7.2: A plate compressed by loading P with a number of cutouts placed at regular intervals parallel to the loading direction.

most of the studies take a direct computational approach such as finite element method [Rikards et al., 2001, Moen and Schafer, 2009b, Nguyen-Thoi et al., 2013], mesh-free and semi-analytical methods [Byklum et al., 2004, Peng et al., 2006] or resort to experimental characterisation [Cheng et al., 2013]. While both of these approaches provide valuable estimation of the structural response with regards to stability, they do not provide insight in the sense of being able to predict behaviour as a function of structural parameters. The approach in this thesis is inspired by the practical need to gain understanding of the generic instability behaviour in simple terms with some analytical handle, so that this could be utilised in practical design scenarios.

7.2 Buckling of plates with periodic cut outs

We study the elastic stability of a plate featuring multiple nominally identical rectangular cut outs positioned regularly along the width of the plate. The plate edges perpendicular to the loading direction are considered fixed (i.e. their out-of-plane deflections and rotations are set to zero) while the other two edges are considered free. A schematic diagram of the structure under study is shown in Fig. 7.2.

A detailed spatial view of the plate is depicted in Fig. 7.3 and features a plate with N rectangular cut outs (only three are shown) that are spaced regularly along the plate width. The length of the plate is L and the width of the plate is b. The figure also contains a unit cell of the structure– a subregion of the plate that possesses translational periodicity along plate width. The green curve reflects a schematic representation of the plate deflection along width while the brown curve shows a schematic representation of the plate deflection along the length. The strips deform approximately cylindrically and are nearly twist-free, thus containing only the x-wise curvature of the strips, whereas the plate-web that connects two strips deforms in a complex manner and contributions to the strain energy due to the two curvatures and also the twist needs to be accounted for. To account for twist energy, we need ansatz that contains at least the product of the coordinates, i.e. xy terms, or any higher-order polynomial jointly, in the spatial variables x and y.

We assume all cut outs to be identical. Note the geometric resemblance between the problem considered here and that of the plate with a single cut out studied in Chapter 6. In fact, the previous problem may be viewed as a two-bay solution for the present one. For simplicity, we chose a unit cell as shown in Fig. 7.3. This problem approaches perfect periodicity as the number of cut outs tends to infinity. This is similar to how a chain of rigid rods approaches periodicity as the number of rods increases. In reality, infinite chains do not exist, however, plates with large

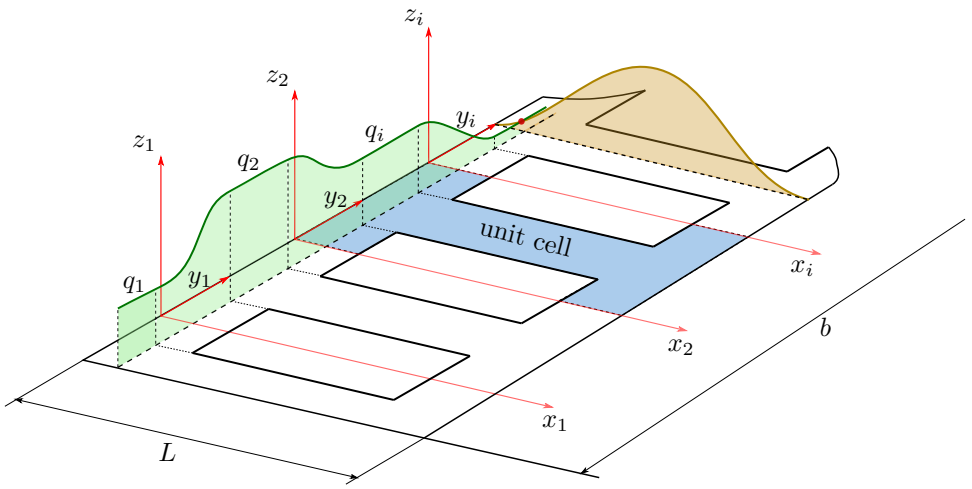

FIGURE 7.3: A schematic representation of the plate with the overall length L and width b. A unit-cell is shaded in blue. A schematic of the out-of-plane deflection profile of the plate along the width is indicated with green. The schematic of the out-of-plane deflection along plate length is indicated with brown.

numbers of cut outs approach periodicity and can be approximated as infinite. For example, even a relatively small size plates with hundreds of regularly placed rectangular perforations may be approximately treated as periodic. We study such a plate in the following section starting with a two-cut-out plate.

We introduce a local coordinate system associated with each unit cell. For the i-th unit cell, the x_i axis is parallel to plate length L, y_i is parallel to plate width b and z_i is perpendicular to the plane of the plate. This is shown in Fig. 7.3. Here, i is an index of a unit cell, $i = 1, \ldots, N$, which serves as the strip number. The buckled shape of the plate would be a function of two independent coordinates x and y, in general. In Fig. 7.3 we pick an arbitrary line parallel to the x-axis and an arbitrary line parallel to the y-axis and plot the schematic representation of the buckling profiles on the x-z and y-z planes. Our manner of choosing the deflected shape of the plate with multiple cut-outs enables us to turn a rather complex structural problem to one that is simple because there is just one degree of freedom per strip that describes the amplitude of the strip. Each degree of freedom per strip provides independence from other strips, in order to allow different *phases* of the strips relative to each other. While doing so, we are also able to account for the strain energy of the web that has forms associated with curvatures in both directions as well as twist, by smoothly matching the two surfaces associated with the deflected strips. By *phase*, here we mean the modulations of the the same shape common to each "bay" or strip moving from one strip to the next, just as a travelling wave, or a vibrating system, has (it is unfortunate that the word phase is also used for instability maps, as in phase diagrams. In the present context the meaning is different).

The deformed shape of the plate is thus built of the identical deformed shapes of each strip, which are modulated in space by unknown magnitudes of generalised coordinates. One generalised coordinate is assigned per strip. The generalised coordinates need determining by an appropriate minimum energy principle. Moreover, the complex deformed shape is described by simple cubic functions whose second derivatives need to be used inside the strain energy expression. This greatly simplifies the computations and the approach is ideal for carrying out a large number

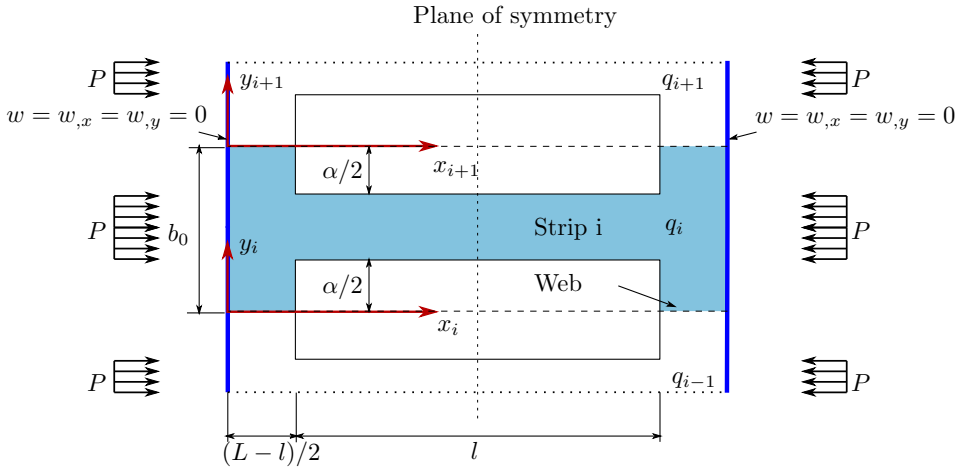

FIGURE 7.4: A schematic of an i-th unit cell (blue), which consists of a strip and a web part. The boundary conditions and loading are specified along the plate edges, which are indicated by thick blue lines.

of computations, which is the case now, as we need to determine instability maps that require the buckling modes to be determined for a very large number of combinations of geometrical parameters.

To give a formal mathematical representation to the buckled profiles, we assume the functional forms for the transverse displacement $w(x, y)$ of the complex plan form of the plate. The economy in representing the transverse displacement is achieved by constructing ansatz that is global, making use of the simplest interpolation, i.e. cylindrical bending with cubic variation along x, combined with cubic in both directions for webs where the deformation is complex and needs both direction curvatures and the twist energy terms accounted for. Moreover, these cubic functions are carefully chosen, so that there is exactly one unknown per function and they are smoothly matched for displacements and slopes at the boundaries of the adjacent bays or unit cells. Natural or kinetic boundary conditions, involving higher-order derivatives, do not need to be satisfied.

As stated above, the assumed deflected shapes must satisfy all the kinematic boundary conditions as shown in Fig. 7.4, which implies that the left edge of each unit cell is restrained from deflection and rotation i.e. $w = w_{,x} = 0$, where w is out-of-plane deflection. The right edge of each unit cell is restrained from out-of-plane deflection and rotation, i.e. $w = w_{,x} = 0$, but the in-plane deflection along $x-$ axis is allowed. A detailed view of the $i-$th unit cell that consists of a strip and the web is shaded in blue and shown in Fig. 7.4. The boundaries of a unit cell separate the coupling regions into half-regions (see dashed lines). Also, the unit cell is symmetric length-wise as indicated by the plane of geometric symmetry, hence only half of it needs to be considered. The loading as shown in Fig. 7.4 is specified in a piece-wise manner similar to Chapter 6. The strips are assumed to be compressed by a constant force $N_x = P/N(b_0 - \alpha)$, where N_x is force per unit length, N is the number of strips, b_0 is the width of the unit cell, and α is the width of the web.

In the case of periodically placed cut outs, the structure can be modelled as an infinite chain of periodic structures along the plate width b. The strategy is inspired by the dynamic analogy of waves in periodic media, and also computational observations, that the shape of displacement

field within each bay does not vary across bays. However, their amplitude is modulated, the modulation is referred to as the spatial phase variation across the bays. So we need to allow at least one independent generalised coordinate per bay and minimise the total potential energy of the whole system, after making a judicious choice on the assumed *shape* within a bay. When the number of cut outs is small, the first and the last bays may show small end effects.

The loading is shown in detail in Fig. 7.4 is specified in a piece-wise manner similar to Chapter 6. Due to the reasons explained before, we shall consider loading such that the coupling regions, i.e. webs between strips, are not loaded while the strips themselves are compressed with a constant loading $N_x = P/N(b_0 - \alpha)$, where N is the number of strips. This is to ensure consistency with other similar problems considered in the literature, where a similar loading pattern is assumed. Another way of looking at it is that there is no differential in-plane displacement along the whole line $x = 0$ across the strips and the webs.

As discussed in Chapter 5, one-dimensional periodic structures can be either cyclic, i.e. the first and the last members are joined, or form an infinite chain. The structure studied here possesses translational symmetry along $y-$axis and can be modelled as an infinite chain for a sufficiently large number of unit cells.

We seek to write a close form approximate expression for the deformed profile of the plate employing the Hermite's cubic splines. The deformation profile along the $x-$axis for $0 \leq x \leq L/2$ (brown colour in Fig. 7.3) is well approximated by the third Hermite's cubic $h_3(\xi) = -2\xi^3 + 3\xi^2$, where $\xi = 2x/L$. We consider only half of the unit cell length-wise due to symmetry (see Fig. 7.4).

To construct the suitable assumed mode shapes of the plate, we will use only two Hermite cubics: h_1 and h_3 which read

$$h_1(\xi) = -2\xi^3 + 3\xi^2, \tag{7.4}$$

$$h_3(\xi) = 2\xi^3 - 3\xi^2 + 1, \tag{7.5}$$

where ξ is some coordinate, such that $0 \leq \xi \leq 1$. The plots of these polynomials were shown in Fig. 4.5 (*right*). The deflected shape of the i-th strip along the plate length for $0 \leq L/2$ (brown curve in Fig. 7.3) is written using h_3 as

$$w_{\text{Strip i}}(\xi, \zeta) = q_i \left(-2\xi^3 + 3\xi^2\right), \tag{7.6}$$

where q_i is the buckling amplitude of the i-th strip (generalised coordinate), $\xi = 2x/L$ and $\zeta = y/\alpha$ are the non-dimensional coordinates. Note that $w_{\text{Strip i}}$ is assumed constant along beam width, hence, it is constant with ζ.

The deformation profile along the y-axis needs a detailed consideration. As can be seen from Fig. 7.3, the profile consists of a number of flat sections interposed with "S"-shaped segments joined together ensuring continuous and smooth across bays deflected shape. The flat sections correspond to the strips. This is a reasonable assumption since each strip is in cylindrical bending as was discussed in Chapter 6. Therefore, we are able to write the deflected shapes of each strip in both coordinates as given by Equation (7.6). The y-dependent deflection of each strip is constant, it is reflected by q_i. The web deflections then have to be modelled by a cubic polynomial that interpolates between the subsequent strips q_i and q_{i+1}. in Fig. 7.5.

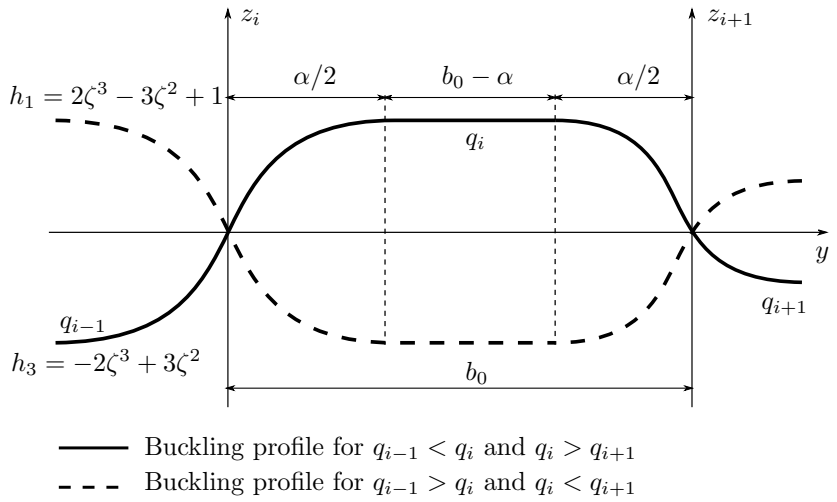

FIGURE 7.5: The buckling profile of a unit cell with adjacent webs for the two arbitrary ratios between q_{i-1}, q_i and q_{i+1}. When $q_{i-1} < q_i$ (solid line) the third Hermite cubic h_3 is used. When $q_{i-1} > q_i$ (dashed line), the first Hermite cubic h_1 is used.

Consider the black solid line in Fig. 7.5. It specifies the possible buckling profile of a unit cell i, as a function of the y-coordinate is a section of the plate consisting of one half a web $\alpha/2$, a strip $b_0 - \alpha$, and a half of the second web $\alpha/2$. The two webs interpolate between the amplitude q_{i-1} of the Strip $i-1$, amplitude q_i of the Strip i and the amplitude q_{i+1} of the Strip $i+1$. Depending on the relative values of q_{i-1}, q_i and q_{i+1}, different shape functions for the webs should be chosen. If $q_{i-1} < q_i$, the buckling profile of the web can be assumed in the form of h_3 as shown in Fig. 7.5 with the solid black curve. Alternatively, if $q_{i-1} > q_i$, the buckling profile of the web can be assumed in the form of h_1, as indicated by the dashed curve in Fig. 7.5. The same logic holds for the web between strips i and $i+1$.

As we do not have a prior knowledge of the relative magnitudes of the generalised coordinates, we write the assumed shape of the web in non-dimensional coordinates $\xi = 2x/L$ and $\zeta = y/\alpha$ as

$$w^{(i)}_{\text{Web}}(\xi,\zeta) = \left[q_{i-1}\left(2\zeta^3 - 3\zeta^2 + 1\right) + q_i\left(-2\zeta^3 + 3\zeta^2\right)\right]\left(-2\xi^3 + 3\xi^2\right), \tag{7.7}$$

where $w^{(i)}_{\text{Web}}(\xi,\zeta)$ is the deflected shape of the web between strips $i-1$ and i, (i) is an index, the expression in the square brackets is the interpolation between the amplitudes q_{i-1} and q_i, which becomes h_3 for $q_{i-1} < q_i$ and h_1 for $q_{i-1} > q_i$. The expression within the round brackets is the deflected shape of the web along plate length. The deflected shapes for other webs are obtained by simply changing i to a respective number in Equation (7.7). The continuity of the displacement and slope between the web and the attached strips is satisfied by Equation (7.7) because of the carefully chosen dependencies with respect to ξ given by the coefficient of q_{i-1} and q_i. This ensures that $w^{(i)}_{\text{Web}}(\xi,0) = q_{i-1}$, $w^{(i)}_{\text{Web}}(\xi,1) = q_i$ and $\partial w^{(i)}_{\text{Web}}(\xi,0)/\partial\zeta = \partial w^{(i)}_{\text{Web}}(\xi,1)/\partial\zeta = 0$.

Based on the geometric parameters shown in Fig. 7.3 and Fig. 7.4 we introduce the non-dimensional ratio. $A = b/L$, where b is overall width and L is the overall length of the plate. The width of a unit cell is $b_0 = b/N = AL/N$ in terms of plate aspect ratio, plate length and number of unit cells N. Then, the ratio of the cut out length to the overall length is $\bar{l} = l/L$ and the ratio of cut out width to the unit cell width is $\bar{\alpha} = \alpha/b_0$ or $\bar{\alpha} = \alpha N/AL$. The energy calculations will be performed for half of the plate length-wise and then doubled due to the symmetry.

The strain energy of the strip can be analytically evaluated since the mode shape is independent of y in this region and the integrand is a simple polynomial. The expression that needs evaluating in

$$U_{\text{Strip}} = \frac{D}{2} \iint\limits_{\Omega_{\text{Strip}}} (w_{,xx})^2 \, \mathrm{d}y \, \mathrm{d}x, \tag{7.8}$$

where w is given by Equation (7.6), which is a function of the non-dimensional spatial coordinate $\xi = 2x/L$ and is independent of ζ. A subscript after coma denotes differentiation with respect to the relevant spatial coordinate. The rectangular region of the strip is specified in x-y-coordinates as

$$\Omega_{\text{Strip}} = \{(x, y) \in \mathbb{R}^2 : 0 \leq x \leq L/2; 0 \leq y \leq b_0 - \alpha\}. \tag{7.9}$$

The strain energy of the web incorporates bending in the x-direction, bending in the y-direction, and x-y twist, so the complete strain-energy expression

$$U_{\text{Web}} = \frac{D}{2} \iint\limits_{\Omega_{\text{Web}}} \Big[\left(w_{,xx} + w_{,yy}\right)^2 - 2(1-\nu) \left(w_{,xx} w_{,yy} - (w_{,xy})^2\right) \Big] \, \mathrm{d}y \, \mathrm{d}x, \tag{7.10}$$

needs to be evaluated. Here w is given by Equation (7.7), and the rectangular region of each web in x-y coordinates is

$$\Omega_{\text{Web}} = \{(x, y) \in \mathbb{R}^2 : 0 \leq x \leq (L-l)/2; 0 \leq y \leq \alpha/2\}. \tag{7.11}$$

The potential energy of external loading within the unit cell can be written as the in-plane loading N_x times the movement of the edge in the direction of the force, i.e.

$$V = \frac{1}{2} \iint\limits_{\Omega_{\text{Strip}}} N_x(y) \left(w_{,x}\right)^2 \, \mathrm{d}y \, \mathrm{d}x = \frac{-P}{2N(b_0 - \alpha)} \iint\limits_{\Omega_{\text{Strip}}} (w_{,x})^2 \, \mathrm{d}y \, \mathrm{d}x, \tag{7.12}$$

where $N_x = -P/N(b_0 - \alpha)$ is the compressive loading acting on each strip and Ω_{Strip} is the rectangular region of each strip.

The strain energy of the unit cell i is the sum of the strain energy of the strip i and strain energy of the adjacent webs. Note, that half of the web is connected to the left of the i-th strip and half of the web is connected to the right of the $i-$th strip as shown in Fig. 7.4. Therefore, the strain energy reads

$$U_i = U^{(i)}_{\text{Strip}} + U^{(i)}_{\text{Web}}, \tag{7.13}$$

where U_i is the strain energy of i-th unit cell, $U^{(i)}_{\text{Strip}}$ is calculated using Equation (7.8) and the shape functions given by Equation (7.6). U_{Web} for web i and $i+1$ is calculated using Equation (7.10) with the shape function given by Equation (7.7). The strain energy of the unit cell is a quadratic form in generalised coordinates q_{i-1}, q_i and q_{i+1}

$$U_i = u_0 q_i^2 + q_{i-1}^2 u_1 + q_{i-1} q_i u_2 + 2 q_i^2 u_1 + q_i q_{i+1} u_2 + q_{i+1}^2 u_1, \tag{7.14}$$

where coefficients u_0, u_1 and u_2 come from the integration and are functions of parameters $\bar{l}$, $\bar{\alpha}$, A, N and ν

$$u_0 = \frac{96A_0D}{L^2}(1-\bar{\alpha}), \tag{7.15}$$

$$u_1 = \frac{96D}{5\bar{\alpha}^3A_0^3L^2}\left(\frac{13}{7}(\bar{\alpha}A_0)^7Q_1 - \frac{3}{10}(\bar{\alpha}A_0)^5Q_2 + \frac{1}{112}Q_3\right), \tag{7.16}$$

$$u_2 = \frac{96D}{5\bar{\alpha}^3A_0^3L^2}\left(\frac{9}{7}(\bar{\alpha}A_0)^7Q_1 + \frac{3}{5}(\bar{\alpha}A_0)^5Q_2 - \frac{1}{56}Q_3\right), \tag{7.17}$$

where $A_0 = A/N$ is the aspect ratio of the unit cell and factors Q_1 and Q_3 are functions of the non-dimensional cut out length $\bar{l}$ and the Poisson ratio

$$Q_1 = \left(1-\bar{l}\right)\left(4\bar{l}^2 - 2\bar{l} + 1\right), \tag{7.18}$$

$$Q_2 = \left(1-\bar{l}\right)^3\left((2\bar{l}^2 + \bar{l})(5\nu - 3) - 1\right), \tag{7.19}$$

$$Q_3 = \left(1-\bar{l}\right)^5\left(20\bar{l}^2 + 30\bar{l} + 13\right). \tag{7.20}$$

The unit cells correspond to $i = 2, \ldots, N$, while for $i = 1$ and $i = N+1$ we have the first strip and the last strip which are coupled to the inner webs but do not have any outer webs. These strips have widths $(b_0 - \alpha)/2$, which are half those of the inner strips. The strain energy of the strips at the end is

$$U_{\text{End}} = \frac{1}{2}u_0q_i^2, \quad i = 1, \ldots, N+1. \tag{7.21}$$

The potential energy of the external loading is calculated for each strip i within unit cells $i = 2, \ldots, N$ using Equation (7.12)

$$V_{\text{Strip}}^{(i)} = -\frac{12P}{5NL}q_i^2 = v_0q_i^2, \quad i = 2, \ldots, N. \tag{7.22}$$

At the same time, the potential energy of external loading of the strips at the boundary will be two times smaller

$$V_{\text{End}} = -\frac{12P}{10NL}q_i^2 = \frac{v_0}{2}q_i^2, \quad i = 1, \ldots, N+1. \tag{7.23}$$

The total potential energy of the unit cell is the sum of its strain energy and the potential energy of external loading

$$\Pi_i = U_{\text{Strip}}^{(i)} + U_{\text{Web}}^{(i)} + V_{\text{Strip}}^{(i)}, \quad i = 2, \ldots, N. \tag{7.24}$$

Adding the total potential energies of the unit cells and the contributions from the boundaries, we obtain an expression for the total potential energy of the entire plate

$$\Pi = U_{\text{End}}^{(0)} + \sum_{i=2}^{N}\left(U_{\text{Strip}}^{(i)} + U_{\text{Web}}^{(i)}\right) + U_{\text{End}}^{(N+1)} + V_{\text{End}}^{(0)} + \sum_{i=2}^{N}V_{\text{Strip}}^{(i)} + V_{\text{End}}^{(N+1)}, \tag{7.25}$$

where the summation from $i = 2$ to $i = N$ is for the strips within unit cells, i.e. the periodic part. The components for $i = 1$ and $i = N+1$ are for the first and the last strips.

The condition for equilibrium requires $\delta\Pi = 0$, i.e. $\partial\Pi/\partial q_j = 0$. Taking the derivatives with respect to each of the generalised coordinates we write

$$\frac{\partial \Pi}{\partial q_j} = u_2 q_{j-1} + (2u_0 + 4u_1)\, q_j + u_2 q_{j+1} - 2v_0 q_j = 0, \quad j = 2, \ldots, N, \tag{7.26}$$

which is a set of linear equations in q_j for all unit cells. A special case for strips $i = 0$ and $i = N$ at the boundaries yields

$$\frac{\partial \Pi}{\partial q_1} = (u_0 + 2u_1)\, q_1 + u_2 q_2 - v_0 q_1 = 0, \tag{7.27}$$

$$\frac{\partial \Pi}{\partial q_{N+1}} = u_2 q_N\, (u_0 + 2u_1)\, q_{N+1} - v_0 q_{N+1} = 0. \tag{7.28}$$

We combine Equation (7.26), Equation (7.27) and Equation (7.28) together and compose the generalised eigenvalue problem

$$\mathbf{K}\mathbf{q} = P\mathbf{K}_g\mathbf{q}, \tag{7.29}$$

which can be written in terms of the two matrices

$$\mathbf{K} = \begin{bmatrix} u_0 + 2u_1 & u_2 & 0 & \cdots & \cdots & \cdots & \cdots & 0 \\ u_2 & 2u_0 + 4u_1 & u_2 & \ddots & & & & \vdots \\ 0 & u_2 & 2u_0 + 4u_1 & u_2 & \ddots & & & \vdots \\ \vdots & \ddots & \ddots & \ddots & \ddots & \ddots & & \vdots \\ \vdots & & \ddots & \ddots & \ddots & \ddots & \ddots & \vdots \\ \vdots & & & \ddots & u_2 & 2u_0 + 4u_1 & u_2 & 0 \\ \vdots & & & & \ddots & u_2 & 2u_0 + 4u_1 & u_2 \\ 0 & \cdots & \cdots & \cdots & \cdots & 0 & u_2 & u_0 + 2u_1 \end{bmatrix}, \tag{7.30}$$

where $\mathbf{K}$ is the tridiagonal stiffness matrix of size $(N+1) \times (N+1)$ for the plate with N cut outs. The first and the last rows are different due to the boundary strips. The geometric stiffness matrix $\mathbf{K}_g$ is a diagonal matrix given by

$$\mathbf{K}_g = \begin{bmatrix} v_0 & 0 & 0 & \cdots & \cdots & \cdots & \cdots & 0 \\ 0 & 2v_0 & 0 & \ddots & & & & \vdots \\ 0 & 0 & 2v_0 & 0 & \ddots & & & \vdots \\ \vdots & \ddots & \ddots & \ddots & \ddots & \ddots & & \vdots \\ \vdots & & \ddots & \ddots & \ddots & \ddots & \ddots & \vdots \\ \vdots & & & \ddots & 0 & 2v_0 & 0 & 0 \\ \vdots & & & & \ddots & 0 & 2v_0 & 0 \\ 0 & \cdots & \cdots & \cdots & \cdots & 0 & 0 & v_0 \end{bmatrix}. \tag{7.31}$$

Vector $\mathbf{q}$ is the vector of generalised coordinates and P is the eigenvalue or critical buckling load. Similarly as before, we scale P by the buckling load of a uniform plate in cylindrical bending $P_{cr} \approx 40AD/L$ and calculate the non-dimensional buckling load $\bar{P} = P/P_{cr}$.

The eigenvalue problem given by Equation (7.29) contains a tridiagonal stiffness matrix similar in structure to the one derived for a long chain of rigid rods. This is natural since the entire plate except for the ends can be viewed as a regular assembly of identical strips coupled to each other. This is a topology very similar to the chain of coupled rigid rods. The EVP in Equation (7.29) is parameter-dependent and the nature of the eigensolution will be parameter-dependent too, the parameters concerned are those that describe the geometry.

We now solve the generalised eigenvalue problem given by Equation (7.29) for several geometrical cases. Let us first look at matrices $\mathbf{K}$ and $\mathbf{K}_g$ given by Equation (7.30) and Equation (7.31). We pre-multiply both sides of the generalised EVP in Equation (7.29) by $\mathbf{K}_g^{-1}$ and obtain

$$\mathbf{K}_g^{-1}\mathbf{K}\mathbf{q} = P\mathbf{I}\mathbf{q}, \tag{7.32}$$

where $\mathbf{I}$ is the identity matrix. We can define a system matrix $\mathbf{A} = \mathbf{K}_g^{-1}\mathbf{K}$, which can be written in terms of the identity matrix and a tridiagonal matrix $\mathbf{A}_l$ as

$$\mathbf{A} = \frac{u_0 + 2u_1}{u_2 v_0}\mathbf{I} + \frac{1}{v_0}\mathbf{A}_l. \tag{7.33}$$

Here, the factor in front of the identity matrix will be called $\beta = \frac{u_0+2u_1}{u_2 v_0}$ and the tridiagonal matrix $\mathbf{A}_l$ has the following form

$$\mathbf{A}_l = \begin{bmatrix} 0 & 1 & 0 & \cdots & 0 \\ \frac{1}{2} & 0 & \frac{1}{2} & \ddots & \vdots \\ 0 & \frac{1}{2} & 0 & \ddots & \vdots \\ \vdots & \ddots & \ddots & \ddots & \vdots \\ 0 & \cdots & \cdots & 1 & 0 \end{bmatrix}. \tag{7.34}$$

Therefore, the generalised eigenvalue problem can be rewritten as

$$\left[\beta\mathbf{I} + \frac{1}{v_0}\mathbf{A}_l\right]\mathbf{q} = P\mathbf{q}, \tag{7.35}$$

where all the parameters $\bar{l}$, $\bar{\alpha}$ and A are contained within the factor β in front of the identity matrix, v_0 does not depend on $\bar{l}$ and $\bar{\alpha}$. Then, the eigenvalues of Equation (7.35) are β plus the eigenvalues of $(1/v_0)\boldsymbol{A}_l$ for any size of the EVP since $\boldsymbol{I}$ is the identity matrix. The proof of this is immediate, once we take $\beta\mathbf{I}\mathbf{q}$ term to the right side, and recognise that $(P - \beta)$ is the eigenvalue of the rearranged eigenvalue problem, associated with $(1/v_0)\boldsymbol{A}_l$. The eigenvalues of $\mathbf{A}_l$ are all distinct. From the study in Chapter 6, we concluded that the phase boundary between the in-phase and the out-of-phase buckling exists when the two buckling loads are equal, i.e. degenerate. If we expect the nature of the lowest buckling modes to change in the case of the plate with many cut outs, such a combination of $\bar{l}$ and $\bar{\alpha}$ should exist for which Equation (7.35) have multiple eigenvalues. This is possible only if $\beta = \infty$, or $u_2 = 0$. Hence, for the combination of values of $\bar{l}$ and $\bar{\alpha}$, for which $u_2 = 0$, the buckling loads of the plate will be degenerate.

We start by considering a partial case of a plate with only two cut outs as shown in Fig. 7.6. This plate can be described using the proposed convention by assuming the strips at the boundaries (q_0 and q_2) to be half as wide as the strip in the middle (q_1). A schematic diagram of the plate

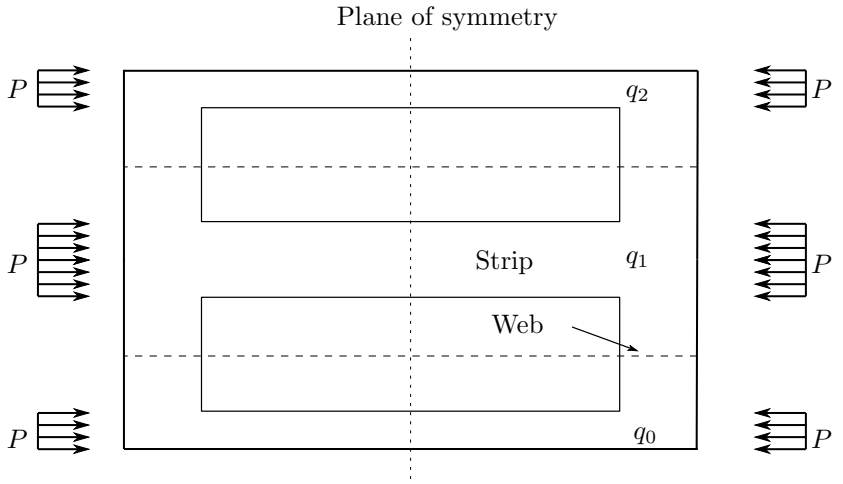

FIGURE 7.6: A schematic representation of a partial case: a plate with two cut outs. The plate is characterised by three generalised coordinates q_1, q_2 and q_3. It consists of two strips at the boundary and a wide strip in the middle coupled through coupling regions.

depicted in Fig. 7.6. There are three strips, i.e. $N+1=3$, and two unit cells, i.e. $N=2$. Therefore, we write Equation (7.29) for this case, which is a 3×3 EVP that can be solved analytically substituting expressions for u_0, u_1 and u_2 given by Equation (7.15), Equation (7.16), and Equation (7.17) respectively.

The expressions for the three eigenvalues (scaled critical buckling loads) in terms of model parameters are given by

$$\bar{P}_1 = 1 - \bar{\alpha}\left(4\bar{l}^3 - 6\bar{l}^2 + 3\bar{l}\right), \tag{7.36}$$

$$\bar{P}_2 = 1 - \frac{\bar{\alpha}\left(104\bar{l}^3 - 156\bar{l}^2 + 78\bar{l} + 9\right)}{35} + \frac{3N^4\left(1-\bar{l}\right)^3\left(2\bar{l}^2(5\nu-3) + \bar{l}(5\nu-3) - 1\right)}{25A^2\bar{\alpha}},$$
$$\frac{N^2\left(1-\bar{l}\right)^5\left(13 + 30\bar{l} + 20\bar{l}^2\right)}{280A^4\bar{\alpha}^3}, \tag{7.37}$$

$$\bar{P}_3 = 1 - \frac{\bar{\alpha}\left(18 + 51\bar{l} - 102\bar{l}^2 + 68\bar{l}^3\right)}{35} + \frac{6N^4\left(1-\bar{l}\right)^3\left(2\bar{l}^2(5\nu-3) + \bar{l}(5\nu-3) - 1\right)}{25A^2\bar{\alpha}} +$$
$$\frac{N^2\left(1-\bar{l}\right)^5\left(13 + 30\bar{l} + 20\bar{l}^2\right)}{140A^4\bar{\alpha}^3}. \tag{7.38}$$

Note that $\bar{P}_1$ in Equation (7.36) differs from $\bar{P}_1$ for a plate with a single cut out given by Equation (6.13) and $\bar{P}_3$ in Equation (7.38) differs from $\bar{P}_2$ for a plate with a single cut out given by Equation (6.14) by presence of factors N^4 and N^2 which account for the number of unit cells and the number of strips $(N+1)$. When the cut out is negligibly small, i.e., $\bar{l}\to 0$ and $\bar{\alpha}\to 0$, the first critical buckling load $\bar{P}_1$ approaches the buckling load of the uniform plate and the higher loads $\bar{P}_2$ and $\bar{P}_3$ tend to infinity as $1/\bar{\alpha}^3$ due to bending response of infinitesimally small coupling parts being too stiff.

The associated eigenvectors turn out to be parameter independent and are given by

$$\mathbf{q}_1 = \{1,1,1\}^\top, \mathbf{q}_2 = \{-1,0,1\}^\top, \mathbf{q}_3 = \{1,-1,1\}^\top, \tag{7.39}$$

where the first eigenvector $\mathbf{q}_1$ represents the lowest buckling mode of the plate characterised by all strips deflecting in the same direction cooperatively or in-phase. This corresponds to the in-phase buckling of a plate with a single cut out discussed in Chapter 6. The critical buckling loads $\bar{P}_1$ in both cases are the same. The eigenvector $\mathbf{q}_3$ corresponds to the out-of-phase buckling as the strips have deflections equal in magnitude but with opposite signs. This buckling state and the associated critical buckling load match the out-of-phase buckling of the plate with a single cut out in Chapter 6. The eigenvector $\mathbf{q}_2$ corresponds to the critical load $\bar{P}_2$ which lies between $\bar{P}_1$ and $\bar{P}_3$. There is no such load in the case of a plate with a single cut out. This buckling state is neither in-phase nor out-of-phase buckling and has one node – the central strip does not deflect. There is a strong analogy between these modes and those of vibration of 3 coupled pendula.

The critical buckling loads $\bar{P}_1$, $\bar{P}_2$, $\bar{P}_3$ are plotted as functions of $\bar{l}$ and $\bar{\alpha}$ keeping N, A and ν constant. The surfaces are shown in Fig. 7.7 with brown surface corresponding to $\bar{P}_1$, blue surface corresponding to $\bar{P}_2$ and green surface corresponding to $\bar{P}_3$. The Poisson ratio was assumed to be $\nu = 0.3$ and the aspect ratio of each unit cell was taken $A_0 = A/N = 0.5$. The discussed

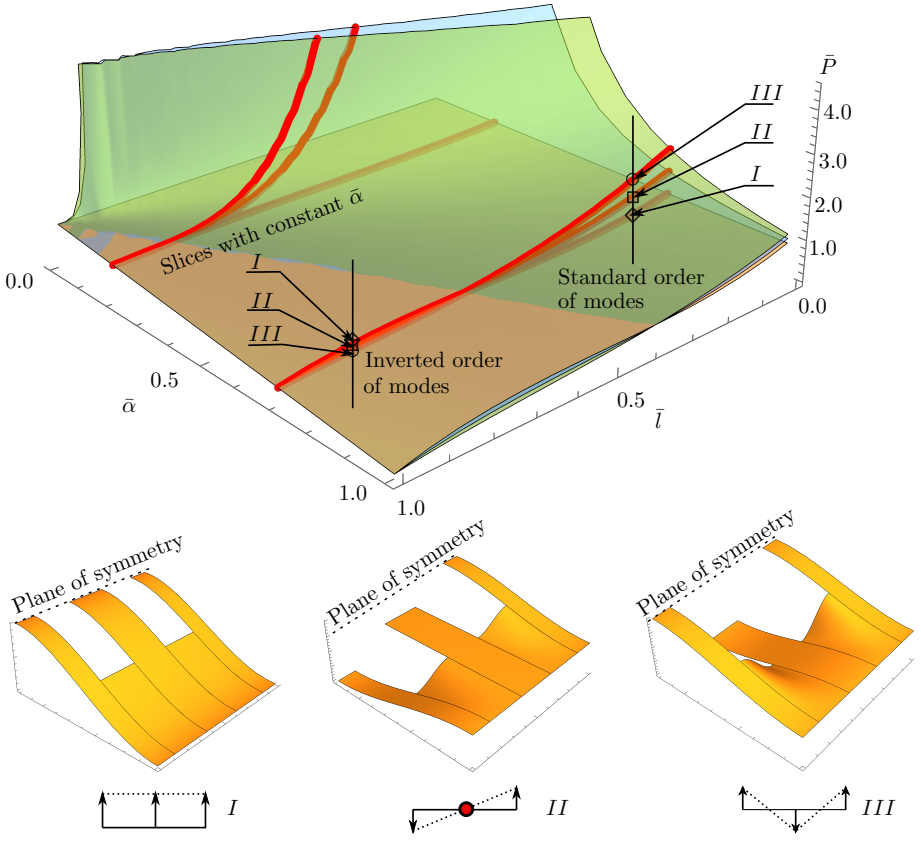

FIGURE 7.7: Expressions for scaled buckling loads $\bar{P}_1$, $\bar{P}_2$, $\bar{P}_3$ plotted as functions of $\bar{l}$-$\bar{\alpha}$ coordinates. The solid red lines indicate the slices of the surfaces for selected fixed values of $\bar{\alpha}$. The standard and inverted order of modes are depicted for two chosen points on $\bar{l}$-$\bar{\alpha}$. The respective mode shapes labelled as *mode I*, *mode II*, *mode III* are depicted in the respective subplots. The schematic diagrams under each mode indicate the relative deflections of the midpoints of each strip for each mode type with arrows.

eigenvectors are plotted in the subplots at the bottom of the figure and are labelled *mode I*, *mode II* and *mode III*.

The buckling load surfaces differ from those of a plate with a single cut out only by one extra surface, i.e., $\bar{P}_2$ (blue colour), which lies between $\bar{P}_1$ and $\bar{P}_3$. *Mode I* and *mode III* in this case exactly correspond to the modes exhibited by the plate with the single cut out. The in-phase buckling (*mode I*) is characterised by all the strips deflecting identically in the same direction. In this case, coupling does not affect the relative magnitudes of strip deflections. The out-of-phase buckling (*mode III*) is characterised by strips deflecting in opposite directions by the same amplitude. In this case, the coupling has a maximum effect on the modulation of buckling amplitude. Finally, *mode II* is characterised by the intermediate regime. In contrast to *mode I*, coupling does affect the modulation of buckling amplitude, but, in contrast to *mode III*, the effect is smaller.

From Fig. 7.7, we observe that the ordering of critical buckling loads $\bar{P}_1$, $\bar{P}_2$, $\bar{P}_3$ and the associated modes changes with structural parameters. The surfaces $\bar{P}_1$, $\bar{P}_2$ and $\bar{P}_3$ cross along a single spatial curve implying $\bar{P}_1 = \bar{P}_2 = \bar{P}_3$. The curve on $\bar{l} - \bar{\alpha}$ plane corresponding to the crossing of the three surfaces defines a phase boundary on the parameter plane. Note that we continue to use the word phase diagram and phase boundary etc. to mean the fundamental mode instability map. These are non-standard usages, although appropriate here. Traversing the phase boundary is associated with the dramatic change in the buckling mode character of the plate.

Numerical investigation of the equations $\bar{P}_1 = \bar{P}_2$ and $\bar{P}_2 = \bar{P}_3$ strongly suggests that all three surfaces indeed cross along exactly the same curve. The equations are non-linear algebraic equations in terms of the geometric parameters of the problem. We further prove that by solving equations $\bar{P}_1 = \bar{P}_2$ and $\bar{P}_2 = \bar{P}_3$ in terms of $\bar{l}$ and $\bar{\alpha}$ analytically and comparing the results. Note that this gives equivalent result as solving for $u_2 = 0$. The equations have four solution branches, two of which are complex. Also, there is a partial case of $\bar{l} = 1$ satisfying the equation for any $\bar{\alpha}$. We consider only the real solutions, hence we have

$$A\bar{\alpha} + \frac{N}{2\sqrt{15}}\left(1 - \bar{l}\right)\sqrt{F(\bar{l},\nu)} = 0 \quad \text{for} \quad F(\bar{l},\nu) > 0, \tag{7.40}$$

$$A\bar{\alpha} - \frac{N}{2\sqrt{15}}\left(1 - \bar{l}\right)\sqrt{F(\bar{l},\nu)} = 0 \quad \text{for} \quad F(\bar{l},\nu) > 0. \tag{7.41}$$

Here, the expression under the square root sign is given by

$$F(\bar{l},\nu) = \frac{14 + \bar{l}Q_0 28 + \bar{l}^2 Q_1 + \sqrt{16(\bar{l}^4 + \bar{l}^3)Q_2 + \bar{l}^2 Q_3 + \bar{l}Q_4 + 423}}{4\bar{l}^2 - 2\bar{l} + 1}, \tag{7.42}$$

where $Q_0, \ldots, Q_4$ are polynomials in Poisson ratio

$$\begin{aligned} &Q_0 = 42 - 70\nu, Q_1 = 3 - 5\nu, Q_2 = 1225\nu^2 - 1470\nu + 691, \\ &Q_3 = 2450\nu^2 - 4900\nu + 2358, Q_4 = 688 - 980\nu. \end{aligned} \tag{7.43}$$

Note, that $Q_0, \ldots, Q_4$ are exactly the same here as in the case of a plate with the single cut out given by Equation (6.18) and are invariants on the number of cut outs.

The case of $\bar{l} = 1$ corresponds to the degeneracy of the critical buckling loads when the cut outs split the plate into several uncoupled strips, each of which has exactly the same buckling load. Further, Equation (7.40) yields negative values of $\bar{\alpha}$ for any real value of $\bar{l} \neq 1$. Negative values of $\bar{\alpha}$ are not physical, hence, we will ignore this solution branch. Finally, Equation (7.41) is the

solution branch which gives real and positive values of both $\bar{l}$ and $\bar{\alpha}$ and we will consider it in detail. Solving Equation (7.41) by expressing $\bar{\alpha}$ in terms of $\bar{l}$, we obtain

$$\bar{\alpha} = \frac{1}{2\sqrt{15}} \frac{N}{A} \left(1 - \bar{l}\right) \sqrt{F(\bar{l}, \nu)}, \tag{7.44}$$

which is the functional form of the phase boundary derived from the intersection of all three buckling loads $\bar{P}_1$, $\bar{P}_2$ and $\bar{P}_3$. In such a way, we have shown that the standard order of buckling modes, e.g., *mode I* $\rightarrow$ *mode II* $\rightarrow$ *mode III* is inverted to *mode III* $\rightarrow$ *mode II* $\rightarrow$ *mode I* upon traversing a single boundary on the parameter plane as shown in Fig. 7.7. The inversion of the order of buckling states is also apparent from Fig. 7.8(a) which shows the instability map or a phase diagram, on the $\bar{l} - \bar{\alpha}$ plane with a phase boundary given by Equation (7.44) for the fixed aspect ratio of the unit cells $A_0 = A/N = 1$. Equation (7.44) is an exact functional form of

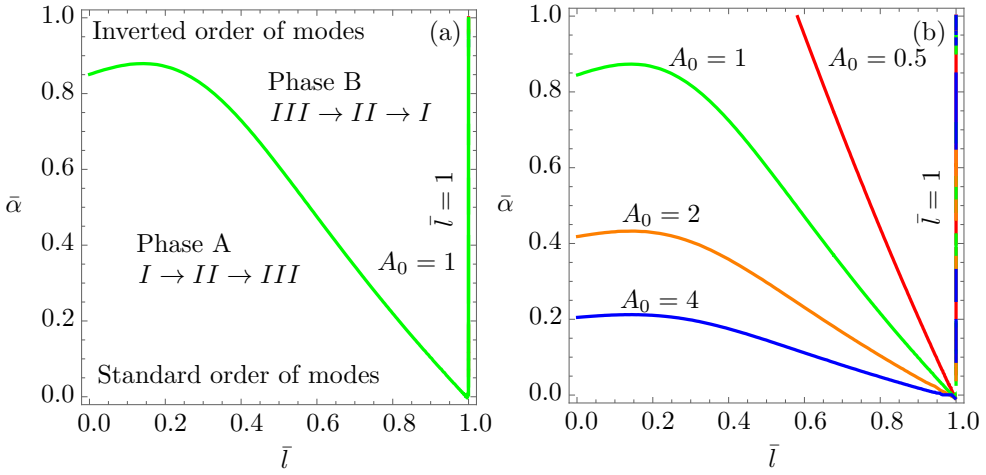

FIGURE 7.8: Phase diagrams of buckling states plotted in $\bar{l} - \bar{\alpha}$ coordinates. The phase boundary of the square plate ($A = 1$) that separates the region with the standard order of modes from the region with the inverted order of modes is shown in (a). A number of phase boundaries for the fixed $N = 3$ and several plate aspect ratio A is shown in (b).

the phase boundary which depends on the ratio of the number of strips to the aspect ratio of the plate N/A or inversely proportional to the aspect ratio of the unit cell $A_0 = A/N$. Phase boundaries for $A_0 = 0.5, 1, 2, 4$ with $N = 2$ i.e. three strips are plotted in Fig. 7.8(b).

Equation (7.44) is almost linear except for when $\bar{l} < 0.2$ as in this case, a nonlinear factor $\sqrt{F\left(\bar{l}, \nu\right)}$ plays a dominant role. We can derive a much simpler linearised expression for the phase boundaries using Tailor series expansion of Equation (7.44) around $\bar{l} = 1$, such that

$$\bar{\alpha} = \frac{N\sqrt{28 - 42\nu + \sqrt{14}\sqrt{83 - 168\nu + 126\nu^2}}}{6A} \left(1 - \bar{l}\right) + \mathcal{O}\left((\bar{l} - 1)^2\right). \tag{7.45}$$

Note, that Equation (7.45) differs from Equation (6.20) only by the presence of factor N in the numerator. Therefore, we can conclude that the phase boundaries for a plate with one cut out and for a plate with many cut outs differ only by a slope which is proportional to the number of cut outs N. If we consider aspect ratio of each unit cell as $A_0 = A/N$ and the Poisson ratio $\nu = 0.3$, Equation (7.45) simplifies to

$$\bar{\alpha} \approx \frac{1}{A_0} \left(1 - \bar{l}\right). \tag{7.46}$$

In this case, the slope is governed by the aspect ratio of the unit cell alone. Therefore, Fig. 7.8(b) gives the most generic phase diagram of the buckling states of the plate with an arbitrary number of cut outs. The exact phase boundaries given by Equation (7.44) are depicted in Fig. 7.9 for

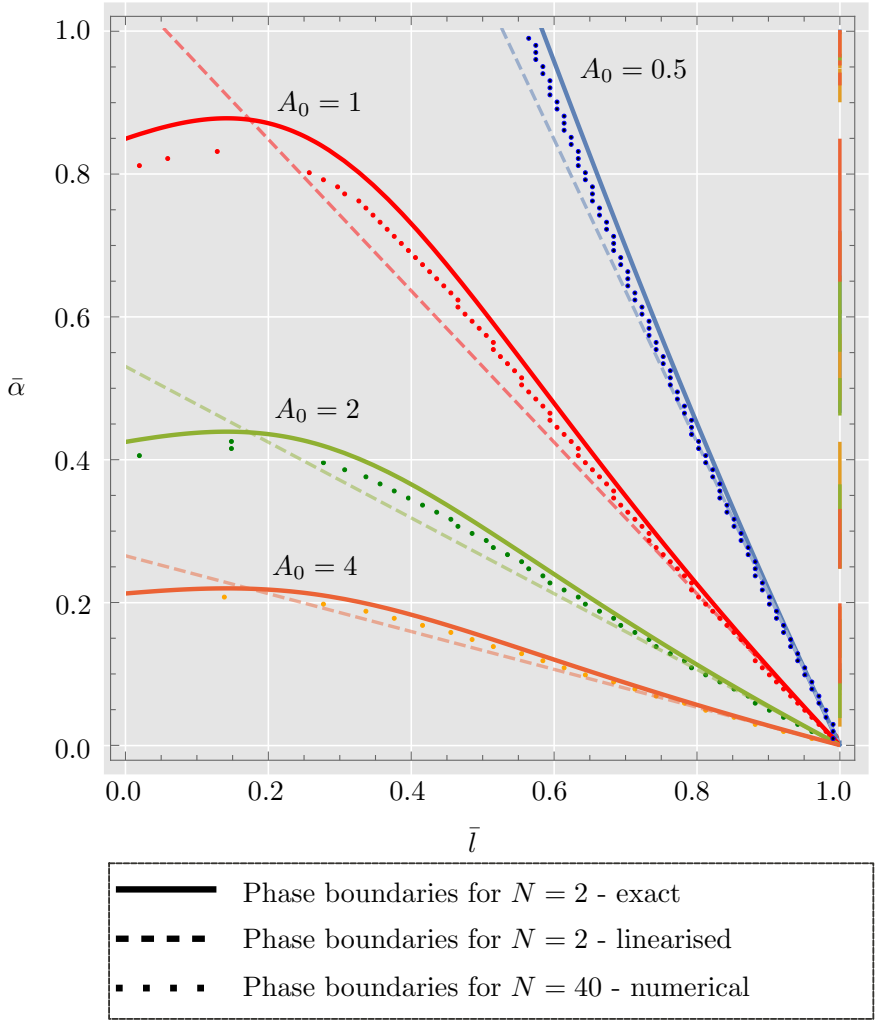

FIGURE 7.9: A phase diagram of the plate with multiple cut outs for various aspect ratio of the unit cell. Solid lines correspond to the phase boundaries for $N = 2$ unit cells, dashed lines are linear approximations of these boundaries and dots indicate similar boundaries calculated numerically for $N = 40$ unit cells.

several values of unit cell aspect ratio A_0 for a plate with two cut outs $N = 2$ with solid lines. The linearised boundaries given by Equation (7.45) are plotted for the same A_0 on the same graph with dashed lines. Finally, we also computed the phase boundaries for the same A_0 but for a plate with $N = 10$, $N = 20$, $N = 40$, $N = 80$ and $N = 100$ cut outs numerically and compare how the respective phase boundaries change. For $N > 40$, the boundaries practically are not affected by N. Hence we plot them for this number of cut outs in Fig. 7.9 with dots. It is apparent from the graph that the boundary between the phases remains constant for any number of cut outs in a plate provided we keep increasing the aspect ratio of the plate A proportionally to keep A_0 constant. Furthermore, the linearised expressions give a fairly good approximation to the phase boundaries for $\bar{l} > 0.2$.

It is apparent from Fig. 7.9 that the linear expansion of Equation (7.44) at $\bar{l} = 1$ is good at predicting the phase boundary for large cut lengths but is not optimal for all values of $\bar{l}$. Therefore, we also present the expansion around $\bar{l} = 0.5$ which yields

$$\bar{\alpha} \approx \frac{1.2489}{A_0} \left(1 - \bar{l}\right), \tag{7.47}$$

for $\nu = 0.3$ and $A_0 = A/N$. The quality of the linear approximation at $\bar{l}$ can be seen in Fig. 7.10. Here, the exact solutions of Equation (7.44) (*solid lines*) are compared with the linear approximations given by Equation (7.47) (*dashed lines*) for a number of aspect ratios of the unit cell A_0. Indeed, the linear approximation at $\bar{l} = 0.5$ is more accurate for the cut outs of moderate length.

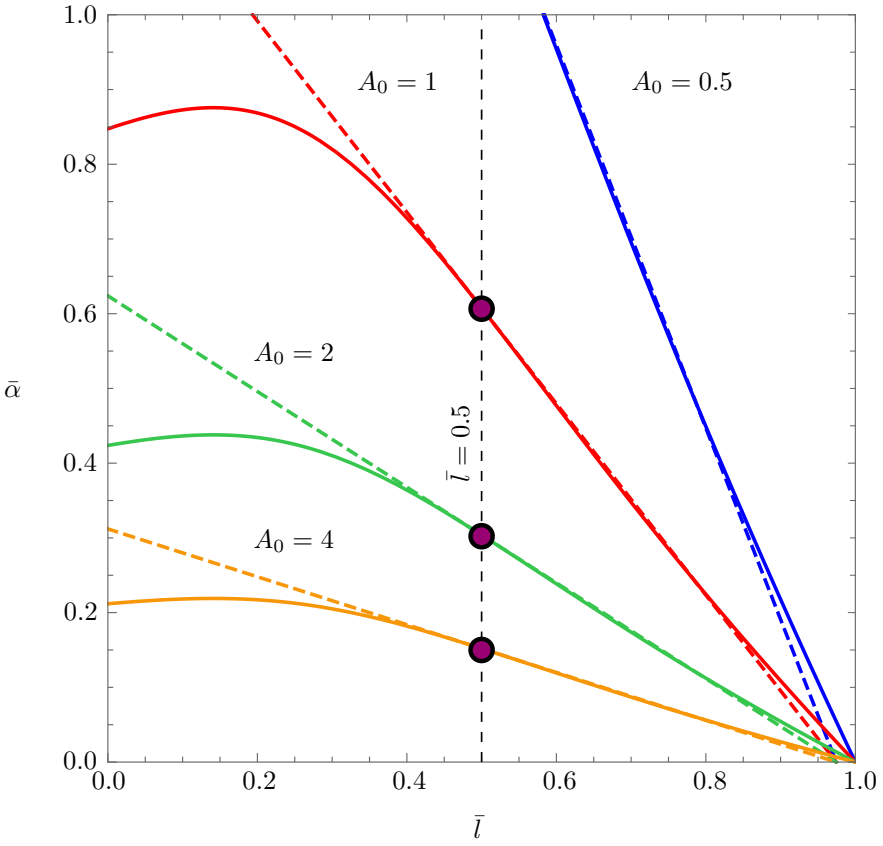

FIGURE 7.10: A comparison between the exact phase boundaries (*solid lines*) and the linear approximations at $\bar{l} = 0.5$ (*dashed lines*) for a number of aspect ratios of the unit cell A_0.

Let us now draw some generalisations for a plate with the large numbers of cut outs. If the number of the unit cells in the plate is sufficiently large and if we neglect the first and the last strips, such a plate may be regarded as an infinite chain similar to the chain of rigid rods discussed in Section 5.4 and in Section 5.6. Indeed, the structures of the stiffness matrix $\mathbf{K}$ of the plate with multiple cut outs given by Equation (7.30) and the tridiagonal matrix $\mathbf{C}$ in the case of a chain of rigid rods given by Equation (5.12) are very similar.

Let us first consider a case of strict periodicity, which corresponds to a cyclic chain. If the plate is infinitely wide, $b \to \infty$ but, instead of being flat, it is twisted in such a way that the two boundary strips are "glued" so that the plate appears as a cylinder with infinite radius $r \to \infty$

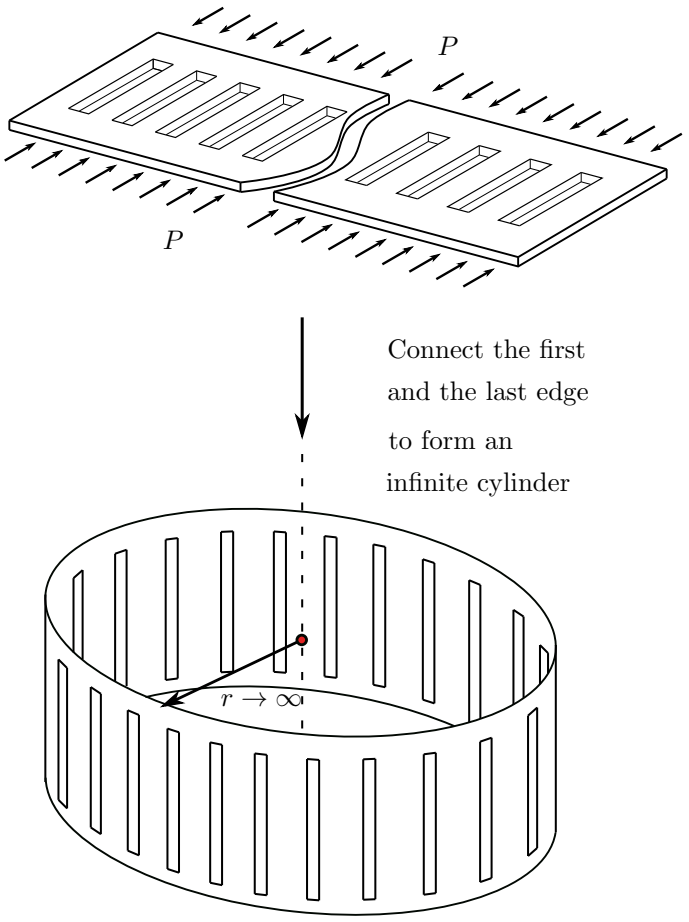

FIGURE 7.11: A schematic representation of the transformation of an infinitely wide plate into a cylinder of infinite radius.

as shown in Fig. 7.11. Such a transformation does not affect the underlying mechanics since the curvature of the cylinder is infinite, it can be still mathematically treated as a flat plate. However, by performing such a transformation, we manage to change the boundary conditions. We have eliminated the special cases for the first and the last strips by jointing them together. The corresponding rows and columns are thus deleted from the $\mathbf{K}$ and $\mathbf{K}_g$ matrices. Furthermore, since the first and the last strips are now essentially the same, the off-diagonal elements are $K_{1,N} = K_{N,1} = u_2$ and the stiffness matrix $\mathbf{K}$ becomes the circulant matrix while the geometric stiffness matrix $\mathbf{K}_g$ is the identity matrix $\mathbf{I}$ times a factor $2v_0$ obtained from Equation (7.22) as $12P/(5NL)$. Therefore, we can define a circulant matrix $\mathbf{C} = \mathbf{K}_g^{(-1)}\mathbf{K}$ with elements

$$c_1 = (u_0 + 2u_1)/v_0, \tag{7.48}$$

$$c_2 = u_2/(2v_0). \tag{7.49}$$

Here, u_0, u_1 and u_2 are given by Equation (7.15), Equation (7.16), and Equation (7.17) respectively. Elements c_1 are on the main diagonal, while elements c_2 are off-diagonal. Hence, the element c_1 reflects strip stiffness. It is the ratio of the total strip stiffness $u_0 + 2u_1$ and geometric stiffness v_0. The total strip stiffness is the stiffness of the strip u_0 plus the stiffness of coupling with the two neighbouring strips u_1. At the same time, element c_2 reflects the effect of pure coupling. It is defined as a ratio of coupling stiffness u_2 and twice the geometric stiffness $2v_0$.

Drawing analogies with the chain of coupled rigid rods discussed in Chapter 5, c_1 reflects the "total stiffness of a bay" and c_2 reflects the coupling between the bays.

The eigenvalues of $\mathbf{C}$ are the critical buckling loads of the structure, while the eigenvectors of $\mathbf{C}$ correspond to the mode shapes. Since $\mathbf{C}$ is the circulant matrix, we can employ the same logic as in the case of a chain of rigid rods in Section 5.4, e.g., calculate the eigenvalues and the eigenvectors using roots of unity. Consider m-th equation in the circulant EVP

$$c_2 q_{m-1} + c_1 q_m + c_2 q_{m+1} = P_n q_m,$$

where q_m is the generalised coordinate or buckling amplitude of m-th strip. A unique combination of q_m forms an n-th eigenvector $\boldsymbol{q}_n$, where $m = 1, \ldots, N+1$ and $n = 1, \ldots, N+1$. Assuming $q_m = Z_N^{mn}$ to be m-th root of unity and substituting into the chain rule, as well as scaling it by P_{cr} we can write a non-dimensional equation

$$\bar{c}_2 Z_N^{(m-1)n} + \bar{c}_1 Z_N^{mn} + \bar{c}_2 Z_N^{(m+1)n} = \bar{P}_n Z_N^{mn}. \tag{7.50}$$

Here, $\bar{c}_1 = c_1/P_{cr}$, $\bar{c}_2 = c_2/P_{cr}$ and $\bar{P} = P_n/P_{cr}$ are non-dimensional quantities. Dividing both sides by Z_N^{mn}, we express the $n-$th critical buckling load

$$\bar{P}_n = \bar{c}_1 + \bar{c}_2 \left(Z_N^{(-n)} + Z_N^{(n)} \right). \tag{7.51}$$

Recalling that n-th root of unity is expressed as a complex exponential, we can write

$$Z_N^{(-n)} + Z_N^{(n)} = \mathrm{e}^{-\frac{2\pi i(n+1)}{N}} + \mathrm{e}^{\frac{2\pi i(n-1)}{N}} = 2\cos\left(\frac{2\pi n}{N}\right). \tag{7.52}$$

Finally, Equation (7.51) is simplified and provides analytical solutions to the critical buckling loads, given by

$$\bar{P}_n = \bar{c}_1 + 2\bar{c}_2 \cos\left(\frac{2\pi n}{N}\right), \tag{7.53}$$

which is a cluster of modes with identical strip shapes but modulated phase across bays. We will call this cluster of modes as the *Instability cluster* of the infinite plate assuming that the first and the last strips are joined to form a circular chain of infinite radius. Here n is the mode number, $\varphi_n = \frac{2\pi n}{N}$ is the *general mode number* while the period of the cosine function is $N/2n$ and is analogous to the first Brillouin zone encountered in the context of a one-dimensional lattice. The component $\bar{c}_1$ is identical for all buckling loads while the distinction between $\bar{P}_n$ is given solely by $\bar{c}_2 \cos(\varphi_n)$ which reflects the effect of coupling. In the absence of coupling ($\bar{c}_2 = 0$), the circulant eigenvalue problem returns N identical critical buckling loads, which corresponds to the N-fold degeneracy. In the presence of coupling, the degeneracy is removed and the buckling loads are split into a cluster of N distinct values. The cluster structure depends on the sign and magnitude of the coupling term $\bar{c}_2$ in the EVP. The band structure refers to the distribution of critical buckling force within a cluster of modes. Typically, the coupling term appears constant and negative, such as the one derived from the spring energy in the chain of rigid rods in Section 5.4. Therefore, the instability cluster is defined by $\bar{P}_n = \bar{c}_1 - 2\bar{c}_2 \cos(\varphi_n)$ and is shown in Fig. 7.12 with a solid blue line. Its shape is similar to the shape of the instability cluster for a chain of rigid rods as depicted in Fig. 5.6. Such a cluster contains pairs of degenerate eigenvalues, meaning that only $N/2$ eigenvalues of the circulant matrix are distinct. Furthermore,

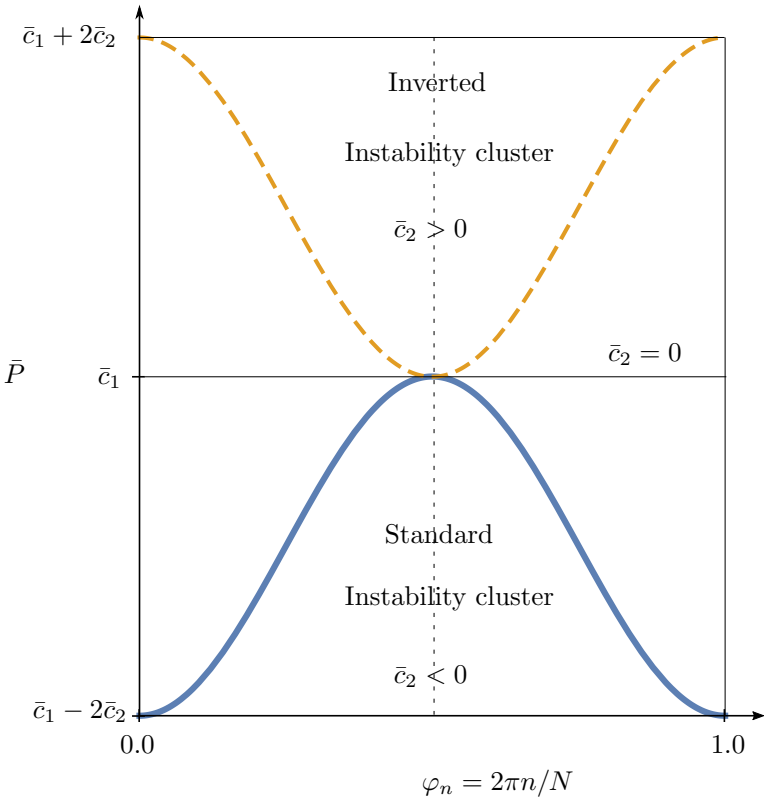

FIGURE 7.12: The standard instability cluster for negative coupling term $\bar{c}_2 < 0$ (blue curve). The inverted instability cluster for positive coupling term $\bar{c}_2 > 0$ (orange dashed line). The two clusters meet at the degeneracy point $\bar{c}_2 = 0$.

the smallest buckling loads are $\bar{P}_1$ and $\bar{P}_n$ and they correspond to the eigenvectors with no nodes (recall Fig. 5.6). The largest is the buckling load $\bar{P}_{N/2}$, which corresponds to the eigenvector with N nodes. Note, that for simplicity we assume N to be even. For odd N, the highest buckling load is $\bar{P}_{(N-1)/2}$ and the respective indexing is shifted by 1.

In our case, both $\bar{c}_1$ and $\bar{c}_2$ are continuous functions of $\bar{l}$ and $\bar{\alpha}$ parameters. Therefore, $\bar{c}_2$ may be negative, zero or positive depending on the structural parameters. The case of $\bar{c}_2 < 0$ is previously discussed and gives the instability cluster shown with the blue line in Fig. 7.12. If $\bar{c}_2 = 0$, we have an N-fold degeneracy (see the horizontal line corresponding to $\bar{P}_n = \bar{c}_1$ in Fig. 7.12). But, if $\bar{c}_2 > 0$, the cluster equation is written as $\bar{P}_n = \bar{c}_1 + 2\bar{c}_2 \cos(\varphi_n)$ and the cluster is inverted as shown in Fig. 7.12 with orange dashed line. Indeed, when $n = 0$ and $n = N$, $\varphi_n = 0$ and $\bar{P}_1 = \bar{P}_N = \bar{c}_1 + 2\bar{c}_2$ which are the largest buckling loads of the instability cluster. On the other hand, $\bar{P}_{N/2} = \bar{c}_1$ is the smallest buckling load in this cluster. Since the eigenvectors are associated with the same eigenvalues before and after the crossing point, the mode with N nodes corresponds to the lowest buckling load and the modes with 0 nodes correspond to the largest buckling loads $\bar{P}_1$ and $\bar{P}_N$ after the crossing point.

Let us check where the coupling term $\bar{c}_2$ changes its sign on the $\bar{l} - \bar{\alpha}$ plane. The dependence of $\bar{c}_2$ on structural parameters is due to $\bar{u}_2$ term, which is obtained by scaling the expression of u_2 given in Equation (7.17) by $P_{cr} = 40AD/L$, and we will inspect its sign here. The plot of the values of $\bar{u}_2$ versus $\bar{l}$ and $\bar{\alpha}$ is shown in Fig. 7.13. It is apparent that $\bar{u}_2$ increases from the negative values for small $\bar{l}$ and $\bar{\alpha}$ up until it reaches zero along a red curve (derived from the

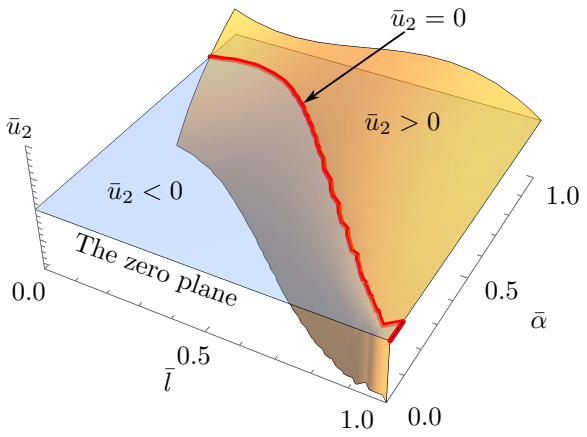

FIGURE 7.13: Surface plot of the magnitude of $\bar{u}_2$ as a function of the structural parameters $\bar{l}$ and $\bar{\alpha}$. It shows the alteration of coupling sign upon traversing a curve of $\bar{u}_2 = 0$.

intersection of the $\bar{u}_2$ surface with the zero plane) and then becomes positive for larger values of $\bar{l}$ and $\bar{\alpha}$. Finally, $\bar{u}_2$ reaches zero again along the line of $\bar{l} = 1$. It is easy to see, that the red curve and the case of $\bar{l} = 1$ are exactly the same as the solutions of $\bar{P}_1 = \bar{P}_2$ or $\bar{P}_2 = \bar{P}_3$ for the case of a plate with two cut outs. Therefore, the condition of $u_2 = 0$ is another condition that could be used to calculate the phase boundaries as all the buckling loads become equal only in the case of $N-$fold degeneracy which happens only when the coupling vanishes. This also shows that the phase boundary is independent of the number of cut outs and is the same for a plate and for our artificially constructed case i.e. a cylinder with infinite radius.

Returning to the original problem of a flat plate with N cut outs for which a simple formula for the eigensolution is not available. Instead, we substitute discrete values from the intervals $0 \leq \bar{l} \leq 1$ and $0 \leq \bar{\alpha} \leq 1$ into Equation (7.29) and compute the eigensolution at each step numerically. Fig. 7.14(a) contains scaled critical buckling load surfaces $\bar{P}_i$ $(i = 1, \ldots, N)$ for a plate with 9 cut outs plotted as a function $\bar{l}$ and $\bar{\alpha}$ for a fixed unit cell aspect ratio $A_0 = 1$. The magnitudes of $\bar{P}$ are plotted in logarithmic scale to make visualisation clearer. It is apparent that all the surfaces of $\bar{P}$ cross along the same spatial curve (red curve in Fig. 7.14(a)) which defines the boundary on the $\bar{l}-\bar{\alpha}$ plane (see Fig. 7.14(b)) that separates the region of parameters for which the two different buckling characters are observed.

Consider the cross-section of the surface plot in Fig. 7.14(a) by the plane $\bar{\alpha} = 0.5$ and the plane $\bar{l} = 0.5$. The locations of the slicing planes on the surface plot in Fig. 7.14(a) are indicated with the dotted lines. The projections of the surfaces on the slicing planes are depicted in Fig. 7.14(c) and Fig. 7.14(d) respectively. The slices contain the trajectories of the scaled critical buckling loads $\bar{P}_i$ as functions of $\bar{l}$ (subplot (c)) and as functions of $\bar{\alpha}$ (subplot(d)). The trajectories of $\bar{P}_1$ (red), $\bar{P}_2$ (grey) and $\bar{P}_N$ (dark blue) are indicated on the plots, while the rest $\bar{P}_3, \ldots, \bar{P}_{N-1}$ lie within the shaded area.

Let us follow the trajectories in Fig. 7.14(c) and Fig. 7.14(d) from left to right. The points on the trajectories for any fixed value of the parameter ($\bar{l}$ or $\bar{\alpha}$) collectively define the first buckling band of the plate. We pick an arbitrary value of ($\bar{l}$ or $\bar{\alpha}$) to the left of the crossing point and label the critical buckling loads by their magnitude $\bar{P}_1, \bar{P}_2, \ldots, \bar{P}_N$. The buckling bands that they form are depicted with the red dots in the upper right subplots in Fig. 7.14(c) and Fig. 7.14(d).

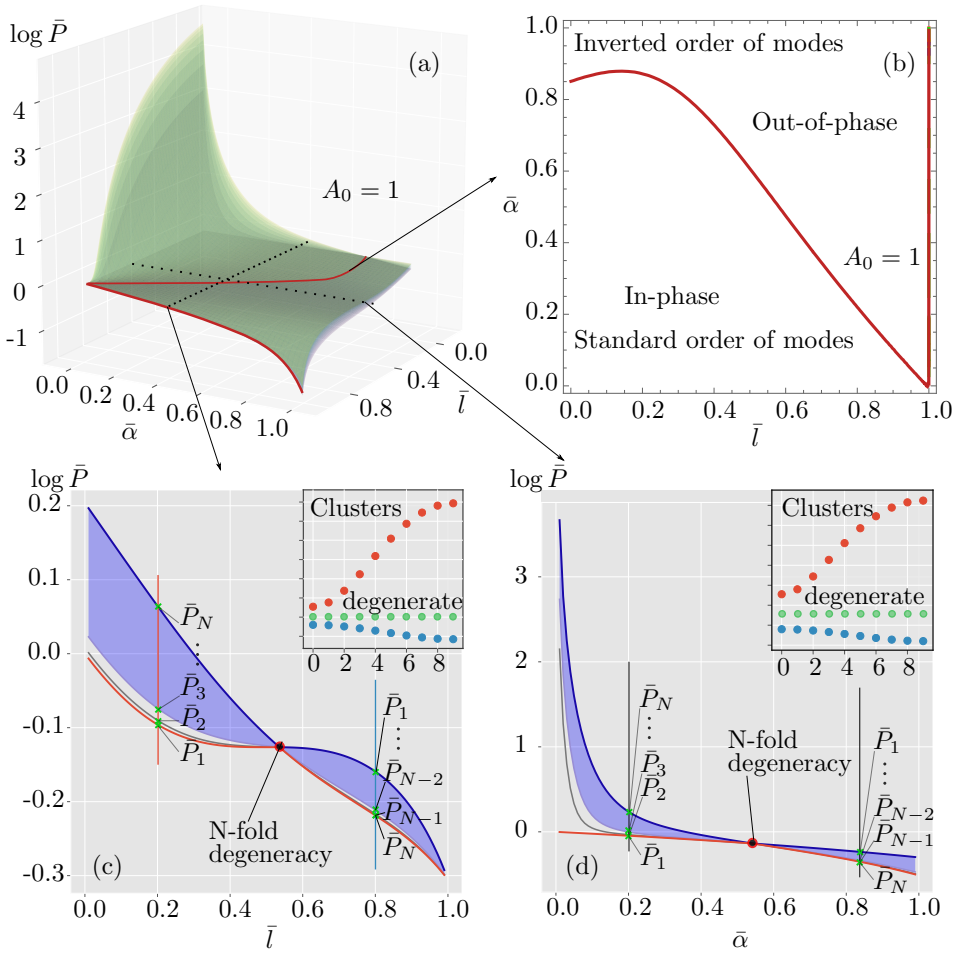

FIGURE 7.14: Inversion of instability clusters via N-fold degeneracy. (a) Crossing of 10 critical buckling load surfaces ($\bar{P}$) for $A_0 = 1$ along a red curve. (b) The crossing curve defines a phase boundary in $\bar{l}$-$\bar{\alpha}$ plane. The standard order of modes starting from in-phase buckling is in Phase A. Inverted order of modes starting from out-of-phase buckling is in Phase B. (c) The section view of the surfaces of $\bar{P}$ sliced by a plane $\bar{\alpha} = 0.5$. (d) reveals the N-fold crossing of buckling load trajectories as functions of $\bar{l}$. (d) A slice of the surfaces of $\bar{P}$ by a plane $\bar{l} = 0.5$ reveals the N-fold crossing of buckling load trajectories as functions of $\bar{\alpha}$. The instability clusters for the three chosen points are shown within the subplots in (c) and (d).

Note, that the band (cluster) in this case is exactly the left half of the symmetric buckling band (cluster) depicted in Fig. 7.12 with the blue line. This is natural as the tridiagonal matrix $\mathbf{K}$ is no longer circulant and its eigenvalues are all distinct. The scattered points nicely fit a cosine trend with half the period of the circulant matrix. This is apparent since the eigenvalues of the infinite chain are known exactly and are governed by $\cos\varphi_n$, where φ_n is half of that for a cyclic chain. This is shown by Equation (5.32). Therefore,

$$\bar{P}_n = \bar{c}_1 - 2\bar{c}_2 \cos\frac{\varphi_n}{2}. \tag{7.54}$$

The associated mode structure is shown in Fig. 7.15. The mode order is now reversed and can be compared with that in Fig. 7.16. Note that modes for P_{N-1}, P_{N-2} etc. are not shown, but they resemble modes for P_2, P_3, ..., etc. As we approach the crossing point, the coupling term vanishes $\bar{c}_2 = 0$ and the distinct buckling loads become degenerate $\bar{P}_n = \bar{c}_1$ as shown by the green dots in the upper right subplots in Fig. 7.14(c) and Fig. 7.14(d). Finally, as we move

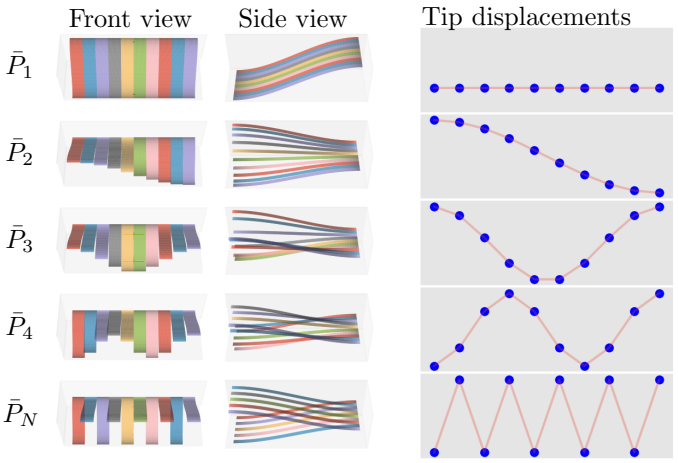

FIGURE 7.15: Extended modes (front view, side view and schematic view) of the plate with $N = 10$ strips for $\bar{l} = 0.4$ and $\bar{\alpha} = 0.4$. The plate exhibits the standard order of modes, e.g., the in-phase mode corresponds to the lowest buckling load $\bar{P}_1$, while the out-of-phase mode corresponds to the highest load $\bar{P}_N$.

to the right of the crossing point, the buckling loads separate and form a new buckling band (blue dots), which appears to be inverted exactly as the left half of the symmetric buckling band (cluster) depicted in Fig. 7.12 with the orange dashed line. In fact, the inverted band is well approximated by

$$\bar{P}_n = \bar{c}_1 + 2\bar{c}_2 \cos \frac{\varphi_n}{2}, \tag{7.55}$$

and the associated mode structure is depicted in Fig. 7.16.

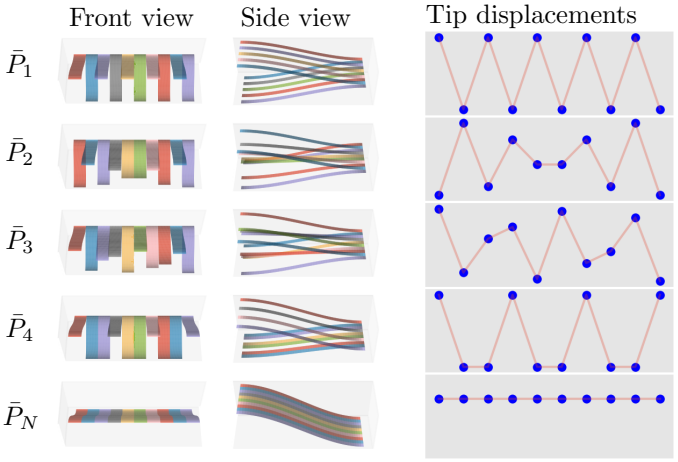

FIGURE 7.16: Extended modes (front view, side view and schematic view) of the plate with $N = 10$ strips for $\bar{l} = 0.8$ and $\bar{\alpha} = 0.8$. The plate exhibits the inverted order of extended modes. The out-of-phase mode corresponds to the lowest buckling load $\bar{P}_1$, while the in-phase mode corresponds to the highest buckling load $\bar{P}_N$.

Therefore, we can conclude that the standard order of buckling states is characterised by buckling loads from the buckling band defined by $\bar{P}_n = \bar{c}_1 - 2\bar{c}_2 \cos(\varphi_n)$ for negative coupling. Mechanically this implies that the energy cost of the deformation due to coupling should be added to the cost of bending deformation. Therefore, the modes with a higher level of coupling deformation have higher buckling loads. Contrary to this, the inverted order of buckling states is characterised by the buckling loads from the inverted buckling band (cluster) defined by $\bar{P}_n = \bar{c}_1 + \bar{c}_2 \cos(\varphi_n)$

for positive coupling. Mechanically this implies that the energy cost of the deformation due to coupling should be subtracted from the cost of bending deformation. Therefore, the modes with the higher coupling contribution are energetically "cheaper" and have lower buckling loads. The boundary between the two phases is defined by the absence of coupling which implies that all the buckling states are degenerate. In case of steel with $\nu = 0.3$ The boundary shape can be represented by a straight line in $\bar{l} - \bar{\alpha}$ coordinate defined by a negative slope of $-1/A_0$, where A_0 is the aspect ratio of the unit cell – $A_0 = A/N$. In the case of a generic material, the slope of the linearised phase boundary also depends on Poisson ratio ν and is given by Equation (7.45).

7.3 Elastic stability of a periodic plate with irregularities

While the perfectly ordered periodic structure like those studied in the last section is a good model to gain insight into the essential physical mechanisms driving the behaviour, many real-life structures are rarely perfectly periodic due to material inhomogeneity, inevitable manufacturing tolerances, etc. Therefore, one has to study how the deviation of the behaviour from the perfect case manifests itself in real structures. From the previous discussion in Chapter 5, we see that even small disorder can have a dramatic effect on the structural behaviour in the cases when the coupling between structural members is small. In this section, we demonstrate that the structural sensitivity to the disorder in the case of a plate with multiple cut outs varies dramatically with the parameters $\bar{l}$ and $\bar{\alpha}$. We will also present a map of the strength of sensitivity of the structure to the disorder.

The plate with a perfectly ordered arrangement of cut outs from the previous section is now perturbed by the introduction of a small disorder. We also assume that the number of cut outs N is large and that the first and the last strips can be neglected. Also, consider that the generalised EVP given by Equation (7.29) is transformed to a standard one by inverting the geometric stiffness matrix and multiplying both sides by it $\mathbf{K}_g^{-1}\mathbf{K}\mathbf{q} = P\mathbf{q}$. Therefore, we have a system matrix $\mathbf{A} = \mathbf{K}_g^{-1}\mathbf{K}$ with the elements on the main diagonal

$$A_{ii} = \frac{u_0 + 2u_1}{v_0} + \varepsilon\delta_i \frac{u_0 + 2u_1}{v_0}, \tag{7.56}$$

and the off-diagonal coupling terms given by

$$A_{ij} = u_2/v_0. \tag{7.57}$$

Here we introduced a random perturbation of magnitude $\varepsilon\delta_i$, where δ_i are taken from the gaussian distribution with zero mean and standard deviation 1, ε is the parameter that controls the magnitude of the disorder. For simplicity, we assume that only the main diagonal elements are perturbed while the coupling is unchanged.

Using the previously derived formulas for the buckling clusters, we can get a feel for how buckling loads will change under such perturbation immediately. Recall that depending on the sign of the coupling term, the buckling loads in the case of the infinite chain are $P_n = \bar{c}_1 \pm 2\bar{c}_2 \cos\varphi_n$. In the disordered case, this should change to $P_n = c_{1n} \pm 2\bar{c}_2 \cos\varphi_n$, where $c_{1n} = \bar{c}_1 + \varepsilon\delta_n\bar{c}_1$ are now different for each n due to the random term $\varepsilon\delta_n$. If $\bar{c}_2 \gg \bar{c}_1$ and $\varepsilon \ll 1$ (consistent with the small disorder), we should expect the small disorder to have little effect on critical buckling loads. If,

however, $\bar{c}_2 \approx \bar{c}_1$, the disorder should play out significantly. In the extreme case when $\bar{c}_2 = 0$, which corresponds to the phase boundary, even infinitesimally small but non-zero disorder will have the most significant effect. When there is no disorder, the phase boundary is the curve on which all the eigenvalues of Equation (7.29) are degenerate and equal $P_n = \bar{c}_1$. In the perturbed case, the same eigenvalues would be equal $P_n = c_{1n} = \bar{c}_1 + \varepsilon\delta_n$ which corresponds to the splitting of the eigenvalues by shifting their magnitudes by $\varepsilon\delta_n$. Hence, in the disordered case, we expect that the buckling load trajectories will exhibit a strong avoided crossing behaviour in the vicinity of zero coupling and arbitrarily small disorder.

To demonstrate this behaviour for a real structure, we numerically solved the parametric eigen-

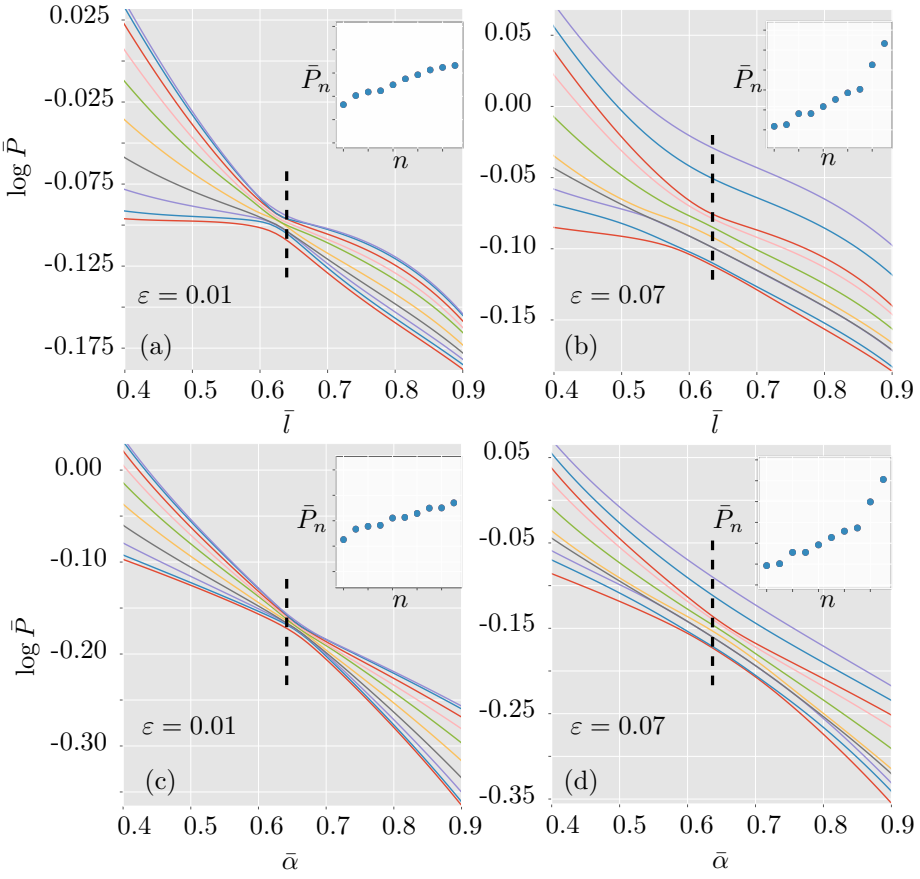

FIGURE 7.17: Critical buckling load trajectories for different magnitudes of disorder in logarithmic scale. (a) Buckling loads as functions of $\bar{l}$ for $\varepsilon = 0.01$. (b) Buckling loads as functions of $\bar{l}$ for $\varepsilon = 0.07$. (c) Buckling loads as functions of $\bar{\alpha}$ for $\varepsilon = 0.01$. (d) Buckling loads as functions of $\bar{\alpha}$ for $\varepsilon = 0.07$. The subplots show the instability clusters in the point of near degeneracy (indicated by a dashed line).

value problem with a disorder representing a plate with $N = 10$ cut outs. We vary structural parameters $\bar{l}$ and $\bar{\alpha}$ in the usual range $[0, 1]$ as well as change the disorder magnitude $\varepsilon \in [0.01, 0.1]$ picking values of δ_i from a Gaussian distribution ($\mu = 0$, $\sigma = 1$) at each step in ε. We plot the computed buckling load trajectories as functions of $\bar{l}$ in Fig. 7.17 (a)–(b) and as functions of $\bar{\alpha}$ in Fig. 7.17 (c)–(d). The plots are presented for the two selected magnitudes of disorder, i.e., $\varepsilon = 0.01$ as shown in Fig. 7.17 (a)–(c) and $\varepsilon = 0.07$ as shown in Fig. 7.17 (b)–(d). We show the curves in a narrow window of the parameters $[0.4, 0.9]$ accentuating the former crossing point to demonstrate the effect of the disorder where it is most prominent. We also extract the magnitudes of the buckling loads for the parameter values indicated by vertical dashed lines. The

scatter of buckling load magnitudes depending on their sequential number are then plotted in the white subfigures in the top right corner of each plot. This is done to demonstrate how the shape of the first buckling cluster changes with the disorder.

It is apparent from the numerically computed trajectories that the structure is ultimately sensitive to the disorder in the vicinity of the former crossing point. Even for a very small disorder $\varepsilon = 0.01$, the degeneracy is removed as the buckling loads are split due to disorder and the avoided crossing of the buckling load trajectories via high curvature veering becomes evident. Note, that the effect of the small disorder is local and most prominent only in the vicinity of the former crossing point. The trajectories increasingly resemble those of the perfectly ordered structure as we move away from the zero coupling region. On the other hand, as the disorder increases (see Fig. 7.17 (b)–(d)), it progressively shifts the trajectories increasing the separation between them. Trajectories for higher buckling loads appear to be well separated even for relatively small disorder $\varepsilon = 0.07$.

In the case of the perfectly ordered plate, we observed that the eigenvectors of Equation (7.29) were parameter independent and stayed associated with their eigenvalues, thus, allowing inversion of the mode order as the buckling cluster was inverted upon traversing the phase boundary. In a disordered case, the symmetry of the EVP is not preserved and the buckling modes are expected to undergo localisation characterised by the amplitude modulation being distorted and the resultant modes changing their character dramatically. To quantify the effect of disorder on the strength of localisation and to understand how it affects the previously proposed phase diagram, we proceed by calculating localisation factors of Lyapunov exponents depending on ε.

Similar to Chapter 5, we start by constructing the transfer matrix which defines the variation of the buckling amplitude from the unit cell to the unit cell. The relation between a vector of generalised coordinates $[q_{n-1}, q_n]$ and $[q_n, q_{n+1}]$ is obtained from the chain rule

$$\frac{u_2}{2v_0} q_{n-1} + \left[\frac{u_0 + 2u_1}{v_0}(1 + \varepsilon\delta_n)\right] q_n + \frac{u_2}{2v_0} q_{n+1} = P_n q_n, \tag{7.58}$$

or, we can write this in a non-dimensional variable by scaling P_{cr} and rearranging by bringing P_n term to the right,

$$\frac{\bar{u}_2}{2} q_{n-1} + \left[(\bar{u}_0 + 2\bar{u}_1)(1 + \varepsilon\delta_n) - \bar{P}_n\right] q_n + \frac{\bar{u}_2}{2} q_{n+1} = 0. \tag{7.59}$$

Expressing q_{n+1} and q_n in terms of q_n and q_{n-1}, we write

$$\begin{bmatrix} q_{n+1} \\ q_n \end{bmatrix} = \begin{bmatrix} -\frac{2(\bar{u}_0 + 2\bar{u}_1)(1+\varepsilon\delta_n)}{\bar{u}_2} + \frac{2\bar{P}_n}{\bar{u}_2} & -1 \\ 1 & 0 \end{bmatrix} \begin{bmatrix} q_n \\ q_{n-1} \end{bmatrix}. \tag{7.60}$$

Thus, the matrix relating $\mathbf{q}_n$ to $\mathbf{q}_{n-1}$, i.e. transfer matrix is given by the coefficient matrix on the right side of the equation above. We label $2(\bar{u}_0 + 2\bar{u}_1)(1 + \varepsilon\delta_n)$ as $\tilde{u}_0$ and include factor 2 in $\bar{P}_n$. Thus, we can write the transfer matrix in a compact form

$$\mathbf{T} = \begin{bmatrix} -\frac{\tilde{u}_0}{\bar{u}_2} + \frac{\bar{v}_0 \bar{P}_n}{\bar{u}_2} & -1 \\ 1 & 0 \end{bmatrix}. \tag{7.61}$$

In the case of a perfectly ordered plate, all the transfer matrices are identical and the transition from $\mathbf{q}_N$ to $\mathbf{q}_1$ is given by

$$\mathbf{q}_N = \mathbf{T}^{N-1}\mathbf{q}_1. \tag{7.62}$$

According to Furstenberg's theorem, the localisation factor $\lambda > 0$ is the limit given by Equation (5.39). Therefore, we can relate eigenvalues of $\mathbf{B}^\top\mathbf{B}$, where $\mathbf{B} = \prod_n^{N-1}\mathbf{T}_n$ to the Lyapunov exponents λ_1 and λ_2 via Equation (5.42) and Equation (5.43). It has been shown in Section 5.6 that eigenvalues of $\mathbf{B}^\top\mathbf{B}$ are $e_1 = |\Lambda_{1,1}|^{N-1}$, $e_2 = |\Lambda_{2,2}|^{N-1}$, where $\Lambda_{1,1}$ and $\Lambda_{2,2}$ are eigenvalues of $\mathbf{T}$, expressions for which are

$$\Lambda_{1,2} = \frac{\bar{P}_n - \tilde{u}_0 \mp \sqrt{\left(\bar{P}_n - \tilde{u}_0\right)^2 - 4u_2}}{2u_2}. \tag{7.63}$$

Therefore, the Lyapunov localisation factors are given by

$$\lambda_{1,2} = \operatorname{sgn}(\Lambda_{1,2}) \ln|\Lambda_{1,2}|. \tag{7.64}$$

According to Equation (7.64) and Equation (7.63), the localisation factor depends on both the compressive load P_n and the effective stiffness of a unit cell $\tilde{u}$, which also accounts for the effect of disorder and coupling strength u_2. Recall, that $\tilde{u}_0$ and $\bar{u}_2$ are functions of $\bar{l}$ and $\bar{\alpha}$. Therefore, the localisation factors depend on structural parameters.

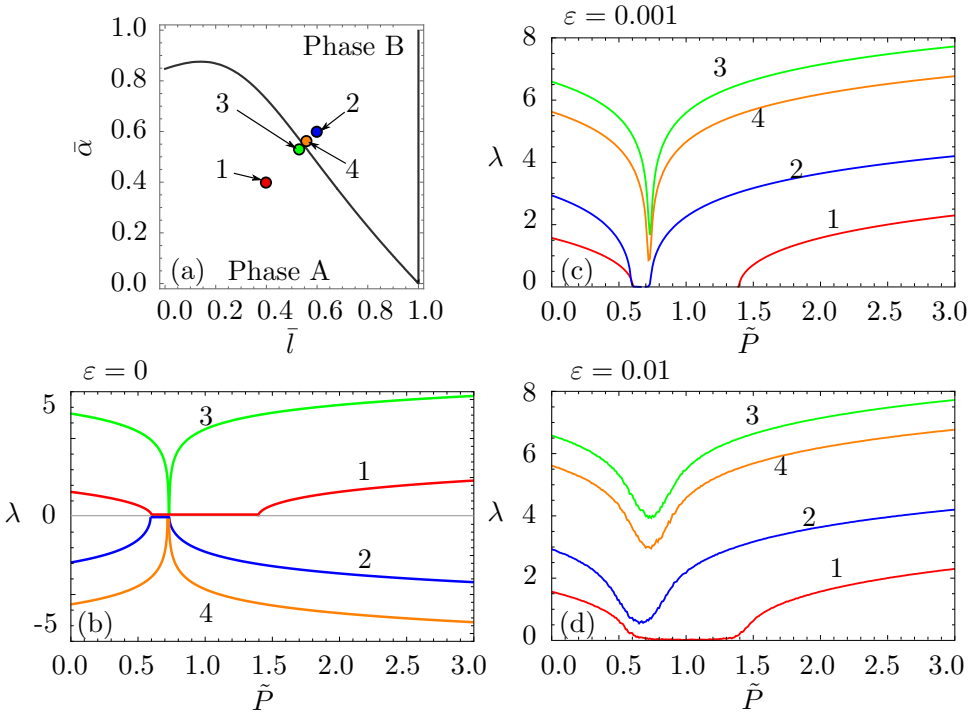

FIGURE 7.18: The localisation factors for the plates associated with the specific points on the phase diagram. (a) The phase diagram for a plate with the aspect ratio of the unit cell $A_0 = 1$. Four selected points on the phase diagram are labelled with dots and numbers $1, 2, 3$ and 4. (b) Lyapunov localisation factors the ordered case ($\varepsilon = 0$) for each selected point labelled $1, 2, 3$, and 4 respectively. (c) Lyapunov localisation factors for the case of disorder $\varepsilon = 0.001$ for the same points. (d) Lyapunov localisation factors for disorder $\varepsilon = 0.01$ for the same points.

We start by selecting several points on the phase diagram for a plate with $N = 10$ cut outs and the aspect ratio of each unit cell $A_0 = 1$. Localisation factors are calculated for each of the four selected points shown in Fig. 7.18 (a) with the numbered dots. Then, we calculate the largest Lyapunov localisation factors λ_1 for each point and plot them as functions of P_n for $\varepsilon = 0$ as shown in Fig. 7.18.

We have deliberately chosen point 1 to be well within the phase with the standard order of modes, point 2 to be within the phase of the inverted order of modes and points 3 and 4 to lie close to the phase boundary. Now we study the behaviour of localisation factors for a perfect case with the help of Equation (7.63) and Equation (7.64). Consider the values that the expression under the square root in Equation (7.63) can take.

If $\left(\bar{P}_n - \tilde{u}_0\right)^2 - 4\bar{u}_2 > 0$:

$$\bar{P}_n < \tilde{u}_0 - 2\bar{u}_2, \tag{7.65}$$

$$\bar{P}_n > \tilde{u}_0 + 2\bar{u}_2, \tag{7.66}$$

which corresponds to $\lambda_1 \in \mathbb{R}$. In this case, $\lambda_1 > 0$ if $\bar{u}_2 < 0$ which corresponds to cases 1 and 3 in Fig. 7.18 (a),(b) and $\lambda_1 < 0$ if $\bar{u}_2 > 0$ which corresponds to cases 2 and 4 in Fig. 7.18 (a),(b). However, as P_n are outside of the buckling band, either no buckling occurs where $\bar{P}_n < \tilde{u}_0 - 2\bar{u}_2$ or the structure has already buckled for $\bar{P}_n > \tilde{u}_0 - 2\bar{u}_2$.

If $\left(\bar{P}_n - \tilde{u}_0\right)^2 - 4\bar{u}_2 = 0$:

$$\bar{P}_n = \tilde{u}_0 \pm 2\bar{u}_2, \tag{7.67}$$

which corresponds to the boundaries of the instability clusters in Fig. 7.12, where the smaller of P_n corresponds to the first buckling load of the standard cluster and the larger P_n corresponds to the first buckling load of the inverted cluster. If $\bar{u}_2 = 0$ and there is no disorder, all $P_n = \tilde{u}_0$ and the buckling band (cluster) degenerates into a single point as shown by 3 and 4 in Fig. 7.12 (b). Lyapunov exponents do not exist for these points.

If $\left(\bar{P}_n - \tilde{u}_0\right)^2 - 4\bar{u}_2 < 0$, we get $\bar{P}_n$ bound within the range

$$\tilde{u}_0 - 2\bar{u}_2 < \bar{P}_n < \tilde{u}_0 + 2\bar{u}_2, \tag{7.68}$$

which corresponds to the standard and the inverted buckling bands (clusters) in Fig. 7.12. Lyapunov exponents are complex in this case. and no localisation occurs as the disorder is set to zero. Instead, buckling mode undergoes amplitude modulation governed by the imaginary part of the root of unity Z_N^n, where n is the mode number.

Essentially, Lyapunov exponents defined by Equation (7.63) and Equation (7.64) carry the complete information about the extendedness or spatial localisation of modes. When there is no disorder, $\lambda_1 \in \mathbb{R}$ and the sign of λ_1 is consistent with the phases as $\lambda_1 > 0$ reflects the standard buckling cluster while $\lambda_1 < 0$ reflects the inverted buckling cluster. The region of $\bar{P}$ for which $\lambda_1 \in \mathbb{C}$ characterises the buckling cluster, its width being governed by the magnitude of the coupling term $\bar{u}_2$. On the phase boundary, the cluster degenerates into a single value $P_n = \tilde{u}_0$, which is associated with a single point on the $\lambda - P_n$ plot where λ_1 does not exist.

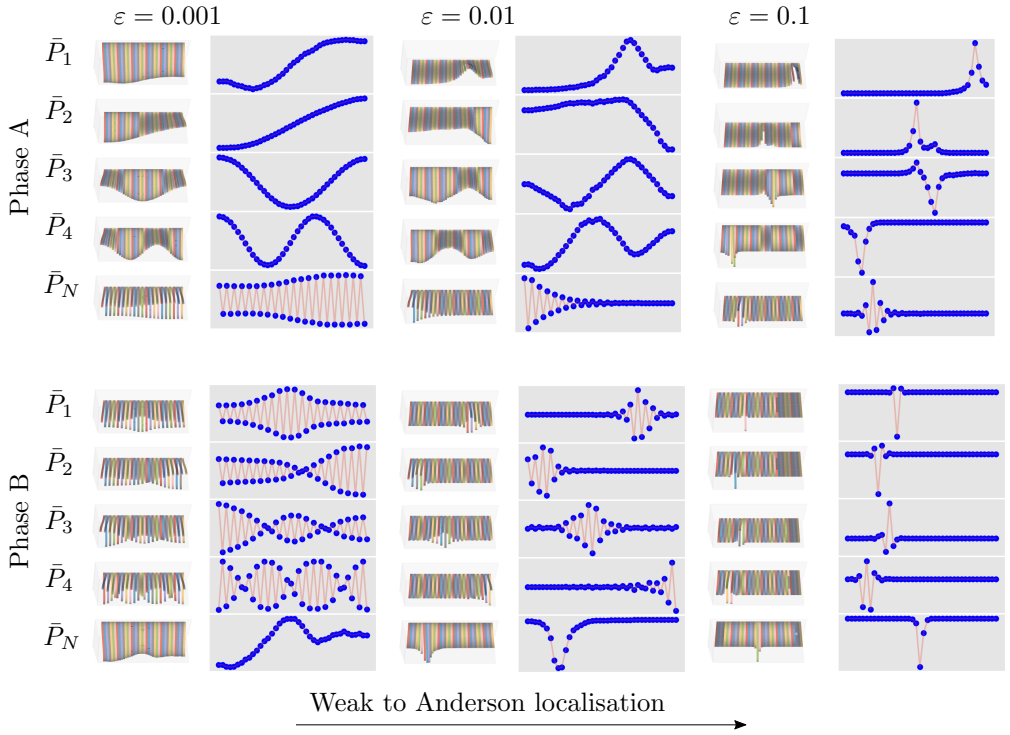

FIGURE 7.19: Transition from weak to strong or Anderson localisation in a plate with multiple cut outs with the disorder. The top row of plots shows buckling modes of a structure in Phase A of the phase diagram for a small disorder, moderate disorder and large disorder. The bottom row of plots shows the buckling modes of a structure in Phase B for the respective disorder magnitudes.

As a small disorder $\varepsilon\delta_n$ is introduced, the Lyapunov localisation factors have to be computed numerically as each $\mathbf{T}$ is different due to the perturbation in $\tilde{u}_0$. Picking δ_n from the normal distribution with $\mu = 0$ and $\sigma = 1$ and $\varepsilon = 0.001$ and $\varepsilon = 0.01$ for a plate with $N = 1000$ cut outs, we calculate a norm of the dot product of transfer matrices and divide it by the number of unit cells according to the Furstenberg's theorem to estimate the magnitude of λ_1. The plots of the localisation factors as functions of $\bar{P}$ are depicted in Fig. 7.18 (c) for $\varepsilon = 0.001$ – a very small disorder and Fig. 7.18 (d) – a moderate disorder. Each curve on the plots is associated with a selected point on the phase diagram in Fig. 7.18 (a). Even a very small disorder dramatically increases localisation in the structures with near-zero coupling as indicated by the curves 3 and 4 while being mostly irrelevant for the structures with larger coupling as shown by curves 1 and 2 in Fig. 7.18 (c). An arbitrarily small disorder drives all localisation factors to become positive (compare the negative λ curves in Fig. 7.18 (b) versus all positive λ curves in Fig. 7.18 (c)). This is associated with the crossing of the buckling load trajectories being replaced by veering. In this case, not all trajectories exchange the associated eigenvectors as some may be well separated as shown in Fig. 7.17. In this case, the inverted buckling cluster appears distorted and the associated modes are subject to strong localisation even for a relatively small disorder. As the disorder increases (see Fig. 7.18 (d)), the λ curves 1 and 2 also become non-zero, which corresponds to localisation occurring in the structures with larger coupling. An example of the mode structure of a plate with $N = 40$ cut outs for various levels of disorder $\varepsilon = 0.001$, $\varepsilon = 0.01$ and $\varepsilon = 0.1$ are shown in Fig. 7.19.

7.4 Conclusions

In this chapter, we studied the problem of elastic stability of a plate with multiple nominally identical regularly placed cut outs. The choice of the functions approximating the out-of-plane displacement of the plate in buckling allowed us to construct the simplest possible energy expressions that still carry all the essential physics of the problem. Thus, the application of the minimum total potential energy principle leads to the generalised eigenvalue problem with a tridiagonal stiffness matrix and a diagonal geometric stiffness matrix. We solved such an EVP for various numbers of cut outs and report that two characteristic types of behaviour exist. The first type is in-phase buckling described by all strips deflecting cooperatively. While the second type is out-of-phase buckling described by the alternating strips deflecting competitively in the opposite directions. These two types correspond to the boundaries of the instability cluster of the plate – a dense spectrum of the EVP, whose eigenvalues correspond to the modes with the spatially modulated amplitude of each strip. We mapped the two characteristic types of behaviour to the plane of cut out length and cut out width and obtained a phase diagram with the slope of the phase boundary being proportional to one over the aspect ratio of the unit cell.

Then we explored the generalised EVP of the problem for N cut outs and report that all the eigenvalue trajectories (surfaces) within the instability cluster cross over the line of N-fold degeneracy which is the phase boundary. After the crossing, the entire cluster appears inverted and the previously lowest (highest) mode becomes the highest (lowest) one after the inversion. This occurs because the off-diagonal term in the system matrix changes its sign via zero which takes place over the phase boundary.

Such a strict inversion takes place only in the perfectly ordered scenario. We demonstrate that even the smallest perturbation causes strong repulsion of the eigenvalue trajectories (surfaces) at the phase boundary. While this has a moderately weak effect on the structures with in-phase buckling as the lowest mode, the structures with out-of-phase buckling the lowest response exhibit strong localisation and the extended mode does not occur. Therefore, for the real-life structures, the proposed phase diagram maps the regions of in-phase buckling and strong localisation on the cut length – cut width plane. Thus, when designing such plates, one can use such a phase diagram to find the optimal parameters that ensure that behaviour ambiguity is avoided. It is expected that some of the features of the behaviour may be exhibited by other practical structural problems that possess spatial periodicity as a feature, e.g. stiffened plates.

Chapter 8

Elastic stability of mitotic spindles

In the previous chapters, we presented the elastic stability of two coupled structures and also a chain of nominally identical slender members. The deviations from perfect regularities were assumed to be small and consistent with the small perturbation theory which greatly simplified the mathematics and even allowed several analytical solutions to be obtained that were previously unknown in the context of structural buckling.

While the previous research proved to be applicable to industrially manufactured structures, our previous assumptions of periodicity, or near periodicity are not easily applicable to some highly irregular structures, such as those appearing in living organisms, since biological structures encountered in nature often display considerable departures from regularity. In many cases, living organisms function by the laws of mechanics, and, in particular, they benefit from controlled buckling, where buckling mode localisation may be regarded as one of the enabling mechanisms for certain biological functions. A remarkable example, when living organisms are able to not just withstand extreme levels of compression but also evolved to benefit from it, is that of cell division – a key biological mechanism and a part of a cycle of life of a cell.

8.1 Principles of mitosis

Here we review relevant literature in a biological context which was not covered in Chapter 2. First, we characterise mitosis – a cell division mechanism – following which, a cell divides its genetic information between the two daughter cells and ensures that they are genetically identical to the parent cell [Bernfield and Slack, 2019]. Then, we present the literature focused on the role of mechanics, particularly, on the elastic stability of the sub-cellular structures that play a key role in mitosis. We also explain how the mechanics studied in the previous chapters may be relevant to mitosis and what biological function it brings. Finally, we describe a custom made software that incorporates the mechanics presented here – SpindleFEA [Iakovliev et al., 2019] and report the preliminary results of modelling the cellular cytoskeleton in mitosis.

Mitosis is a highly complex and extremely reliable process of splitting a parent cell into two daughter cells ensuring exact cloning of the parent DNA (chromosomes) between the daughter cells [Bernfield and Slack, 2019]. The remarkable precision and reliability of mitosis depends,

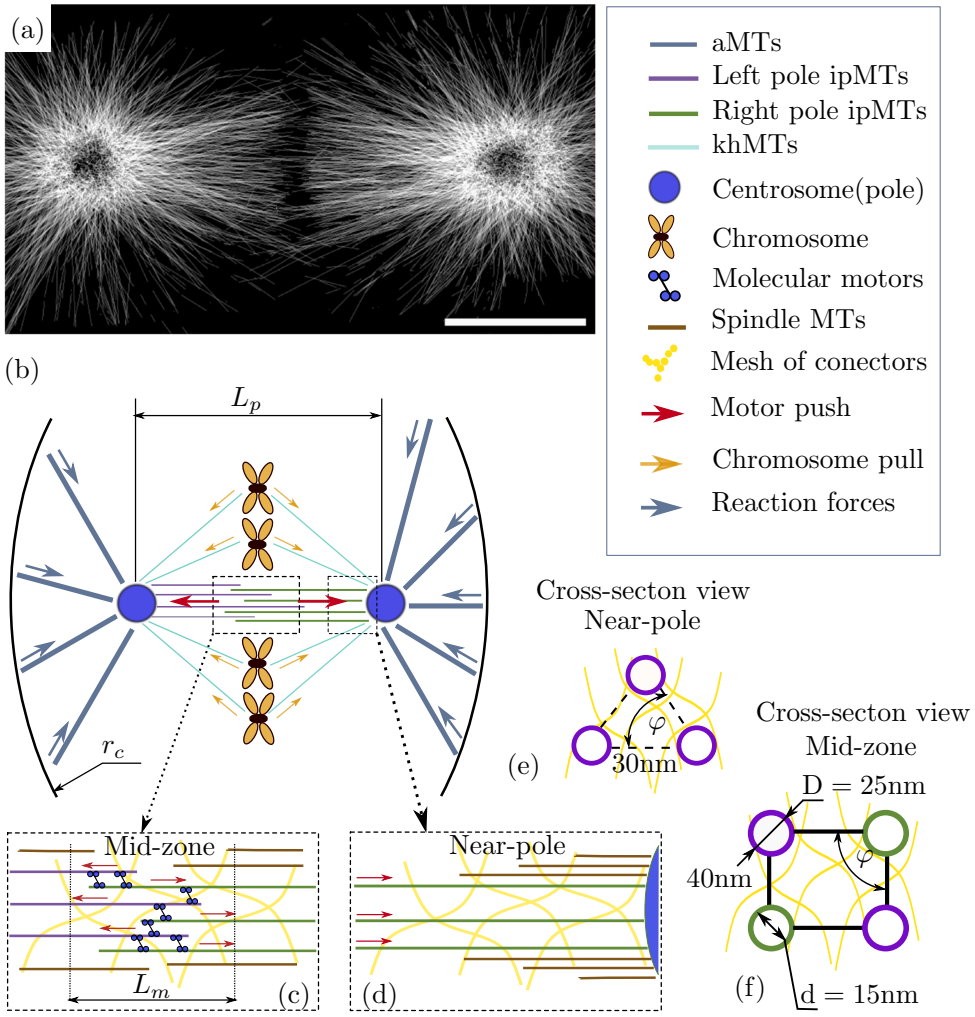

FIGURE 8.1: mitotic spindle architecture at various hierarchical levels. (a) The SEM image of a mitotic spindle in a living cell during division with thin white lines being microtubules and the two black circles – centrosomes). The length of a scale bar is 5μm. The image is adapted from a study by Müller-Reichert et al. [2018]. (b) A schematic representation of the mitotic spindle with all the structural components and loads according to the legend on the right. (c),(d) Schematic representations of Mid-zone and Near-pole zone of the mitotic spindle. (e),(f) Cross-section views of (c) and (d) respectively.

in many ways, on the reliable structural response of a mitotic spindle – a complex biological structure within the cell responsible for the generation of force required to divide the cell and also for the preservation of the outer shape of the cell during division [Müller-Reichert et al., 2018]. Mitotic spindles are stiff assemblies of proteins at a hierarchy of length scales. They typically consist of microtubules (MTs) which are long hollow filaments with a cylindrical cross-section. Also, they contain centrosomes which are specific regions of the cell membrane from which microtubules (MTs) grow and connectors or interlinkers (MT-bridges) – short protein bridges that bind microtubules together to form a bundle. A detailed image of a mitotic spindle in the early embryo of the nematode *Caenorhabditis elegans* obtained from 3D reconstruction of microtubules obtained from electron tomography [Müller-Reichert et al., 2018] is presented in Fig. 8.1 (a). The white lines represent individual MTs, the dark circular regions at the centres from which MTs grow are centrosomes. MT connectors are not visible in this image. The length of a scale bar is 5μm. A classical schematic view of the mitotic spindle obtained from a number

of studies [Dogterom and Surrey, 2013, Petry, 2016, Shelley, 2016, Müller-Reichert et al., 2018] is shown in Fig. 8.1 (b). Here, the cell membrane is schematically shown using two curves of radius r_c and the centrosomes are denoted by two blue circles. The centrosomes are rigidly connected to chromosomes (shown in orange) by kinetochore microtubules (khMTs) which help to split the genetic information into pairs of exact copies called chromatids by pulling the chromosomes apart [Scholey et al., 2016]. The direction of force applied to chromosomes by khMTs is shown with orange arrows. The distance between the centrosomes, sometimes also called poles, is called spindle length or inter-polar length labelled L_p. The spatial architecture is conventionally split into two sub-regions – the Mid-zone and the Near-pole zone [Ward et al., 2014]. These subregions are contained within the dashed rectangles in Fig. 8.1 (b) and in Fig. 8.1 (c),(d). Interpolar region changes as the spindle develops. Typically, five phases of spindle development are identified such as those shown in Fig. 8.2, as adapted from SEM of a human cell by Tolić [2017]. Currently, we are concerned with well established bipolar spindles such as those in late

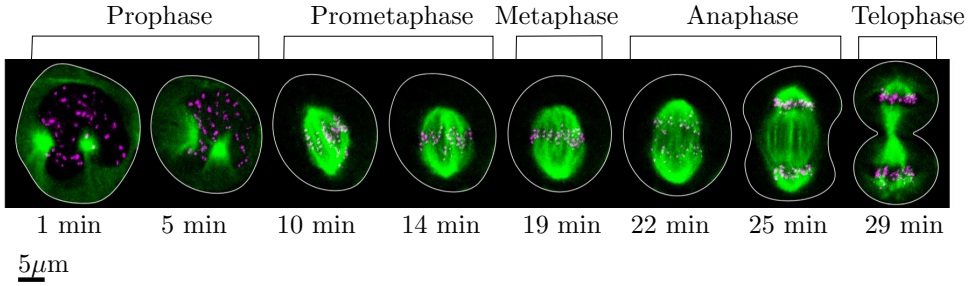

FIGURE 8.2: Phases of mitosis in a human cell adapted from SEM reconstruction by Tolić [2017]. The green lines represent individual microtubules, the purple dots correspond to chromatids. Each phase has an approximate time underneath and the spindle sizes are characterised with a reference to a scale bar of 5 μm.

Anaphase also called Anaphase B [Scholey et al., 2016] and Telophase in Fig. 8.2, where the green lines are MTs and the purple dots denote the position of chromatids. At the later phases, the interpolar region of a spindle is bridge-like as shown in Fig. 8.1 (b),(c),(d) and consists of two bundles of MTs – a bundle growing from the left centrosome towards the right centrosome, and an opposite bundle growing from the right centrosome towards the left one. Both bundles consist of microtubules called ipMTs. In the Mid-zone the two bundles overlap creating an antiparallel arrangement of ipMTs [Dogterom and Surrey, 2013, Ward et al., 2014] as shown in Fig. 8.1 (c). The length of the overlap is L_m which is also the length of a Mid-zone. The antiparallel ipMTs are linked in the Mid-zone by connectors and molecular motors (dynein and kinesin motors) which hydrolyze adenosine triphosphate (ATP) and use the harvested energy to push the antiparallel ipMTs into opposite directions [Jakobs et al., 2015, Wu et al., 2017, Ward et al., 2014] as shown by red arrows in Fig. 8.1 (b),(c). The microtubule also grows from their free ends thanks to a polymerisation process and thus contribute to the generation of push and pull forces in the spindle [Wu et al., 2017]. Finally, the centrosomes are also connected to the cell membrane via a number of aMTs which are indicated with thick blue lines in Fig. 8.1 (b).

Having described the structure of a mitotic spindle, we proceed with discussing its function. For simplicity, we omit here the process of spindle establishment and morphogenesis and focus on late Anaphase and early Telophase (recall Fig. 8.2). At the late stages of mitosis, two poles (centrosomes) are well separated $L_m \approx 10$ μm [Ward et al., 2014] and linked by the antiparallel assembly of ipMTs coupled in the Mid-zone by dynein and kinesin motors which generate forces

proportional to the number of motors and the energy generated by each motor measured in units of k_BT, where k_B is the Boltzmann constant and T is absolute temperature. The direction of these forces is shown by red arrows in Fig. 8.1 (b) and indicates that motors try to pull antiparallel ipMTs apart thus exerting a force transmitted by MTs towards the centrosomes as shown in Fig. 8.1 (d) [Jakobs et al., 2015, Wu et al., 2017]. Being pushed, the centrosomes are compressed and try to move further apart but are being restrained from doing so by the reaction forces from the cell membrane transmitted by aMTs as shown by the blue arrows in Fig. 8.1 (b). Finally, the centrosome separation is also restrained by the reaction forces from chromosomes as shown in Fig. 8.1 (b). Therefore, the spindle is in quasi-stable equilibrium most of the time as is supported by the reports of the slow transformation of spindles in time [Tolić, 2017]. This is an important fact for our further consideration. From the experimental and numerical studies of mitotic spindles by Ward et al. [2014] and Wu et al. [2017], it appears that the major transformations of a spindle occur during the periods when it is not in equilibrium but when growth destabilises certain parts of the spindle which can often be accompanied by the elastic buckling of microtubules and their bundles.

The mitotic spindle is a massive cytoskeletal structure that segregates chromosomes and, at the same time, preserves cell shape under external and internal loading. Its resilience against various mechanical factors ensures the correct division of the genetic material of a cell. The structural performance of spindles is partially facilitated by their highly complex architecture. Therefore, an investigation of the arrangement, properties and interaction of the structural components of a mitotic spindle is essential to understand the high load-bearing capacity of the spindle and the consequent robustness of the biological functions that rely on its mechanical stability.

There is a growing interest in the mechanics of mitotic spindles and their parts from a perspective of studying the elastic stability of mitotic spindles. Recent studies of spindle structure and orientation [Dogterom and Surrey, 2013, Ward et al., 2014, Chaigne et al., 2016], mechanics of MT bundles [Ward et al., 2014, Nixon et al., 2015, Jakobs et al., 2015, Soheilypour et al., 2015], mechanics of individual MTs and connectors [Kasas et al., 2004, Subramanian et al., 2010, Liew et al., 2011, Kabir et al., 2015, Kellogg et al., 2016] as well as the effects of cross-linkers (connectors) on buckling of MTs [Jin and Ru, 2013, Li et al., 2018] demonstrate how purely mechanical principles of buckling of slender beam-like structures (MTs) arranged in bundles manifest itself at the various hierarchies of spindle organisation and provides a solid ground for further research in the area of buckling of cub-cellular protein structures. Many of these experimental and theoretical studies at various levels of spindle organisation and length scales address the questions of force generation, structural performance and stability of spindles. In particular, they include the near-atomic level studies of MT connectors and motors by Kellogg et al. [2016] which reveal the specific nature of the structure of connectors and give suggestion as to their geometric and mechanical properties, investigation of the structural properties of individual MTs by Pampaloni et al. [2006], Wang et al. [2006], Van den Heuvel et al. [2008], Liew et al. [2011], and coupling and positioning of cross-linked MTs by Jin and Ru [2013], Soheilypour et al. [2015], Brangwynne et al. [2006].

Recent research focused on mitotic spindles is mostly concerned either with the hierarchy and organisation of the spindles and how it affects the properties of cell division or with the mechanical properties of individual components of a spindle. Studies focused on the development of unified mechanical frameworks to study spindles, which would also incorporate the properties

of individual components into a multi-scale hierarchy thus providing means of studying their behaviour, are rare and rather incomplete.

One of the first attempts to incorporate all the spindle complexity into a single framework was made by Ward et al. [2014], whose approach is based on random fluctuation dynamics within Langevin formulation [Nedelec and Foethke, 2007]. The authors point out that the mechanics of each component of a spindle at the scales of several μm should be affected by the random thermal fluctuations (thermal noise), which has to be reflected by the appropriate random terms in the mechanical equations (equilibrium equations, the vibration of MTs and connectors, etc.). Then, such random equations are to be written for each component of a spindle and assembled using techniques similar to those of matrix assembly in FEA. Therefore, spindle dynamics is composed of the dynamical equations for each component and, thus, the response of a whole structure can be simulated. Note, that such an approach is associated with considerable complexity arising from the necessity to solve nonlinear time-dependent equations numerically. Another limitation of this approach is the difficulty to introduce new mechanical effects. For instance, each new assumption (such as considering MTs to be orthotropic rather than isotropic) requires major changes to the existing formulation.

Alternatively, there are models that aim at producing closed-form analytical solutions or scaling laws to explain force generation and structural stability of spindles under compression such as a generic mechanical model of an entire spindle by Rubinstein et al. [2009] and the model by Malgaretti and Muhuri [2016] that captures key properties and interactions between the spindle components and is used to generate a generic stability map of the spindle which helps highlighting the relevant effects in a multitude of interactions within a spindle. Finally, the model by Jakobs et al. [2015] is useful for studying detailed interaction between the antiparallel assemblies of ipMTs, and for the estimation of the forces generated by the protein motors.

These studies are of particular interest to us as they lay the foundation for the understanding of the structural behaviour of the mitotic spindle as a whole and, to some extent, incorporate all its hierarchical complexity. Furthermore, they clearly make the case for the importance of the structural models of a spindle and stress the necessity to view it as an entire scaffolding biological mechanism. However, the current global models of spindles are mostly tailored to some specific cell types and/or particular phases of mitosis. On the other hand, while the Langevin dynamics frameworks are extremely powerful and generic, they are inherently computationally complex and may be difficult to adapt to an ever-changing new understanding of spindle mechanics. Further, we will propose our suggestions as to how one can overcome these limitations and provide a generic framework for the study of mitotic spindles in various cell types at various phases of mitosis.

8.2 A continuum mechanics framework for the elastic stability of mitotic spindles

Here, we lay the foundation for a generic computational framework based on continuum mechanics approach and the theory of elastic stability with the help of FEA, while addressing the biophysical question of the mechanical stability of mitotic spindles. The proposed framework

is embedded in a software package called Spindle FEA [Iakovliev et al., 2019] (the interactive manual available at https://spindlefea.soton.ac.uk and the source code are available at https://eprints.soton.ac.uk/423438/). The software developed by us utilises the ABAQUS solver and graphical engine via Python API. It generates a model of an entire spindle based on a list of provided parameters and submits it to ABAQUS solver for elastic buckling analysis. Further, we discuss a high-level architecture of SpindleFEA as well as key assumptions and limitations and demonstrate the tool by studying the elastic stability of the fission yeast spindle in late Anaphase B. We validate our preliminary analysis against the study by Ward et al. [2014].

8.2.1 Spindle structure

Here, we adhere to the canonical scheme of spindle organisation as shown in Fig. 8.1 (b)-(d) enriched by the information about ipMT bundle organisation from Ward et al. [2014] and Shelley [2016] as depicted in Fig. 8.1 (e),(f) and from the recent study by Nixon et al. [2015], who report that the spindle MTs are surrounded by the mesh of cross-linkers as shown with the thin yellow curves in Fig. 8.2 (c)-(f). Using the techniques and assumptions described further, the software (SpindleFEA) translates the canonical scheme and the information about the function of a spindle into a computer-generated structural spindle assembly depicted in Fig. 8.3. The structural model of an entire mitotic spindle of *Fission Yeast* cell is depicted in Fig. 8.3 (a). The centrosomes are depicted in redutilises the ABAQUS solver as two elastic spheres at a distance L_p= 10 μm which is consistent with the late Anaphase B stage in *Fission Yeast* reported by Ward et al. [2014]. The centrosomes are connected by two bundles of ipMTs, one growing from the left pole and the other one growing from the right pole, interlinked with each other in the Mid-zone via connectors and protein motors. The centrosomes are connected to the membrane via a number of radially positioned aMTs that grow from the centrosomes. A detailed diagram of the centrosome is shown in Fig. 8.3 (b) and that of the Mid-zone of the model is shown in Fig. 8.3 (c). It is apparent that the Mid-zone consists of an antiparallel assembly of left and right ipMTs cross-linked by connectors and motors. A detailed view of a protein motor attached to the two antiparallel microtubules is depicted in Fig. 8.3 (d), where arrows indicate the push P exerted by the motor on MTs. Each motor/connector is characterised by its length L_c and bending stiffness EI_c. A detailed view of a section of a microtubule is shown in Fig. 8.3 (f) featuring a hollow cylinder with bending stiffness EI embedded within the rest of the cytoskeleton which is represented by a distributed elastic coupling k per unit length. Further, we will discuss the embedding of various elements of a mitotic spindle in the cytoskeleton in details.

In the present model, we reduce the structural complexity of a mitotic spindle by modelling it as a large aggregation of parts that can be allocated to one of the groups such as centrosomes, microtubules, connectors and the surrounding cytoskeleton. The members of each group may have variability in dimensions and be present in various parts of a spindle, but they share very similar mechanics. As most of the time spindles withstand compression loading, we primarily focus on understanding their elastic buckling response, thus discarding the variety of other mechanical processes and focusing on the buckling of mitotic spindles. This assumption aligns well with a large number of studies [Brangwynne et al., 2006, Fuesler, 2012, Ward et al., 2014] reporting the crucial importance of buckling of mitotic spindles in understanding cell division.

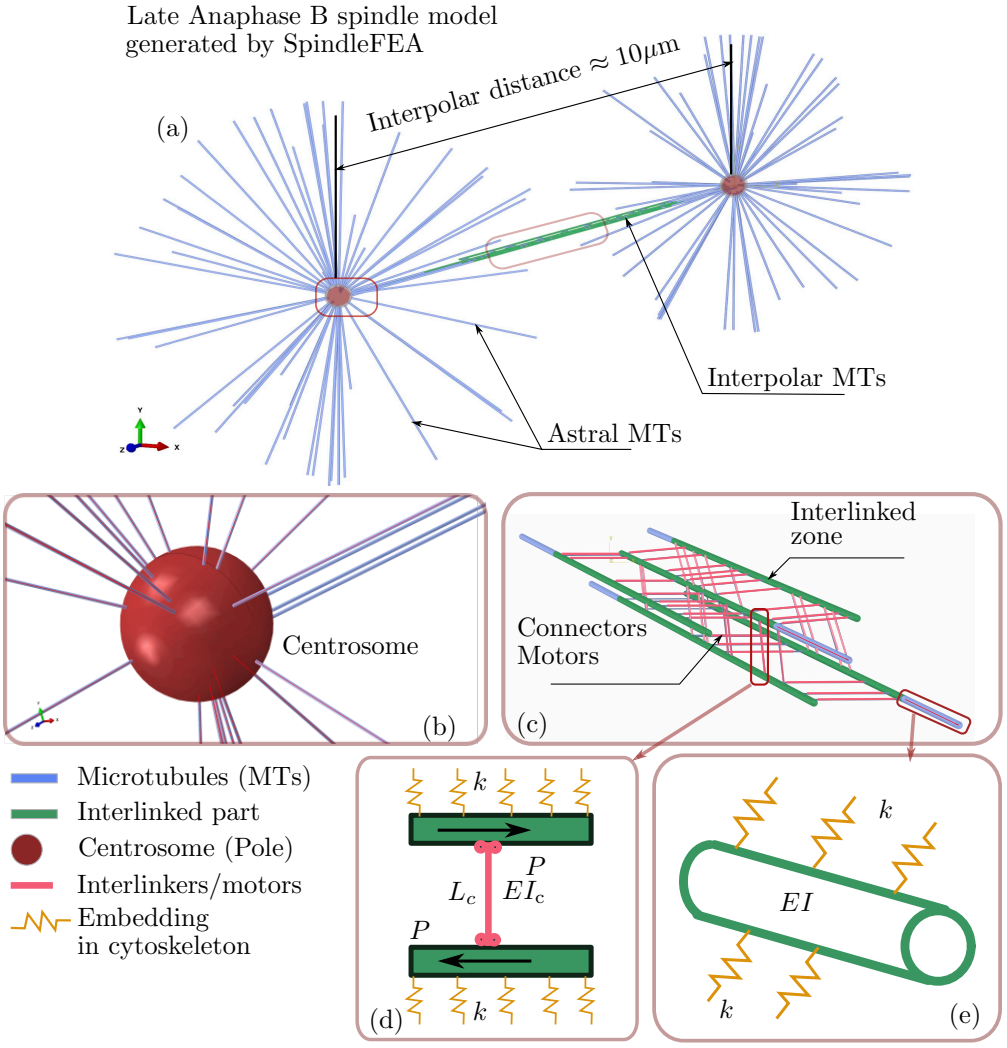

FIGURE 8.3: Late Anaphase B mitotic spindle model generated with SpindleFEA (3D graphics generated in ABAQUS). A generic architecture with centrosomes (red), ipMTs and aMTs (blue) are shown in (a). IpMTs interlinked by connectors (pink) and dynein/kinesin motors (pink) are shaded with green. A magnified view of a centrosome is depicted in (b) with aMTs (purple lines) and ipMTs (blue lines) coming from it. A detailed view of the Mid-zone is shown in (c). The green parts of ipMTs correspond to interlinking between the left pole and the right pole MTs via connectors and protein motors (thin blue lines). A detailed view of a protein motor linking two antiparallel ipMTs is shown in (d), where black arrows indicate the direction of the pull P exerted by the motor on each ipMT. A segment of ipMT is shown in (e), where EI is the bending stiffness of the ipMT and k represents ipMT coupling to the cytoskeleton of a cell.

8.2.2 Structural hierarchy and properties of a microtubule

Classically, MTs are treated as comparatively stiff protein filaments with a hollow circular cross-section [Kasas et al., 2004, Pampaloni et al., 2006, Liew et al., 2015]. The detailed near-atomic structure of MTs at the scales of dozens of Ångströms (Å) has been studied in detail only with the advances of cryo-electron-microscopy technology [Meurer-Grob et al., 2001, Kellogg et al., 2016, Zhang et al., 2018, Manka and Moores, 2018] which revealed a complex structure of the filament. A magnified view of several MTs obtained from electron cryo-micrograph by Manka and Moores [2018] is shown in Fig. 8.4 (a). The image contains both straight and curved microtubules

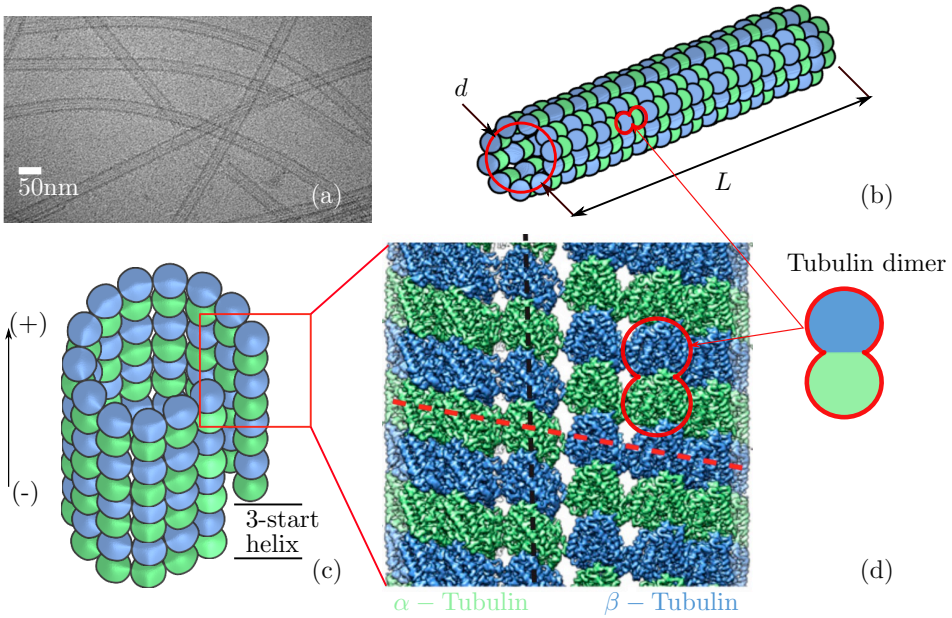

FIGURE 8.4: Molecular structure of a microtubule. (a) Straight and bent MTs at high resolution obtained from cryo-EM by Manka and Moores [2018]. (b) A conceptual diagram of an MT showing cylindrical lattice structure made of tubulin dimers. (c) Helical assembly of $\alpha-$Tubulin and $\beta-$Tubulin from $(-)$ to $(+)$ ends of an MT. The diagram is based on the Tubulin diagrams by Pampaloni et al. [2006], Zhang et al. [2018]. (d) A reconstruction of a near atomic structure of an MT wall based on protein density map obtained by cryo-EM. Image is adapted from Zhang et al. [2018] and sows individual Tubulin dimers in a lattice structure of MT wall.

(indicated by dark grey on the light grey background). A scale bar 50nm long is shown in the bottom-left corner of the image. A conceptual diagram of a typical microtubule-based on the reports by Pampaloni et al. [2006], Zhang et al. [2018] is depicted in Fig. 8.4 (b) showing a cylindrical structure of an MT with length L and average diameter d. A more detailed view at the structure of MT reveals a lattice consisting of polymerised protofilaments (PFs) such as globular subunit called tubulin [Bernfield and Slack, 2019] assembled in a helical manner as shown in Fig. 8.4 (c) for a MT with 13 PFs, where $\alpha-$Tubulin is shown in green and $\beta-$Tubulin – in blue. MTs are polar, i.e., they have a $(-)$ and $(+)$ ends, where $(-)$ ends are stable, while $(+)$ ends undergo a constant polymerisation (growth) and depolymerisation (disassembly) [Bernfield and Slack, 2019]. A near-atomic structure of the MT wall was obtained from a protein density map rendered from cryo-EM of an MT by Zhang et al. [2018]. It is shown in Fig. 8.4 (d) and depicts a 3-start helix (see Fig. 8.4 (c)) along the axial direction of an MT which leads to a shift in $\alpha-\beta$ Tubulin pattern. A strong $\alpha-\beta$ Tubulin bond – Tubulin dimer thus occurs within the lattice.

The conceptual diagram of a cross-section of a typical 13-PF microtubule is depicted in Fig. 8.5 (a). It summarises a number of observations by Meurer-Grob et al. [2001], Pampaloni et al. [2006], Zhang et al. [2018], Manka and Moores [2018]. The individual Tubulin filaments are represented by grey egg-like shapes along with an average radius r of the cross-section. A fine resolution cryo-EM (≈ 14Å) of the cross-section performed by Meurer-Grob et al. [2001] is shown in Fig. 8.5 (b).

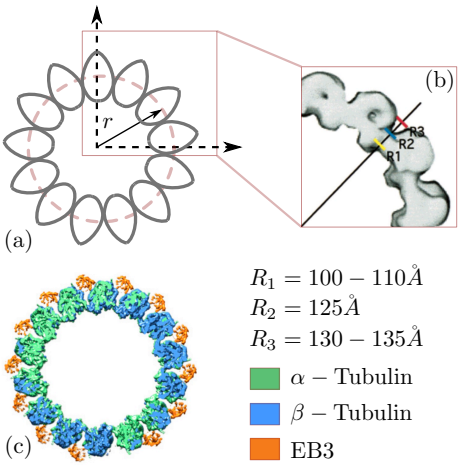

FIGURE 8.5: A cross-sectional view of a microtubule. (a) A an ideal model of the cross-section of a 13-PF microtubule with an average radius r. The diagram is aggregated from the findings by Pampaloni et al. [2006] and Zhang et al. [2018]. (b) A reconstruction of a section of the cross-section of a microtubule from cryo-EM with resolution of 14Å showing tubulin lattice. The image is adapted from [Meurer-Grob et al., 2001]. Density maps of $\alpha-$Tubulin and $\beta-$Tubulin within a 14-PF microtubule cross-section adapted from [Zhang et al., 2018].

The image depicts the density of Tubulin monomers in the cross-section of a microtubule which further demonstrates their lattice-like assembly. Notice, that Meurer-Grob et al. [2001] specified three typical radii of an MT: $R_1 = 100 - 110$Å (yellow dash), $R_2 = 125$Å (blue dash) and $R_3 = 130 - 135$Å (red dash). The density of Tublin type α and Tubulin type β were reported by Zhang et al. [2018] and are shown in Fig. 8.5 (c) with green and blue colours respectively. It is apparent from the Tubulin density maps that there are regions within the MT cross-section dominated by $\alpha-$Tubulin in contrast with the other regions dominated by $\beta-$Tubulin. The presence of end-binding proteins, such as EB3 (as shown in Fig. 8.5 (c)) and others can mediate MT structure and functions. We do not cover the details of structural changes within MT lattices due to end-binding proteins here. Instead, we focus on the the mechanical behaviour of MTs within a spindle by assuming them to be ideal cylinders made of Tubulin dimers.

It is apparent from the experimental observations described above, that at the smallest scale of organisation, microtubules are extremely complex lattice structures that mainly consist of Tubulin dimers but are mediated by the presence of a host of other proteins and amino acids. Nevertheless, MTs have been modelled as isotropic beams in the past with a tubular cross-section [Kasas et al., 2004, Brangwynne et al., 2006, Jin and Ru, 2013, Ward et al., 2014]. However, increasingly, MTs are being modelled as having an orthotropic cross-section with direction-dependent shear effects [Gittes et al., 1993, Janson and Dogterom, 2004, Pampaloni et al., 2006]. With a new understanding of MT structure and mechanics constantly emerging, the first major requirement for the proposed framework is adaptability. Hence, SpindleFEA is developed to have a modular structure, e.g., each structural element of the spindle has a number of possible interchangeable models. Thanks to the versatility of modern FEA frameworks, one can easily replace the isotropic model for a MT cross-section with an orthotropic model without disrupting the modelling of other parts or an entire spindle. At the current stage, we apply SpindleFEA with an isotropic Bernoulli-Euler beam assumption for simplicity. In future, refined models for the MT will be incorporated.

For the initial study, we assume a MT outer diameter $D \approx 25$nm, and a MT inner diameter $d \approx 15$nm. As the MT length dramatically varies between cell types from $1-10$ μm to $50-100$ μm, we restrict ourselves to the *Fission Yeast* spindles studied by Ward et al. [2014] and use their measurements for the structural parameters. Therefore, in Anaphase B the length of ipMTs will vary between $1-10$ μm which is consistent with the interpolar distance $\approx 10\,\mu$m.

Measuring the bending stiffness EI of individual MTs is an extremely challenging task due to the strong effect of thermal fluctuations. Therefore, the stiffness of MTs is derived from the characteristic length scale called *persistence length* l_p [Pampaloni et al., 2006], which is defined as a ratio of the bending moment per unit curvature response κ to the thermal energy k_BT as $l_p = \kappa/k_BT = EI/k_BT$. Here k_B is the Boltzmann constant. In the current idealised case, when we simplify the actual complex cross-section of an MT, and assume it to be a hollow cylinder, we can calculate the second moment of the cross-sectional area I and express an apparent Young's modulus E from bending stiffness EI by treating material modulus and moment of inertia as two independent variables [Gittes et al., 1993]. Typically, persistence length is calculated by approximating the experimentally observed shape of a microtubule with a sine or polynomial series which leads to the strain energy being expressed as a quadratic form in deflection amplitudes

$$U \sim \sum_{n=1}^{\infty} \left(a_n - a_n^0\right)^2, \tag{8.1}$$

where a_n is the $n-$th amplitude of the series expansion of the bending configuration, while a_n^0 is the $n-$th amplitude of the series expansion of the deflected shape of an MT in the absence of loading. Effectively, a_n^0 represent the significance of the contribution of thermal noise to the buckling mode. According to [Gittes et al., 1993], for each n, $\left(a_n - a_n^0\right)^2$ contributes an average of $1/2k_BT$ in the case of equilibrium. Therefore, the authors define the variance of a_n

$$\mathrm{var}(a_n) \sim \frac{k_BT}{EI} L^2, \tag{8.2}$$

where EI is the bending stiffness of a microtubule and L is its length. The persistence length is the arc length above which the angle θ of a tangent to the deflected curve becomes uncorrelated in all three dimensions. Practically, this is the length at which the continuum mechanics effects on average are more significant than the thermal fluctuations. Hence, it can be written as

$$l_p \sim \frac{L^2}{\mathrm{var}(a_n)}. \tag{8.3}$$

This formula was reported to give good results for long MTs $L > 21\,\mu$m [Pampaloni et al., 2006]. Pampaloni et al. [2006] employed single-particle tracking methods combined with fluctuation analysis of individual MTs to conclude that for microtubules with total length $L < 21\,\mu$m, the expression for the persistence length given by Equation (8.3) should be corrected to account for the shear-related effects. The expression for the shear corrected persistent length derived by Pampaloni et al. [2006] is hard to implement without introducing directionality of the mechanical properties within the cross-section of an MT, i.e., orthotropy. Therefore, shear effects will have to be incorporated in SpindleFEA alongside with the orthotropic model for MTs. In the current example, we focus on the Bernoulli-Euler beam theory and use the MT bending stiffness calculated by Ward et al. [2014] to be $EI = 20\,\mathrm{pN}\,\mu\mathrm{m}^2$, $I = \pi\left(D^4 - d^4\right)/64$, where the outer

diameter $D = 0.025\,\text{nm}$ and the inner diameter is $d = 0.015\,\text{nm}$, which are taken from Pampaloni et al. [2006]. Hence, we estimate the apparent elastic modulus as $E = 1.5 \times 10^9\,\text{pN}/\mu\text{m}^2$.

Being the most rigid parts of the cell, MTs play a crucial role in preserving its shape and thus are subject to considerable compressive loading. This fact greatly supports the necessity to understand the stability of MTs and the influence that buckling of a single MT has on the mitotic spindle as a whole. MTs are very slender structures. With diameters of dozens of nanometers and lengths reaching dozens of micrometres, their slenderness ratios are of the order of thousands. According to the Euler buckling theory, an individual MT should buckle and loose its structural function at loads orders of magnitude smaller than those appearing inside a cell [Brangwynne et al., 2006]. Brangwynne et al. [2006] have shown that individual MTs studied *in vitro* buckle at loads consistent with the Euler theory prediction which are ≈ 100 times smaller than the loads that MTs withstand in living cells. The authors demonstrated that such a drastic difference in the performance of MTs *in vitro* and *in vivo* is due to MTs in living cells being able to develop a short-wave buckling mode in contrast to isolated MTs developing a single arch buckling mode consistent with the Euler theory. The theory of short-wavelength buckling proposed by the authors can be explained considering Fig. 8.6. The (*top*) image shows the buckling of an

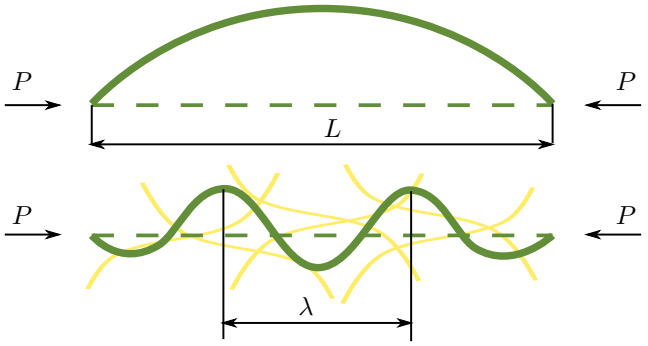

FIGURE 8.6: A single arch L buckling of an elastic rod according to Euler theory (*top*). A short-wavelength λ buckling of a microtubule embedded into a surrounding cytoskeleton (*bottom*). The schematic is adapted from Brangwynne et al. [2006].

ideal rod according to Euler theory. The rod is assumed to be fixed at both ends and not otherwise supported. Buckling of isolated MTs follows this scheme. In contrast, microtubules are not isolated within a cell. They are interconnected by protein motors and connectors to form bundles and even whole bundles are linked to the rest of the cytoskeleton. Therefore, a more realistic model for a microtubule inside a cell is one of a filament constrained due to its elastic environment, which is often represented by fairly heterogeneous support along the length of the filament. Experiments have shown that such soft filaments inside gels buckle very differently and they do not develop a long arch buckling mode, similar to the fundamental mode of Euler buckling, but will have multiple small arches of wavelength λ as shown in Fig. 8.6 (*bottom*). The critical buckling load for an Euler beam is $P \sim EI/L^2$. Brangwynne et al. [2006] show that the critical buckling load of a supported MT is instead $P \sim EI/\lambda^2$, where λ is the wavelength of the buckling mode and is shorter than the arch length. For a theoretical beam embedded in an elastic medium, λ can be written in terms of bending stiffness EI of the rod and the effective coupling to the medium k

$$\lambda = 2\pi \left(\frac{EI}{k}\right)^{1/4}. \tag{8.4}$$

The authors validated this theoretical expression in an experimental study which consisted of buckling tests performed on a number of rods with stiffnesses varying by orders of magnitude. Furthermore, the authors measured the buckling wavelength of the MTs inside living cells to be $\lambda \approx 3\,\mu$m and showed that they agree with the prediction by Equation (8.4) $\lambda \approx 2\,\mu$m.

8.2.3 Actin binding connectors and the mesh

The study by Brangwynne et al. [2006] laid the foundation for the new research in buckling of microtubules [Jin and Ru, 2013, Ward et al., 2014, Kabir et al., 2015, Afrin et al., 2016, Li et al., 2018]. Particularly interesting for us is the experimental study by Nixon et al. [2015] who reconstructed 3D views of a bundle of microtubules from a sequence of EM images taken at intervals along the MT length. The reconstructed images are reproduced here and shown in Fig. 8.7. The

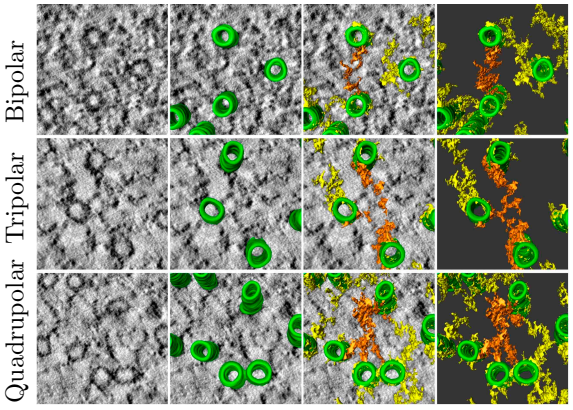

FIGURE 8.7: 3D reconstruction of MTs and the surrounding network of connectors from EM. (*First column*) Raw EM images of the cross-section view of a bundle of MTs. (*Second column*) Raw EM images with detected microtubules. (*Third column*) Raw EM images with detected microtubules and the mesh. (*Fourth column*) Detected microtubules and the mesh without EM background. The rows represent three types of connectors in the mesh. The figure is reproduced from [Nixon et al., 2015].

first column of images shows a typical single snapshot by EM with the black circles representing MTs on a grey background. The second column of images shows a reconstruction of MTs (green) superimposed on the grey background. The third column of images contains reconstructed MTs (green) along with the recognised connectors (yellow and orange mesh) superimposed on the background. The last column of images contains just a reconstruction of MTs (green) and connectors (yellow and orange) without a cell background. The rows correspond to the three types of connectors identified – *Bipolar* (connect two MTs), *Tripolar* (connect three MTs) and *Quadrupular* (connect four MTs). This study is important in understanding the structure and properties of mitotic spindles as it allows for the first time to accurately study the connectivity between the individual MTs and their embedding in the surrounding environment of the cell.

The understanding of MT connectors is further improved by a 4 Å resolution cryo-EM study by Kellogg et al. [2016] of two antiparallel ipMTs. The authors reported a detailed atomic structure of a cross-linker (connector) called PRC1 (protein regulator of cytokinesis 1) and showed how this monomer binds to the Tubulin in MTs.

Based on the observations by Brangwynne et al. [2006], Nixon et al. [2015] and Kellogg et al. [2016] we develop a mechanical model for a connector and the mechanical model for the embedding of MTs in the elastic protein mesh. We consider connectors to be thin struts 6 nm to 40 nm long randomly distributed within the interlinked zone as shown in Fig. 8.3 (a),(c). Ward et al. [2014] adopt from Claessens et al. [2006] the assumption that cross-linkers do not contribute to bending stiffness of the MT bundle. However, recent studies by Nixon et al. [2015] and Kellogg et al. [2016] suggest that one should not completely neglect the stiffness of connectors. Therefore, according to Nixon et al. [2015], we assume the average diameter of the connector to be $d \approx 5\,\text{nm}$ and the apparent elastic modulus E to be the same as the one of a microtubule. Finally, Kellogg et al. [2016] showed that connectors are well coupled to the adjacent MTs, which allows us to assume continuity of displacement and rotation between the adjacent nodes of the connector and the MT in the FE model. The estimated number of connectors coupling ipMTs varies dramatically depending on the phase of mitosis and cell type. Therefore, we keep the number of connectors as a varying model parameter. A detailed scheme of the inter-polar bundle featuring dozens of connectors randomly distributed along five ipMTs is shown in Fig. 8.3 (c). The detailed view of the connector linking two MTs is depicted in Fig. 8.3 (d).

It is important to note that according to Ward et al. [2014], the morphology of antiparallel bundles of MTs stretching between the poles changes between the Mid-zone and Near-pole zone. The cross-sectional views of the MT bundles near poles and in the Mid-zone adapted from the study by Ward et al. [2014] are depicted in Fig. 8.8 (a) and Fig. 8.8 (b) respectively. The purple

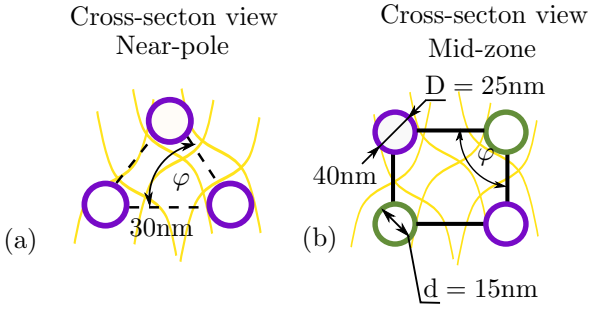

FIGURE 8.8: A schematic representation of ipMT bundle cross-section in Near-pole zone (a) and in Mid-zone (b) with indicated MTs growing from the right pole (purple circles) and from the left pole (green circles) and an elastic mesh of connectors shown with yellow curves in the background. The dashed lines indicate connectivity via elastic mesh only. The solid lines indicate connectivity via elastic mesh and MT connectors and motors.

circles in the figures represent cross-sections of ipMTs from the left pole while the green circles represent ipMTs growing from the right pole. Note that in Near-pole zone in Fig. 8.8 (a) only MTs from the respective pole are present while in the Mid-zone in Fig. 8.8 (b) ipMTs from both poles are interconnected. This has an apparent effect on the cross-section of the bundle indicating that in Near-pole zone, the MTs are assembled in a triangular manner with an average angle $\phi \approx 60^\circ$ and the distance between the neighbouring MTs $\approx 30\,\text{nm}$. On the other hand, the inter-linking between ipMTs in the Mid-zone happens on average at an angle $\phi \approx 90^\circ$ with the distance $\approx 40\,\text{nm}$. We also indicate the inner diameter d and the outer diameter D of a microtubule in Fig. 8.8 (b) for comparison of scales of individual MTs and of the bundle. In the current study, we consider distances between the MTs and the angles of their cross-linking ϕ to be generated from a normal distribution fitted to the measurements by Ward et al. [2014].

Finally, note that we also depicted a schematic view of the elastic mesh (yellow curves in Fig. 8.8) that embed the entire spindle. We model the effect of the embedding of MTs into a cytoskeletal mesh by attaching springs of stiffness k along the length of MTs, while the other end of each spring is grounded. This is intended to mimic the heterogeneous elastic environment around MTs. The proposed springs are sketched in Fig. 8.3 (d),(e). We omit displaying these springs in future to simplify the graphics.

8.2.4 The architecture of the mechanical framework and simplifications

The main requirements that we pose to SpindleFEA are the ability to model the hierarchical complexity of a mitotic spindle, applicability to various cell types and phases of mitosis, extensibility, and scalability & simplicity of use. We aim to develop a platform that can be used by researchers in the field and be extended by them to account for new experimental and theoretical findings as well as to give researchers a numerical tool that they can use to test various modelling assumptions.

Our key assumptions are the applicability of continuum mechanics and a quasi-static approximation. Continuum mechanics at a length scale of dozens of nanometers (length scale of an MT cross-section) has been shown to accurately predict experimental observations in a large number of studies [Brangwynne et al., 2006, Jin and Ru, 2013, Ward et al., 2014, Kabir et al., 2015] which supports its applicability at such scales. FEA has long become a standard tool applied in various mechanical problems. It is versatile and easily adjustable to virtually any mechanical problem at hand. We believe that the use of well-established FEA codes such as ABAQUS is advantageous because of a variety of constitutive models, e.g. isotropic, orthotropic, anisotropic, hyper-elastic models, as well as linear and non-linear models are readily available. Therefore, it is relatively easy to enrich the existent framework with ever-emerging new knowledge about mitotic spindles.

The quasi-static approximation is built upon the notion that the spindle evolves slowly over the course of 20 min to 30 min [Tolić, 2017, Wu et al., 2017], thus, indicating that the structure is at equilibrium most of the time. Therefore, we can disregard the dynamical effects on the stability of the spindle at a larger scale and focus instead on quasi-static linear buckling to predict mode shapes and compressive loads in spindles. Quasi-static modelling of individual microtubules as well as of bundles of microtubules has been carried out before [Brangwynne et al., 2006, Jin and Ru, 2013, Soheilypour et al., 2015], but it has never been applied to an entire spindle model. In fact, we argue that quasi-static analysis is most effective particularly in the case of an entire spindle because the spindle's complexity magnified by the computational cost of dynamical simulations (such as Langevin dynamics approach proposed by Ward et al. [2014]) makes such studies extremely complex and computationally costly. Whereas in our case, we are able to eliminate time from the model and study linear eigenvalue problems instead.

There are two complications that are inherent to such a simplification. Firstly, we are not able to simply neglect the thermal fluctuations which start playing a significant role at the length scale of dozens of nanometers. Secondly, although slowly, the morphology of the spindle changes

dramatically during the phases of mitosis and thus the entire process cannot be captured by a single static model.

To compensate for the first complication, we propose to consider not just the lowest critical load P_0 and associated mode w_0 of the spindle but to study an entire spectrum P_n and w_n of the discretised model, where n is the size of the eigenvalue problem. We have observed in the previous chapters that higher buckling loads and the associated mode shapes can play a significant role in the buckling of structures. This observation is more significant in the case of mitotic spindles since buckling loads often appear in clusters. If two or lower buckling loads of the spectrum have close values i.e. $P_{n-1} \approx P_n$, either of the associated mode shapes or a combination of those are practically observable if the distance between the critical loads is smaller than the average energy contribution of the thermal fluctuations $P_n - P_{n-1} < k_B T$. Therefore, when using SpindleFEA, one should always check how well separated several lowest buckling loads are. If the spacing between the critical loads is small, one should consider the actual buckling mode of the spindle to be a linear combination of the mode shapes with close buckling loads. To compensate for the second complication, we suggest performing a separate buckling analysis after each major shift in the geometry of a spindle. Typically, one should perform a complete analysis at least at the beginning of each phase of mitosis. Therefore, our approach cannot be used to dynamically trace the evolution of the spindle but may still be accurate enough to study the behaviour within each particular phase of mitosis.

For the current study, we assume the following (refer to Fig. 8.3).

- All the structural parts of the spindle are solid and continuous bodies.
- The atomic and molecular thermal fluctuations are to be neglected at the scale of an entire spindle.
- We are studying the situation where a spindle becomes structurally unstable and buckles.
- At the current stage, we also restrict the analysis to small deformations and linear stress strain relation.
- Microtubules and connectors are modelled according to Bernoulli-Euler beam theory.
- In agreement with the assumptions by Ward et al. [2014], we assume centrosomes to be spherical elastic bodies with microtubules growing radially outwards.
- Two types of MTs are considered: interpolar MTs and astral MTs, their mechanical properties being the same.
- Connections between MTs and connectors as well as between MTs and centrosomes are assumed to be ideal – they continuously translate displacement, slope, bending moment and shear force.
- All MTs are embedded in the elastic cytoskeleton which is reflected by continuously distributed springs k attached to each MT acting in all three directions.
- The attachment of MTs to the cell membrane is assumed to be rigid – all deflections and rotations of the (+) ends of aMTs are suppressed.

SpindleFEA is an open-source software package used for pre-processing and model formulation for further analysis using ABAQUS CAE. It is written in Python 2.7 and uses ABAQUS API as a main interface with the FE solver. A standard modelling scenario of a mitotic spindle employing Spindle FEA consists of the automatic execution of the following steps.

- The application reads the parameters of the spindle from a file called "job.py" located in the root of the application directory. The list of spindle parameters used in the current study is presented in a tabular format in Appendix C.
- The application also reads the computational parameters from "job.py" file such as the number of CPUs requested, memory allocation and parallelisation algorithms.
- The analysis may be executed either via ABAQUS graphical user interface (GUI) or from the command line by executing "job.py" file which then triggers the modules of Spindle-FEA.
- The first step is the generation of the geometry of each individual part of a spindle.
- The material properties are then assigned to each part.
- The parts are combined in the mitotic spindle assembly.
- The connectivity between individual parts is specified based on the parameters provided.
- The finite element mesh is generated for each part.
- The analysis input file is generated and submitted to ABAQUS solver. The solver then assembles a generalised eigenvalue problem for the entire structure and works out its eigensolution.
- The analysis is terminated and the output database "job.odb" and the solution data file "job.dat" are created.

By opening the database "job.odb" file in ABAQUS GUI, a user can plot the deformation profiles of the spindle, review critical forces, stresses and strains. In the future, additional modules will be incorporated into SpindleFEA to retrieve deformation profiles from the "job.odb" database and perform the automatic classification of various characters of spindle deformation based on structural parameters.

The model of the Mitotic Spindle generated in *ABAQUS* by the SpindleFEA consists of the three main components (see Fig. 8.3) – elastic spheres of centrosomes (red), microtubules (blue beam-like filaments) and connectors (pink struts coupling MTs in the interlinked zone). Each structural component is an object generated by a dedicated class in SpindleFEA, i.e., MT class, centrosome class, and connector class. Each such class contains several methods or functions that control the geometry of the structural components, their location, orientation and connectivity as well as the mechanical properties. The creation and configuration of the spindle model are performed following the steps described above. These steps are discussed here in greater detail. Detailed information on the SpindleFEA code can be found in the interactive documentation in https://git.soton.ac.uk/ai1v14/SpindleFEA.

- Generation of the geometry is performed by the `SpindleFEA/Parts` package which contains `GeometryBuilder` module and `standard_parts` module:
  - The overall dimensions of the Spindle, physical and mechanical properties of its parts are read from "job.py" file which is specified before the application is started.
  - Centrosome properties are passed to `Parts.standard_parts.centrosome()` function which runs a number of internal classes to instantiate two centrosome objects which are then generated in *ABAQUS* as two elastic spheres with a specified Young's modulus and Poisson ratio. The centrosomes are considered deformable elastic bodies that translate stresses and deformations.
  - The length, the inner and the outer radii of a tubular cross-section of astral microtubules are passed to `Parts.standard_parts.microtubule()` function. It then instantiates a requested number of astral microtubule objects.
  - Geometric and mechanical parameters of the interpolar microtubules are passed to `Parts.standard_parts.microtubule()` function which instantiates a number of interpolar microtubules.
  - Geometric and mechanical properties of connectors as well as their number are passed to the function `Parts.standard_parts.connector()`, which instantiates connector objects.
  - The number of ipMTs, aMTs and connectors to be generated are specified in "job.py".
- Assembly of the Mitotic Spindle is performed by `SpindleFEA/SpindleAssembly` package which contains `SpindleAssembly.AddComponents` module, `SpindleAssembly.PositionComponents` module, `SpindleAssembly.PositionConnectors` module, `SpindleAssembly.PositionIpMTs` module and `SpindleAssembly.assembly_random` module:
  - The centrosomes are added invoking `SpindleAssembly.AddComponents` which positions them at the two poles of the Spindle by translating and rotating the objects by a given amount.
  - Based on the number and the relative position of aMTs, a set of orientation function within `SpindleAssembly.PositionComponents` translates and rotates astral microtubules in a way that they radially extend from the centrosomes.
  - The nodes on the minus ends of each aMT are kinematically coupled to the corresponding nodes on the surfaces of the respective centrosomes. Continuity of forces, moments, stresses and strains is ensured between the nodes.
  - A requested number of left pole and right pole ipMTs is generated and assigned either to the left or to the right pole randomly according to a number of routines defined in `add_and_position_interpolar_mts_and_connectors()` which is a part of `SpindleAssembly.assembly_random` module. Thus, a random architecture of the interpolar assembly is created. The above function uses the information about the cross-sectional organisation of the ipMTs bundle retrieved from "job.py". This allows to strictly control for the distance and the angles between the ipMTs as shown in Fig. 8.8.
  - `add_and_position_interpolar_mts_and_connectors()` calles a specific function which couples the nodes on the minus ends of the ipMTs to the surfaces of the respective

centrosomes. Continuity of forces, moments, stresses and strains is ensured between the nodes.

  - The above mentioned function also invokes `SpindleAssembly.PositionConnectors` module. It contains a number of functions that pick the generated connector objects based on their length, identify both ends of the connectors and couple them to the interpolar microtubules. Thus, ipMTs appear to be bridged by the connectors. `SpindleAssembly.PositionConnectors.position_connectors()` assigns one end of the selected connector to the left ipMT and the other end to the right ipMT thus ensuring that ipMTs are coupled in an antiparallel assembly. Also, the length of the interconnected zone is passed to this function from "job.py" to ensure that the connectors are randomly distributed only within this region.

- Generation of the FE mesh is performed by `SpindleFEA/SpindleMesh` package:
  - Mesh generation is triggered separately on each structural component by passing the ID of the component to `standard_mesh()` function which is a part of `generate_mesh` module within `SpindleFEA/SpindleMesh` package.
  - `standard_mesh()` function retrieves each object within the model, retrieves the edges and faces of the object and assigns mesh seeds on each face and/or edge using the automatic mesh generator supplied with *ABAQUS*.
  - Automatic mesh generator is triggered and FE mesh is generated based on the created seeds.
  - The centrosomes are meshed with solid 3D tetrahedral elements.
  - The microtubules and connectors are meshed with hybrid beam elements.

- Specifying boundary conditions, loading and interaction between elements is done by `SpindleFEA/LoadCase`. The package consists of `Interaction` module and `InteractionHelpers` module (control coupling between components), `LoadsAndBCs` module (specifies loads and boundary conditions) and `Step` module (specifies buckling analysis parameters).
  - The specification of boundary conditions and loading in the spindle consists of the selection of the instances of the geometrical entities to which the BCs are applied, the selection of the respective nodes and the application of the BCs. These steps are executed sequentially.
  - A dedicated function searches for the IDs of the created objects and identifies the growing ends of aMTs. The selected objects are passed to the BC specifier.
  - The boundary conditions specifier takes the end objects (points) and identifies the mesh nodes associated with them. Then, the boundary conditions (restriction of displacements and rotations in all directions) are applied to the nodes at the ends of aMTs. In such a way, the constraints of the spindle within the cell membrane are specified.
  - A dedicated function searches for the IDs of the points that connect the ends of the connectors to ipMTs. It returns the objects (points) that correspond to these IDs to the BC specifier.

  - The BC specifier specifies loading at each such point. The orientation of the loading is chosen in such a way that each ipMT appears under compression as is the case when the connectors and protein motors exert push on the MTs to separate the spindle.
  - A dedicated function retrieves IDs of the neighbouring aMTs. These IDs are passed to the BC specifier.
  - The BC specifier retrieves all the nodes of the selected MTs and attaches springs to each node interconnecting the MTs. This is done to model the effect of the actin networks that provides connectivity between the individual structural components of the cell.

- `LoadCase.Step` module specifies the buckling analysis parameters such as type of analysis (static buckling), number of eigenvalues requested, number of subspace iterations, CPU and memory allocation, etc. These parameters are retrieved from "job.py".
- The analysis is submitted by `job` module and the analysis results are extracted from the analysis databases using `datExtract` module.

The key mechanical assumptions discussed in this chapter are specified at the stages of geometry generation (within `standard_parts` module), meshing (within `standard_mesh()` function) and analysis configuration (within `LoadCase.Step` module). The changes in the spindle geometry can be incorporated by simply changing the corresponding fields in the "job.py" file. A more profound change, such as the introduction of a nonlinear material law, material orthotropy, etc., can be introduced by changing `standard_parts`. Different elements can be specified in `standard_mesh()`. Thus, minimal changes to the source code can introduce novel functionality thanks to the modular structure of the application and flexibility of *ABAQUS API*.

All the structural parameters supplied to SpindelFEA in this study to generate a model of a spindle as shown in Fig. 8.3 are presented in Table C.2, Table C.1, Table C.3, Table C.4 and Table C.5 present in Appendix C. The particular values were selected based on the assumptions discussed previously and/or experimental measurements from a number of sources. The name of a parameter is given in the first column of each table, the source for the particular value of a parameter is presented in the second column of each table while the name of the parameter in "job.py" file is given in the third column. Finally, the values of the parameters are shown in the last column of each table.

The provided values are also the defaults in "job.py" which can be altered based on experimental measurements. Some of these parameters may be selected as governing parameters which will trigger SpindleFEA execution in a *job array mode*. This allows multiple analysis cases to be run on a high-performance computational facility such as a cluster varying the governing parameters in specified intervals and recording the changes in a spindle behaviour depending on the changes in governing parameters. This functionality is currently implemented but is still under testing on IRIDIS high-performance facility at the University of Southampton.

8.3 Results and discussion

We study the deformation profiles, stresses and loads generated by the mitotic spindle in *Fission Yeast* cells thus performing an initial validation of the framework against the experimental measurements and numerical simulations by Ward et al. [2014]. We also qualitatively compare the obtained mode shapes of the spindle with the localised buckling of MT bundles reported by Soheilypour et al. [2015]. Finally, we compare the calculated mode shapes with the torsional buckling of spindles recently observed by Novak et al. [2018] to demonstrate the applicability of the framework to discover novel behaviour that went undetected with other computational frameworks.

Although there is much interest in the study of mitotic spindles, there still remains a great deal of uncertainty as the connection between mechanical behaviour and their structure is still unclear. Therefore, we have a few parameters with respect to which spindle behaviour may be investigated in a parametric study using SpindleFEA. Aiming to validate the framework against known experimental and numerical results, we chose the strength of coupling springs between the spindle and the surrounding cytoskeleton k to be the governing parameter of the study. In addition to just an interpolar assembly studied in 2D by Ward et al. [2014], SpindleFEA allows an entire spindle to be modelled in 3D including the coupling of centrosomes to the cell membrane via astral microtubules.

Six cases of $k = 0.01\,\mathrm{N/m}$, $k = 10\,\mathrm{N/m}$, $k = 15\,\mathrm{N/m}$, $k = 20\,\mathrm{N/m}$, $k = 40\,\mathrm{N/m}$ and $k = 200\,\mathrm{N/m}$ are studied in agreement with the simulations by Ward et al. [2014]. For each case, a full quasi-static buckling analysis was carried out characterised by the spindle parameters presented in Appendix C. A structural model of the studied spindle is depicted in Fig. 8.9. Since several

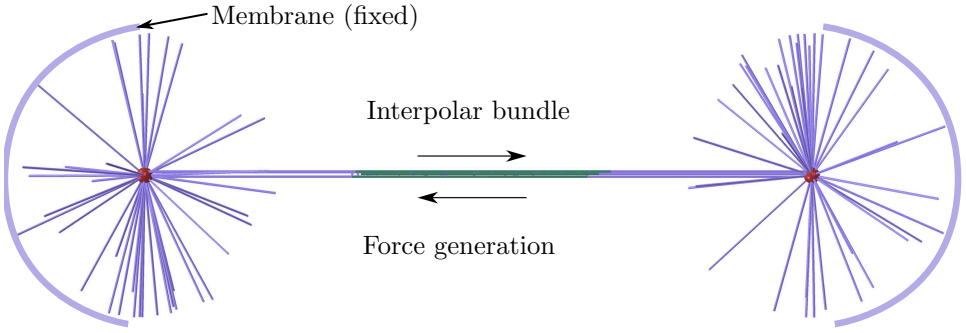

FIGURE 8.9: A geometric model of the spindle under consideration. Interpolar bundles of ipMTs grow from each pole and meet in an antiparallel assembly in the Mid-zone. AMTs stretch out from the poles towards the membrane which is assumed to be fixed. Compressive loading is generated by protein motors in the Mid-zone.

parameters are random, a number of similar studies were performed to calculate the average response of the spindle by averaging the critical buckling loads over the ensemble of models. However, a single characteristic mode shape was selected to correspond to each averaged buckling load. The computed buckling loads of the spindle for the two cases, such as weak cross-linkers and stiff cross-linkers, are plotted versus the stiffness of the coupling with the rest of the cytoskeleton k in Fig. 8.10. The top graph in Fig. 8.10 shows the variation of the buckling load in the spindle with the lateral support stiffness k for the case of weak cross-linkers. Here, the cross-linkers were assumed to have negligible bending stiffness. This implies weak coupling between the

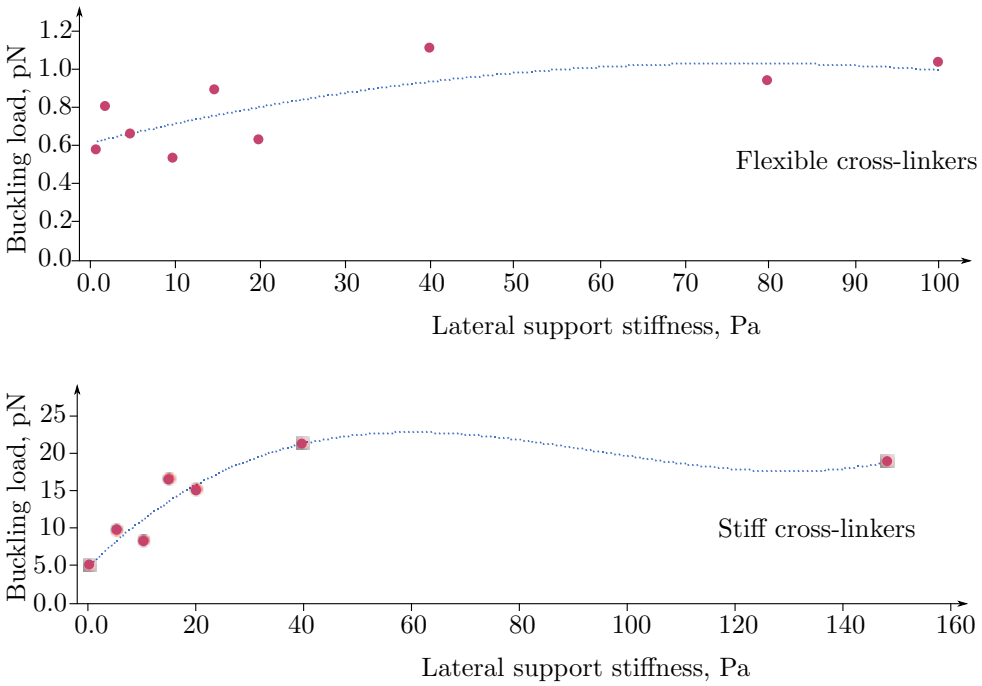

FIGURE 8.10: Buckling load of the spindle depending on the stiffness of connection to the cytoskeleton of the cell. The top plot shows the buckling loads for cross-linkers with small bending stiffness. The bottom plot shows the buckling loads for cross-linkers with realistic stiffness.

microtubules which leads to very small buckling loads even for increasing lateral support. The critical buckling loads, in this case, are consistent with Ward et al. [2014] who report that the buckling loads of the unsupported spindles 10 μm long are within 1 pN to 10 pN. Ward et al. [2014] predict a slightly stiffer response since they assume poles of the spindle to be fixed. In our study, however, the poles are allowed to move as the aMTs buckle and deform. Also, note that the buckling loads vary dramatically as the cross-section organisation of the spindle changes. The points in Fig. 8.10 are averages over 10 repetitive studies. However, spindles with the same parameters specified yield loads that vary between 0.5 pN to 5 pN. Therefore, more extensive analysis is needed to gather reliable statistics. Nevertheless, from the present study, we conclude that the assumption of weak cross-linkers does not hold against the results in the literature Ward et al. [2014] as it gives buckling loads that are too low.

Therefore, in Fig. 8.10 we present the dependency of the buckling load on the lateral support stiffness for the spindle with stiff cross-linkers, i.e., the cross-linkers are assumed to have bending stiffness EI, where E is taken to be the same as for microtubules and I is calculated for a rod with the circular cross-section with radius r =5 nm. As a result, we see much higher buckling loads. Our buckling loads appear smaller than those calculated by Ward et al. [2014], who predict P to be between 100 pN to 200 pN. At the same time, we report P to reach 40 pN, with an average maximum of 20 pN. This difference is explained by buckling of astral microtubules in our model, which triggered the displacement of the poles and earlier onset of buckling of the entire spindle. This behaviour is not observable if the centrosomes are assumed fixed.

The computed deformed configurations of the spindle are presented in Fig. 8.11 for a number of values of k. Each deformed configuration is characterised by the mode shape which is obtained from the eigenvector of the generalised eigenvalue problem constructed using the minimisation

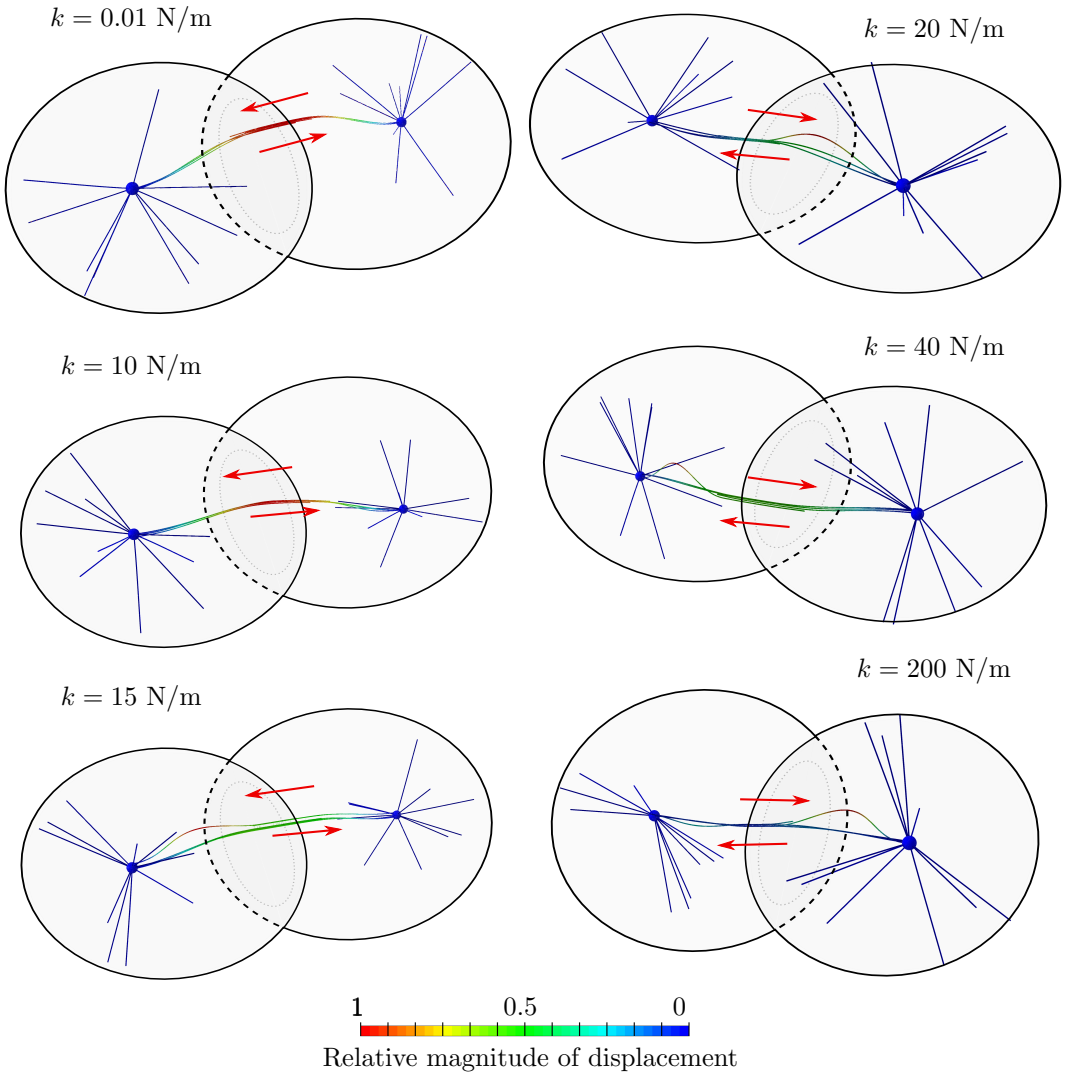

FIGURE 8.11: Buckling configuration of late Anaphase B mitotic spindle for various strengths of coupling to the cytoskeleton k. The colour code represents the non-dimensional relative displacement amplitude of the buckling mode with near-zero deflection being blue and the near-one deflection labelled with red colour.

of the total potential energy according to the FE method. The eigenvector is determined up to an unknown scaling constant or amplitude of the buckling mode. Therefore, the analysis returns the shape of the deformation profile of the beam normalised to unity rather than the actual displacement in meters. The correspondent eigenvalue is, however, a physical critical buckling load in pN. It is essential to calculate the critical buckling loads of the spindle and the associated buckling modes as they give an estimate of the deformation pattern developing in a spindle should it be loaded to a particular critical load magnitude.

In Fig. 8.11, a large relative displacement is indicated in red while the small relative displacement is shown in blue. The black circles represent the cell membrane which starts to split in the middle to form two new cells. The dotted circles show the central plane of cell division with respect to which the division may be symmetric or asymmetric. The red arrows indicate the direction of the antiparallel push by protein motors.

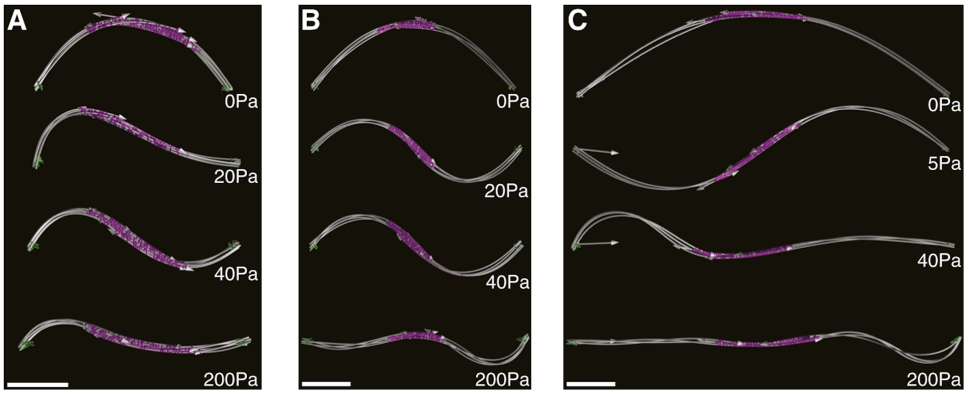

FIGURE 8.12: Examples of buckling modes of the Mitotic Spindle computed by Ward et al. [2014] for short spindles (A), moderate spindles (B) and long spindles $\approx 10\,\mu$m (C). Each mode corresponds to the strength of the lateral reinforcement shown in Pa.

For $k = 0.01\,\mathrm{N/m}$ we observe that the interpolar MT bridge consisting of two antiparallel bundles of ipMTs evolves a single arch buckling mode resembling the Euler's mode with both ends clamped. This observation agrees well with the buckling mode of the spindles reported by Ward et al. [2014]. These are reproduced in Fig. 8.12 for comparison. Indeed, Ward et al. [2014] report a single arch buckling of the spindle for $k = 0\,\mathrm{Pa}$ which matches with our observation in Fig. 8.11. As the elastic embedding k is small, it does not affect the behaviour and the two bundles of MTs deflect cooperatively being stiffly joined by the connectors. The astral microtubules buckle at much higher loads as they are considered to be strongly coupled to the surrounding cytoskeleton (actin network). Notice also that the arch remains fairly symmetric with respect to the plane of cell division (shown with a small dashed circle on the interface between the two daughter cells in Fig. 8.11) in spite of the two bundles being not identical. This indicates that a single arch buckling is rather insensitive to the irregularities in the interpolar bridge.

As we increase the coupling of the interpolar bridge to the actin network $k = 10\,\mathrm{N/m}$, we observe that the relative amplitude of the mode reduces and the single arch exhibited by the spindle possesses a small but visible degree of asymmetry which is dramatically magnified for $k = 15\,\mathrm{N/m}$. In this case, the buckling mode consists of a combination of a single arch buckling and a highly localised buckling near one of the poles. The high curvature zone indicated in red is now fully shifted to the left pole suggesting the possibility of a violation of the division symmetry with respect to the central plane. In this case, the motor push may be unevenly distributed between the left and the right halves of the spindle. Also note, the local buckling of one or two MTs prevails over the global buckling mode of the whole spindle. Such an asymmetric response for $k = 15\,\mathrm{N/m}$ and for $k = 20\,\mathrm{N/m}$ appears to be in a good qualitative agreement with the asymmetric mode reported by Ward et al. [2014] for $k = 20\,\mathrm{Pa}$ shown in Fig. 8.12 (A) and for $k = 40\,\mathrm{Pa}$ shown in Fig. 8.12 (C).

As we increase k past $40\,\mathrm{N/m}$, we observe that although the general tendency of a spindle to develop modes with shorter wavelengths is apparent and agrees with Brangwynne et al. [2006] and with Ward et al. [2014], we see that as k reaches $200\,\mathrm{N/m}$, the short-wavelength buckling mode is not entirely localised near either of the poles as reported by Ward et al. [2014] and shown here in Fig. 8.12 (C). Instead, local peaks of deformation appear near both poles. However, most interestingly, these peaks do not lie in the same plane but are rotated with respect to each other by approximately 90°. This suggests that under the high levels of compression and coupling

to the actin network, the interpolar bridge exhibits a different buckling mode, i.e., the mode with bending and torsion components. Such a mode was not reported by Ward et al. [2014] since they studied the spindle in 2D. In contrast to the study by Ward et al. [2014], our 3D

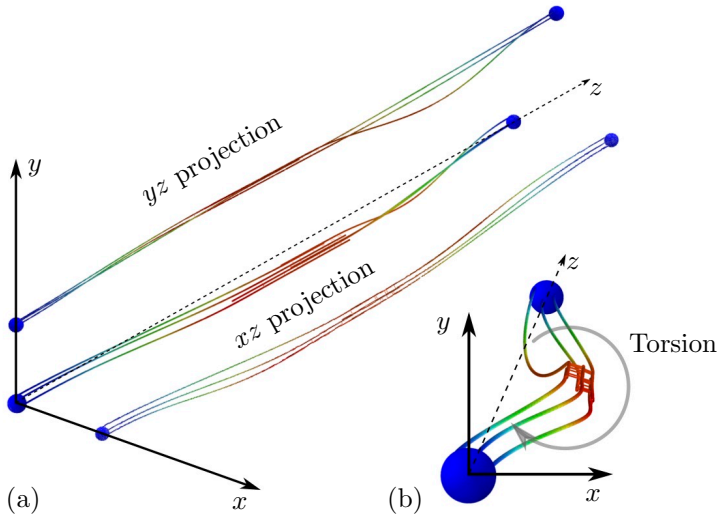

FIGURE 8.13: Three-dimensional view of a bending-torsion buckling mode for $k = 200\,\mathrm{N/m}$ with projection views. (a) The mode is depicted along with xz and yz projections. (b) A rotated view of the buckling mode which demonstrates twisting of the cross-section rotation of the interpolar MT bridge and the development of helical buckling shape.

model clearly demonstrates that for high k, it is energetically favourable not only to shorten the buckling wavelength but also to develop another type of deformation such as torsion. In fact, the observed bending-torsion mode shares a certain degree of similarity with the mode exhibited by an MT bundle with the free end reported by Soheilypour et al. [2015]. However, we do not see a strong localisation at a free end, which looks more realistic from the physiological point of view. Also unlike the results reported by Ward et al. [2014], Soheilypour et al. [2015], the bending-torsion mode shows a less asymmetric localisation of buckling with respect to the division plane, which may suggest a mechanical aspect of complex mechanisms allowing cells to persevere an extremely reliable symmetric divisions despite high levels of compression as seen in a number of experiments [Ward et al., 2014, Tolić, 2017].

In Fig. 8.13 we plot a buckling mode of another randomly generated interpolar MT bridge (recall that orientation of MTs, MT length and separation between MTs are random parameters) for

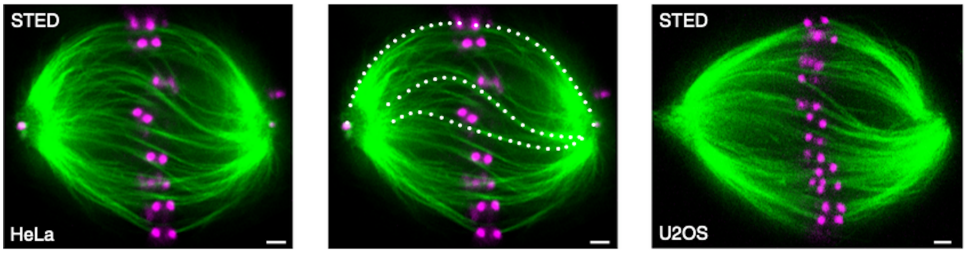

FIGURE 8.14: Experimental images of the mitotic spindles exhibiting bending and torsion reprinted from Novak et al. [2018]. (*left*) STED image of HeLa cell; microtubule bundles are in green. (*centre*) STED image of HeLa cell with traces of MT bundles (white dots) that demonstrate helical shapes of MTs. (*right*) STED image of U2OS cell spindle also demonstrating helical shape due to torsion.

$k = 200\,\mathrm{N/m}$. Fig. 8.13 (a) contains a 3D view of the mode along with the two projections on xz and yz planes, while Fig. 8.13 (b) shows a rotated and magnified view of the same mode with the bundle cross-section visible in detail. Such a behaviour can be obtained only from a three-dimensional analysis. The presence of torsion is suggested by the space curve that is not in a plane. The torsional part of the buckling mode arises from the rotation of the cross-section of the interpolar bridge about the axis that goes through the shear centre of the cross-section (which is yet to be formally identified). The direction of rotation of the cross-section with respect to the undeformed configuration is indicated with the grey arrow in Fig. 8.13 (b). Note, that each MT in a bundle develops a helix-like deformation profile exhibiting both bending and torsion components of the deformation.

Only recently a first 3D computational model for a single microtubule randomly cross-linked to the cytoskeleton was reported to yield three-dimensional buckling modes with torsion component [Li et al., 2018]. At the time of the study by SpindleFEA, the torsional buckling of an entire spindle was unknown until a new experimental study by Novak et al. [2018] was performed and reported previously unseen helical buckling of mitotic spindles in HeLa cells (see Fig. 8.14 (*left*) and *centre*) and in U2OS cells (see Fig. 8.14 (*right*)). This study proves experimentally that combined bending-torsion modes predicted by SpindleFEA occur in real spindles.

8.4 Conclusions

Concluding from our study, we acknowledge that mitotic spindles are highly complex structures which are still poorly understood. Due to the variation in MT length, number and stiffness of connectors and a multitude of other factors that need further refinement, mitotic spindles vary considerably in stiffness and structural geometry which, in turn, affects their structural response. Therefore, the current results, although quite qualitative, should still be considered informative. In the future, a large scale parametric study will have to be carried out to be able to describe the structural behaviour of spindles in averaged terms. Furthermore, we also aim to automatically construct a number of phase diagrams that could be used to generically characterise the multitude of various types of spindle behaviour depending on a number of structural parameters.

Chapter 9

Conclusions and future work

In this work, the instability of several classes of structures, representative of a wider class of geometries found in a variety of seemingly unrelated fields from structural engineering and composite materials, to strata, nano-electromechanical devices and nano-composites, has been studied. Geometries of a similar type are found in living organisms, particularly, in the bundles of sub-cellular protein filaments.

The structures studied here possess two principal types of geometric features. The first type of the geometry is broadly characterised by a structure consisting of two or more identical slender parts coupled at their ends. The second type includes structures with one or many symmetrically placed cut outs or splits. Both types of structures, although apparently different in external details, or manufacturing intent, have strong similarities with regards to their structural stability.

From the review of the literature in a number of fields, we observed that studies that involve these types of geometries focus primarily on solving specific problems in very specific contexts, without the perspective to reveal the generic mechanics common to this class of problems arising from similarities in the underlying geometric features that may connect the effects in various fields. To bring this out, we studied the instability of a bilayer beam, a chain of coupled rods, a plate with a rectangular cut out and a plate with multiple rectangular cut outs as 1-D and 2-D representatives of the discussed types of geometries. Finally, we studied the instability of a mitotic spindle that consists of bundles of microtubules as a 3-D structural assembly that consists of coupled members.

The bilayer beam was chosen as an expository device for a number of problems focused on buckling of delaminated composites. The problem was studied for the isotropic case and to a single symmetrically placed delamination. In this way, we reduced the mechanical complexity to a minimum and studied the effect that bilayer geometry has on buckling.

We performed buckling experiments on the bilayer beam structures. A number of samples, varying in their geometrical parameters were tested. Each sample type is described by the specific beam thickness relative to beam length and split length relative to beam length. We report that each sample type exhibits a distinct type of buckling mode. Here we report that, depending on the thickness and on the split length, the bilayer beam exhibits one of the three mode types, i.e., cooperative, splitting or antisymmetric. Interestingly, this is similar to the buckling character, also reported for an orthotropic laminate with delamination in the literature.

Then, we focused on a comprehensive characterisation of the buckling behaviour by performing computations by systematically changing both split length and beam thickness parameters in small steps. We then classified the computed mode shapes using a proposed technique based on Modal Assurance Criterion. Thus, we are able to organise the buckling behaviour in a phase diagram that maps the types of modes to the regions of geometric parameters. We also studied the mechanisms of a sudden change of the mode type upon traversing the phase boundaries. We reported that the lowest eigenvalues of the bilayer beam nearly degenerate on the phase boundary which is responsible for the mode order swapping and allows the realisation of the higher modes. Finally, we report that a triple-near-degeneracy (triple) point exists in the phase diagram. Around this point, either of the three buckling mode types may occur due to the slightest perturbations in the structure or experimental setup. This was also confirmed by the experiments performed in the vicinity of the triple point.

We extended the ideas behind the bilayer beam buckling further. We performed compression tests of the stack of identical sheets glued at the ends and observed a curious phenomenon of the rapid decay of buckling amplitude from sheet to sheet. Taking into account the observed behaviour and the regular geometric structure of the problem (that implies periodicity), we made a connection between buckling of periodic structures and vibration and wave propagation in periodic media. To investigate this further quantitatively, we proposed an expository device for such types of problems – a chain of rigid rods coupled with light springs. The proposed model allowed us to derive the fundamental descriptors of the periodic structure in buckling. We calculated the buckled shape of each rod using the spatial periodic modulation of the buckling amplitudes of each rod. We call such solutions extended buckling modes, which is analogous to the so-called *extended modes of a vibrating periodic structure*. They are discrete static analogues of the Bloch waves in periodic structures. Furthermore, we calculated all the buckling loads of the chain of rigid rods associated with the extended modes and plotted them versus the mode number. In such a way, we presented a buckling analogy of the first Brillouin zone.

The model was then extended to address the case of a periodic chain with small randomly distributed disorder. The transfer matrix method was used to calculate how buckling amplitude changes from rod to rod. The strength of coupling between the rods and the magnitude of the disorder were the two governing parameters of the model. Increasing their ratio from zero (perfectly ordered case), we observed slight deviations from the perfect periodicity of the extended modes to weak localisation followed by strong localisation phenomenon. In this case, strong localisation is characterised by the onset of buckling only in a local domain of the chain while the other parts remain stable due to disorder. This closely resembles the rapid decay of the buckling amplitude along the stacked sheets observed experimentally.

Having studied the simplest case of coupled beams, a 2-D geometry with analogous features was considered next. A rectangular plate with a symmetrically placed rectangular cut out is in some ways similar to the split beam problem. Instability of such structures often results from thermal buckling in fire doors. Typical fire doors have one or two rectangular windows. In the present study, we considered plates with cut outs, when the parameters are changed systematically.

To investigate the buckling of plates with cut outs, we first performed some compression tests. The samples made of a rectangular sheet with a symmetrically placed rectangular cut out were fabricated and tested in compression. The experimentation showed that depending on the size

of the cut out relative to the size of the split, the plate exhibits two types of buckling modes. Both of them are associated with the out-of-plane deflection of the two halves of the plate. The first type is reflected by the joined deflection of the two halves in the same direction. This is analogous to cooperative buckling of a bilayer beam. The second type is reflected by the opposite deflection of the halves, e.g., one half deflects upwards while the other deflects downwards. This is analogous to competitive or splitting buckling of a bilayer beam.

To comprehensively characterise the behaviour, we developed an analytical model of the cut plate buckling and employed it to identify the regions of geometric parameters associated with the particular mode type. Thus, we derived a phase diagram of the cut plate buckling analytically. This allowed us to identify the phase boundary between cooperative and competitive buckling in terms of relative cut length $\bar{l}$ and relative cut width $\bar{\alpha}$. It turned out that the location of the phase boundary depends only on the ratio of Poisson coefficient to plate aspect ratio. For the steel plate, the boundary is almost a straight line with the slope $-L/b$, where L is the length and b is the width of the plate. The computational investigation of the problem revealed that unlike the split beam problem, the elastic plate with a cut out shows much more sensitivity in its response to small perturbations and disorder. The main message is that the two modes are so close that inevitable swapping between nearly degenerate modes is favoured by the disorder, even due to numerical noise. In other words, there are doublet of modes, even though theoretically there should be two close but distinct modes due to elastic coupling. By comparison, the split beam shows a much more robust instability behaviour.

We studied the instability of a rectangular plate with a number of regularly placed rectangular cut outs next, in order to explore the role of periodicity in such structures, that is present *across the length* of plate strips. By applying the similar mathematical tools, but with a much more carefully chosen ansazt, we obtained the extended mode shapes for the plate. We arranged the mode numbers within the first Brillouin zone and calculated the associated buckling loads that form the first instability cluster. The name is given drawing upon the analogy to the passband in vibrations and wave propagation literature. We showed that this structure also exhibits two types of buckling that were mapped to a respective phase diagram. When each strip of material between the two cut outs deflects in the same direction the plate exhibits in-phase buckling. The second type of buckling is the out-of-phase buckling, which happens when each alternating strip deforms in the opposite direction. We observed theoretically the change of buckling type happening suddenly when crossing the phase boundary. We also report that this is accompanied by the inversion of a spectrum of the generalised eigenvalue problem. To understand this phenomenon better, we investigated the tridiagonal stiffness matrix of the problem. We report that the spectrum inverts due to the off-diagonal terms in the matrix changing the sign from negative to positive via zero. Here, zero off-diagonal terms occur exactly on the phase boundary where the eigenvalue problem of size N has exactly N multiple eigenvalues.

The phase diagram of a plate with multiple cut outs changes when the small random disorder is introduced to the structure. It so turned out that disorder has a dramatic effect on the out-of-phase buckling and much weaker effect on the in-phase buckling. This is explained by the small coupling between strips as cut outs are large in this region of parameters. In this case, the eigenvalue trajectories as functions of parameters do not cross (spectrum is not inverted) but experience a strong repulsion near the phase boundary. Therefore, even small disorder quickly

distorts the periodic pattern of the out-of-phase mode and imposes strong localisation. The in-phase buckling remains relatively insensitive to the disorder of such magnitude. Therefore, in the real-life structures, that inevitably possess a certain degree of irregularity, the phase boundary effectively separates the region of parameters where in-phase buckling occurs from the region of strong localisation which happens even for the small disorder.

Finally, having considered 1-D and 2-D cases, we turned to a more generic problem of buckling of 3-D assemblies of coupled *slender* members that arise in the context of biophysics. Such a geometry appears in bundles of microtubules that form a mitotic spindle – a complex cytoskeletal structure that facilitates cell division (mitosis) under compression, thus buckling being the underlying physics behind a biological function. At the current stage, we investigated this problem computationally. The systematic review of the literature in the field allowed the formulation of the main assumptions employed in the model. The fundamental physical assumption that differentiates the present study from most of the existing ones, is the quasi-static evolution of the mitotic spindle. Effectively, this allows treating different phases of mitosis as static problems governed by linear and/or nonlinear buckling. Thus, the time dependence is removed and the modelling is simplified dramatically. We incorporated this assumption along with a number of structural characteristics of a mitotic spindle in a custom made software used to solve the static instability problem for the entire spindle. The computations revealed considerable localisation of the buckling mode of the interpolar bundle of microtubules. In addition to that, it predicted coupled bending and torsion deformation of the bundle in buckling. This behaviour was only recently observed in the experiments from the literature.

In summary, the present thesis explores the elastic instability behaviour of a number of sub-classes of problems within the wider class of the problem of elastically coupled slender structures. The simplest case is that of two such substructures coupled together, followed by several of these perfectly ordered structures that are elastically linked. Finally the role of disorder was brought out. Analogies with waves in periodic and disordered periodic media were made. The observed behaviour was analytically characterised, organised using suitable instability behaviour maps, and also experimentally verified.

9.1 Future work

The research carried out has revealed some interesting instability behaviour in bilayer structures, multilayer structures and plates with cut outs as well as mitotic spindles. Yet, it has also posed numerous new questions that are worth investigating.

The instability behaviour of the bilayer beam discussed in Chapter 3 and Chapter 4 may be of particular interest to the studies on nano-electromechanical devices as switch-like behaviour is afforded by buckling. Especially interesting is the possibility to use the near-triple-degeneracy of the structure in the vicinity of the triple point. A thorough investigation of the literature on nano-electromechanical devices is needed to understand in what circumstances the bilayer beam may be used as a nano-mechanical triple switch. Although futuristic, there are possibilities of 3-state logic in computing; here we have a mechanical element that provides such a theoretical possibility.

Experimental observation of the localisation of buckling amplitude along the stacking direction of a number of sheets presented in Chapter 5 also needs a thorough follow-up study. A more detailed experiment with further numerical modelling and analysis based on the theory of periodicity is essential to describe the instability features of such a structure in detail. This study is planned to be carried out next.

The in-phase and out-of-phase buckling of a plate with a rectangular cut-out reported in Chapter 6 is of high practical importance since it demonstrates not only that a simple plate with a cut out may have dramatic variation in the buckling character because of cut out dimensions, but also shows that computational modelling of such a problem using FEA is not easy since the computational results may easily be incorrect due to small numerical errors in the regions of high sensitivity. Therefore, several additional parametric FEA studies need to be carried out by changing element types and meshing techniques to understand what are the limits of accuracy of FEA in this problem. This is essential since such plates are common in engineering and standard buckling analysis of such problems using FEA without realisation of the limitations of the numerical methods may lead to erroneous results.

Further, the study of the instability behaviour of a plate with numerous regularly placed cut outs discussed in Chapter 7 poses a number of questions. While it is consistent with the theory of periodicity that the entire clusters of buckling loads have to be inverted via N-fold degeneracy of the spectrum, such behaviour is very unusual. The proof of this behaviour experimentally and numerically is difficult due to the onset of strong localisation even for the very small disorder. Yet, very precise experiments need to be carried out both computationally and in the laboratory to indirectly show the inversion of the instability clusters even in the presence of localisation. This can be done if the localisation is weak and the modes still resemble the periodic ones. Then, even slightly localised, the amplitudes are expected to follow the out-of-phase pattern which would prove the inversion of the cluster.

Another interesting problem can be defined based on the analysis of the plate with multiple cut outs. The problem of elastic stability of a periodic plate with contrasting material properties naturally arises if the cut outs in the plate are assumed to be filled with a soft material. This problem relates to the body of literature on the vibration of multicomponent structures with contrasting properties. However, buckling is considered in this case instead of the normal vibrations or wave propagation. The application of the theory of periodicity, similar to that discussed in Chapter 7, will allow complex structures to be analysed semi-analytically. This also may lead to the discovery of novel types of instability behaviour depending on the stiffness of the filling material.

Finally, the research on the instability behaviour of mitotic spindles discussed in 8 needs to be carried out further. Firstly, we need to perform an extensive parametric study using SpindleFEA to gather enough data for further statistical quantification of the response. Secondly, an extended classification methodology base on Modal Assurance Criterion needs to be developed and applied to the gathered computational data to identify the main types of spindle behaviour. Finally, this allows further insights as to what mechanisms drive particular characters of spindle behaviour and relate those to physiological parameters.

Appendix A

Energy expressions for the bilayer beam

The strain energy U of the mode type $\mathbb{A}$ is derived from Equation (4.32) using the 4^{th} order polynomial assumed mode shape given by Equation (4.43) as

$$\begin{aligned} U_{\text{A}} =& \frac{EI}{20}\Big[q_1^2\left(32-90\bar{l}^3+90\bar{l}^4-24\bar{l}^5\right)-9q_1q_2\left(-4+20\bar{l}^3-25\bar{l}^4+8\bar{l}^5\right) \\ & 3q_2^2\left(4-30\bar{l}^3+45\bar{l}^4-18\bar{l}^5\right)\Big]. \end{aligned} \tag{A.1}$$

The potential energy due to the external loading V is derived using Equation (4.21)

$$V_{\text{A}} = -\frac{P}{210}\left(32q_1^2+33q_1q_2+9q_2^2\right). \tag{A.2}$$

Minimisation of the total potential energy leads to the generalised EVP

$$\frac{EI}{5}\begin{bmatrix} 16-45\bar{l}^3+45\bar{l}^4-12\bar{l}^5 & \frac{9}{4}\left(4-20\bar{l}^3+25\bar{l}^4-8\bar{l}^5\right) \\ \frac{9}{4}\left(4-20\bar{l}^3+25\bar{l}^4-8\bar{l}^5\right) & \frac{3}{2}\left(4-40\bar{l}^3+45\bar{l}^4-18\bar{l}^5\right)\end{bmatrix}\begin{bmatrix}q_1\\q_2\end{bmatrix} = P\begin{bmatrix}\frac{32}{105} & \frac{11}{70}\\ \frac{11}{70} & \frac{3}{35}\end{bmatrix}\begin{bmatrix}q_1\\q_2\end{bmatrix}, \tag{A.3}$$

with the lowest eigenvalue P_1. We scale it by $P_{cr} = \pi^2 EI$ and obtain the scaled buckling load associated with the cooperative mode

$$\bar{P}_{\text{A}} \approx 2.6-24\bar{l}^3+47\bar{l}^4-25\bar{l}^5-\sqrt{2.6-74\bar{l}^3+151\bar{l}^4-81\bar{l}^5+576\bar{l}^6-2268\bar{l}^7+3440\bar{l}^9+635\bar{l}^{10}}. \tag{A.4}$$

Similarely, substituting w_{C} given by Equation (4.45) and γ_{C} given by Equation (4.48) into the strain energy expression in Equation (4.47) we derive the expression for the strain energy U for the antisymmetric mode $\mathbb{C}$. We do not present this lengthy expression here. For reference we provide only the entries of the 4×4 stiffness matrix

$$\mathbf{K} = EI\begin{bmatrix} K_{11} & K_{12} & K_{13} & K_{14} \\ K_{21} & K_{22} & K_{23} & K_{24} \\ K_{31} & K_{32} & K_{33} & K_{34} \\ K_{41} & K_{42} & K_{43} & K_{44}\end{bmatrix}, \tag{A.5}$$

where $\mathbf{K}$ is symmetric. The unique elements are

$$K_{11} = -9\bar{l}^3 + 18\bar{l}^2 - 12\bar{l} + 4, \tag{A.6}$$

$$K_{22} = -\frac{3}{5}\left(36\bar{l}^5 - 135\bar{l}^4 + 195\bar{l}^3 - 135\bar{l}^2 + 45\bar{l} - 8\right), \tag{A.7}$$

$$K_{33} = 4 - 12\bar{l} - 9\bar{l}^3 + 18\bar{l}^2 - \frac{3\left(27\bar{l}^5 - 90\bar{l}^4 + 110\bar{l}^3 - 60\bar{l}^2 + 15\bar{l} - 4\right)}{10h^2}, \tag{A.8}$$

$$K_{44} = K_{22} - \frac{9\left(80\bar{l}^7 - 420\bar{l}^6 + 903\bar{l}^5 - 1015\bar{l}^4 + 630\bar{l}^3 - 210\bar{l}^2 + 35\bar{l} - 6\right)}{70h^2}, \tag{A.9}$$

$$K_{12} = \frac{1}{2}\left(27\bar{l}^4 - 78\bar{l}^3 + 81\bar{l}^2 - 36\bar{l} + 8\right), \tag{A.10}$$

$$K_{13} = -K_{11}, \tag{A.11}$$

$$K_{14} = -K_{12}, \tag{A.12}$$

$$K_{23} = K_{12}, \tag{A.13}$$

$$K_{24} = -K_{22}, \tag{A.14}$$

$$K_{34} = K_{12} + \frac{9\left(20\bar{l}^6 - 86\bar{l}^5 + 145\bar{l}^4 - 120\bar{l}^3 + 50\bar{l}^2 - 10\bar{l} + 2\right)}{20h^2}. \tag{A.15}$$

The potential energy due to the external loading V is derived using Equation (4.21)

$$V_{\mathrm{A}} = -\frac{P}{210}\left(14q_1^2 + 21q_1q_2 + 9q_2^2\right), \tag{A.16}$$

and the respective geometric stiffness matrix is

$$\mathbf{K}_g = P\begin{bmatrix} \frac{2}{15} & \frac{1}{10} & 0 & 0 \\ \frac{1}{10} & \frac{3}{35} & 0 & 0 \\ 0 & 0 & 0 & 0 \\ 0 & 0 & 0 & 0 \end{bmatrix}. \tag{A.17}$$

This eigenvalue problem apparently has two infinite and two finite eigenvalues. We are interested only in the lowest eigenvalue P_1. We calculate it and scale by $P_{cr} = \pi^2 EI$ to obtain the scaled buckling load $\bar{P}_{\mathrm{C}}$.

The expression for the scaled critical load for mode type C is

$$\bar{P}_C = \frac{P_{cr}^{(\mathrm{C})}}{P_E} = -\frac{4(P_5(\bar{l}) + 2\sqrt{P_{10}(\bar{l})})}{33\pi^2}, \tag{A.18}$$

where $P_5(\bar{l})$ and $P_{10}(\bar{l})$ are defined as

$$P_5(\bar{l}) = 8400\bar{l}^5 - 23625\bar{l}^4 + 25000\bar{l}^3 - 12375\bar{l}^2 + 3000\bar{l} - 528, \tag{A.19}$$

$$\begin{aligned} P_{10}(\bar{l}) =& 17640000\bar{l}^{10} - 99225000\bar{l}^9 + 244387500\bar{l}^8 - 346500000\bar{l}^7 + 313137500\bar{l}^6 \\ & - 189334350\bar{l}^5 + 78685125\bar{l}^4 - 22765875\bar{l}^3 + 4477500\bar{l}^2 - 532125\bar{l} + 31581. \end{aligned} \tag{A.20}$$

Appendix B

The stiffness and the geometric stiffness matrices for the plate with a cut out

---

The entries of the stiffness matrix are formed by taking the derivatives of $U = 2U_{\text{Strip}} + U_{\text{Web}}$ with respect to q_1 and q_2. Here $2U_{\text{Strip}}$ is given by Equation (6.6) and U_{Web} is given by Equation (6.8). Likewise, the entries of the geometric stiffness matrix are derived by taking the derivatives of $2V_{\text{Strip}}$ with respect to q_1 and q_2 in tern. Here V_{Strip} is given by Equation (6.7). In such a way, the entries of the stiffness matrix are

$$K_{11} = K_{22} = 1 + \frac{(20\bar{l}^2 + 30\bar{l} + 13)(1-\bar{l})^5}{280A^4\bar{\alpha}^3} - \frac{3\left(1-\bar{l}\right)^3\left(\left(2\bar{l}^2+\bar{l}\right)(5\nu-3)-1\right)}{25A^2\bar{\alpha}} + \frac{26}{35}\left(1+\bar{l}\left(-4\bar{l}^2+6\bar{l}-3\right)\right)\bar{\alpha} - \bar{\alpha}, \tag{B.1}$$

$$K_{12} = K_{21} = \frac{(20\bar{l}^2 + 30\bar{l} + 13)(1-\bar{l})^5}{280A^4\bar{\alpha}^3} + \frac{3\left(1-\bar{l}\right)^3\left(\left(2\bar{l}^2+\bar{l}\right)(5\nu-3)-1\right)}{25A^2\bar{\alpha}} + \frac{9}{35}\left(1+\bar{l}\left(-4\bar{l}^2+6\bar{l}-3\right)\right)\bar{\alpha} - \bar{\alpha}. \tag{B.2}$$

Note that the dimensional factor $96AD/L^2$ is brought in from of the matrix the stiffness matrix $\mathbf{K}$.

At the same time, the entries of the geometric matrix times the dimensional factor $12P/(5L)$ are written as

$$K_{g11} = K_{g22} = 1, \tag{B.3}$$

and the off-diagonal elements are zero. Thus, the geometric stiffness matrix is diagonal.

The diagonal entries K_{ii} and off-diagonal entries K_{ij} have similar looking expressions. This plays a crucial role when calculating the eigenvalues and the eigenvectors of the EVP as some terms cancel out leading to relatively simple expressions for the eigenvalues P_1 and P_2 and for the eigenvectors $\mathbf{q}_1$ and $\mathbf{q}_2$ which is discussed in the main text of the chapter.

Appendix C

Sets of parameters used in the modelling of a mitotic spindle

Tables below contain the set of parameters employed in the modelling of mitotic spindles. The parameter values are presented along with the sources where they are taken from.

TABLE C.1: Main parameters specifying the structure and properties of microtubules in SpindleFEA.

Properties of microtubules			
Parameter name	Adapted from	Name in "job.py"	Values
MT inner diameter	Pampaloni et al. [2006]	`d`	$0.015\,\mu$m
MT outer diameter	Pampaloni et al. [2006]	`D`	$0.025\,\mu$m
Inter-polar MT lengths were chosen from a normal distribution	–	`lengthInterval`	$\sigma = 5\,\mu$m, $\mu = 2\,\mu$m
Astral MT length	Cell diameter minus spindle length	`aMTlength`	$2\,\mu$m
Number of ipMTs	Ward et al. [2014]	`ipMTnumber`	6
Number of aMTs	Typically hundreds [Müller-Reichert et al., 2018]. Considered 20 for demonstration.	`aMTnumbers`	20
Distance between ipMTs	Taken from a normal distribution fitted to Ward et al. [2014]	`separation`	$\sigma = 0.029\,\mu$m, and $\mu = 0.04\,\mu$m
Angle between ipMTs	Taken from a normal distribution fitted to Ward et al. [2014]	`angle`	$\sigma = 96.4°$, $\mu = 11.1°$
Elastic modulus of MTs	Pampaloni et al. [2006]	`ElasticModulus`	1.5×10^9 pN/μm^2
Poisson ratio of MT material for isotropic case	–	`PoissonRatio`	0.3

TABLE C.2: Main parameters reflecting architecture of a spindle in SpindleFEA.

Spindle architecture			
Parameter name	Adapted from	Name in "job.py"	Values
Total spindle length	Ward et al. [2014]	–	$14.3\,\mu$m
Cell radius	Ward et al. [2014]	–	$1.6 \pm 1.0\,\mu$m
Distance between centrosomes	Ward et al. [2014]	`SpindleLength`	$10\,\mu$m
Length of interlinked zone in Fig. 8.3 (a),(c)	Ward et al. [2014]	–	$2\,\mu$m

TABLE C.3: Main parameters specifying the structure and properties of centrosomes (poles) in SpindleFEA.

Properties of centrosomes			
Parameter name	Adapted from	Name in "job.py"	Values
Centrosome radius	Minimal dimensions that satisfy ipMT bundle size	`CentrosomeRadius`	120 nm
Centrosome length	Between 1x to 2x the centrosome diameter according to Ward et al. [2014]	`CentrosomeLength`	120 nm
Elastic modulus of centrosome material	Ward et al. [2014]	`CentrosomeE`	1.5×10^9 pN/μm^2
Poisson ratio of centrosome material	–	`CentrosomeNu`	0.3

TABLE C.4: Main parameters specifying properties of MT connectors in SpindleFEA.

Properties of connectors			
Parameter name	Adapted from	Name in "job.py"	Values
Connector radius	Nixon et al. [2015]	`connectorRadius`	5 nm
Connector length	Subramanian et al. [2010]	–	20 nm to 50 nm
Number of connectors per MT	50 according to Ward et al. [2014]	`Nconnectors`	10
Elastic modulus of connector material	Ward et al. [2014]	`connectorE`	1.5×10^9 pN/μm^2
Poisson ratio of connector material	–	`connectorNu`	0.3

TABLE C.5: Other parameters controlling the effect of mechanical coupling between the spindle parts and the number of critical buckling loads to be calculated by SpindleFEA.

Other parameters			
Parameter name	Adapted from	Name in "job.py"	Values
Strength of elastic embedding of aMTs	Governing parameter	`aMTspring`	0 pN/μm^2 to 200 pN/μm^2
Strength of interpolar bridge elastic embedding	Governing parameter	`groundSpring`	0 pN/μm^2 to 200 pN/μm^2
Number of requested eigenvalues	–	`NumberOfEigs`	5

Bibliography

BS EN 1634-1:2014+A1:2018: Fire resistance and smoke control tests for door and shutter assemblies, openable windows and elements of building hardware. Fire resistance test for door and shutter assemblies and openable windows. Standard, British Standards, Jan. 2014.

Vestas-Aircoil. https://www.vestas-aircoil.com/, 2017.

T. Afrin, A. M. R. Kabir, K. Sada, A. Kakugo, and T. Nitta. Buckling of microtubules on elastic media via breakable bonds. *Biochemical and Biophysical Research Communications*, 480(1): 132–138, 2016. ISSN 10902104. doi:10.1016/j.bbrc.2016.09.133.

R. J. Allemang. The modal assurance criterion - Twenty years of use and abuse. *Sound and Vibration*, 37(August):14–21, 2003. ISSN 15410161. doi:10.1016/j.chemgeo.2006.02.014.

P. W. Anderson. Absence of diffusion in certain random lattices. *Physical Review*, 109(5): 1492–1505, 1958. ISSN 0031899X. doi:10.1103/PhysRev.109.1492.

K. K. Ang and C. M. Wang. Shear–flexural buckling of columns. *Journal of Engineering Mechanics*, 116(6):1220–1241, 1990. ISSN 07339399. doi:10.1061/(ASCE)0733-9399(1990)116:6(1220).

J. Argyris and L. Tenek. Buckling of multilayered composite plates by natural shear deformation matrix theory. *Computer Methods in Applied Mechanics and Engineering*, 111:37–59, 1994. ISSN 00457825. doi:10.1016/0045-7825(94)90039-6.

S. Ariaratnam and W.-C. Xie. Wave Localization in Randomly Disordered Nearly Periodic Long Continuous Beams. *Journal of Sound and Vibration*, 181:7–22, 1995. ISSN 0022460X. doi:10.1006/jsvi.1995.0122.

V. I. Arnold. *Mathematical Methods of Classical Mechanics*. Graduate Texts in Mathematics. Springer-Verlag, New York, 1978. ISBN 978-1-4757-1693-1.

M. Aßmus, K. Naumenko, and H. Altenbach. A multiscale projection approach for the coupled global–local structural analysis of photovoltaic modules. *Composite Structures*, 158:340–358, Dec. 2016. ISSN 02638223. doi:10.1016/j.compstruct.2016.09.036.

R. Atif and F. Inam. Modeling and Simulation of Graphene Based Polymer Nanocomposites: Advances in the Last Decade. *Graphene*, 5(5):96–142, 2016. doi:10.4236/graphene.2016.52011.

N. Ayrilmis, Z. Candan, and S. Hiziroglu. Physical and mechanical properties of cardboard panels made from used beverage carton with veneer overlay. *Materials & Design*, 29(10): 1897–1903, Dec. 2008. ISSN 02613069. doi:10.1016/j.matdes.2008.04.030.

M. T. Bah, P. B. Nair, A. Bhaskar, and A. J. Keane. Forced response statistics of mistuned bladed disks: A stochastic reduced basis approach. *Journal of Sound and Vibration*, 263(2): 377–397, May 2003. ISSN 0022-460X. doi:10.1016/S0022-460X(02)01058-1.

J. Banerjee. Dynamic stiffness formulation for structural elements: A general approach. *Computers & Structures*, 63(3):101–103, 1997. ISSN 00457949. doi:10.1016/S0045-7949(96)00326-4.

S. Bauer. Buckling of Cold-Formed-Steel Columns. https://classes.mst.edu/civeng120/lessons/compression/examples/column_buckling/index.html, 2019.

H. Benaroya. Waves in periodic structures with imperfections. *Composites Part B: Engineering*, 28(1-2):143–152, 1997.

M. R. Bernfield and J. M. Slack. Cell. *Encyclopædia Britannica*, Mar. 2019.

K. Bertoldi, P. M. Reis, S. Willshaw, and T. Mullin. Negative Poisson's Ratio Behavior Induced by an Elastic Instability. *Advanced Materials*, 22(3):361–366, 2010. ISSN 1521-4095. doi:10.1002/adma.200901956.

A. Bhaskar. Waveguide modes in elastic rods. *Proceedings of the Royal Society A: Mathematical, Physical and Engineering Sciences*, 459(2029):175–194, Jan. 2003. ISSN 1364-5021, 1471-2946. doi:10.1098/rspa.2002.1013.

A. Bhaskar. Elastic waves in Timoshenko beams: The 'lost and found' of an eigenmode. *Proceedings of the Royal Society A: Mathematical, Physical and Engineering Sciences*, 465(2101): 239–255, Jan. 2009. ISSN 1364-5021, 1471-2946. doi:10.1098/rspa.2008.0276.

F. Bloch. Über die Quantenmechanik der Elektronen in Kristallgittern. *Z. Physik*, 52(7):555–600, July 1929. ISSN 0044-3328. doi:10.1007/BF01339455.

R. D. Borcherdt. *Viscoelastic Waves in Layered Media*. Cambridge University Press, Cambridge, 2009. ISBN 978-0-511-58099-4. doi:10.1017/CBO9780511580994.

A. Bozzolo, C. Ferrando, A. Tonelli, and E. Cabella. Numerical methodology for thermal-mechanical analysis of fire doors. In *10th European LS-Dyna Conference*, page 11, 2015.

C. P. Brangwynne, F. C. MacKintosh, S. Kumar, N. A. Geisse, J. Talbot, L. Mahadevan, K. K. Parker, D. E. Ingber, and D. A. Weitz. Microtubules can bear enhanced compressive loads in living cells because of lateral reinforcement. *Journal of Cell Biology*, 173(5):733–741, 2006. ISSN 00219525. doi:10.1083/jcb.200601060.

L. Brillouin. *Wave Propagation in Periodic Structures*. Courier Corporation, 2003. ISBN 0-486-49556-6.

S. Budday, P. Steinmann, and E. Kuhl. The role of mechanics during brain development. *Journal of the Mechanics and Physics of Solids*, 72:75–92, Dec. 2014. ISSN 00225096. doi:10.1016/j.jmps.2014.07.010.

E. Byklum, E. Steen, and J. Amdahl. A semi-analytical model for global buckling and post-buckling analysis of stiffened panels. *Thin-Walled Structures*, 42(5):701–717, May 2004. ISSN 02638231. doi:10.1016/j.tws.2003.12.006.

M. Castanier and C. Pierre. Lyapunov exponents and localization phenomena in multi-coupled nearly periodic systems. *Journal of Sound and Vibration*, 183(3):493–515, 1995. ISSN 0022460X. doi:10.1006/jsvi.1995.0267.

M. Castanier and C. Pierre. Predicting Localisation Via Lyapunov Exponent Statistics. *Journal of Sound and Vibration*, 203(1):151–157, 1997. ISSN 0730725X. doi:10.1016/0002-9610(92)90118-B.

H. Chai, C. Babcock, and W. Knauss. One dimensional modelling of failure in laminated plates by delamination buckling. *International Journal of Solids and Structures*, 17(11):1069–1083, 1981. ISSN 00207683. doi:10.1016/0020-7683(81)90014-7.

A. Chaigne, C. Campillo, R. Voituriez, N. S. Gov, C. Sykes, M.-H. Verlhac, and M.-E. Terret. F-actin mechanics control spindle centring in the mouse zygote. *Nature Communications*, 7: 10253, Jan. 2016. ISSN 2041-1723. doi:10.1038/ncomms10253.

Y. Chen, T. Li, Z. Jia, F. Scarpa, C.-W. Yao, and L. Wang. 3D printed hierarchical honeycombs with shape integrity under large compressive deformations. *Materials & Design*, 137:226–234, Jan. 2018. ISSN 02641275. doi:10.1016/j.matdes.2017.10.028.

B. Cheng and J. Zhao. Strengthening of perforated plates under uniaxial compression: Buckling analysis. *Thin-Walled Structures*, 48(12):905–914, 2010. ISSN 02638231. doi:10.1016/j.tws.2010.06.001.

B. Cheng, J. Wang, and C. Li. Compression tests and numerical analysis of perforated plates containing slotted holes in steel pylons. *Thin-Walled Structures*, 67:129–143, 2013. ISSN 02638231. doi:10.1016/j.tws.2013.02.005.

M. Cho and J.-S. Kim. Higher-Order Zig-Zag Theory for Laminated Composites With Multiple Delaminations. *Journal of Applied Mechanics*, 68(6):869, 2001. ISSN 00218936. doi:10.1115/1.1406959.

M. Claessens, M. Bathe, E. Frey, and A. R. Bausch. Actin-binding proteins sensitively mediate F-actin bundle stiffness. *Nature Materials*, 5(9):748–753, 2006. ISSN 1476-1122. doi:10.1038/nmat1718.

C. Coulais, J. T. B. Overvelde, L. A. Lubbers, K. Bertoldi, and M. Van Hecke. Discontinuous Buckling of Wide Beams and Metabeams. *Physical Review Letters*, 115(4), 2015. ISSN 10797114. doi:10.1103/PhysRevLett.115.044301.

S. W. Cranford. Buckling induced delamination of graphene composites through hybrid molecular modeling. *Applied Physics Letters*, 102(3):31902–235501, 2013. ISSN 00036951. doi:10.1063/1.4788734.

M. Damghani, D. Kennedy, and C. Featherston. Critical buckling of delaminated composite plates using exact stiffness analysis. *Computers and Structures*, 89(13-14):1286–1294, 2011. ISSN 00457949. doi:10.1016/j.compstruc.2011.04.003.

Dassault Systèmes. ABAQUS 6.14 Documentation. Technical report, Dassault Systèmes, Providence, RI, USA, 2014.

C. U. E. Departement. *Materials Data Book*. Cambridge University, two thousand, third edition, 2003.

T. Dodwell and G. Hunt. Convoluted accommodation structures in folded rocks. *Philosophical Magazine*, 92(28-30):3418–3438, 2012. ISSN 1478-6435. doi:10.1080/14786435.2012.685771.

T. Dodwell, G. Hunt, M. Peletier, and C. Budd. Multi-layered folding with voids. *Philosophical Transactions of the Royal Society A: Mathematical, Physical and Engineering Sciences*, 370 (1965):1740–1758, 2012a. ISSN 1364-503X. doi:10.1098/rsta.2011.0340.

T. J. Dodwell and G. W. Hunt. Periodic Void Formation in Chevron Folds. *Mathematical Geosciences*, pages 1011–1028, 2014. ISSN 1874-8961. doi:10.1007/s11004-014-9562-x.

T. J. Dodwell, M. A. Peletier, C. J. Budd, and G. W. Hunt. Self-Similar Voiding Solutions of a Single Layered Model of Folding Rocks. *Journal of Applied Mathematics*, 72(1):444–463, 2012b.

M. Dogterom and T. Surrey. Microtubule organization in vitro. *Current Opinion in Cell Biology*, 25:23–29, 2013. doi:10.1016/j.ceb.2012.12.002.

R. Edmunds, G. W. Hunt, and M. A. Wadee. Parallel folding in multilayered structures. *Journal of the Mechanics and Physics of Solids*, 54(2):384–400, 2006. ISSN 00225096. doi:10.1016/j.jmps.2005.08.013.

K. M. El-Sawy and A. S. Nazmy. Effect of aspect ratio on the elastic buckling of uniaxially loaded plates with eccentric holes. *Thin-Walled Structures*, 39(12):983–998, 2001. ISSN 02638231. doi:10.1016/S0263-8231(01)00040-4.

I. Elishakoff, Y. Li, and J. Starnes Jr. Buckling mode localization in elastic plates due to misplacement in the stiffener location. *Chaos, Solitons & Fractals*, 5(8):1517–1531, Aug. 1995. ISSN 09600779. doi:10.1016/0960-0779(94)00158-M.

I. Elishakoff, J. Kaplunov, and E. Nolde. Celebrating the Centenary of Timoshenko's Study of Effects of Shear Deformation and Rotary Inertia. *Applied Mechanics Reviews*, 67(6), Nov. 2015. ISSN 0003-6900, 2379-0407. doi:10.1115/1.4031965.

B. Embleton. Geograph: Rock Strata, Durdle Door. https://www.geograph.org.uk/photo/274762, Nov. 2006.

S. Engineering. Structural Design of Light Gauge Steel, 2019.

G. Floquet. Sur les équations différentielles linéaires à coefficients périodiques. *Annales scientifiques de l'École normale supérieure*, 12:47–88, 1883. ISSN 0012-9593, 1873-2151. doi:10.24033/asens.220.

J. A. Fuesler. Dynamic instability -a common denominator in prokaryotic and eukaryotic DNA segregation and cell division. *Cellular & Molecular Biology Letters*, 17:542–548, 2012. doi:10.2478/s11658-012-0026-3.

H. Furstenberg. Noncommuting Random Products. *Transactions of the American Mathematical Society*, 108(3):377–428, 1963. ISSN 0002-9947.

F. Gittes, B. Mickey, J. Nettleton, and J. Howard. Flexural rigidity of microtubules and actin filaments measured from thermal fluctuations in shape. *The Journal of cell biology*, 120(4): 923–934, 1993. doi:DOI: 10.1083/jcb.120.4.923.

F. M. Goodman, P. de la Harpe, and V. F. R. Jones. *Coxeter Graphs and Towers of Algebras*. Springer Science & Business Media, Dec. 2012. ISBN 978-1-4613-9641-3.

T. Gorishnyy, M. Maldovan, C. Ullal, and E. Thomas. Phononic crystals are novel materials that offer exceptional control over phonons, sound and other mechanical waves. Taras Gorishnyy, Martin Maldovan, Chaitanya Ullal and Edwin Thomas report on a revolution in acoustics. *Phononic crystals*, page 6, 2005.

R. M. Gray. Toeplitz and Circulant Matrices: A Review. *Foundations and Trends® in Communications and Information Theory*, 2(3):155–239, 2005. ISSN 1567-2190, 1567-2328. doi:10.1561/0100000006.

Y. He, G.-h. Xue, and J.-z. Fu. Fabrication of low cost soft tissue prostheses with the desktop 3D printer. *Scientific Reports*, 4(1), May 2015. ISSN 2045-2322. doi:10.1038/srep06973.

C. H. Hodges and J. Woodhouse. Vibration isolation from irregularity in a nearly periodic structure: Theory and measurements. *Journal of the Acoustical Society of America*, 74(September 1983):894–905, 1983.

N. Hu, H. Fukunaga, H. Sekine, and K. Mohammad Ali. Compressive buckling of laminates with an embedded delamination. *Composites Science and Technology*, 59(8):1247–1260, 1999. ISSN 02663538. doi:10.1016/S0266-3538(98)00166-3.

G. W. Hunt, R. Edmunds, C. J. Budd, and J. W. Cosgrove. Serial parallel folding with friction: A primitive model using cubic B-splines. *Journal of Structural Geology*, 28(3):444–455, 2006. ISSN 01918141. doi:10.1016/j.jsg.2005.11.006.

J. Hutchinson and T. Wu, editors. *Advances in Applied Mechanics*. Academic Press, Nov. 1983. ISBN 978-0-08-056401-2.

A. Iakovliev. Exact elastic stability analysis based on Dynamic stiffness method. *Journal of Mechanical Engineering NTUU "Kyiv Polytechnic Institute"*, 2(77):108–118, 2016. ISSN 2409-5966. doi:10.20535/2305-9001.2016.77.78904.

A. Iakovliev, S. Dasmahapatra, and A. Bhaskar. Stability of mitotic spindle using computational mechanics. In *ACM Conference Proceedings*, pages 67–74, Singapore, Jan. 2019. ACM. ISBN 978-1-4503-6654-0. doi:10.1145/3314367.3314373.

M. Jakobs, K. Franze, and A. Zemel. Force Generation by Molecular-Motor-Powered Microtubule Bundles; Implications for Neuronal Polarization and Growth. *Frontiers in Cellular Neuroscience*, 9(9):4413389–441, 2015. ISSN 1662-5102. doi:10.3389/fncel.2015.00441.

M. E. Janson and M. Dogterom. A bending mode analysis for growing microtubules: Evidence for a velocity-dependent rigidity. *Biophysical journal*, 87(4):2723–2736, 2004. doi:10.1529/biophysj.103.038877.

F. Javid, J. Liu, J. Shim, J. C. Weaver, A. Shanian, and K. Bertoldi. Mechanics of instability-induced pattern transformations in elastomeric porous cylinders. *Journal of the Mechanics and Physics of Solids*, 96:1–17, 2016. ISSN 00225096. doi:10.1016/j.jmps.2016.06.015.

M. Z. Jin and C. Q. Ru. Localized buckling of a microtubule surrounded by randomly distributed cross linkers. *Physical Review E - Statistical, Nonlinear, and Soft Matter Physics*, 88(1), 2013. ISSN 15393755. doi:10.1103/PhysRevE.88.012701.

J. D. Joannopoulos, editor. *Photonic Crystals: Molding the Flow of Light*. Princeton University Press, Princeton, 2nd ed edition, 2008. ISBN 978-0-691-12456-8.

A. P. Joglekar, D. Bouck, K. Finley, X. Liu, Y. Wan, J. Berman, X. He, E. D. Salmon, and K. S. Bloom. Molecular architecture of the kinetochore-microtubule attachment site is conserved between point and regional centromeres. *Journal of Cell Biology*, 181(4):587–594, 2008. ISSN 00219525. doi:10.1083/jcb.200803027.

C. G. Johnson, U. Jain, A. L. Hazel, D. Pihler-Puzović, and T. Mullin. On the buckling of an elastic holey column. *Proceedings of the Royal Society A: Mathematical, Physical and Engineering Sciences*, 473(2207):20170477, Nov. 2017. ISSN 1364-5021, 1471-2946. doi:10.1098/rspa.2017.0477.

Z. Juhász and A. Szekrényes. The effect of delamination on the critical buckling force of composite plates: Experiment and simulation. *Composite Structures*, 168:456–464, 2017. ISSN 02638223. doi:10.1016/j.compstruct.2017.02.052.

A. M. R. Kabir, D. Inoue, T. Afrin, H. Mayama, K. Sada, and A. Kakugo. Buckling of Microtubules on a 2D Elastic Medium. *Scientific reports*, 5:17222, 2015. ISSN 2045-2322. doi:10.1038/srep17222.

L. M. Kachanov. Separation failure of composite materials. *Mechanics of Composite Materials*, 12(5):812–815, 1976.

J. Kaplunov, D. Prikazchikov, and L. Prikazchikova. Dispersion of elastic waves in a strongly inhomogeneous three-layered plate. *International Journal of Solids and Structures*, 113-114: 169–179, May 2017. ISSN 00207683. doi:10.1016/j.ijsolstr.2017.01.042.

J. Kaplunov, D. Prikazchikov, L. Prikazchikova, and O. Sergushova. The lowest vibration spectra of multi-component structures with contrast material properties. *Journal of Sound and Vibration*, 445:132–147, Apr. 2019. ISSN 0022460X. doi:10.1016/j.jsv.2019.01.013.

S. Kasas, A. Kis, B. M. Riederer, L. Forró, G. Dietler, and S. Catsicas. Mechanical Properties of Microtubules Explored Using the Finite Elements Method. *ChemPhysChem*, 5(2):252–257, Feb. 2004. ISSN 1439-7641. doi:10.1002/cphc.200300799.

E. H. Kellogg, S. Howes, S.-C. Ti, E. Ramírez-Aportela, T. M. Kapoor, P. Chacón, and E. Nogales. Near-atomic cryo-EM structure of PRC1 bound to the microtubule. *Proceedings of the National Academy of Sciences*, 113(34):9430–9439, 2016. ISSN 0027-8424. doi:10.1073/pnas.1609903113.

J.-H. Kim, J. M. Rhee, Y. Enyo, W. C. Hutton, and S.-S. Kim. A biomechanical comparison of 360° stabilizations for corpectomy and total spondylectomy: A cadaveric study in the thoracolumbar spine. *Journal of orthopaedic surgery and research*, 10(1):99, 2015. ISSN 1749-799X. doi:10.1186/s13018-015-0240-6.

C. Kittel. *Introduction to Solid State Physics*. Wiley, Hoboken, NJ, 8th ed edition, 2005. ISBN 978-0-471-41526-8.

A. Kudaibergenov, A. Nobili, and L. Prikazchikova. On low-frequency vibrations of a composite string with contrast properties for energy scavenging fabric devices. *Journal of Mechanics of Materials and Structures*, 11(3):231–243, Mar. 2016. ISSN 1559-3959, 1559-3959. doi:10.2140/jomms.2016.11.n3p3.

I. M. Kulić, A. E. X. Brown, H. Kim, C. Kural, B. Blehm, P. R. Selvin, P. C. Nelson, V. I. Gelfand, I. M. Kulic, A. E. X. Brown, H. Kim, C. Kural, B. Blehm, P. R. Selvin, P. C. Nelson, V. I. Gelfand, I. M. Kulić, A. E. X. Brown, H. Kim, C. Kural, B. Blehm, P. R. Selvin, P. C. Nelson, and V. I. Gelfand. The role of microtubule movement in bidirectional organelle transport. *Proceedings of the National Academy of Sciences*, 105(29):10011–10016, 2008. ISSN 0027-8424. doi:10.1073/pnas.0800031105.

C.-C. Lai and C.-S. Lin. An analysis of the design of a fire-resistant elevator landing door. *Journal of the Chinese Institute of Engineers*, 40(5):428–440, July 2017. ISSN 0253-3839, 2158-7299. doi:10.1080/02533839.2017.1336116.

P.-L. Larsson. On Delamination Buckling And Growth In Circular And Annular Orthotropic Plates. *International Journal of Solids and Structures*, 27(1984), 1989.

J. Lee, Z. Giirdal, H. Griffin, Z. Gürdal, and O. Griffin. Buckling and postbuckling of circular plates containing concentric penny-shaped delaminations. *Computers & Structures*, 58(5): 1045–1054, Mar. 1996. ISSN 00457949. doi:10.1016/0045-7949(95)00194-L.

J.-H. Lee and J. Kim. Sound Transmission Through Periodically Stiffened Cylindrical Shells. *Journal of Sound and Vibration*, 251(3):431–456, Mar. 2002. ISSN 0022460X. doi:10.1006/jsvi.2001.4009.

O. Lehtinen, S. Kurasch, A. V. Krasheninnikov, and U. Kaiser. Atomic Scale Study of the Life Cycle of a Dislocation in Graphene From Birth to Annihilation. *Nature Communications*, 4: 2098, 2013. ISSN 2041-1723. doi:10.1038/ncomms3098.

F. M. Li, Y. S. Wang, C. Hu, and W. H. Huang. Localization of elastic waves in periodic rib-stiffened rectangular plates under axial compressive load. *Journal of Sound and Vibration*, 281(1-2):261–273, 2005. ISSN 0022460X. doi:10.1016/j.jsv.2004.01.055.

S. Li, C. Wang, and P. Nithiarasu. Effects of the cross-linkers on the buckling of microtubules in cells. *Journal of Biomechanics*, 72:167–172, Apr. 2018. ISSN 00219290. doi:10.1016/j.jbiomech.2018.03.002.

Y. Li, I. Elishakoff, and J. Starnes. Buckling mode localization in a multi-span periodic structure with a disorder in a single span. *Chaos, Solitons & Fractals*, 5(6):955–969, 1995. ISSN 09600779. doi:10.1016/0960-0779(94)00211-8.

K. Liew, P. Xiang, and Y. Sun. A continuum mechanics framework and a constitutive model for predicting the orthotropic elastic properties of microtubules. *Composite Structures*, 93(7): 1809–1818, June 2011. ISSN 02638223. doi:10.1016/j.compstruct.2011.01.017.

K. M. Liew, P. Xiang, and L. W. Zhang. Mechanical properties and characteristics of microtubules: A review. *Composite Structures*, 123:98–108, 2015. doi:10.1016/j.compstruct.2014.12.020.

P. F. Liu, S. J. Hou, J. K. Chu, X. Y. Hu, C. L. Zhou, Y. L. Liu, J. Y. Zheng, a. Zhao, and L. Yan. Finite element analysis of postbuckling and delamination of composite laminates using virtual crack closure technique. *Composite Structures*, 93:1549–1560, 2011. ISSN 02638223. doi:10.1016/j.compstruct.2010.12.006.

A. E. H. Love. *A Treatise on the Mathematical Theory of Elasticity*. University Press, 1906.

A. Luongo. Mode localization in dynamics and buckling of linear imperfect continuous structures. *Nonlinear Dynamics*, 25(1-3):133–156, 2001. ISSN 0924090X. doi:10.1023/A:1012954700751.

B. R. Mace and E. Manconi. Wave motion and dispersion phenomena: Veering, locking and strong coupling effects. *The Journal of the Acoustical Society of America*, 131(2):1015–1028, 2012. ISSN 0001-4966. doi:10.1121/1.3672647.

P. Malgaretti and S. Muhuri. Mechanical stability of bipolar spindle assembly. *EPL (Europhysics Letters)*, 115(2):28001, July 2016. ISSN 0295-5075, 1286-4854. doi:10.1209/0295-5075/115/28001.

S. W. Manka and C. A. Moores. Microtubule structure by cryo-EM: Snapshots of dynamic instability. *Essays In Biochemistry*, 62(6):737–751, Dec. 2018. ISSN 0071-1365, 1744-1358. doi:10.1042/EBC20180031.

R. McDowell, K. Lee Avary, D. Matchen, R. Diecchio, H. McCoy, and A. Rutledge. Preliminary Bedrock Geologic Map of the Snowy Mountain Quadrangle Publication OF-0101. http://www.wvges.wvnet.edu/www/statemap/statemap01.htm, Nov. 2005.

D. M. Mead. Wave Propagation in Continuous Periodic Structures: Research Contributions From Southampton, 1964-1995. *Journal of Sound and Vibration*, 190(3):495–524, 1996. ISSN 0022460X. doi:10.1006/jsvi.1996.0076.

P. Meurer-Grob, J. Kasparian, and R. H. Wade. Microtubule Structure at Improved Resolution †. *Biochemistry*, 40(27):8000–8008, July 2001. ISSN 0006-2960, 1520-4995. doi:10.1021/bi010343p.

C. D. Moen and B. W. Schafer. Elastic buckling of cold-formed steel columns and beams with holes. *Engineering Structures*, 31(12):2812–2824, 2009a. ISSN 01410296. doi:10.1016/j.engstruct.2009.07.007.

C. D. Moen and B. W. Schafer. Elastic buckling of thin plates with holes in compression or bending. *Thin-Walled Structures*, 47(12):1597–1607, 2009b. ISSN 02638231. doi:10.1016/j.tws.2009.05.001.

A. Movchan, N. Movchan, and S. Haq. Localised vibration modes and stop bands for continuous and discrete periodic structures. *Materials Science and Engineering: A*, 431(1-2):175–183, Sept. 2006. ISSN 09215093. doi:10.1016/j.msea.2006.05.145.

A. Movchan, N. Movchan, and R. McPhedran. Bloch–Floquet bending waves in perforated thin plates. *Proceedings of the Royal Society A: Mathematical, Physical and Engineering Sciences*, 463(2086):2505–2518, Oct. 2007. ISSN 1364-5021, 1471-2946. doi:10.1098/rspa.2007.1886.

T. Müller-Reichert, R. Kiewisz, and S. Redemann. Mitotic spindles revisited – new insights from 3D electron microscopy. *Journal of Cell Science*, 131(3):jcs211383, Feb. 2018. ISSN 0021-9533, 1477-9137. doi:10.1242/jcs.211383.

T. Mullin, S. Deschanel, K. Bertoldi, and M. C. Boyce. Pattern Transformation Triggered by Deformation. *Physical Review Letters*, 99(8), Aug. 2007. ISSN 0031-9007, 1079-7114. doi:10.1103/PhysRevLett.99.084301.

N. I. Muskhelishvili. *Some Basic Problems of the Mathematical Theory of Elasticity*. Springer Netherlands, 1977. ISBN 978-90-01-60701-2.

F. Nedelec and D. Foethke. Collective Langevin dynamics of flexible cytoskeletal fibers. *New Journal of Physics*, 9(9), 2007. ISSN 13672630. doi:10.1088/1367-2630/9/11/427.

T. Nguyen-Thoi, T. Bui-Xuan, P. Phung-Van, H. Nguyen-Xuan, and P. Ngo-Thanh. Static, free vibration and buckling analyses of stiffened plates by CS-FEM-DSG3 using triangular elements. *Computers & Structures*, 125:100–113, Sept. 2013. ISSN 00457949. doi:10.1016/j.compstruc.2013.04.027.

F. M. Nixon, C. Gutiérrez-Caballero, F. E. Hood, D. G. Booth, I. A. Prior, and S. J. Royle. The mesh is a network of microtubule connectors that stabilizes individual kinetochore fibers of the mitotic spindle. *eLife*, 4(JUNE2015):1–21, 2015. ISSN 2050084X. doi:10.7554/eLife.07635.

B. Nour-Omid, B. N. Parlett, and R. L. Taylor. Lanczos versus subspace iteration for solution of eigenvalue problems. *International Journal for Numerical Methods in Engineering*, 19(6): 859–871, 1983. ISSN 10970207. doi:10.1002/nme.1620190608.

M. Novak, B. Polak, J. Simunić, Z. Boban, B. Kuzmić, A. W. Thomae, I. M. Tolić, and N. Pavin. The mitotic spindle is chiral due to torques within microtubule bundles. *Nature Communications*, 9(1):3571, Sept. 2018. ISSN 2041-1723. doi:10.1038/s41467-018-06005-7.

L. Novotny. Strong coupling, energy splitting, and level crossings: A classical perspective. *American Journal of Physics*, 78(11):1199–1202, Nov. 2010. ISSN 0002-9505, 1943-2909. doi:10.1119/1.3471177.

J. W. Obreimoff. The splitting strengh of mica. *Proc. Roy. Soc. Lond.*, A127(805):290–297, 1930.

B. J. Olson, S. W. Shaw, C. Shi, C. Pierre, and R. G. Parker. Circulant Matrices and Their Application to Vibration Analysis. *Applied Mechanics Reviews*, 66(4):040803, June 2014. doi:10.1115/1.4027722.

V. I. Oseledets. A multiplicative ergodic theorem. Characteristic Ljapunov, exponents of dynamical systems. *Trans. Moscow Math. Soc.*, 19:33, 1968.

S. Paik, S. Gupta, and R. Batra. Localization of buckling modes in plates and laminates. *Composite Structures*, 120:79–89, 2015. ISSN 02638223. doi:10.1016/j.compstruct.2014.09.035.

F. Pampaloni, G. Lattanzi, A. Jonas, T. Surrey, E. Frey, and E.-L. Florin. Thermal fluctuations of grafted microtubules provide evidence of a length-dependent persistence length. *Proceedings of the National Academy of Sciences*, 103(27):10248–10253, 2006. ISSN 0027-8424. doi:10.1073/pnas.0603931103.

M. Pastor, M. Binda, and T. Harčarik. Modal assurance criterion. In *Procedia Engineering*, volume 48, pages 543–548, 2012. ISBN 1877-7058. doi:10.1016/j.proeng.2012.09.551.

L. Peng, K. Liew, and S. Kitipornchai. Buckling and free vibration analyses of stiffened plates using the FSDT mesh-free method. *Journal of Sound and Vibration*, 289(3):421–449, Jan. 2006. ISSN 0022460X. doi:10.1016/j.jsv.2005.02.023.

P. Peralta. Polymer Matrix Composites. http://faculty.engineering.asu.edu/pperalta/?page_id=95, Oct. 2013.

S. Petry. Mechanisms of Mitotic Spindle Assembly. *Annual Review of Biochemistry*, 85(1): 659–683, 2016. doi:10.1146/annurev-biochem-060815-014528.

A. S. Phani, J. Woodhouse, and N. A. Fleck. Wave propagation in two-dimensional periodic lattices. *The Journal of the Acoustical Society of America*, 119(4):1995–2005, Apr. 2006. ISSN 0001-4966. doi:10.1121/1.2179748.

S. S. Photos. Stair hole in the Jurassic coast. https://www.sciencestockphotos.com/free/geology/slides/stair_hole.html, 2019.

C. Pierre. Mode localization and eigenvalue loci veering phenomena in disordered structures. *Journal of Sound and Vibration*, 126(3):485–502, Nov. 1988. ISSN 10958568. doi:10.1016/0022-460X(88)90226-X.

C. Pierre and R. H. Plaut. Curve veering and mode localization in a buckling problem. *ZAMP Journal of Applied Mathematics and Physics*, 40(5):758–761, 1989. ISSN 00442275. doi:10.1007/BF00945875.

D. Pihler-Puzović, A. L. Hazel, and T. Mullin. Buckling of a holey column. *Soft Matter*, 12(34): 7112–7118, 2016. ISSN 1744-683X. doi:10.1039/C6SM00948D.

Pizhong Qiao and Fangliang Chen. On the Compliance and Energy Release Rate of Generically-unified Beam-type Fracture Specimens. *Journal of Composite Materials*, 45(1):65–101, 2011. doi:10.1177/0021998310371545.

J. R. Raney, N. Nadkarni, C. Daraio, D. M. Kochmann, J. A. Lewis, and K. Bertoldi. Stable propagation of mechanical signals in soft media using stored elastic energy. *Proceedings of the National Academy of Sciences*, 113(35):9722–9727, Aug. 2016. ISSN 0027-8424, 1091-6490. doi:10.1073/pnas.1604838113.

D. Raviv, W. Zhao, C. McKnelly, A. Papadopoulou, A. Kadambi, B. Shi, S. Hirsch, D. Dikovsky, M. Zyracki, C. Olguin, R. Raskar, and S. Tibbits. Active Printed Materials for Complex Self-Evolving Deformations. *Scientific Reports*, 4(1), May 2015. ISSN 2045-2322. doi:10.1038/srep07422.

J. Remmers and R. de Borst. Delamination buckling of fibre–metal laminates. *Composites Science and Technology*, 61(15):2207–2213, 2001. ISSN 02663538. doi:10.1016/S0266-3538(01)00114-2.

D. P. Richman, R. M. Stewart, J. W. Hutchinson, and V. S. Caviness. Mechanical Model of Brain Convolutional Development. *Science*, 189(4196):18–21, 1975. ISSN 0036-8075.

R. Rikards, A. Chate, and O. Ozolinsh. Analysis for buckling and vibrations of composite stiffened shells and plates. *Composite Structures*, page 10, 2001.

U. Rodman, M. Saje, I. Planinc, and D. Zupan. Exact buckling analysis of composite elastic columns including multiple delamination and transverse shear. *Engineering Structures*, 30(6): 1500–1514, 2008. ISSN 01410296. doi:10.1016/j.engstruct.2007.10.003.

B. Rosenstock and E. M. Richard. Vibrations of Disordered Solids. *Physical Review*, 176(3): 1004–1014, 1968.

H. B. Rosenstock and R. E. McGill. Vibrational Modes of Disordered Linear Chains. *Journal of Mathematical Physics*, 3(1):200, 1962. ISSN 00222488. doi:10.1063/1.1703780.

B. Rubinstein, K. Larripa, P. Sommi, and A. Mogilner. The elasticity of motor–microtubule bundles and shape of the mitotic spindle. *Physical Biology*, 6(1):016005, Feb. 2009. ISSN 1478-3975. doi:10.1088/1478-3975/6/1/016005.

S. Savel'ev and F. Nori. Magnetic and mechanical buckling: Modified Landau theory approach to study phase transitions in micromagnetic disks and compressed rods. *Physical Review B*, 70(21), Dec. 2004. ISSN 1098-0121, 1550-235X. doi:10.1103/PhysRevB.70.214415.

S. Savel'ev, X. Hu, and F. Nori. Quantum electromechanics: Qubits from buckling nanobars. *New Journal of Physics*, 8(6):105–105, June 2006. ISSN 1367-2630. doi:10.1088/1367-2630/8/6/105.

I. C. Scheperboer, E. Efthymiou, and J. Maljaars. Local buckling of aluminium and steel plates with multiple holes. *Thin-Walled Structures*, 99:132–141, 2016. ISSN 02638231. doi:10.1016/j.tws.2015.11.009.

J. Scholey, G. Civelekoglu-Scholey, and I. Brust-Mascher. Anaphase B. *Biology*, 5(4):51, Dec. 2016. ISSN 2079-7737. doi:10.3390/biology5040051.

M. J. Shelley. The Dynamics of Microtubule/Motor-Protein Assemblies in Biology and Physics. *Annual Review of Fluid Mechanics*, 48(1):487–506, 2016. ISSN 0066-4189. doi:10.1146/annurev-fluid-010814-013639.

J. Shim, C. Perdigou, E. R. Chen, K. Bertoldi, and P. M. Reis. Buckling-induced encapsulation of structured elastic shells under pressure. *Proceedings of the National Academy of Sciences*, 109(16):5978–5983, 2012. ISSN 0027-8424. doi:10.1073/pnas.1115674109.

P. Singhatanadgid and T. Singhanart. The Kantorovich method applied to bending, buckling, vibration, and 3D stress analyses of plates: A literature review. *Mechanics of Advanced Materials and Structures*, 26(2):170–188, Jan. 2019. ISSN 1537-6494, 1537-6532. doi:10.1080/15376494.2017.1365984.

M. Soheilypour, M. Peyro, S. J. Peter, and M. R. K. Mofrad. Buckling behavior of individual and bundled microtubules. *Biophysical Journal*, 108(7):1718–1726, 2015. ISSN 15420086. doi:10.1016/j.bpj.2015.01.030.

K. Son, J. S. Guasto, and R. Stocker. Bacteria can exploit a flagellar buckling instability to change direction. *Nature Physics*, 9(8):494–498, Aug. 2013. ISSN 1745-2473, 1745-2481. doi:10.1038/nphys2676.

S. H. Strogatz. *Nonlinear Dynamics and Chaos : With Applications to Physics, Biology, Chemistry, and Engineering*. CRC Press, May 2018. ISBN 978-0-429-49256-3. doi:10.1201/9780429492563.

Studco. Steel Stud Framing Systems from Studco. https://www.archdaily.com/catalog/us/products/16209/crocstud-steel-stud-framing-systems-studco, 2019.

R. Subramanian, E. M. Wilson-Kubalek, C. P. Arthur, M. J. Bick, E. A. Campbell, S. A. Darst, R. A. Milligan, and T. M. Kapoor. Insights into Antiparallel Microtubule Crosslinking by PRC1, a Conserved Nonmotor Microtubule Binding Protein. *Cell*, 142(3):433–443, Aug. 2010. ISSN 00928674. doi:10.1016/j.cell.2010.07.012.

E. Q. Sun. Shear Locking and Hourglassing in MSC Nastran, ABAQUS, and ANSYS. In *2006 VPD Conference - Proceedings*, page 9, Huntington Beach, California, July 2006. MSC Software.

M. Tabaddor, P. D. Gandhi, and G. Jones. Thermo-mechanical Analysis of Fire Doors Subjected to a Fire Endurance Test. *Journal of Fire Protection Engineering*, 19(1):51–71, Feb. 2009. ISSN 1042-3915. doi:10.1177/1042391508098899.

S. Timoshenko and J. N. Goodier. Theory of Elasticity. *Journal of Elasticity*, 49:427–143, 1986. ISSN 0070858055. doi:10.1007/BF00046464.

S. P. S. Timoshenko and J. M. J. Gere. *Theory of Elastic Stability*. Courier Corporation, 2012. ISBN 0-486-13480-6.

I. M. Tolić. Mitotic spindle: Kinetochore fibers hold on tight to interpolar bundles. *European Biophysics Journal*, July 2017. ISSN 0175-7571, 1432-1017. doi:10.1007/s00249-017-1244-4.

M. G. L. Van den Heuvel, M. P. De Graaff, and C. Dekker. Microtubule curvatures under perpendicular electric forces reveal a low persistence length. *Proceedings of the National Academy of Sciences*, 105(23):7941–7946, 2008. doi:10.1073/pnas.0704169105.

A. Vizzini and P. Lagace. The Buckling of a Delaminated Sublaminate on an Elastic Foundation. *Composite Materials*, 21(12):1106–1117, 1987. ISSN 0021-9983. doi:10.1177/002199838702101202.

Y. Wan-Lee. Axisymmetric buckling and growth of a circular delamination in a compressed laminate. *International Journal of Solids and Structures*, 21(5):503–514, 1985. ISSN 00207683. doi:10.1016/0020-7683(85)90011-3.

C. Y. Wang, C. Q. Ru, and A. Mioduchowski. Orthotropic elastic shell model for buckling of microtubules. *Physical Review E*, 74(5):052901, Nov. 2006. ISSN 1539-3755. doi:10.1103/PhysRevE.74.052901.

J. Wang and P. Qiao. Mechanics of Bimaterial Interface: Shear Deformable Split Bilayer Beam Theory and Fracture. *Journal of Applied Mechanics*, 72(5):674, 2005. ISSN 00218936. doi:10.1115/1.1978920.

P. Wang, J. Shim, and K. Bertoldi. Effects of geometric and material nonlinearities on tunable band gaps and low-frequency directionality of phononic crystals. *Physical Review B*, 88(1), July 2013. ISSN 1098-0121, 1550-235X. doi:10.1103/PhysRevB.88.014304.

P. Wang, L. Lu, and K. Bertoldi. Topological Phononic Crystals with One-Way Elastic Edge Waves. *Physical Review Letters*, 115(10), Sept. 2015. ISSN 0031-9007, 1079-7114. doi:10.1103/PhysRevLett.115.104302.

J. J. Ward, H. Roque, C. Antony, and F. Nédélec. Mechanical design principles of a mitotic spindle. *eLife*, 3:e03398, 2014. ISSN 2050084X. doi:10.7554/eLife.03398.

G. Weick, F. Pistolesi, E. Mariani, and F. Von Oppen. Discontinuous Euler instability in nano-electromechanical systems. *Physical Review B - Condensed Matter and Materials Physics*, 81 (12), 2010. ISSN 10980121. doi:10.1103/PhysRevB.81.121409.

G. Weick, F. von Oppen, and F. Pistolesi. Euler buckling instability and enhanced current blockade in suspended single-electron transistors. *Physical Review B*, 83(3), Jan. 2011. ISSN 1098-0121, 1550-235X. doi:10.1103/PhysRevB.83.035420.

F. Williams and W. Wittrick. An Automatic Computational Procedure For Calculating Natural Frequencies Of Skeletal Structures. *International Journal of Mechanical Sciences*, 12:781–791, 1970.

A. Wolf, J. B. Swift, H. L. Swinney, and J. A. Vastano. Determining Lyapunov exponents from a time series. *Physica D: Nonlinear Phenomena*, 16(3):285–317, July 1985. ISSN 0167-2789. doi:10.1016/0167-2789(85)90011-9.

H.-Y. Wu, E. Nazockdast, M. J. Shelley, and D. J. Needleman. Forces positioning the mitotic spindle: Theories, and now experiments. *BioEssays*, 39(2):1600212, Feb. 2017. ISSN 02659247. doi:10.1002/bies.201600212.

W.-C. Xie. Buckling mode localization in randomly disordered multispan continuous beams. *AIAA Journal*, 33(6):1142–1149, June 1995. ISSN 0001-1452, 1533-385X. doi:10.2514/3.12534.

W.-C. Xie. Buckling mode localization in nonhomogeneous beams on elastic foundations. *Chaos, Solitons and Fractals*, 8(3):411–431, 1997. ISSN 09600779. doi:10.1016/S0960-0779(96)00099-9.

W.-C. Xie. Buckling mode localization in rib-stiffened plates with randomly misplaced stiffeners. *Computers & structures*, 67(1-3):175–189, 1998.

W.-C. Xie and I. Elishakoff. Buckling mode localization in rib-stiffened plates with misplaced stiffeners. Kantorovich approach. *Chaos, Solitons & Fractals*, 11(10):1559–1574, 2000.

W.-C. Xie and A. Ibrahim. Buckling mode localization in rib-stiffened plates with misplaced stiffeners in a fnite strip approach. *Chaos, Solitons & Fractals*, 11(10):1543–1558, 2000.

W.-C. Xie and X. Wang. Vibration Mode Localization in One-Dimensional Systems. *AIAA Journal*, 35(10):1645–1652, Oct. 1997a. ISSN 0001-1452, 1533-385X. doi:10.2514/2.4.

W.-C. Xie and X. Wang. Vibration Mode Localization in Two-Dimensional Systems. *AIAA Journal*, 35(10):1653–1659, Oct. 1997b. ISSN 0001-1452, 1533-385X. doi:10.2514/2.5.

F. Xu, M. Potier-Ferry, S. Belouettar, and H. Hu. Multiple bifurcations in wrinkling analysis of thin films on compliant substrates. *International Journal of Non-Linear Mechanics*, 76: 203–222, 2015. ISSN 00207462. doi:10.1016/j.ijnonlinmec.2014.12.006.

D. Yang, B. Mosadegh, A. Ainla, B. Lee, F. Khashai, Z. Suo, K. Bertoldi, and G. M. Whitesides. Buckling of Elastomeric Beams Enables Actuation of Soft Machines. *Advanced Materials*, 27 (41):6323–6327, 2015. ISSN 1521-4095. doi:10.1002/adma.201503188.

G. L. Yu, Y. S. Wang, and J. Lan. Vibration localization in disordered periodically stiffened double-leaf panels. *Archive of Applied Mechanics*, 80(6):687–697, 2010. ISSN 09391533. doi:10.1007/s00419-009-0339-5.

C. Zener. Non-Adiabatic Crossing of Energy Levels. *Proceedings of the Royal Society*, pages 696–702, 1932.

R. Zhang, B. LaFrance, and E. Nogales. Separating the effects of nucleotide and EB binding on microtubule structure. *Proceedings of the National Academy of Sciences*, 115(27):E6191–E6200, July 2018. ISSN 0027-8424, 1091-6490. doi:10.1073/pnas.1802637115.

L. Ziman. *Principles of the Theory of Solids*. Cambridge University Press, second edition edition, 1972.